

COSMOLOGICAL DYNAMICS OF ANISOTROPIC KANIADAKIS HOLOGRAPHIC DARK ENERGY MODEL IN BRANS-DICKE GRAVITY

 A. Vijaya Prasanthi^{a,b},  G. Suryanarayana^c,  Y. Aditya^{d*},  U.Y. Divya Prasanthi^e

^aAU Trans-Disciplinary Research Hub, Andhra University, Visakhapatnam-530003, India

^bDepartment of Mathematics, Sri Vishnu Engineering College for Women, Bhimavaram-534201, India

^cDepartment of Mathematics, ANITS, Visakhapatnam-533003, India

^dDepartment of Mathematics, GMR Institute of Technology, Rajam-532127, India

^eDepartment of Statistics & Mathematics, College of Horticulture, Dr. Y.S.R. Horticultural University, Parvathipuram-535502, India

*Corresponding Author e-mail: aditya.y@gmrit.edu.in

Received January 23 2024; revised March 2, 2024; accepted April 8, 2024

The present study examines the Kaniadakis holographic dark energy in the context of the Brans-Dicke scalar-tensor theory of gravity (Phys. Rev. 124: 925, 1961). This paper focuses on a background with an anisotropic Kantowski-Sachs space-time that is homogeneous in space. Under these circumstances, the Brans-Dicke scalar field denoted as ϕ is used as a function of the average scale factor $a(t)$. Using a graphical model to analyze the model's physical behaviour is part of the inquiry into the Universe's accelerating expansion. We evaluate the cosmological parameters such as the scalar field, the equation of state parameter and the deceleration parameter. Furthermore, the models' stability is assessed through the application of the squared sound speed (v_s^2). For our models, we derive the widely accepted cosmic planes such as $\omega_{kde} - \omega'_{kde}$ and statefinder (r,s) planes. It is found that the scalar field is a decreasing function of cosmic time and hence the corresponding kinetic energy increases. The deceleration parameter exhibits accelerated expansion of the Universe. It is mentioned here that the equation of state parameter lies in the phantom region and finally attains the Λ CDM model. Also, the $\omega_{kde} - \omega'_{kde}$ plane provides freezing and thawing regions. In addition, the statefinder plane also corresponds to the Λ CDM model. Finally, it is remarked that all the above constraints of the cosmological parameters show consistency with Planck observational data.

Keywords: Scalar-tensor theory; Scalar field; Holographic dark energy; Kantowski-Sachs model

PACS: 98.80.-k, 95.36.+x

1. INTRODUCTION

Recent observational data on the history of cosmic expansion have enabled the discovery of the universe's accelerating expansion conceivable, as provided in the works of Perlmutter et al. [1] and Riess et al. [2]. As a mysterious and intensely pressured force, dark energy (DE) is thought to be the fundamental reason. Nevertheless, the traits and behaviours of DE remain a mystery. Two main approaches are available to tackle the problem of cosmic acceleration: the first one includes introducing a DE component into the Universe and studying its dynamics. (Caldwell [3]; Padmanabhan [4]; Santhi et al. [5], The alternative, however, involves investigating changes to Einstein's theory of gravitation and viewing them as a flaw in general relativity.

Among dynamical differential equation models, the holographic DE (HDE) model has become an important instrument to study the mystery of DE in recent years. Based on the quantum characteristics of black holes (BHs), which have been thoroughly studied in the literature to analyze the idea of quantum gravity, this study's research was carried out. [6]. The vacuum energy \mathcal{A} of a system of size L should not be greater than the mass of a BH of the same size, according to the holographic principle, a hypothesis in quantum field theory. Within the context of quantum field theory, this idea is essential to comprehend the genesis of BHs. The study carried out established the formal energy density of HDE by Cohen et al. [7]. The equation provided may be rewritten more academically as follows:

$$\rho_{kde} = 3d^2 m_p^2 L^{-2}. \quad (1)$$

In this case, the Planck mass reduction is represented by m_p , the numerical constant is represented by $3d^2$, and the IR cutoff is indicated as L . The literature has researched several infrared cutoffs in great detail, including the Hubble horizon H^{-1} , the event horizon, the particle horizon, the conformal universe age, the Ricci scalar radius, and the Granda-Oliveros cutoff [8]. Examining the current acceleration of the universe is made possible by the use of HDE models with various IR cutoffs, offering insights into the transition redshift value that signifies the change from early deceleration ($q > 0$) to present acceleration ($q < 0$). This research shows that the transition redshift value aligns with current observational data. Moreover, it could offer a possible resolution to the puzzle of cosmic coincidence, which concerns the puzzling topic of why, in the current state of the universe, the energy densities originating from dark matter and DE display a constant ratio. A respectable degree of agreement between the HDE model and observational data has been demonstrated by numerous investigations [9]. Nojiri and Odintsov [10] presented a methodology in their work that uses

phantom cosmology and generalized HDE to try and reconcile the early and late epochs of the universe. In research by Ghaffari [11], the HDE model was examined to determine whether the generalized laws of thermodynamics held in the context of the D-dimensional Kaluza-Klein-type FRW world. Various cosmological components of new and updated HDE models have been investigated by Aditya and Reddy [12]. As a generic entropy metric, Kaniadakis statistics have recently been used to examine various gravitational and cosmological implications [13]. The generalized \mathcal{K} -entropy (Kaniadakis), a single free parameter entropy of a BH is obtained as [14]

$$S_{\mathcal{K}} = \frac{1}{\mathcal{K}} \sinh(\mathcal{K}S_{BH}), \quad (2)$$

where \mathcal{K} is an unknown parameter.

Consequently, a new model of DE known as Kaniadakis Holographic DE (KHDE) [14] is presented utilizing this entropy and holographic DE theory, which exposes considerable properties. Jawad and Sultan [15] have discussed KHDE models in different theories of gravity. As Tsallis and Kaniadakis, Sadeghi et al. [16] have examined the dynamic structures of HDE within the context of the Brans-Dicke theory of gravity.

Many entropy-related formalisms have been applied recently to the development and examination of cosmological models. Several new HDE models have been put out, such as the Renyi HDE (RHDE) model [17], the Tsallis HDE (THDE) [18], and the Sharma-Mittal HDE (SMHDE) [19]. Conversely, in the case of non-interacting cosmic systems, the SMHDE theory exhibits classical stability. The RHDE theory shows better stability when viewed individually and is predicated on the idea that cosmic sectors are not connected. The Tsallis, Renyi, and Sharma-Mittal entropies are investigated in the work by Younas et al. [20] in a flat Friedmann-Robertson-Walker (FRW) universe with Chern-Simons modified gravity. In the THDE, Aditya et al. [21] examined the empirical constraints on the logarithmic Brans-Dicke theory of gravity. The authors Prasanthi and Aditya have conducted a study on the observational restrictions in RHDE [22, 23]. In their study, Sharma and Dubey [23] examined the SMHDE models using several diagnostic methods. In light of the aforementioned research, we have chosen to examine the HDE using a novel entropy formalism known as the SMHDE, with the Hubble horizon serving as the infrared cutoffs in our investigation.

The statistical isotropy of the universe is called into question discovery of large variances in cosmic microwave background radiation at wide angles. Even in the absence of inflation, the universe may have some anisotropic geometry within the framework of cosmological theories. Several researchers have recently become quite interested in investigating different cosmological models with anisotropic backdrops. Within the context of the Brans-Dicke theory of gravity [25], this study attempts to explore the Kantowski-Sachs universe taking into account the effects of pressureless matter and KHDE. The suggested work plan's outline is given below. Both the derivation of field equations and their solutions are covered in Section 2. Section 3 examines the model's physical properties. Section 4 contains the comparison of our work with the observational data. The paper's conclusions and a final summary are presented in the last section.

2. FIELD EQUATIONS AND THE MODEL

There have been several gravitational theories put forth as alternatives to Einstein's general theory of gravity. But the most effective substitute for Einstein's theory is thought to be the scalar-tensor theory created by Brans and Dicke [25]. Assume that the universe is composed of DE with a density of ρ_{kde} and pressure-free matter with an energy density of ρ_m . For the combined scalar and tensor fields, the Brans-Dicke field equations are thus provided in this instance by

$$R_{ij} - \frac{1}{2}Rg_{ij} = -\frac{8\pi}{\phi}(T_{ij} + \bar{T}_{ij}) - \phi^{-1}(\phi_{;i,j} - g_{ij}\phi_{;,\alpha}^{\alpha}) - w\phi^{-2}(\phi_{;i}\phi_{;j} - \frac{1}{2}g_{ij}\phi_{;,\alpha}\phi^{;\alpha}), \quad (3)$$

$$\phi_{;,\alpha}^{\alpha} = \frac{8\pi}{(3+2w)}(T + \bar{T}), \quad (4)$$

and the energy conservation equation is

$$(T_{ij} + \bar{T}_{ij})_{;j} = 0, \quad (5)$$

which is the result of field equations (3) and (4). In this case, R is a Ricci scalar, R_{ij} is a Ricci tensor, and w is a dimensionless coupling constant. T_{ij} and \bar{T}_{ij} are energy-momentum tensors for pressure-less matter and KHDE, which are defined as

$$T_{ij} = \rho_m u_i u_j; \quad \bar{T}_{ij} = (\rho_{kde} + p_{kde})u_i u_j - p_{kde}g_{ij}, \quad (6)$$

here p_{kde} and ρ_{kde} are the pressure and energy density of DE respectively and ρ_m is the energy density of matter. The equation of state (ω_{kde}) parameter of DE is defined as $\omega_{kde} = \frac{p_{kde}}{\rho_{kde}}$.

We consider the Kantowski-Sachs space-time in the following form

$$ds^2 = dt^2 - A^2 dr^2 - B^2(d\psi^2 + \sin^2\psi d\varphi^2), \quad (7)$$

where A and B are metric potentials and only cosmic time t functions. The Kantowski-Sachs class of metrics describes anisotropic and homogenous yet expanding cosmologies. They also provide models for estimating and comparing the consequences of anisotropies with the FRW class of cosmologies (Thorne [26]). For the Kantowski-Sachs model (7), we define the main parameters:

Hubble's parameter of the model

$$H = \frac{\dot{a}}{a} \tag{8}$$

where

$$a(t) = (AB^2)^{1/3} \tag{9}$$

is the average scale factor. Anisotropic parameter A_h is given by

$$A_h = \frac{1}{3} \sum_{i=1}^3 \left(\frac{H_i - H}{H} \right)^2, \tag{10}$$

where $H_1 = \frac{\dot{A}}{A}, H_2 = H_3 = \frac{\dot{B}}{B}$ are directional Hubble's parameters, which express the expansion rates of the universe in the directions of x, y and z respectively.

Expansion scalar and shear scalar are defined as

$$\theta = u^i_{;i} = \frac{\dot{A}}{A} + 2 \frac{\dot{B}}{B}, \tag{11}$$

$$\sigma^2 = \frac{1}{2} \sigma^{ij} \sigma_{ij} = \frac{1}{3} \left(\frac{\dot{A}}{A} - \frac{\dot{B}}{B} \right)^2, \tag{12}$$

where σ_{ij} is the shear tensor, A_h is the deviation from isotropic expansion and the universe expands isotropically if $A_h = 0$. The deceleration parameter is given by

$$q = \frac{d}{dt} \left(\frac{1}{H} \right) - 1. \tag{13}$$

If $-1 \leq q < 0$, the universe expands at an accelerating rate, decelerating volumetric expansion if $q > 0$. If $q = 0$, the universe expands at a constant rate.

The field equations (3)-(5) for the metric (7) produce the following equations when adopting co-moving coordinates:

$$2 \frac{\ddot{B}}{B} + \frac{\dot{B}^2}{B^2} + \frac{1}{B^2} + \frac{w \dot{\phi}^2}{2 \phi^2} + \frac{\ddot{\phi}}{\phi} + 2 \frac{\dot{B} \dot{\phi}}{B \phi} = - \frac{\omega_{kde} \rho_{kde}}{\phi}, \tag{14}$$

$$\frac{\ddot{A}}{A} + \frac{\dot{B}}{B} + \frac{\dot{A} \dot{B}}{AB} + \frac{w \dot{\phi}^2}{2 \phi^2} + \frac{\ddot{\phi}}{\phi} + \frac{\dot{\phi}}{\phi} \left(\frac{\dot{A}}{A} + \frac{\dot{B}}{B} \right) = - \frac{\omega_{kde} \rho_{kde}}{\phi}, \tag{15}$$

$$2 \frac{\dot{A} \dot{B}}{AB} + \frac{\dot{B}^2}{B^2} + \frac{1}{B^2} - \frac{w \dot{\phi}^2}{2 \phi^2} + 3 \frac{\dot{\phi}}{\phi} H = \frac{\rho_m + \rho_{kde}}{\phi}, \tag{16}$$

$$\ddot{\phi} + 3 \dot{\phi} H = \frac{8\pi}{\phi(3+2w)} (\rho_{kde} - 3p_{kde} + \rho_m), \tag{17}$$

and the conservation equation is given by

$$\dot{\rho}_m + \dot{\rho}_{kde} + 3H(\rho_m + (1 + \omega_{kde})\rho_{kde}) = 0. \tag{18}$$

We assume that there is minimal interaction between the DE, $\bar{T}_{ij} = 0$ and that the pressure-less matter component is minimally interacting, $T_{ij} = 0$, due to the energy conservation equation (5). Consequently, two additive conserved components have been extracted from the energy conservation equation (5): maintenance of the DE's energy-momentum tensor

$$\dot{\rho}_{kde} + 3H(1 + \omega_{kde})\rho_{kde} = 0, \tag{19}$$

and the conservation of the energy-momentum tensor of the pressure-less matter

$$\dot{\rho}_m + 3H\rho_m = 0, \tag{20}$$

here the overhead dot represents ordinary differentiation for cosmic time t .

$A, B, \phi, \omega_{kde}, \rho_{kde}$, and ρ_m are six unknown variables in the four equations (14)-(17). As a result, some extra constraints are required to solve the above system of equations. We build our computations on the following physically acceptable assumptions:

The shear scalar (σ) is regarded as proportionate to the expansion scalar (θ). As a result, the metric potentials are related to one another. (Collins et al. [27]), i.e.,

$$A = B^k. \quad (21)$$

where $k > 1$ is a constant that accounts for space-time anisotropy (we have taken the integration constant as a unity). The physical foundation for this assumption can be found in observations of the velocity redshift relation for extragalactic sources, which indicate that the Hubble expansion of the universe may achieve isotropy when σ/θ is constant.

In addition, it is common in the literature to employ a power-law relationship between scalar field ϕ and average scale factor $a(t)$ of the form (Johri and Sudharsan [28]; Johri and Desikan [29]) $\phi \propto [a(t)]^n$ where n denotes a power index. Many authors have looked into different aspects of this type of scalar field ϕ . Given the physical significance of the preceding relationship, we employ the following assumption to reduce the mathematical complexity of the system

$$\phi(t) = \phi_0[a(t)]^n, \quad (22)$$

where ϕ_0 is the proportionality constant.

From Eqs. (14), (15), (21) and (22), we obtain the metric potentials as

$$A = \left(\frac{t^2}{k-1} - A_1(k-1) \right)^{\frac{k}{2}}, \quad (23)$$

$$B = \sqrt{\frac{t^2}{k-1} - A_1(k-1)}, \quad (24)$$

where A_1 is integrating constant and $n(k+2) + 3k = 0$. Now, the scalar field ϕ calculated as

$$\phi(t) = \phi_0 \left(\frac{t^2}{k-1} - A_1(k-1) \right)^{\frac{1}{6n(k+2)}}. \quad (25)$$

Now the metric (7) can be rewritten as

$$ds^2 = dt^2 - \left(\frac{t^2}{k-1} - A_1(k-1) \right)^k dr^2 - \left(\frac{t^2}{k-1} - A_1(k-1) \right) (d\psi^2 + \sin^2\psi d\varphi^2). \quad (26)$$

3. COSMOLOGICAL PARAMETERS AND DISCUSSION

Equation (26), in conjunction with equation (25) illustrates the Kantowski-Sachs universe with Kaniadakis HDE in Brans-Dicke's theory of gravity. The following geometrical and physical factors are crucial to the debate of cosmology. The spatial volume (V) and average scale factor ($a(t)$) of the model are given by

$$V(t) = [a(t)]^3 = \left(\frac{t^2}{k-1} - A_1(k-1) \right)^{\frac{k+2}{2}}. \quad (27)$$

Mean Hubble's parameter (H) and expansion scalar (θ) are obtained as

$$H = \frac{\theta}{3} = \frac{(k+2)t}{3t^2 - 3A_1(k-1)^2}. \quad (28)$$

The shear scalar (σ^2) and anisotropic parameter (A_h) are

$$\sigma^2 = \frac{(k-1)^2 t^2}{3(t^2 - A_1(k-1)^2)^2}, \quad (29)$$

$$A_h = \frac{2(k-1)^2}{(k+2)^2}. \quad (30)$$

Eq. (26) indicates the spatially homogeneous and anisotropic Kantowski - Sachs KHDE cosmological model in the Brans-Dicke theory of gravity. There is no initial singularity in our model, i.e. at $t = 0$. From a finite volume when $t = 0$, the model's spatial volume increases with time. This indicates that the model's spatial expansion. At $t = 0$, the parameters $H(t)$, $\theta(t)$, and σ^2 are finite and tend to infinity as $t \rightarrow \infty$. The mean anisotropic parameter A_h represents the deviation from isotropic expansion. It establishes the anisotropic or isotropic nature of the model. When $k = 1$, A_h equals 0. In this instance, the expansion of the universe is isotropic. In addition, if $V \rightarrow \infty$ and $A_h = 0$ as $t \rightarrow \infty$, The model steadily gets closer to isotropy.

According to the HDE, if DE is meant to regulate the universe's current, accelerated expansion, then, taking into account the Kaniadakis BH entropy equation (2), the total vacuum energy contained in a box of a certain size L^3 must not surpass the energy of a BH of the same mass. Next, one obtains

$$\Lambda^4 \equiv \rho_{kde} \propto \frac{\delta \mathcal{K}}{L^4}, \tag{31}$$

for the vacuum energy ρ_{kde} . Now, taking the Hubble horizon of the universe as the IR cutoff (i.e., $L = \frac{1}{H}, A = \frac{4\pi}{H^2}$),

$$\rho_{kde} = \frac{3\mathcal{C}^2 H^4}{\mathcal{K}} \sinh\left(\frac{\pi \mathcal{K}}{H^2}\right), \tag{32}$$

where the constant \mathcal{C}^2 is unknown, \mathcal{K} belongs to a set of real numbers, and $H = \frac{\dot{a}}{a}$ is the Hubble parameter. Now, it's evident that we have $\rho_{kde} \rightarrow \frac{3\mathcal{C}^2 H^4}{\mathcal{K}}$ (the well-known Bekenstein entropy-based HDE) when $k \rightarrow 0$. Considering the pressureless fluid (with energy density ρ_m) and the DE candidate (with pressure p_{kde} and density ρ_{kde}). The fractional energy densities of matter (Ω_m) and DE (Ω_{kde}) are given as

$$\Omega_m = \frac{\rho_m}{\rho_{cr}} = \frac{\rho_m}{3H^2} \quad \text{and} \quad \Omega_{kde} = \frac{\rho_{kde}}{\rho_{cr}} = \frac{\mathcal{C}^2 H^2}{\mathcal{K}} \sinh\left(\frac{\pi \mathcal{K}}{H^2}\right), \tag{33}$$

ρ_{cr} is the critical energy density. The above equation can be written using Eq. (28) as

$$\rho_{kde}(t) = \frac{3d^2(k+2)^4 t^4}{(3t^2 - 3A_1(k-1)^2)^4 \delta} \sinh\left(\frac{\pi \delta (3t^2 - 3A_1(k-1)^2)^2}{(k+2)^2 t^2}\right). \tag{34}$$

From Eqs. (14) and (27), we get the energy density of matter as

$$\rho_m(t) = \rho_0 \left[\frac{t^2}{k-1} - A_1(k-1) \right]^{\frac{-(k+2)}{2}}. \tag{35}$$

Using Eqs. (23)-(25) in Eq. (14), we get the EoS parameter as

$$\begin{aligned} \omega_{kde}(t) = & -\frac{\phi_0(3t^2 - 3A_1(k-1)^2)^4 \delta}{3d^2(k+2)^4 t^4} \left(\frac{t^2}{k-1} - A_1(k-1) \right)^{\frac{1}{6n(k+2)}} \left\{ \frac{-3A_1(k-1)^2}{(t^2 - A_1(k-1)^2)^2} + \frac{k(k-1)(t^2 - A_1(k-1))}{(t^2 - A_1(k-1)^2)^2} + \right. \\ & \frac{(k+1)t^2}{(t^2 - A_1(k-1)^2)^2} + \frac{wn^2(k+2)^2 t^2}{(3t^2 - 3A_1(k-1)^2)^2} + \frac{2n(k+2)(n(k+2)t^2 - 3t^2 - 3A_1(k-1)^2)}{9(t^2 - A_1(k-1)^2)^2} + \frac{n(k+3)(k+2)t^2}{3(t^2 - A_1(k-1)^2)^2} \\ & \left. + \left(\frac{t^2}{k-1} - A_1(k-1) \right)^{-1} \right\} \left(\sinh\left(\frac{\pi \delta (3t^2 - 3A_1(k-1)^2)^2}{(k+2)^2 t^2}\right) \right)^{-1}. \end{aligned} \tag{36}$$

Scalar field: We plotted a scalar field's behaviour against cosmic time for a range of parameter values. k in Fig. 1. One way to conceptualize the scalar field is as a positive, declining function that ultimately approaches a minimum positive value. Because of the scalar field's diminishing behaviour, the corresponding kinetic energy rises. This behaviour closely resembles that of scalar fields in DE models that have been developed by several writers and published in literature (Aditya and Reddy [30]). Moreover, it is evident that when parameter k rises, the scalar field contracts. Hence, in this work, Examining the additional dynamical parameters in the context of the BD scalar field is our goal.

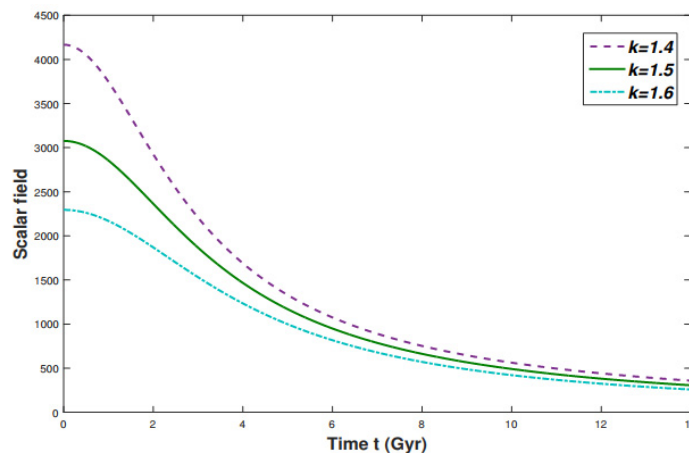


Figure 1. Plot of scalar field ϕ versus cosmic time t for $\phi_0 = 28000$ and $A_1 = -38$

Energy conditions: The Raychaudhuri equations provide the foundation for the study of energy conditions and are essential to any analysis of the congruence of time-like and null geodesics. Energy conditions are used to illustrate other general conclusions regarding the behaviour of powerful gravitational fields. These are the typical energy scenarios:

- Dominant energy condition (DEC): $\rho_{kde} \geq 0, \rho_{kde} \pm p_{kde} \geq 0$.
- Strong energy conditions (SEC) : $\rho_{kde} + p_{kde} \geq 0, \rho_{kde} + 3p_{kde} \geq 0$,
- Null energy conditions (NEC): $\rho_{kde} + p_{kde} \geq 0$,
- Weak energy conditions (WEC): $\rho_{kde} \geq 0, \rho_{kde} + p_{kde} \geq 0$,

Fig. 2 depicts the energy conditions for our KHDE model. It is clear that the NEC is violated, and the model results in a Big Rip. Furthermore, the WEC is observed to comply with the requirement $\rho_{de} \geq 0$. In addition, Fig. 2 shows that the DEC $\rho_{de} + p_{de}$ is not satisfied. Furthermore, our model appropriately violates the SEC. This tendency, Which results from the late-time acceleration of the universe, corresponds with current observational data.

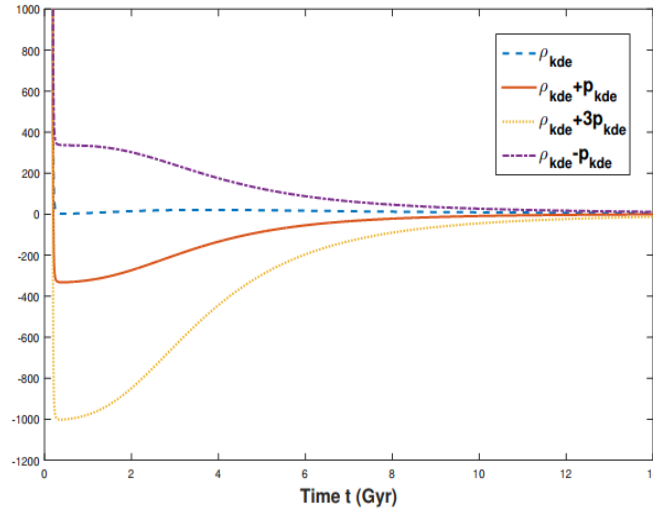


Figure 2. Plot of energy conditions versus cosmic time t for $\phi_0 = 28000, w = 0.025, \mathcal{K} = 0.001, \mathcal{C} = 9.2$ and $A_1 = -38$

EoS parameter: The definition of the EoS parameter is the correlation between DE’s pressure p_{kde} and energy density ρ_{kde} , which is expressed as $\omega_{kde} = \frac{p_{kde}}{\rho_{kde}}$. The universe’s accelerated and decelerated expansion are categorized using the EoS parameter, which separates epochs into the following groups: For $\omega = 1$ stiff fluid, $\omega = \frac{1}{3}$ radiation, and $\omega = 0$ matter commanded (dust) (decelerating phases). It symbolizes the quintessence $-1 < \omega < -1/3$, the cosmological constant $\omega = -1$, and the phantom $\omega < -1$.

The EoS parameter of our DE model is depicted in Fig. 3 for various values of \mathcal{C} . We note that the EoS parameter of our model starts in the aggressive phantom area ($\omega_{kde} \ll -1$) and finally attains Λ CDM model ($\omega_{kde} = -1$) and phantom region ($\omega_{kde} < -1$). According to current observational data, this behaviour is consistent, and the current value (at $t = 13.7 \text{ Gyr}$) of our DE model’s EoS parameter is in close approximation with current Planck data (Aghanim et al. [31]).

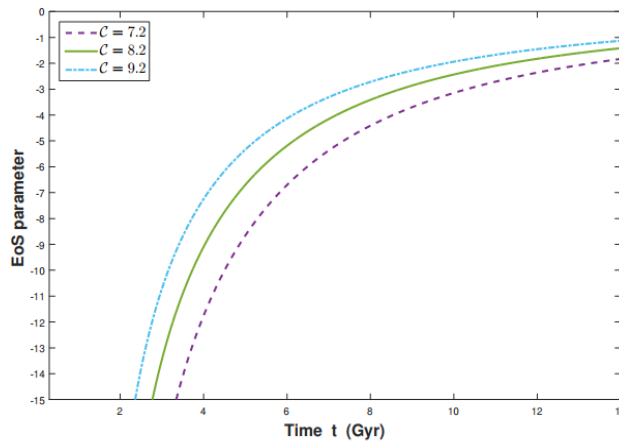


Figure 3. Plot of EoS parameter ω_{kde} versus cosmic time t for $\phi_0 = 28000, w = 0.025, \mathcal{K} = 0.001$ and $A_1 = -38$

$\omega_{kde} - \omega'_{kde}$ plane: The dynamical characteristic of models of DE is examined through the $\omega_{kde} - \omega'_{kde}$ plane analysis, where prime ($'$) signifies derivative with regard to $\ln a$. Caldwell and Linder [32] proposed this approach to analyse the behaviour of the quintessence model. They divided the $\omega_{kde} - \omega'_{kde}$ plane into thawing ($\omega_{kde} < 0$ and $\omega'_{kde} > 0$)

and freezing ($\omega_{kde} < 0$ and $\omega'_{kde} < 0$) areas. Researchers have expanded the scope of this planar study to analyze the dynamic behaviour of several DE models and modified theories of gravity [33]. Our DE model's $\omega_{kde}-\omega'_{kde}$ trajectory is depicted in Fig. 4 for distinct values of parameter \mathcal{C} as the $\omega_{kde}-\omega'_{kde}$ plane remains same for various values of \mathcal{C} . Both the thawing and freezing zones exhibit variation in the model; however, our model primarily fluctuates in the freezing region. The freezing region is where observational evidence indicates that the universe is expanding much more quickly. As a result, the behaviour of the $\omega_{kde}-\omega'_{kde}$ plane is in line with the available observations.

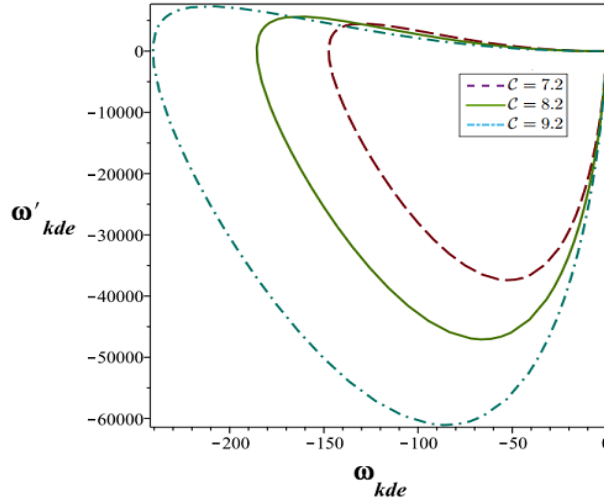


Figure 4. Plot of $\omega_{kde} - \omega'_{kde}$ plane for $\phi_0 = 28000$, $w = 0.025$, $\mathcal{K} = 0.001$, $\mathcal{C} = 9.2$ and $A_1 = -38$

Stability analysis: In this case, we evaluate our DE model's stability against minor perturbations using the squared speed of sound. The sign of the square of sound speed plays a vital role, as its negative ($v_s^2 < 0$) denotes instability and its positive ($v_s^2 > 0$) shows stability. It can be described as follows:

$$v_s^2 = \frac{\dot{p}_{kde}}{\dot{\rho}_{kde}} \tag{37}$$

By differentiating the EoS parameter $\omega_{kde} = \frac{p_{kde}}{\rho_{kde}}$ about time t and dividing by $\dot{\rho}_{kde}$, we get

$$v_s^2 = \omega_{kde} + \frac{\rho_{kde}}{\dot{\rho}_{kde}} \dot{\omega}_{kde} \tag{38}$$

We build the squared speed of sound trajectories in terms of cosmic time in the current scenario, as illustrated in Fig. 5 for various values of \mathcal{C} . We can witness from Fig. 5 that v_s^2 curve shows positive behaviour in the first epoch and changes in the negative section. As a result, our model is unstable at the present and in subsequent epochs of the universe, but stable at the beginning.

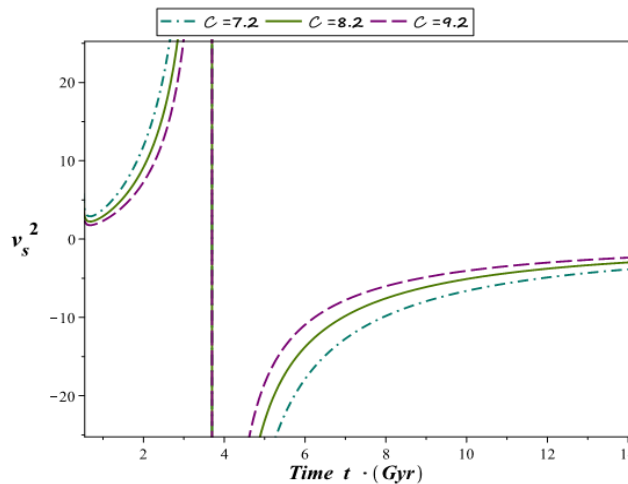


Figure 5. Plot of squared sound speed v_s^2 versus cosmic time t for $\phi_0 = 28000$, $w = 0.025$, $\mathcal{K} = 0.001$, $\mathcal{C} = 9.2$ and $A_1 = -38$

Deceleration parameter (DP): One crucial kinematical quantity is the deceleration parameter (q). This parameter shows the speed and slowness of the universe. There is an accelerating expansion if $-1 < q < 0$, a decelerating expansion if

$q > 0$, and a constant rate of expansion if $q = 0$. In addition, for $q = -1$, we get an exponential expansion and for $q < -1$, Our current growth is exponential. DP obtained for our model as

$$q(t) = \frac{3t + 3A_1(k-1)^2}{(k+2)t} - 1. \tag{39}$$

In Fig. 6, we have displayed the DP against cosmic time over a range of parameter k values. For all values of k , we observe that DP stays less than -1 and ultimately approaches -1 at late times. k , indicating that the universe is accelerating. As a result, The universe is expanding at an exponential rate.

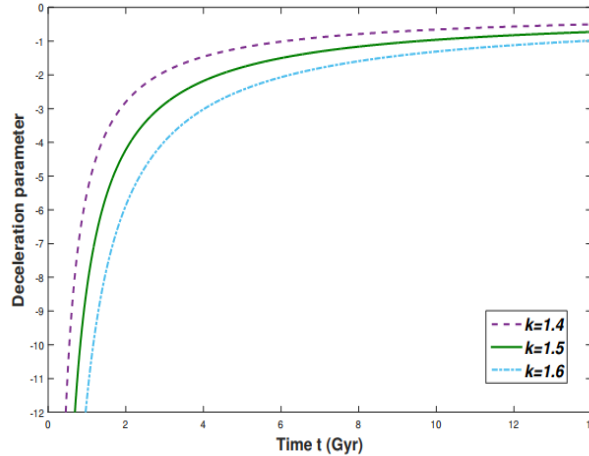


Figure 6. Plot of deceleration parameter q versus cosmic time t for $A_1 = -38$.

Statefinder parameters (r, s): The accelerated expansion of the universe has been explained by a variety of DE hypotheses. Sahni et al. [34] have presented statefinder parameters (r, s) to test the validity of these models. The $r - s$ plane is the cosmological plane corresponding to these parameters, and it indicates how far a certain DE model is from the Λ CDM limit. The cosmic planes of these parameters describe several well-known regions of the universe, e.g., $s > 0$ and $r < 1$ give the phantom and quintessence DE eras, respectively. $(r, s) = (1, 0)$ is the Λ CDM limit, $(r, s) = (1, 1)$ is the CDM limit, and $s < 0$ and $r > 1$ are the Chaplygin gas limits. Our models' statefinder parameters are provided by

$$r(t) = \frac{3t + 3A_1(k-1)^2}{(k+2)t} - 1 + 2 \left(\frac{3t + 3A_1(k-1)^2}{(k+2)t} - 1 \right)^2 + \frac{9A_1(k-1)^2(t^2 - A_1(k-1)^2)}{(k+2)^2 t^3}, \tag{40}$$

$$s(t) = \frac{\left\{ \frac{3t + 3A_1(k-1)^2}{(k+2)t} - 2 + 2 \left(\frac{3t + 3A_1(k-1)^2}{(k+2)t} - 1 \right)^2 + 9 \frac{A_1(k-1)^2(t^2 - A_1(k-1)^2)}{(k+2)^2 t^3} \right\}}{\left(\frac{3t + 3A_1(k-1)^2}{(k+2)t} - 4.5 \right)}. \tag{41}$$

Plotting r versus s yields the statefinders plane, as shown in Fig. 7 for different values of k . The regions of quintessence and phantom models can be found in the $r - s$ plane for our model. Our model coincides with the Λ CDM model in its evolution.

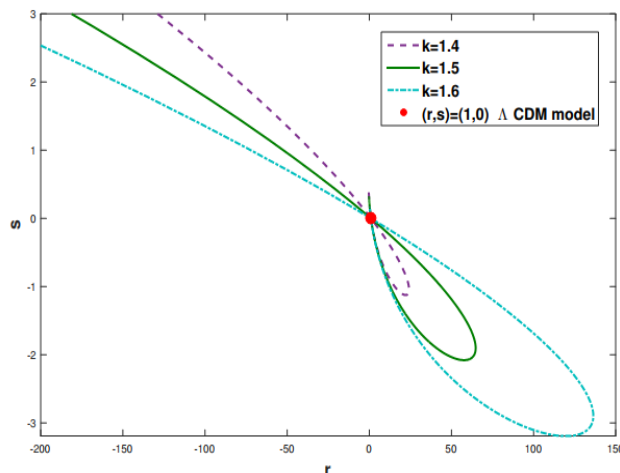


Figure 7. Plot of statefinder's plane for $A_1 = -38$.

4. DISCUSSION AND COMPARISON

In this section, we present a comparison of our work with the recent work on this subject and discuss the comparison with observational data.

Rao and Prasanthi [35] have discussed Bianchi type-I and III modified holographic Ricci DE models in Saez–Ballester theory of gravitation which evolve from the phantom region and ultimately reach the quintessence region. Rao et al. [36] have investigated a non-static plane-symmetric universe filled with matter and anisotropic modified holographic Ricci DE components within the framework of Saez–Ballester's theory of gravitation. In this model, the EoS parameter varies from matter-dominated to the phantom region by crossing the phantom divide line and then goes towards the quintessence region in the latter epoch. Sadri and Vakili [37] have studied the FRW new HDE model in the framework of the Brans–Dicke scalar–tensor theory of gravitation taking into account the interaction between dark matter and HDE. They have obtained an EoS parameter that can reach the phantom era without the necessity of interaction between DE and dark matter. Aditya and Reddy [38] have studied locally rotationally symmetric Bianchi type-I universe within the framework of the Saez–Ballester scalar–tensor theory of gravitation, where the models start in the matter-dominated era, varies in the quintessence region, cross phantom divided line and attains a constant value in the phantom region. Prasanthi and Aditya [39] have discussed Bianchi type-VI₀ RHDE models in general relativity where the model exhibits quintom as well as the phantom behaviour of the universe. Naidu et al. [40] have investigated the dynamical behaviour of Kaluza-Klein FRW-type DE cosmological models in the framework of a scalar-tensor theory of gravitation formulated by Saez and Ballester. Aditya [41] studied the Bianchi type-I RHDE model in the Saez-Ballester theory of gravitation, here the model displays quintom behaviour and consistent ranges with the observational data. Aditya and Prasanthi [42] have discussed the dynamics of SMHDE in the Brans-Dicke theory of gravity, here the model starts in the matter-dominated era, crosses the phantom division line, and finally reaches a constant value in the aggressive phantom region. Dasunaidu et al. [43] discussed Kaluza-Klein FRW type DE cosmological models in the context of Saez and Ballester's scalar-tensor theory of gravitation, where models begin in the matter-dominated era, evolves to the quintessence DE era, and finally approaches the vacuum DE and phantom era. In our KHDE model the study of the EoS parameter reveals that the model starts The EoS parameter analysis shows that the model starts in the aggressive phantom area ($\omega_{kde} \ll -1$) and finally attains Λ CDM model ($\omega_{kde} = -1$) and phantom region ($\omega_{kde} < -1$). This is quite in contrast with the models discussed above. Also, it is worthwhile to present, here, Planck's observational data given by Aghanim et al. [31] which gives the constraints on the EoS parameter of DE $\omega_{de} = -1.56^{+0.60}_{-0.48}$ (Planck + TT + lowE); $\omega_{de} = -1.58^{+0.52}_{-0.41}$ (Planck+ TT, TE, EE + lowE); $\omega_{de} = -1.57^{+0.50}_{-0.40}$ (Planck + TT, TE, EE + lowE + lensing); $\omega_{de} = -1.04^{+0.10}_{-0.10}$ (Planck + TT, TE, EE + lowE + lensing + BAO) by implying different combinations of observational schemes at 95% confidence level. It can be observed from Fig. 3 that the EoS parameter of our model lies within the above observational limits which shows the consistency of our results with the above cosmological data. The above comparison shows that our KHDE model is more viable than the DE models obtained by several authors, in the BD scalar–tensor theory, discussed above.

5. SUMMARY AND CONCLUSIONS

In this work, we study the Kantowski-Sachs universe and the Kaniadakis holographic dark energy in the context of the Brans–Dicke scalar-tensor theory of gravity. Field equations are solved using a few physically possible circumstances. We may analyze the dynamical properties of the DE model by constructing the cosmological parameters of our models. The following are some conclusions:

- This model starts with a finite volume and extends from there with no initial singularity. As $t \rightarrow \infty$ approaches, the physical parameters H, θ, σ^2 diverge and all drop to constant values at $t = 0$. Our model also becomes isotropic (because $A_h = 0$) and shear free when $K = 1$. The scalar field of our models decreases with cosmic time and is positive (Fig. 1). This behaviour is comparable to various theories' scalar field models (Aditya and Reddy [30,38]).
- Based on the deceleration parameter, we conclude that our model exhibits a super-exponential expansion (Fig. 6). The trajectory of statefinder parameters varies in both quintessence and phantom zones (Fig. 7). There is an obvious breach of the NEC, which causes a Big Rip in the model. Similar to what is predicted, our model likewise breaks the other energy requirements. This is because fresh observational data supports the late-time acceleration of the universe.
- We produce the sound's squared speed v_s^2 trajectory for our DE model in this scenario (Fig. 5). That v_s^2 fluctuates fully in the negative area indicates that the model is unstable. The EoS parameter analysis shows that the model starts in the aggressive phantom area ($\omega_{kde} \ll -1$) and finally attains Λ CDM model ($\omega_{kde} = -1$) and phantom region ($\omega_{kde} < -1$). We looked into the $\omega_{kde} - \omega'_{kde}$ plane study and found that it happens during the freezing and thawing phases of the history of the universe (Fig. 4). We find observationally that the expansion of the universe is significantly faster in the freezing region. Thus, the behaviour of the $\omega_{kde} - \omega'_{kde}$ plane agrees with the available data.

Furthermore, we have examined how each dynamical parameter behaves for a range of \mathcal{C} and k values. The pictures make it abundantly evident that the dynamics of cosmological parameters are significantly influenced by the BD scalar field $\phi(t)$.

Acknowledgements

The authors are grateful to the anonymous reviewer for constructive comments which have improved the presentation of the work. Y. Aditya acknowledges the National Board for Higher Mathematics under the Department of Atomic Energy, Govt. of India for financial support to carry out the Research project No.: 02011/8/2023 NBHM(R.P.)/R & D II/3073.

ORCID

✉ **A. Vijaya Prasanthi**, <https://orcid.org/0000-0002-4608-900X>; ✉ **G. Suryanarayana**, <https://orcid.org/0000-0002-4866-4020>
 ✉ **Y. Aditya**, <https://orcid.org/0000-0002-5468-9697>; ✉ **U.Y. Divya Prasanthi**, <https://orcid.org/0009-0004-5397-050X>

REFERENCES

- [1] S. Perlmutter, et al., “Measurements of ω and δ from 42 high-redshift supernovae,” *Astrophysical Journal*, **517**, 565-586 (1999). <https://doi.org/10.1086/307221>
- [2] A.G. Riess, et al., « Observational evidence from supernovae for an accelerating universe and a cosmological constant,” *Astron. J.* **116**, 1009–1038 (1998). <https://doi.org/10.1086/300499>
- [3] R.R. Caldwell, “A Phantom Menace? Cosmological consequences of a dark energy component with the super-negative equation of state,” *Phys. Lett. B*, **545**, 23-29 (2002). [https://doi.org/10.1016/S0370-2693\(02\)02589-3](https://doi.org/10.1016/S0370-2693(02)02589-3)
- [4] T. Padmanabhan, “Dark Energy and Gravity,” *Gen. Relativ. Gravit.* **40**, 529-564 (2008). <https://doi.org/10.1007/s10714-007-0555-7>
- [5] M.V. Santhi, et al., “Anisotropic generalized ghost pilgrim dark energy model in general relativity,” *Int. J. Theor. Phys.* **56**, 362-371 (2017). <https://doi.org/10.1007/s10773-016-3175-8>
- [6] M. Li, “A Model of Holographic Dark Energy,” *Phys. Lett. B*, **603**, 1-5 (2004). <https://doi.org/10.1016/j.physletb.2004.10.014>
- [7] A. Cohen, D. Kaplan, and A. Nelson, “Effective Field Theory, Black Holes, and the Cosmological Constant,” *Phys. Rev. Lett.* **82**, 4971 (1999).
- [8] Z.K. Gao, et al., “Two-field quintom models in the $\omega - \omega'$ plane,” *Phys. Rev. D*, **74**, 127304 (2006). <https://doi.org/10.1103/PhysRevD.74.127304>
- [9] L. Xu, and Y. Wang, “Observational constraints to Ricci dark energy model by using: SN, BAO, OHD, and fgas data sets,” *J. Cosmol. Astropart. Phys.* **06**, 002 (2010). <https://doi.org/10.1088/1475-7516/2010/06/002>
- [10] S. Nojiri, and S.D. Odintsov, “Unifying phantom inflation with late-time acceleration: scalar phantom-non-phantom transition model and generalized holographic dark energy,” *Gen. Rel. Grav.* **38**, 1285-1304 (2006). <https://doi.org/10.1007/s10714-006-0301-6>
- [11] S. Ghaffari, “Holographic dark energy model in the DGP braneworld with time-varying holographic parameters,” *New Astronomy*, **67**, 76-84 (2019). <https://doi.org/10.1016/j.newast.2018.09.002>
- [12] Y. Aditya, and D.R.K. Reddy, “FRW type Kaluza-Klein modified holographic Ricci dark energy models in Brans-Dicke theory of gravitation,” *Eur. Phys. J. C*, **78**, 619 (2018). <https://doi.org/10.1140/epjc/s10052-018-6074-8>
- [13] E.M.C. Abreu, J.A. Neto, A.C.R. Mendes, A. Bonilla, and R.M. de Paula, “Cosmological considerations in Kaniadakis statistics,” *Europhysics Letters*, **124**(3), 30003 (2018). <https://doi.org/10.1209/0295-5075/124/30003>
- [14] H. Moradpour, A.H. Ziaie, and M.K. Zangeneh, “Generalized entropies and corresponding holographic dark energy models,” *Eur. Phys. J. C*, **80**, L32 (2020). <https://doi.org/10.1140/epjc/s10052-020-8307-x>
- [15] A. Jawad, and A.M. Sultan, “Cosmic Consequences of Kaniadakis and Generalized Tsallis Holographic Dark Energy Models in the Fractal Universe,” *Adv. High Energy Phys.* **2021**, 5519028 (2021). <https://doi.org/10.1155/2021/5519028>
- [16] J. Sadeghi, S.N. Gashti, and T. Azizi “Tsallis and Kaniadakis holographic dark energy with Complex Quintessence theory in Brans-Dicke cosmology,” (2022). <https://doi.org/10.48550/arXiv.2203.04375>
- [17] M. Tavayef, A. Sheykhi, K. Bamba, and H. Moradpour, “Tsallis holographic dark energy in the Brans-Dicke theory with a logarithmic scalar field,” *Phys. Lett. B*, **781**, 195 (2018). <https://doi.org/10.1016/j.physletb.2018.04.001>
- [18] C. Tsallis, and L.J.L. Cirto, “Black hole thermodynamical entropy,” *Eur. Phys. J. C*, **73**, 2487 (2013). <https://doi.org/10.1140/epjc/s10052-013-2487-6>
- [19] A.S. Jahromi, et al., “Generalized entropy formalism and a new holographic dark energy model,” *Phys. Lett. B*, **780**, 21-24 (2018). <https://doi.org/10.1016/j.physletb.2018.02.052>
- [20] M. Younas, et al., “Cosmological Implications of the Generalized Entropy Based Holographic Dark Energy Models in Dynamical Chern-Simons Modified Gravity,” *Advances in High Energy Physics*, **2019**, 1287932 (2019). <https://doi.org/10.1155/2019/1287932>
- [21] Y. Aditya, S. Mandal, P.K. Sahoo, and D.R.K. Reddy, “Observational constraint on interacting Tsallis holographic dark energy in logarithmic Brans-Dicke theory,” *Eur. Phys. J. C*, **79**, 1020 (2019). <https://doi.org/10.1140/epjc/s10052-019-7534-5>
- [22] U.Y. Divya Prasanthi, and Y. Aditya, “Anisotropic Renyi holographic dark energy models in general relativity,” *Results of Physics*, **17**, 103101 (2020). <https://doi.org/10.1016/j.rinp.2020.103101>
- [23] U.Y. Divya Prasanthi, and Y. Aditya, “Observational constraints on Renyi holographic dark energy in Kantowski-Sachs universe,” *Physics of the Dark Universe*, **31**, 100782 (2021). <https://doi.org/10.1016/j.dark.2021.100782>
- [24] U.K. Sharma, and V.C. Dubey, “Exploring the Sharma–Mittal HDE models with different diagnostic tools,” *The European Physical Journal Plus*, **135**, 391 (2020). <https://doi.org/10.1140/epjp/s13360-020-00411-x>
- [25] CBrans, and R.H. Dicke, “Mach’s Principle and a Relativistic Theory of Gravitation,” *Phys. Rev.* **124**, 925 (1961). <https://doi.org/10.1103/PhysRev.124.925>
- [26] K.S. Thorne, “Primordial Element Formation, Primordial Magnetic Fields, and the Isotropy of the Universe,” *Astrophysical Journal*, **148**, 51 (1967). <http://dx.doi.org/10.1086/149127>
- [27] C.B. Collins, E.N. Glass, and D.A. Wilkinson, “Exact spatially homogeneous cosmologies,” *Gen. Relativ. Gravit.* **12**, 805 (1980). <https://doi.org/10.1007/BF00763057>
- [28] V.B. Johri, and R. Sudharsan, “BD-FRW Cosmology with Bulk Viscosity,” *Australian Journal of Physics*, **42**(2), 215-222 (1989). <https://doi.org/10.1071/PH890215>
- [29] V.B. Johri, and K. Desikan, “Cosmological models with constant deceleration parameter in Brans-Dicke theory,” *Gen. Relat. Gravit.* **26**, 1217-1232 (1994). <https://doi.org/10.1007/BF02106714>

- [30] Y. Aditya, and D.R.K. Reddy, “Dynamics of perfect fluid cosmological model in the presence of massive scalar field in $f(R,T)$ gravity,” *Astrophys. Space Sci.* **364**, 3 (2019). <https://doi.org/10.1007/s10509-018-3491-y>
- [31] N. Aghanim, et al., [Plancks Collaboration], (2018). <https://doi.org/10.48550/arXiv.1807.06209>
- [32] R. Caldwell, and E.V. Linder, “Limits of quintessence,” *Phys. Rev. Lett.* **95**, 141301 (2005). <https://doi.org/10.1103/PhysRevLett.95.141301>
- [33] T. Chiba, “ ω and ω' of scalar field models of dark energy,” *Phys. Rev. D*, **73**, 063501 (2006). <https://doi.org/10.1103/PhysRevD.73.063501>
- [34] V. Sahni, T. D. Saini, A.A. Starobinsky, and U. Alam, “Statefinder – A new geometrical diagnostic of dark energy,” *J. Exp. Theor. Phys. Lett.* **77**, 201-206 (2003). <https://doi.org/10.1134/1.1574831>
- [35] V.U.M. Rao, and U.Y.D. Prasanthi, “Bianchi type-I and-III modified holographic Ricci Dark energy models in Saez-Ballester theory,” *The European Physical Journal Plus*, **132**, 64-73 (2017). <https://doi.org/10.1140/epjp/i2017-11328-9>
- [36] V.U.M. Rao, U.Y. Divya Prasanthi, and Y. Aditya, “Plane symmetric modified holographic Ricci dark energy model in Saez-Ballester theory of gravitation,” *Results in Physics*, **10**, 469-475 (2018). <https://doi.org/10.1016/j.rinp.2018.06.027>
- [37] E. Sadri, and B. Vakili, “A new holographic dark energy model in Brans-Dicke theory with a logarithmic scalar field,” *Astrophysics and Space Science*, **363**, 13-21 (2018). <https://doi.org/10.1007/s10509-017-3237-2>
- [38] Y. Aditya, and D.R.K. Reddy, “Anisotropic new holographic dark energy model in Saez-Ballester theory of gravitation,” *Astrophys. Space Sci.* **363**, 207 (2018). <https://doi.org/10.1007/s10509-018-3429-4>
- [39] U.Y.D. Prasanthi, and Y. Aditya, “Anisotropic Renyi holographic dark energy models in general relativity,” *Results in Physics*, **17**, 103101 (2020). <https://doi.org/10.1016/j.rinp.2020.103101>
- [40] R.L. Naidu, Y. Aditya, K.D. Raju, T. Vinutha, and D.R.K. Reddy, “Kaluza-Klein FRW dark energy models in Saez-Ballester theory of gravitation,” *New Astronomy*, **85**, 101564 (2021). <https://doi.org/10.1016/j.newast.2020.101564>
- [41] Y. Aditya, “Dynamics of anisotropic Renyi holographic dark energy model,” *Bulgarian Astronomical Journal*, **40**, 95-114 (2024). <https://astro.bas.bg/AIJ/issues/n40/YAditya.pdf>
- [42] Y. Aditya, and U.Y.D. Prasanthi, “Dynamics of Sharma-Mittal holographic dark energy model in Brans-Dicke theory of gravity,” *Bulgarian Astronomical Journal*, **38**, 52-67 (2023). <https://astro.bas.bg/AIJ/issues/n38/YAditya.pdf>
- [43] K. Dasunaidu, et al., “Kaluza-Klein FRW Tsallis holographic dark energy model in scalar-tensor theory of gravitation,” *Bulgarian Astronomical Journal*, **39**, 72-86 (2023). <https://astro.bas.bg/AIJ/issues/n39/KDasunaidu.pdf>

КОСМОЛОГІЧНА ДИНАМІКА АНІЗОТРОПНОЇ ГОЛОГРАФІЧНОЇ МОДЕЛІ ТЕМНОЇ ЕНЕРГІЇ КАНІАДАКІСА В ГРАВІТАЦІЇ БРАНСА-ДІКЕ

А. Віджая Прасанті^{a,b}, Г. Сурьянараяна^c, Ю. Адітья^d, У.Ю. Дів'я Прасанті^e

^aЦентр міждисциплінарних досліджень АУ, Університет Андра, Вісахапатнам-530003, Індія

^bКафедра математики, Шрі Вішну Інженерний коледж для жінок, Бхімаварам-534201, Індія

^cДепартамент математики, ANITS, Вісахапатнам-533003, Індія




^dВідділ математики, Технологічний інститут GMR, Раджам-532127, Індія

^eКафедра статистики та математики коледжу садівництва, Dr. Y.S.R. Університет садівництва, Парватіпурам, Індія

У цій роботі досліджується голографічна темна енергія Каніадакіса в контексті скалярно-тензорної теорії гравітації Бранса-Дікке (Phys. Rev. 124: 925, 1961). Ця стаття присвячена фону з анізотропним простором-часом Кантовського-Сакса, який є однорідним у просторі. За цих обставин скалярне поле Бренса-Дікке, позначене як ϕ , використовується як функція середнього масштабного коефіцієнта $a(t)$. Використання графічної моделі для аналізу фізичної поведінки моделі є частиною дослідження прискореного розширення Всесвіту. Ми оцінюємо космологічні параметри, такі як скалярне поле, параметр рівняння стану та параметр уповільнення. Крім того, стабільність моделей оцінюється за допомогою квадрата швидкості звуку (v_s^2). Для наших моделей ми виводимо загальноприйняті космічні площини, такі як $\omega_{kde} - \omega'_{kde}$ і площини вимірювача стану (r,s). Виявлено, що скалярне поле є спадною функцією космічного часу t , отже, відповідна кінетична енергія зростає. Параметр уповільнення демонструє прискорене розширення Всесвіту. Тут згадується, що рівняння параметра стану лежить у фантомній області i , нарешті, досягає моделі Λ CDM. Крім того, площина $\omega_{kde} - \omega'_{kde}$ забезпечує області замерзання і відтавання. Крім того, модель Λ CDM також відповідає площині вимірювача стану. Нарешті, зауважується, що всі вищезазначені обмеження космологічних параметрів узгоджуються з даними спостережень Планка.

Ключові слова: скалярно-тензорна теорія; скалярне поле; голографічна темна енергія; модель Кантовського-Сакса

BEHAVIOUR OF QUARK AND STRANGE QUARK MATTER FOR HIGHER DIMENSIONAL BIANCHI TYPE - I UNIVERSE IN $f(R, T)$ GRAVITY

 R.V. Mapari^{a*},  S.S. Thakre^b,  V.A. Thakare^c

^aDepartment of Mathematics, Government Science College, Gadchiroli (M.S.) India- 442605

^bDepartment of Mathematics, Independent Junior College, Amravati (M.S.), India - 444604

^cDepartment of Mathematics, Shri Shivaji Science, Amravati (M.S.) - 444604 India

*Corresponding Author e-mail: r.v.mapari@gmail.com

Received January 12, 2024; revised February 11, 2024; in final form March 4, 2024; accepted March 11, 2024

This research paper delves into a thorough examination of the behaviour exhibited by higher dimensional Bianchi Type-I universes, incorporating the presence of quark and strange quark matter within the framework of $f(R, T)$ gravity. The solutions derived for the field equations encompass both exponential volumetric expansion and power law scenarios. Under the exponential expansion model, both the pressure (p_q) and energy density (ρ_q) associated with quark matter are initially finite at the inception of cosmic time, gradually diminishing to zero as time progresses towards infinity. Conversely, within the power law model, these parameters start off infinitely large at $t = 0$, subsequently decreasing to zero as time approaches infinity. Furthermore, an exploration of the physical and geometrical attributes of the model is conducted. Notably, in power law expansion models, the behaviour of strange quark matter mirrors that of quark matter concerning pressure (p) and energy density (ρ). But in exponential expansion model quark pressure and strange quark pressure behave differently. The bag constant emerges as a critical factor influencing the universe's expansion, with observations revealing that both pressure and energy density tend towards the bag constant at large time scales ($t \rightarrow \infty$). Specifically, the pressure $p \rightarrow -B_C$ and the energy density $\rho \rightarrow B_C$ as time approach infinity. The negative pressure sign denotes the universe's expansion during later epochs.

Keywords: *Quark and Strange quark matter; Bag constant; Higher dimensional Bianchi Type-I universe; $f(R, T)$ gravity*

PACS: 04.98.80cq, 04.5-h, 98.80.-k, 04.50.Kd, 04.20.Jb

1. INTRODUCTION

Modern cosmology has attracted an enormous amount of attention due to its outstanding ability to explain the natural phenomenon of rapid expansion that takes place in the conclusive stages of the universe. As we endeavour to explore the universe this field is establishing itself as the one that is advancing the most quickly. An important discovery of accelerated expansion was made primarily through the analysis of type- I_a supernovae experiment performed by various researchers [1, 2, 3, 4, 5]. These investigations have produced strong evidence revealing the universe is presently going through an accelerated expansion phase. Notably, many scientists have made major attempts to find confirmation of dark energy an idea put forward in Einstein's theory permeating the universe. These researchers came to the conclusion after an exhaustive examination of observational evidence suggesting dark energy often regarded as the primary driving force shaping the universe is characterised by negative pressure.

Researchers in cosmology have a strong desire to learn more about how the universe functions. Albert Einstein stands out among them for his work on the general theory of relativity which attracted a lot of curiosity for its effectiveness in building cosmological models as well as offering insights into the development and the formation of the universe. However, it fails to tackle a significant issue associated with modern cosmology the late-time acceleration. As a result, several attempts to alter the theory of gravity have been established in order to explain the current accelerated phase. To solve this constraint and offer brief explanations for the universe's late-time rapid expansion cosmologists have created a number of alternative theories including $f(R)$ [6], $f(T)$ [7] and $f(R, T)$ [8] theories to the general theory of relativity.

One such alternative theory that has garnered interest and motivation is the $f(R, T)$ theory of gravity. This theory proposed by Harko et al. in 2011 incorporates the Ricci scalar (R) and the trace of the stress-energy tensor (T). The researchers derived the gravitational field equations in the metric formalism as well as the equation of motion for test particles based on the covariant divergence of the stress-energy tensor. Within this particular field, various forms of the $f(R, T)$ function have been extensively explored and discussed by researchers. This motivates the researchers [9, 10, 11, 12, 13] to construct various models in the context of $f(R, T)$ gravity.

Cite as: R.V. Mapari, S.S. Thakre, V.A. Thakare, East Eur. J. Phys. 2, 21 (2024), <https://doi.org/10.26565/2312-4334-2024-2-02>

© R.V. Mapari, S.S. Thakre, V.A. Thakare, 2024; CC BY 4.0 license

Considerable progress has been made in the field of $f(R, T)$ theory of gravity using various kinds of matter. Among these, two notable examples are quarks and strange quarks. Jokwani et al. [15] have explored locally rotationally symmetric Bianchi-I model filled with strange quark matter in $f(R, T)$ gravity and found that model is shear - free at late time but remains anisotropic throughout the evolution. Pawar et al. [16] have discussed LRS Bianchi type-V Cosmological model in $f(R, T)$ theory of gravity and they found universe has an initial singularity. Several authors [17, 18, 19] have explored evolution of cosmic universe by analysing Kalunza-Klien cosmological model with strange quark matter in different theories of gravitation. Pawar et al. [20] have obtained exact solutions of field equations with quark and strange quark matter for FRW universe in fractal gravity with the help of assumption a fractal parameter and fractal function in the form of power law.

According to the established standard model of physics quarks are the smallest known units found within the nuclei of atoms. However, isolating individual quarks proves challenging as they are perpetually bound in groups of three. The family of quarks comprises six members: up (u), down (d), charm (c), strange (s), top (t), and bottom (b) quarks, with up, down, and strange quarks being the primary types. Quarks serve as the fundamental building blocks of particles. During an early phase transition of the universe, when the cosmic temperature was around $T \sim 200\text{MeV}$ it is widely accepted that a state known as quark-gluon plasma existed. The possibility of quark matter's existence was initially proposed in the early 1970s by Itoh [21], Bodmer [22], and Witten [23], who suggested two pathways for its formation: the quark-hadron phase transition in the early universe and the conversion of neutron stars into strange stars under ultrahigh densities. In theories related to strong interaction, the concept of quark bag models assumes the occurrence of vacuum breaking within hadrons. Consequently, a notable distinction arises between the vacuum energy densities inside and outside a hadron leading to a significant difference in the pressure on the bag wall and the pressure exerted by the quarks. This equilibrium stabilizes the system. The equation of state for strange quark matter based on the phenomenological bag model of quark matter is given by $p = \frac{(\rho - 4B_c)}{3}$ within this equation the bag constant (B_c) represents the disparity between the energy density of the perturbative and non-perturbative QCD vacuum. Here, ρ and p denote the energy density and thermodynamic pressure of the quark matter respectively. In this model, quarks are treated as degenerate fermi gases existing within a region of space characterized by the vacuum energy density (B_c) known as the bag model. Within this framework, the quark matter is composed of massive s quarks and electrons, alongside massless u and d quarks. A simplified version of this bag model assumed that quarks are massless and noninteracting. Therefore, we have quark pressure $p_q = \frac{\rho_q}{3}$, where ρ_q is the quark energy density. The total energy density and pressure is $\rho = \rho_q + B_c$ and $p = p_q - B_c$ respectively.

Mak and Harko [24] have conducted an investigation on spherically symmetric space-time in the presence of charged strange quark matter considering conformal motion. Dixit et al. [25] have derived deterministic solution of Kontowski-Sachs space-time with strange quark matter in $f(R)$ gravity and they noticed that the function $f(R)$ satisfies the cosmological viability constraint. Sahoo and Mishra [26] have confined their work to strange quark matter attached to string cloud in general relativity for higher dimensional Bianchi type - III universe. Katore [27] has discussed the FRW cosmological model incorporating strange quark matter attached to a string cloud. Santhikumar et al. [28] have discussed the properties of axially symmetric cosmological models with strange quark matter attached to a string cloud. Katore and Shaikh [29] have discussed the properties of axially symmetric space-time incorporate strange quark matter attached to a string cloud within the framework of general relativity. Yilmaz et al. [30, 31] have explored the implications of quark and strange quark matter in Bianchi type-I and V space-times within the context of $f(R)$ theory of gravity. Additionally, they have also investigated the presence of strange quark matter within a Robertson-Walker cosmological model using the general theory of relativity. Adhav et al. [32] have investigated the behaviour of quark and strange quark matter for Kantowski-Sachs cosmological model within the context of $f(R)$ theory of gravity. Chirde and Sheikh [33] investigated plane symmetric cosmological model with the distribution of quark and strange quark matter in deformations of the Einstein's theory of General Relativity. Hatkar et al. [34] have studied Bianchi-I universe incorporating quark and strange quark matter in $f(G)$ theory of gravity and they observed that quark matter is transformed into strange quark matter for power law and exponential law model. Aygün et al. [35] have explored FRW cosmological model with quark and strange quark matter in creation field cosmology.

Furthermore, Pawar and Agrawal [36] have examined the behaviour of quark and strange quark matter within the context of $f(R, T)$ gravity for a plane symmetric cosmological model and they found that the mean anisotropy parameter remains constant throughout the evolution. Pawar and Mapari [37] have explored magnetized strange quark matter within the Lyra geometry for a plane symmetric cosmological model, revealing that the model remains anisotropic throughout its evolution except for the case where $n = 1$. Sahoo et al. [38] have discussed magnetized strange quark matter distribution for LRS Bianchi type-I with cosmological constant Λ in $f(R, T)$ gravity. Kumbhare and Khadekar [39] have investigated higher dimensional spherically symmetric space time with magnetized quark and strange quark matter admitting conformal motion. Nagpal et al. [40] have explored the FLRW cosmological model incorporating magnetized quark matter and strange quark matter within the framework of $f(R, T)$ theory of gravity.

Chirde and Shekh [41] have investigated a plane symmetric dark energy model represented by a wet dark fluid incorporating $f(R, T)$ gravity. The precise solution of LRS Bianchi type-I spacetime with strange quark

matter and variable cosmological term Λ in the context of $f(R, T)$ theory of gravity has discussed by Singh and Beesham [42]. Khadekar and Shelote [43] have analysed Kalunza-Klein cosmological model with Quark and Strange Quark matter. Aygün et al. [44] have investigated higher dimensional FRW universe in presence of quark and strange quark matter for cloud string with perfect fluid in Lyra geometry. They obtained that cloud of string with perfect fluid is non-existent for higher dimensional FRW universe. Aygün et al. [45] examined Marder's universe with strange quark matter in $f(R, T)$ gravity. Pawar et al. [46] investigated interacting field model for plane symmetric universe with cosmological constant in the framework of $f(R, T)$ theory. Krishna et al. [47] have studied plane symmetric cosmological model with bulk viscous and cosmic strings in Lyra's geometry and they observed inflation phase. Mete et al. [48] have delved into higher dimensional plane symmetric cosmological models featuring two fluid sources within the realm of general relativity. Thakre et al. [49] analysed higher dimensional plane symmetric cosmological model with quadratic equation of state in $f(R, T)$ gravity. Plane symmetric inflationary models play a crucial role in the formation of the universe's structure and are of significant astrophysical interest. While the present state of the universe exhibits overall spherical symmetry and isotropy its early stages of evolution did not possess such a smoothed-out characteristic. Hence, we consider the less restrictive plane symmetry, allowing for deviations from isotropy.

Furthermore, the objective of this study is to explore a higher dimensional Bianchi type I cosmological model incorporating quark and strange quark matter within the framework of $f(R, T)$ theory of gravity. The paper is structured as follows: Section 1 provides an introduction to the research topic, while Section 2 presents the general framework of $f(R, T)$ gravity. In Section 3, we have studied the metric and the field equations for quark and strange quark matter within the context of $f(R, T)$ gravity. Furthermore, in Section 4, we obtained the solutions of field equation by considering power law model and exponential expansion model. In section 5, we explored the results that were obtained in the preceding section. It is important to note that our investigation builds upon the previous works conducted by [36].

2. GRAVITATIONAL FIELD EQUATIONS OF $f(R, T)$ GRAVITY

The $f(R, T)$ theory of gravity [8] is proposed by Harko et al. (2011) which is the modification of General Relativity. In this theory, the gravitational action is given by the following equation:

$$s = \frac{1}{16\pi G} \int f(R, T) \sqrt{-g} d^5x + \int L_m \sqrt{-g} d^5x \quad (1)$$

where $f(R, T)$ is an arbitrary function of Ricci scalar R and trace T of energy momentum tensor of matter T_{ij} . L_m is the matter Lagrangian density. The energy momentum tensor T_{ij} can be stated as

$$T_{\kappa\beta} = -\frac{2}{\sqrt{-g}} \frac{\partial(\sqrt{-g}L_m)}{\partial g^{\kappa\beta}} \quad (2)$$

In simpler terms, the $f(R, T)$ theory proposes a modified version of General Relativity that considers additional terms involving the Ricci scalar, trace of the energy-momentum tensor, and matter Lagrangian density. These modifications are incorporated into the gravitational action to describe the behavior of gravity in a different manner than predicted by General Relativity. On varying the action with respect to metric tensor g_{ij} , the field equations of $f(R, T)$ gravity are obtained as

$$f_{R(R, T)} R_{\kappa\beta} - \frac{1}{2} f(R, T) g_{\kappa\beta} - f_R(R, T) (\nabla_\kappa \nabla_\beta - g_{\kappa\beta} \square) = 8\pi T_{\kappa\beta} - f_T(R, T) (T_{\kappa\beta} + \theta_{\kappa\beta}) \quad (3)$$

where,

$$\theta_{\kappa\beta} = -2T_{\kappa\beta} + g_{\kappa\beta} L_m - 2g^{lk} \frac{\partial^2 L_m}{\partial g^{\kappa\beta} \partial g^{l\alpha}} \quad (4)$$

Here

$$f_R(R, T) = \frac{\partial f(R, T)}{\partial R}, f_T(R, T) = \frac{\partial f(R, T)}{\partial T}, \square = \nabla^\kappa \nabla_\kappa \quad (5)$$

where ∇_κ is the co-variant derivative. Now Contraction of equation (4) gives

$$f_R(R, T) R + 3\square f_R(R, T) - 2f(R, T) = 8\pi T - f_T(R, T) (T + \theta) \quad (6)$$

where $\theta = \theta_\kappa^\kappa$ equation (5) gives relation between Ricci Scalar R & the trace T of energy momentum tensor. In the present study, we assume that the stress energy tensor of matter is given by,

$$T_{\kappa\beta} = (\rho + p) u_\kappa u_\beta - p g_{\kappa\beta} \quad (7)$$

where five-velocity vector $u_\kappa = (1, 0, 0, 0, 0)$ and satisfies the conditions, $u_\kappa u^\kappa = 1$ and $u^\kappa \nabla_\beta u_\kappa = 0$. ρ indicates energy density and p indicates pressure of the matter. Here the matter Lagrangian is assumed as $L_m = -p$. Therefore equation (4) becomes

$$\theta_{\kappa\beta} = -pg_{\kappa\beta} - 2T_{\kappa\beta} \tag{8}$$

The $f(R, T)$ theory of gravity takes into account the presence of matter fields, and as a result, various theoretical models can be formulated based on different types of matter. Three distinct functional forms of $f(R, T)$ gravity is described below

$$f(R, T) = \begin{cases} R + 2f(T) \\ f_1(R) + f_2(T) \\ f_1(R) + f_2(R)f_3(T) \end{cases} \tag{9}$$

In this paper we are going to focus on the case, $f(R, T) = R + 2f(T)$ where, $f(T)$ is an arbitrary function of stress energy tensor of matter and given by $f(T) = \lambda T$ where λ is a constant. In this particular case, the field equations take the form

$$R_{\kappa\beta} - \frac{1}{2}g_{\kappa\beta}R = 8\pi T_{\kappa\beta} + 2\dot{f}(T)T_{\kappa\beta} + [f(T) + 2P\dot{f}(T)]g_{\kappa\beta} \tag{10}$$

where, an overhead dot denotes differentiation with respect to the argument T .

3. METRIC AND FIELD EQUATIONS

Higher dimensional Bianchi type -I universe given by

$$ds^2 = dt^2 - A^2(dx^2 + dy^2) - B^2dz^2 - C^2d\omega^2 \tag{11}$$

where A, B, C are metric potentials which are functions of cosmic time t and fifth coordinate is taken as space-like. The energy momentum tensor for quark is defined as

$$T_{\kappa\beta}^{(quark)} = (\rho + p)u_\kappa u_\beta - pg_{\kappa\beta}$$

or

$$T_{\kappa\beta}^{(quark)} = \text{dia}(\rho, -p, -p, -p, -p) \tag{12}$$

where $\rho = \rho_q + B_c$ is quark matter total energy density and $p = p_q - B_c$ is the quark matter total pressure and u_κ is the five velocity such that $u_\kappa u^\kappa = 1$ The EoS parameter for quark matter is defined as

$$p_q = \omega\rho_q \quad 0 \leq \omega \leq 1 \tag{13}$$

Also, the linear equation of state for strange quark matter is

$$p = \omega(\rho - \rho_o) \tag{14}$$

where ρ_o is the energy density when pressure p is zero and ω is a constant. when $\omega = \frac{1}{3}$ and $\rho_o = 4B_c$ the above linear equation of state is reduced to the following equation

$$p = \frac{\rho - 4B_c}{3} \tag{15}$$

where B_c denotes the bag constant. In co-moving co-ordinate system, the field equation (10) for metric (11) with the help of equation (12) can be written as

$$\frac{\dot{A}}{A} + \frac{\dot{B}}{B} + \frac{\dot{C}}{C} + \frac{\dot{A}\dot{B}}{AB} + \frac{\dot{A}\dot{C}}{AC} + \frac{\dot{B}\dot{C}}{BC} = p_q - B_c - \lambda(\rho_q + 5B_c - 4p_q) \tag{16}$$

$$2\frac{\ddot{A}}{A} + 2\frac{\dot{A}\dot{C}}{AC} + \left(\frac{\dot{A}}{A}\right)^2 + \frac{\ddot{C}}{C} = p_q - B_c - \lambda(\rho_q + 5B_c - 4p_q) \tag{17}$$

$$2\frac{\ddot{A}}{A} + \frac{\ddot{B}}{B} + \left(\frac{\dot{A}}{A}\right)^2 + 2\frac{\dot{A}\dot{B}}{AB} = p_q - B_c - \lambda(\rho_q + 5B_c - 4p_q) \tag{18}$$

$$2\frac{\dot{A}\dot{B}}{AB} + 2\frac{\dot{A}\dot{C}}{AC} + \frac{\dot{B}\dot{C}}{BC} + \left(\frac{\dot{A}}{A}\right)^2 = -\rho_q - B_c - \lambda(3\rho_q + 5B_c - 2p_q) \tag{19}$$

Dynamical parameters for Bianchi type-I are defined as follows :

Average scale factor

$$a(t) = (A^2 BC)^{\frac{1}{4}}$$

Spatial volume V is defined as

$$V = A^2 BC$$

The directional Hubble parameters

$$H_x = H_y = \frac{\dot{A}}{A}, H_z = \frac{\dot{B}}{B}, H_\omega = \frac{\dot{C}}{C} \quad (20)$$

The generalized average Hubble's parameter H is defined as

$$H = \frac{1}{4} \left(2 \frac{\dot{A}}{A} + \frac{\dot{B}}{B} + \frac{\dot{C}}{C} \right) \quad (21)$$

The mean anisotropic parameter is defined as

$$\Delta = \frac{1}{4} \sum_{i=1}^4 \left(\frac{H_i - H}{H} \right)^2 \quad (22)$$

where $H_i (i = 1, 2, 3, 4)$ represent the directional parameters.

Dynamical scalar expansion θ is given by,

$$\theta = 4H = 2 \frac{\dot{A}}{A} + \frac{\dot{B}}{B} + \frac{\dot{C}}{C} \quad (23)$$

The Shear Scalar is given by

$$\sigma^2 = \frac{1}{2} \left(\sum_{i=1}^4 H_i^2 - 4H^2 \right) = \frac{4}{2} AH^2 \quad (24)$$

The deceleration parameter q is defined by

$$q = \frac{d}{dt} \left(\frac{1}{H} \right) - 1 \quad (25)$$

The positive sign of q corresponds to standard decelerating model, whereas the negative sign accelerated expansion.

4. SOLUTION OF THE FIELD EQUATIONS

Subtracting equation (17) from equation (16), we get

$$\frac{d}{dt} \left(\frac{\dot{A}}{A} - \frac{\dot{B}}{B} \right) + \left(\frac{\dot{A}}{A} - \frac{\dot{B}}{B} \right) \frac{\dot{V}}{V} = 0$$

which on integration gives

$$\frac{A}{B} = c_1 \exp \left[d_1 \int \frac{dt}{V} \right] \quad (26)$$

Subtracting equation (18) from equation (17), we get

$$\frac{d}{dt} \left(\frac{\dot{B}}{B} - \frac{\dot{C}}{C} \right) + \left(\frac{\dot{B}}{B} - \frac{\dot{C}}{C} \right) \frac{\dot{V}}{V} = 0$$

which on integration gives

$$\frac{B}{C} = c_2 \exp \left[d_2 \int \frac{dt}{V} \right] \quad (27)$$

Subtracting equation (18) from equation (16)

$$\frac{d}{dt} \left(\frac{\dot{A}}{A} - \frac{\dot{C}}{C} \right) + \left(\frac{\dot{A}}{A} - \frac{\dot{C}}{C} \right) \frac{\dot{V}}{V} = 0$$

which on integration gives

$$\frac{A}{C} = c_3 \exp \left[d_3 \int \frac{dt}{V} \right] \tag{28}$$

where c_1, c_2, c_3 and d_1, d_2, d_3 are constant of integration which satisfies the relation $c_3 = c_1 c_2$ and $d_3 = d_2 + d_1$. In the view of $V = A^2 BC$, we write metric potentials in explicit form

$$A = C_1 V^{\frac{1}{4}} \exp \left[D_1 \int \frac{dt}{V} \right] \tag{29}$$

$$B = C_2 V^{\frac{1}{4}} \exp \left[D_2 \int \frac{dt}{V} \right] \tag{30}$$

$$C = C_3 V^{\frac{1}{4}} \exp \left[D_3 \int \frac{dt}{V} \right] \tag{31}$$

where $C_i (i = 1, 2, 3)$ and $D_i (i = 1, 2, 3)$ which satisfies the relation $C_1^2 C_2 C_3 = 1$ and $2D_1 + D_2 + D_3 = 0$

Since we have set of four equations (16),(17),(18), (19) with five unknown which are highly nonlinear. Therefore, to solve the system completely we required additional condition. Here we used two different volumetric expansion law

$$V = \alpha_1 e^{4\beta_1 t} \text{ (Exponential Expansion)} \tag{32}$$

and

$$V = \alpha_1 t^{4n} \text{ (Power Law Expansion)} \tag{33}$$

where α_1, β_1, n are positive constants.

4.1. Model for Exponential Law

The exponential expansion of volume factor is

$$V = \alpha_1 e^{4\beta_1 t}$$

Using the equation (31) in (28)- (30), the scale factor obtained as follows:

$$A = C_1 \alpha_1^{\frac{1}{4}} e^{\beta_1 t} \exp \left(\frac{-D_1}{4\alpha_1 \beta_1} e^{-4\beta_1 t} \right) \tag{34}$$

$$B = C_2 \alpha_1^{\frac{1}{4}} e^{\beta_1 t} \exp \left(\frac{-D_2}{4\alpha_1 \beta_1} e^{-4\beta_1 t} \right) \tag{35}$$

$$C = C_3 \alpha_1^{\frac{1}{4}} e^{\beta_1 t} \exp \left(\frac{-D_3}{4\alpha_1 \beta_1} e^{-4\beta_1 t} \right) \tag{36}$$

where C_1, C_2, C_3 are the constant of integration.

It must be stated that, the metric potentials accept constant value at initial time, after which they evolve with time without a singularity and eventually diverge to infinity.

The directional Hubble parameter $H_x = H_y, H_z, H_\omega$ are given as

$$H_x = H_y = \beta_1 + \frac{D_1}{\alpha_1} e^{-4\beta_1 t} \tag{37}$$

$$H_z = \beta_1 + \frac{D_2}{\alpha_1} e^{-4\beta_1 t} \tag{38}$$

$$H_\omega = \beta_1 + \frac{D_3}{\alpha_1} e^{-4\beta_1 t} \tag{39}$$

Mean Hubble parameter H is given by

$$H = \beta_1 \tag{40}$$

Anisotropy parameter of the expansion is

$$\Delta = \frac{\mu^2}{4\beta_1^2 (V_1 e^{4\beta_1 t})^2} \tag{41}$$

Where $\mu^2 = 2D_1^2 + D_2^2 + D_3^2$
Dynamical scalar is given by

$$\theta = 4H = 4\beta_1 \quad (42)$$

The Dynamical scalar is constant throughout the evolution Shear scalar

$$\sigma^2 = \frac{\mu^2}{2(V_1 e^{4\beta_1 t})^2} \quad (43)$$

The deceleration parameter

$$q = \frac{d}{dt} \left(\frac{1}{H} \right) - 1 = -1 \quad (44)$$

In the context of the exponential expansion model when deceleration parameter $q = -1$ and $\frac{dH}{dt} = 0$ it signifies the most optimal value for the decelerating parameter. This optimal value indicates that the universe is undergoing acceleration, experiencing the fastest possible rate of expansion. The value of anisotropic parameter shows anisotropic universe, but for large time it approaches to isotropic Universe. Additionally, when the anisotropic parameter exhibits a particular value, it suggests an anisotropic universe meaning that the universe appears uniform and consistent in all directions. on subtracting equation (19) from (18), we get,

$$2\frac{\ddot{A}}{A} + \frac{\ddot{B}}{B} - 2\frac{\dot{A}\dot{C}}{AC} - \frac{\dot{B}\dot{C}}{BC} = (p_q + \rho_q)(1 + 2\lambda) \quad (45)$$

Substituting the values metric potentials, A, B, C from equation (34) (35) and (36) also by using equation of state (13) for $\omega = \frac{1}{3}$, we obtained quark pressure as follows,

$$p_q = \frac{\left(\frac{e^{-4\beta_1 t}}{\alpha_1}\right)^2 [2D_1^2 + D_2^2 - 2D_1D_3 - D_2D_3]}{4(1 + 2\lambda)} \quad (46)$$

The quark matter density is given as

$$\rho_q = \frac{\left(\frac{e^{-4\beta_1 t}}{\alpha_1}\right)^2 [2D_1^2 + D_2^2 - 2D_1D_3 - D_2D_3]}{12(1 + 2\lambda)} \quad (47)$$

Using equation (34), (35),(36) in equation(45) with the help of equation of state in equation (13) for $\omega = \frac{1}{3}$, the pressure and energy density of strange quark matter is found to be,

$$p = \frac{\left(\frac{e^{-4\beta_1 t}}{\alpha_1}\right)^2 [2D_1^2 + D_2^2 - 2D_1D_3 - D_2D_3]}{4(1 + 2\lambda)} - B_C \quad (48)$$

$$\rho = \frac{\left(\frac{e^{-4\beta_1 t}}{\alpha_1}\right)^2 [2D_1^2 + D_2^2 - 2D_1D_3 - D_2D_3]}{12(1 + 2\lambda)} + B_c \quad (49)$$

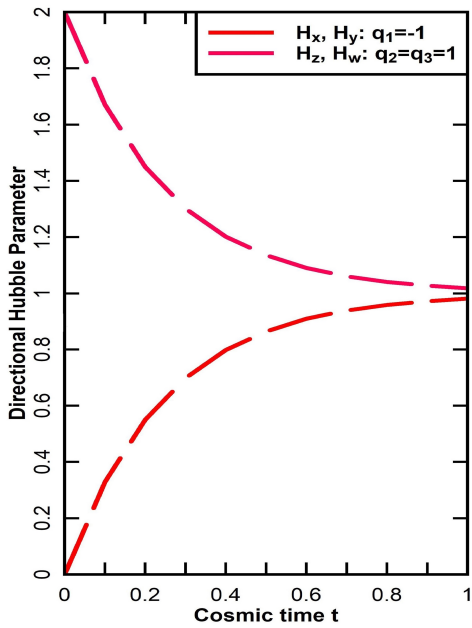


Figure 1. Directional Hubble Parameter Vs Cosmic time t for $\beta_1, D_2, D_3, \alpha_1 = 1, D_1 = -1$.

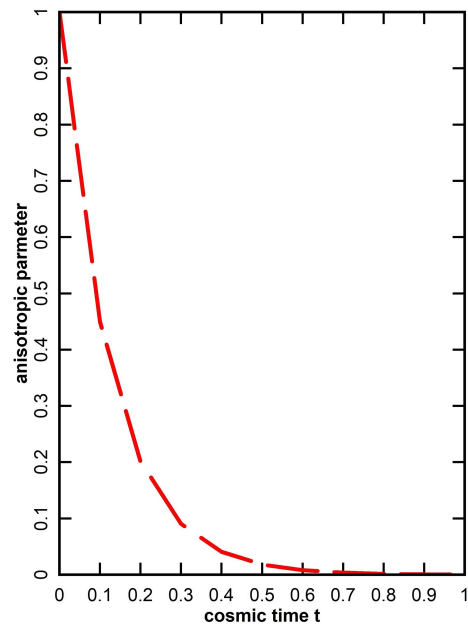


Figure 2. Anisotropic Parameter Vs Cosmic time t for $\beta_1, V_1, D_2, D_3 = 1, D_1 = -1$.

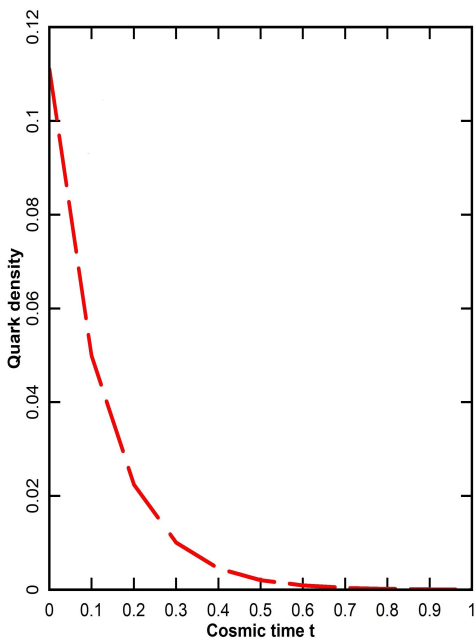


Figure 3. Quark density Vs Cosmic time t for $\beta_1, \alpha_1, D_2, D_3, \lambda = 1, D_1 = -1$

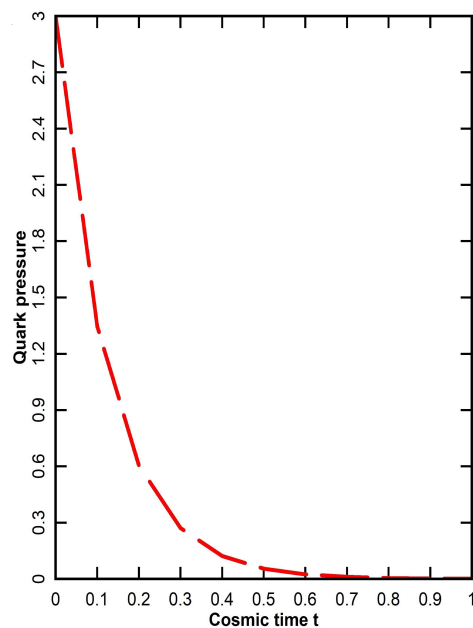


Figure 4. Quark Pressure Vs Cosmic time t for $\beta_1, \alpha_1, D_2, D_3, \lambda = 1, D_1 = -1$.

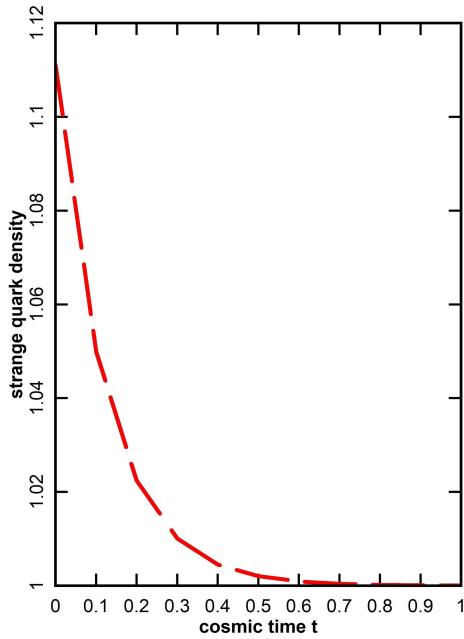


Figure 5. Strange Quark density Vs Cosmic time t for $\beta_1, \alpha_1, D_2, D_3, \lambda, B_c = 1, D_1 = -1$.

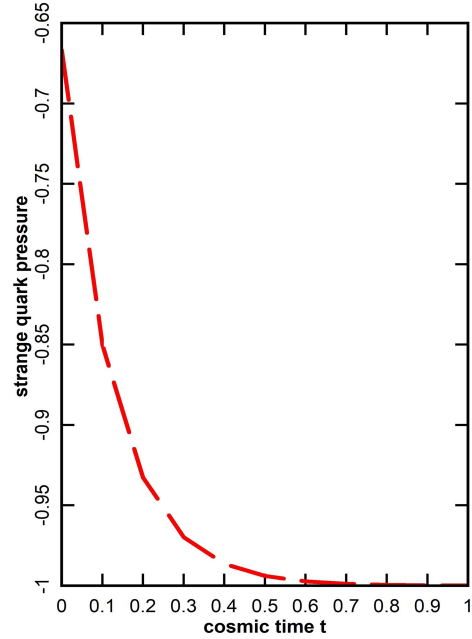


Figure 6. Strange Quark pressure Vs Cosmic time t for $\beta_1, \alpha_1, D_2, D_3, \lambda, B_c = 1, D_1 = -1$.

4.2. Model for Power Law Expansion

Here, a power law volumetric expansion is given by

$$V = \alpha_1 t^{4n}$$

Using the Equation (33) in (29)- (31), the scale factor obtained as follows:

$$A = C_1 \alpha_1^{\frac{1}{4}} t^n \exp \left[\frac{D_1}{\alpha_1} \frac{t^{1-4n}}{1-4n} \right] \tag{50}$$

$$B = C_2 \alpha_1^{\frac{1}{4}} t^n \exp \left[\frac{D_2}{\alpha_1} \frac{t^{1-4n}}{1-4n} \right] \tag{51}$$

$$C = C_3 \alpha_1^{\frac{1}{4}} t^n \exp \left[\frac{D_3}{\alpha_1} \frac{t^{1-4n}}{1-4n} \right] \tag{52}$$

At initial time $t = 0$, all the metric potentials are vanishing and finally they diverge to infinity as $t \rightarrow \infty$. Thus, the model compatible with a big bang model.

The directional Hubble parameter $H_x = H_y, H_z, H_\omega$ are given as

$$H_x = H_y = \frac{n}{t} + \frac{D_1}{\alpha_1 t^{4n}} \tag{53}$$

$$H_z = \frac{n}{t} + \frac{D_2}{\alpha_1 t^{4n}} \tag{54}$$

$$H_\omega = \frac{n}{t} + \frac{D_3}{\alpha_1 t^{4n}} \tag{55}$$

Mean Hubble parameter H is given by

$$H = \frac{n}{t} \tag{56}$$

Anisotropy parameter of the expansion is

$$\Delta = \left[\sum_{i=1}^4 \left(\frac{H_i - H}{H} \right)^2 \right] = \frac{\mu^2}{4n^2 \alpha_1^2 t^{2(2n-1)}} \tag{57}$$

where $\mu^2 = 2D_1^2 + D_2^2 + D_3^2$
 Dynamical scalar is given by

$$\theta = 4H = \frac{4n}{t} \tag{58}$$

Shear scalar is given by

$$\sigma^2 = \frac{\mu^2}{2\alpha_1^2 t^{4n}} \tag{59}$$

It is noticed that at initial time $t = 0$ the Hubble parameter H , dynamical scalar expansion θ starts with infinite value and finally tends to zero as $t \rightarrow \infty$. Deceleration parameter q is given by,

$$q = \frac{1}{n} - 1 \tag{60}$$

For $n > 1$ the deceleration parameter is always negative which represent the accelerating universe. Substituting the values metric potentials, A, B, C from equations(50) (51) and (52) in equation (45) also by using equation (13) for $\omega = \frac{1}{3}$, we obtained quark pressure as follows,

$$p_q = \frac{\left(\frac{2D_1^2 + D_2^2 - 2D_1 D_3 - D_2 D_3}{(\alpha_1 t^{4n})^2} \right) - \frac{3n}{t^2}}{4(1 + 2\lambda)} \tag{61}$$

The quark matter density is given as

$$\rho_q = \frac{\left(\frac{2D_1^2 + D_2^2 - 2D_1 D_3 - D_2 D_3}{(\alpha_1 t^{4n})^2} \right) - \frac{3n}{t^2}}{12(1 + 2\lambda)} \tag{62}$$

Using equation (50),(51), (52) in equation (45) with the help of equation of state in equation (13) for $\omega = \frac{1}{3}$, the pressure and energy density of strange quark matter as follows,

$$\rho = \frac{\left(\frac{2D_1^2 + D_2^2 - 2D_1 D_3 - D_2 D_3}{(\alpha_1 t^4)^2} \right) - \frac{3n}{t^2}}{12(1 + 2\lambda)} + B_c \tag{63}$$

$$p = \frac{\left(\frac{2D_1^2 + D_2^2 - 2D_1 D_3 - D_2 D_3}{(\alpha_1 t^2)^2} \right) - \frac{3n}{t^2}}{4(1 + 2\lambda)} - B_c \tag{64}$$

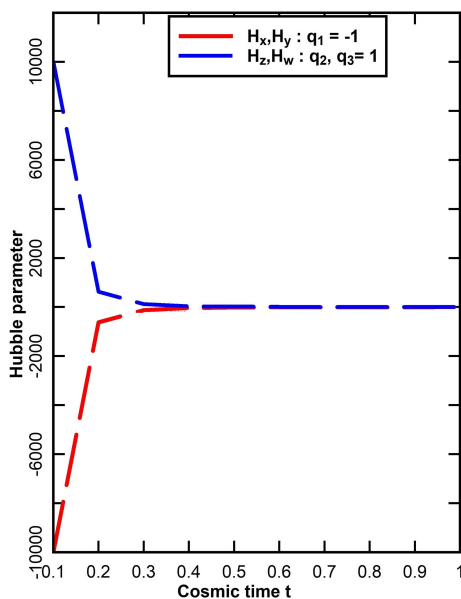


Figure 7. Directional Hubble Parameter Vs Cosmic time t for $\beta_1, V_1, D_2, D_3 = 1, D_1 = -1$

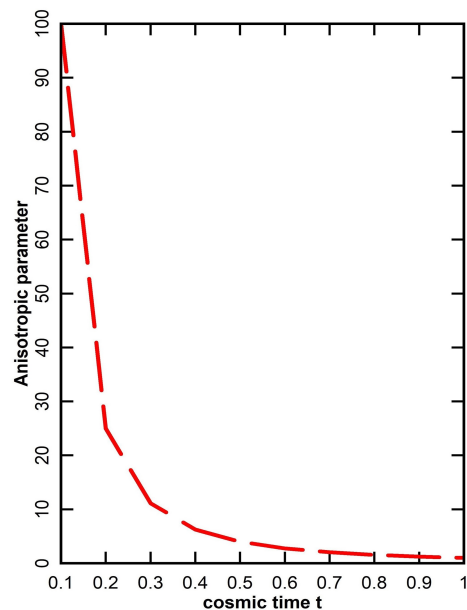


Figure 8. Anisotropic Parameter Vs Cosmic time t for $D_1 = -1, n, \alpha_1 D_2, D_3 = 1$

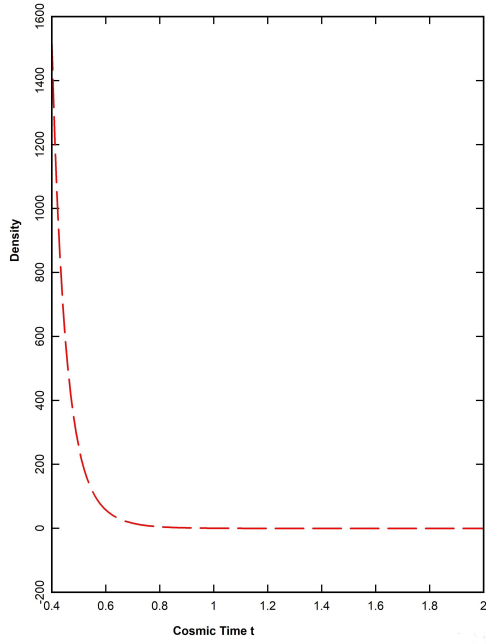


Figure 9. Quark density Vs Cosmic time t for $\beta_1, V_1, D_2, D_3, \lambda = 1, D_1 = -1$.

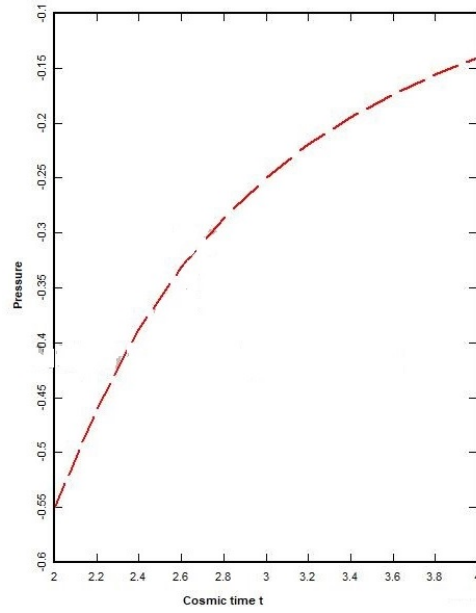


Figure 10. Quark Pressure Vs Cosmic time t for $\beta_1, V_1, D_2, D_3, \lambda = 1, D_1 = -1$.

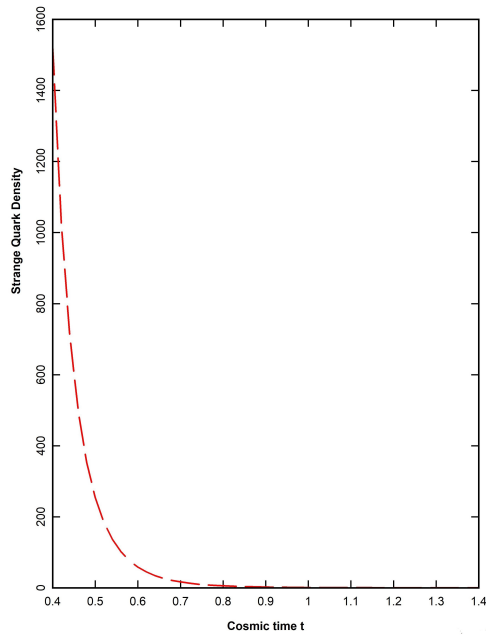


Figure 11. Strange Quark density Vs Cosmic time t for $\beta_1, V_1, D_2, D_3, \lambda, B_c = 1, D_1 = -1$.

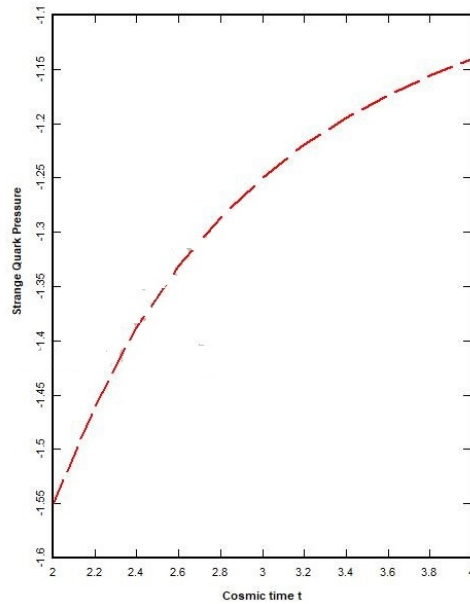


Figure 12. Strange Quark Pressure Vs Cosmic time t for $\beta_1, V_1, D_2, D_3, \lambda, B_c = 1, D_1 = -1$.

5. CONCLUSION

In this work, we have explored the higher dimensional plane symmetric cosmological model with quark and strange quark matter in the context of $f(R, T)$ gravity theory. We have obtained the exact solutions of field equations by assuming two different volumetric expansion laws namely, exponential expansion and power-law expansion.

In exponential expansion model

- The metric potentials accept constant value at initial time, after which they evolve with time without a singularity and eventually diverge to infinity. This result compatible with big bang scenario bear resemblance to [41].

- From Figure 1 and equations ((37), (38), (39)) represent that at initial epoch the directional Hubble parameters are finite whereas gradually decreases to constant β_1 as time tends to infinity.
- From equation (41), the mean anisotropy parameter shows a constant value at initial epoch, while as time increases the anisotropy parameter exponentially to null. Thus, universe approaches isotropy in this model as shown in Figure. 2.
- From equation (42), Dynamical scalar θ exhibits constant value throughout the evolution which shows uniform exponential expansion i.e., universe expands homogeneously as time t increases from initial epoch to infinity.
- From equation (43), Shear scalar measures constant value at $t = 0$ while vanish as $t \rightarrow \infty$.
- From equation (44), The deceleration parameter $q = -1$ represents universe is accelerating with highest rate which is in good agreement with present day observation.
- From equation (46) and (47) the pressure p_q and energy density ρ_q for the quark matter are finite in beginning of cosmic time and gradually decrease to zero as time tends to infinity as shown in Figure 3 and Figure 4. This result agreed with [36].
- The energy density (ρ_q) of strange quark matter exhibits the same behavior as quark matter. However, the difference in ρ values compared to ρ_q is attributed to the inclusion of an extra term, the bag constant B_c , in equation (49). Notably, while the quark pressure (p_q) shows a positive value, the strange quark pressure (p) is observed to be negative for the same constant values (refer to Figure 5 and Figure 6).

In power law expansion model

- The metric potentials vanish at initial time $t = 0$ and eventually they diverge to infinity as $t \rightarrow \infty$. thus, the model compatible with a big bang model and has a initial singularity.
- The directional Hubble parameter are diverging at initial epoch and as the time tends to infinity, they approach to zero monotonically, from Figure 7. Also, Hubble parameter is decreasing as time increases and agreed with the results of [50].
- From equation (57) and Figure 8, mean anisotropic parameter decreases with time and tends to zero as time tends to infinity. Which shows that at early stage of evolution universe was anisotropic and at large time it approaches to isotropy.
- At initial epoch the directional Hubble parameter H , dynamical scalar expansion θ , mean anisotropic parameter, shear scalar starts with infinite value and finally tends to zero as $t \rightarrow \infty$. This suggest that in the initial phase of universe, the expansion of the model is notably rapid and progressively decreases over time. This observation indicates that universe evolution began with exceptionally rapid expansion and subsequently moderated as it continues to expand. i.e., it decreases with the expansion of universe.
- For the value $n > 1$, the deceleration parameter shows negative value which indicates that universe undergoes accelerated expansion while the positive value of decelerating parameter shows decelerating model from equation (60).
- From equation (61) and (62) the pressure p_q and energy density ρ_q for the quark matter are infinitely large as $t = 0$ and it gradually decrease to zero as $t \rightarrow \infty$ shown in Figure 9 and Figure 10. This result agreed with [51].
- The pressure (p) and energy density (ρ) of strange quark matter exhibit behaviour similar to quark matter. The difference in p and ρ values compared to p_q and ρ_q is attributed to the inclusion of an extra term, the bag constant, in equation (63) and (64). Also, we have observed the shifting of graph in Figure 11 and Figure 12 because of additional term Bag constant B_c .




In both the model, the pressure p and energy density ρ of strange quark matter behave same as quark matter. The bag constant plays a vital role in the expansion of universe. We observed that the pressure and energy density approaches to bag constant for large time ($t \rightarrow \infty$) energy density. In particular, pressure $p \rightarrow -B_c$ and energy density $\rho \rightarrow B_c$ as $t \rightarrow \infty$. Negative sign for pressure indicates the expansion of the universe in late time [42].

Finally, exact solutions introduced in this section might be valuable for better comprehension of development of the universe.

Acknowledgments

We extend our heartfelt thanks to the diligent referees who meticulously reviewed our research article. Their valuable insights and suggestions significantly enhanced the quality and clarity of our work. Lastly, we extend our gratitude to the esteemed editorial board of this renowned journal for their consideration of our research article.

ORCID

 **R.V. Mapari**, <https://orcid.org/0000-0002-5724-9734>;  **S.S. Thakre**, <https://orcid.org/0009-0009-9665-5530>;  **V.A. Thakare**, <https://orcid.org/0009-0007-5951-8321>

REFERENCES

- [1] A.G. Riess, A.V. Filippenko, P. Cgallis, et al., "Observational evidence from supernovae for an accelerating universe and a cosmological constant," *Astron. J.* **116**(3), 1009 (1998). <https://doi.org/10.1086/300499>
- [2] S. Perlmutter, G. Aldering, G. Goldhaber, et al., "Measurement of Ω and Λ from 42 High - redshift Supernovae," *Astrophys. J.* **517**, 565 (1999). <https://doi.org/10.1086/307221>
- [3] S. Perlmutter, et al., "New Constraints on Ω_M, Ω_Λ and W from an independent set of 11 High-Redshift Supernovae Observed with the Hubble Space Telescope," *Astrophys. J.* **598**, 102 (2003). <https://doi.org/10.1086/378560>
- [4] J. Hoftuft, et al., "Increasing Evidence for Hemispherical power Asymmetry in the FiveYear WMAP Data," *Astrophysical Journal*, **699**, 985 (2009). <https://doi.org/10.1088/0004-637X/699/2/985>
- [5] C.L. Bennett, et al., "First - Year Wilkinson Microwave Anisotropy Probe (WMAP) Observations: Preliminary Maps and Basics Results," *Astrophys. J. Suppl. Ser.* **148**, 1 (2003). <https://doi.org/10.1086/377253>
- [6] R. Ferraro, and F. Fiorini, "Modified teleparallel gravity: inflation without an inflaton," *Phys. Rev. D*, **75**, 084031 (2007). <https://doi.org/10.1103/PhysRevD.75.084031>
- [7] G.R. Bengochea, and R. Ferraro, "Dark torsion as the cosmic speed-up," *Phys. Rev. D*, **79**, 124019 (2009). <https://doi.org/10.1103/PhysRevD.79.124019>
- [8] T. Harko, F.S.N. Lobo, S. Nojiri, S.D. Odintsov, " $f(R, T)$ gravity," *Phys. Rev. D*, **84**, 024020 (2011). <https://doi.org/10.1103/PhysRevD.84.024020>
- [9] S.D. Katore, and S.P. Hatkar, "Bianchi type III and Kantowski -Sachs domain wall cosmological models in the $f(R, T)$ theory of gravitation," *Prog. Theor. Exp. Phys.* **2016**, 033E01 (2016). <https://doi.org/10.1093/ptep/ptw009>
- [10] A.Y. Shaikh, "Binary Mixture of Perfect Fluid and Dark energy in Modified Theory of Gravity," *Int. J. Theor. Phys.* **55**, 3120-3136 (2016). <https://doi.org/10.1007/s10773-016-2942-x>
- [11] R. K. Tiwari, A. Beesham, and A. Pradhan, "Transit cosmological model with domain wall in $f(R, T)$ gravity," *Gravit. Cosmol.* **23**, 392 (2017). <https://doi.org/10.1134/S020228931704020X>
- [12] K. Dasunaidu, Y. Aditya, and D.K. Reddy, "Cosmic strings in a five dimensional spherically symmetric background in $f(R, T)$ gravity," *Astrophys. Space Sci.* **363**, 158 (2018). <https://doi.org/10.1007/s10509-018-3380-4>
- [13] A.K. Biswal, K.L. Mahanta, and P.K. Sahoo, "Kalunza-Klein cosmological model in $f(R, T)$ gravity with domain walls," *Astrophys. Space Science*, **359**, 42 (2015). <https://doi.org/10.1007/s10509-015-2493-2>
- [14] D.D. Pawar, R.V. Mapari, and P.K. Agrawal, "A Modified holographic Ricci dark energy model in $f(R, T)$ theory of gravity," *Astrophys. Astron.* **40**, 13 (2019). <https://doi.org/10.1007/s12036-019-9582-5>
- [15] S.K. Jokwani, and V. Singh, "LRS Bianchi I Cosmological Model with Strange Quark Matter in $f(R, T)$ Gravity," *Phys. Sci. Forum*, **7**(1), 12 (2023). <https://doi.org/10.3390/ECU2023-14037>
- [16] D.D. Pawar, R.V. Mapari, and J.L. Pawade, "Perfect fluid and heat flow in $f(R, T)$ theory," *Pramana-J. Phys.* **95**, 10 (2021). <https://doi.org/10.1007/s12043-020-02058-w>
- [17] D.D. Pawar, B.L. Jakore, and V.J. Dagwal, "Kaluza - Klein cosmological model with strange - quark - matter in Lyra geometry," *Int. J. Geom. Methods Mod. Phys.* **20**(5), 2350079 (2023). <https://doi.org/10.1142/S0219887823500792>
- [18] S. Kalkan, C. and Aktaş, "Behavior of Magnetized Strange Quark Matter in 5D Cosmological Model," *Iranian Journal of Science and Technology, Transactions A: Science*, **46**(11), 1505 (2022). <https://doi.org/10.1007/s40995-022-01363-w>
- [19] Y. Sobhanbabu, and M.V. Santhi, "Five-dimensional strange quark matter cosmological model with string cloud," *Int. J. Geom. Methods Mod. Phys.* **20**(7), 2350108 (2023). <https://doi.org/10.1142/S0219887823501086>
- [20] D.D. Pawar, D.K. Raut, and W.D. Patil, "FRW cosmological models with quark and strange quark matters in fractal gravity," *Mod. Phys. Letts. A*, **37**(19), 2250122 (2022). <https://doi.org/10.1142/S021773232250122X>
- [21] N. Itoh, "Hydrostatic equilibrium of hypothetical quark star," *Prog. The. Phys.* **44**, 291-292 (1970). <https://doi.org/10.1143/PTP.44.291>
- [22] A.R. Bodmer, "Collapsed Nuclei," *Phys. Rev. D*, **4**, 1601-1606 (1971). <https://doi.org/10.1103/PhysRevD.4.1601>

- [23] E. Witten, "Cosmic Separation of Phases," *Phys. Rev. D*, **30**, 272-285 (1984). <https://doi.org/10.1103/PhysRevD.30.272>
- [24] M.K. Mak, and T. Harko, "Quark stars admitting a one parameter group of conformal motions," *International Journal of Modern Physics D*, **13**, 149 (2004). <https://doi.org/10.1142/S0218271804004451>
- [25] A. Dixit, V.K. Bhardwaj, A. Pradhan, and S. Krishnannair, "Observational constraint in Kantowski-Sachs $f(R)$ gravity model with strange quark matter," *Indian Journal of Physics*, **55**, 55 (2023). <https://doi.org/10.1007/s12648-023-02669-0>
- [26] P.K. Sahoo, and B. Mishra, "Higher- dimensional Bianchi type - III universe with strange quark matter attached to string cloud in general relativity," *Turkish Journal of Phys.* **39**, 43-53 (2015). <https://doi.org/10.3906/fiz-1403-5>
- [27] S.D. Katore, "Strange Quark Matter Attached to String Cosmology in FRW Space-Time," *International Journal of Theoretical Physics*, **51**, 83-89 (2012). <https://doi.org/10.1007/s10773-011-0880-1>
- [28] R. Santhikumar, B. Satyannarayana, and D.R.K. Reddy, "On Axially Symmetric Cosmological Model with Strange Quark Matter Attached to String Cloud in General Relativity," *Int. J. of Phys. and Math. Sci.* **5**, 40 (2015). <https://www.cibtech.org/J-PHYSICS-MATHEMATICAL-SCIENCES/PUBLICATIONS/2015/Vol-5-No-2/04-JPMS-002-SANTHI-KUMAR-Axially-Symmetric.pdf>
- [29] S.D. Katore, and A.Y. Shaikh, "Cosmological Model with Strange Quark Matter Attached to Cosmic String for Axially Symmetric Space-Time," *Int. J. Theor. Phys.* **51**, 1881-1888 (2012). <https://doi.org/10.1007/s10773-011-1064-8>
- [30] I. Yilmaz, et al., "Quark and Strange quark matter in $f(R)$ gravity for Bianchi type I and V space-times," *Gen. Relat. Gravit.* **44**, 2313-2328 (2012). <https://doi.org/10.1007/s10714-012-1391-y>
- [31] I. Yilmaz, A. Kucukarslan, and S. Ozder, "The Behavior of Strange Quark Matter in the FRW Universes," *Int. J. Mod. Phys. A*, **22**, 2283-2291 (2007). <https://doi.org/10.1142/S0217751X07036622>
- [32] K.S. Adhav, A.S. Bansod, and S.L. Mundhe, "Kantowski-Sachs Cosmological model with quark and strange quark matter in $f(R)$ theory of gravity," *Open Physics*, **13**, 90 (2015). <https://doi.org/10.1515/phys-2015-0010>
- [33] V.R. Chirde, and S.H. Shekh, "Transition between general relativity and quantum gravity using quark and strange quark matter with some kinematical test," *Journal of Astrophysics Astronomy*, **39**, 56 (2018). <https://doi.org/10.1007/s12036-018-9555-0>
- [34] S.P. Hatkar, C.D. Wadale, and S.D. Katore, "Bianchi Type -I Quark and Strange Quark Cosmological Models in $f(G)$ Theory of Gravitation," *Bulgarian Journal of Physics*, **47**, 59 (2020). https://www.bjpb-bg.com/papers/bjp2020_1-2_059-074.pdf
- [35] S. Aygün, C. Aktas, I. Yilmaz, and M. Sahin, "Higher Dimensional FRW Universe Solutions with Quark and Strange Quark Matter in Creation Field Cosmology," *Chinese Journal of Physics*, **54**, 810 (2016). <https://doi.org/10.1016/j.cjph.2016.08.006>
- [36] P.K. Agrawal, and D.D. Pawar, "Plane Symmetric Cosmological Model with Quark and Strange Quark matter in $f(R, T)$ Theory of Gravity," *Journal of Astrophysics Astronomy*, **38**, 2-7 (2017). <https://doi.org/10.1007/s12036-016-9420-y>
- [37] D.D. Pawar, R.V. Mapari, and V.M. Raut, "Magnetized Strange Quark Matter in Lyra Geometry," *Bulgarian Journal of Physics*, **48**, 225-235 (2021). <https://www.bjpbg.com/papers/bjpb2021>
- [38] P.K. Sahoo, P. Sahoo, B.K. Bishi, and S. Aygün, "Magnetized strange quark matter in $f(R, T)$ gravity with bilinear and special form of time varying deceleration parameter," *New Astronomy*, **60**, 80-87 (2018). <https://doi.org/10.1016/j.newast.2017.10.010>
- [39] S.R. Kumbhare, and G.S. Khadekar, "Magnetized Quark and Strange Quark Matter in the Higher Dimensional Spherically Symmetric Space Time Admitting One Parameter Group of Conformal Motions," *Journal of Dynamical Systems and Geometric Theories*, **20**(1), 67 (2022). <https://doi.org/10.1080/1726037X.2022.2079265>
- [40] R. Nagpal, J.K. Singh, and S. Aygün, "FLRW cosmological models with quark and strange quark matters in $f(R, T)$ gravity," *Astrophysics Space Science*, **363**, 6(2018). <https://doi.org/10.1007/s10509-018-3335-9>
- [41] V.R. Chirde, and S.H. Shekh, "Plane Symmetric Dark Energy Model in the Form of Wet Dark Fluid in $f(R, T)$ Gravity," *Journal of Astrophysics and Astronomy*, **37**, 15 (2016). <https://doi.org/10.1007/s12036-016-9391-z>
- [42] V. Singh, and A. Beesham, "LRS Bianchi I model with strange quark matter and $\Lambda(t)$ in $f(R, T)$ gravity," *New Astronomy*, **89**, 101634 (2021). <https://doi.org/10.1016/j.newast.2021.101634>
- [43] G.S. Khadekar, and R. Shelote, "Higher Dimensional Cosmological Model with Quark and Strange Quark Matter," *Int. J. Theor. Phys.* **51**, 1442-1447 (2012). <https://doi.org/10.1007/s10773-011-1020-7>
- [44] S. Aygün, H. Caglar, D. Taşer, and C. Aktas, "Quark and strange quark matter solutions for higher dimensional FRW universe in Lyra geometry," *Eur. Phys. J. Plus*, **130**, 12 (2015). <https://doi.org/10.1140/epjp/i2015-15012-x>
- [45] S. Aygün, C. Aktas, and I. Yilmaz, "Strange quark matter solutions for Mader's universe in $f(R, T)$ gravity with λ ," *Astrophys. Space Sci.* **361**, 380 (2016). <https://doi.org/10.1007/s10509-016-2956-0>

- [46] D.D. Pawar, and R.V. Mapari, "Plane Symmetry Cosmology Model of Interacting Field in $f(R, T)$ Theory," Journal of Dynamical Systems and Geometric Theories, **20**(1), 115 (2022). <https://doi.org/10.1080/1726037X.2022.2079268>
- [47] M. Krishna, S. Kappala, and R. Santhikumar, "Accelerating Plane Symmetric Cosmological Model with Bulk Viscous and Cosmic Strings in Lyra's Geometry", <https://doi.org/10.48550/arXiv.2306.10579>
- [48] V.G. Mete, V.M. Umankar, and A.M. Pund, "Higher Dimensional Plane Symmetric Cosmological Models with Two- Fluid Source in General Relativity," Int. J. Theor. Phys. **52**, 4439 (2013). <https://doi.org/10.1007/s10773-013-1763-4>
- [49] V.A. Thakare, R.V. Mapari, and S.S. Thakre, 'Five Dimensional Plane Symmetric Cosmological Model With Quadratic Equation of State Theory of Gravity," East European Journal of Physics, (3), 108 (2023). <https://doi.org/10.26565/2312-4334-2023-3-08>
- [50] V.R. Patil, J.L. Pawde, R.V. Mapari, and P. Bolke, "Energy Conditions with Interacting Field in $f(R)$ Gravity," East European Journal of Physics, (3), 62 (2023). <https://doi.org/10.26565/2312-4334-2023-3-04>
- [51] S.D. Katore, S.P. Hatkar, and R.J. Baxi, "Stability of Strange Quark Matter Cosmology in Modified Theory of Gravitation," Prespace Time Journal, **8**(2), 158-173 (2017). <https://www.prespacetime.com/index.php/pst/article/download/1208/1169>

ПОВЕДІНКА КВАРКА ТА ДИВНОЇ КВАРКОВОЇ МАТЕРІЇ ДЛЯ ВСЕСВІТУ ВИЩОГО ВИМІРУ ТИПУ Б'ЯНКІ-І У $f(R, T)$ ГРАВІТАЦІЇ

Р.В. Мапарі^а, С.С.Такре^б, В.А. Тхакаре^с

^а Департамент математики, Державний науковий коледж, Гадчиролі (М.С.), Індія - 442605

^б Департамент математики, Незалежний молодший коледж, Амраваті (М.С.), Індія - 444604

^с Департамент математики, Shri Shivaji Science, Amravati (M.S.) - 444604 India

Ця дослідницька стаття присвячена ретельному дослідженню поведінки, яку демонструють всесвіти типу Б'янкі у вищих вимірах типу I, включаючи присутність кварка та дивної кваркової матерії в рамках гравітації $f(R, T)$. Рішення, отримані для рівняння поля охоплюють сценарії як експоненційного об'ємного розширення, так і сценарію степеневому закону. Відповідно до моделі експоненціального розширення як тиск (p_q), так і щільність енергії (ρ_q), пов'язані з кварковою матерією, початково скінченні на початку космічного часу, поступово зменшуються до нуля, коли час просувається до нескінченності. І навпаки, у моделі степеневому закону ці параметри починаються нескінченно великими при $t = 0$. згодом зменшуються до нуля, коли час наближається до нескінченності. Крім того, проводиться дослідження фізичних і геометричних атрибутів моделі. Зокрема, у моделях розширення за степеневим законом поведінка дивної кваркової матерії відображає поведінку кваркової матерії щодо тиску (p) і густини енергії (ρ). Але в моделі експоненціального розширення тиск кварків і тиск дивних кварків поводить по-різному. Константа ν_{ag} стає критичним фактором, що впливає на розширення Всесвіту, і спостереження показують, що і тиск, і щільність енергії мають тенденцію до константи ν_{ag} у великих часових масштабах ($t \rightarrow \infty$). Зокрема, тиск $p \rightarrow -\nu_{ag}$ і щільність енергії $\rho \rightarrow \nu_{ag}$ у міру наближення часу до нескінченності. Знак негативного тиску вказує на розширення Всесвіту протягом пізніших епох.

Ключові слова: кварк і дивна кваркова матерія; постійна ν_{ag} ; Всесвіт вищого виміру Б'янкі типу I; $f(R, T)$ гравітація

ANALYSIS OF MARDER'S SPACE-TIME TSALLIS HOLOGRAPHIC DARK ENERGY COSMOLOGICAL MODEL IN $f(R, T)$ THEORY OF GRAVITY

Abhijeet Ompratap Dhore^{a*}, Mohini Ramrao Ugale^b

^aDepartment of Mathematics, Shri. Dr. R.G. Rathod Arts and Science College,
Murtizapur, Dist.-Akola 444 107, Maharashtra, India

^bDepartment of Science and Humanities, Sipna College of Engineering and Technology,
Amravati 444 701, Maharashtra, India

*Corresponding Author e-mail: drabhijeetdhore@gmail.com

Received April 2, 2024; revised May 3, 2024; accepted May 7, 2024

In this paper, the investigation explores an anisotropic cosmological model based on Marder's space-time Tsallis holographic dark energy (THDE) within the framework of $f(R, T)$ theory of gravity, where R represents the Ricci scalar and T signifies the trace of the stress energy-momentum tensor. field equation have solved for class of $f(R, T)$ gravity i.e. $f(R, T) = R + f(T)$. To obtain the precise solution, we employed the density of the THDE model along with the volumetric expansion laws, namely the power law and exponential law. Also explores the physical and geometrical aspects of the model.

Keywords: $f(R, T)$ gravity; Marder's space-time; THDE; Volumetric expansion

PACS: 04.50.kd, 04.20.-q, 98.80.-k

1. INTRODUCTION

Based on the latest observations in astrophysics, there is strong evidence indicating that the universe is presently expanding at an accelerated rate, presenting intriguing opportunities for advancements in modern cosmological theories [1, 2, 3, 4]. The observed accelerated expansion of the universe is thought to be propelled by dark energy (DE). DE constitutes the dominant portion of the universe, making up 68% of the total energy in the observable universe at present. In contrast, dark matter (DM) and ordinary matter (baryonic matter) contribute 26% and 5% respectively [5]. The specific traits of DE continue to elude understanding, leading to the formulation of various theories and explanations. Indeed, within various theories and models, the cosmological constant model is often regarded as the most straightforward choice for DE, characterized by an equation of state (EoS) parameter $\omega = -1$. However, it is not without its challenges, including issues such as cosmic coincidence and fine-tuning problems [6, 7]. To address these challenges, the scientific literature has proposed various DE models, including quintessence, phantom, k -essence, tachyon, holographic dark energy (HDE), and others. In contemporary times, the exploration of HDE models has become a promising pathway for comprehending cosmic expansion, operating within the framework of the holographic principle (HP) [8]. The HP posits that the limit on the vacuum energy Λ of a system with size L should not surpass the threshold of the black hole mass with an equivalent size. This limitation arises from the potential formation of a black hole in the quantum field in a vacuum, and the infrared (IR) and ultraviolet cutoffs [10]. The energy density of HDE is defined as $\rho_{HDE} = 3d^2 m_p^2 L^{-2}$, where m_p is the reduced Planck mass and L represents the IR cutoff, describing the size of the universe in the context of the HP [11].

In recent times, various HDE models, including the Modified Ricci (MRHDE), THDE, Rényi HDE (RHDE), and Sharma-Mittal HDE (SMHDE), have been proposed and introduced. Certainly, within these models, RHDE stands out as it is founded on the absence of interactions between cosmic sectors. Notably, this model exhibits greater stability on its own [12]. M. Tavayef et al. [13] explored the Tsallis and Cirto entropy expressions while incorporating the HDE hypothesis. Their investigation led to the formulation of a novel type of DE called THDE. The study further delved into the dynamics of this THDE within the framework of a non-interacting flat Friedmann-Robertson-Walker (FRW) universe, examining the evolutionary aspects of the system. In the scenario of non-interacting cosmos, SMHDE is acknowledged for its classical stability [13, 14, 15]. M. Abdollahi Zadeh et al. [16] have delved into the repercussions of introducing various IR cutoffs, including the particle horizon, the Ricci horizon, and the Granda-Oliveros (GD) cutoffs, on the properties of the THDE. Spyros Basilakos et al. [17] demonstrated how Tsallis cosmology can effectively address both the Hubble constant (H_0) and the matter density fluctuation amplitude (σ_8) tensions simultaneously. This modified cosmological scenario is achieved by applying the gravity-thermodynamics conjecture with the use of non-additive Tsallis entropy instead of the standard Bekenstein-Hawking entropy. A. Mohammadi et al. [18] conducted a study exploring

the application of the HP within the framework of Bianchi type-III space-time. A. Pradhan and A. Dixit [20] explored a THDE model within a flat FRW space-time, considering the higher derivative theory of gravity. A. Al. Manon et al. [21] have investigated a cosmological scenario illustrating the ongoing acceleration of the universe, featuring the coexistence of DM and THDE. M. Vijaya Santhi and Y. Sobhanbabu [22] have explored the dynamics of THDE, utilizing the Hubble radius as the IR cutoff, in a homogenous and anisotropic Bianchi type-III universe. This investigation was conducted within the context of the Saez-Ballester (SB) theory of gravitation and by solving the field equations associated with SB theory they have developed both interacting and non-interacting DE models. Y. Sobhanbabu and M. Vijaya Santhi [23] have dedicated their efforts to examining THDE, incorporating the Hubble radius as the IR cutoff, within a homogenous and anisotropic Kantowski-Sachs universe. This investigation unfolds within the framework of SB theory of gravitation. They have formulated both non-interacting and interacting models for THDE by solving the field equations and employing the connection between the metric potentials. B. D. Pandey et al. [24] have developed HDE model incorporating Tsallis entropy, a one parameter extension of Boltzmann-Gibbs entropy. R. Saleem et al. [25] have investigated the dynamics of warm inflation within a modified cosmological framework in the context of Rastall gravity. Within this scenario, they altered the standard Friedmann equations by incorporating recently proposed Tsallis and Barrow HDE entropies. M. Vijaya Santhi and Y. Sobhanbabu [26] have formulated both interacting and non-interacting models for THDE in an anisotropic and homogenous Bianchi type- VI_0 space-time. This was accomplished within the context of a scalar-tensor theory proposed by SB. To achieve this, they employed the relationship between the metric potentials of the model and a varying deceleration parameter, resolving the SB field equations. M. Sharif and S. Saba [27] have explored the reconstruction paradigm for the THDE model by incorporating the generalized Tsallis entropy conjecture with the Hubble horizon. This investigation took place within the framework of $f(G, T)$ gravity. M. Zubir and L. Rukh Durrani [28] have investigated THDE in a flat FRW model, utilizing the framework of $f(R, T)$ gravity. Ayman A. Aly [29] has developed a novel $f(T)$ modified gravity model, incorporating a THDE model and a Hubble cutoff. A. Pradhan et al. [30] have explored the Tsallis holographic quintessence, k -essence, and tachyon models of DE within the context of modified $f(R, T)$ gravity, employing the GO cutoff. S. H. Shekh et al. [31] analyzed THDE, transitioning into HDE through a specific selection of the positive non-additivity parameter δ . This study was carried out within the framework of modified $f(T, B)$ gravity, examining the validity of thermodynamics and energy conditions for a homogenous and isotropic FRW universe.

Expanding on the constructive discussions and favorable results emphasized earlier, this article explores the THDE model within the context of $f(R, T)$ gravity. The inquiry focuses on validating both the power law and exponential law components of the model.

2. TSALLIS HOLOGRAPHIC DARK ENERGY

It is essential to remember that the establishment and derivation of the conventional HDE density ($\rho_{HDE} = 3d^2m_p^2L^{-2}$) are contingent upon the entropy area relationship $S \sim A \sim L^2$ of black holes, where $A = 4\pi L^2$ represents the area of the horizon [9]. Nevertheless, the definition of HDE can be adjusted or revised in light of quantum considerations [32, 33]. Tsallis and Cirto illustrated that the horizon entropy of a black hole could potentially be modified according to mathematical expression of the form

$$S_\delta = \gamma A^\delta \quad (1)$$

where, γ is an unknown constant and δ denotes the non-additivity parameter [14]. It is evident that the Bekenstein entropy is registered when the appropriate limit of $\delta = 1$ and $\delta = (4G)^{-1}$. Certainly, at this limit, the power law distribution of probability becomes ineffective, and the system can be described by the conventional probability distribution [14].

Following the HP, which asserts that the number of degrees of freedom of a physical system should scale with its bounding area rather than its volume [34]. Cohen et al. [9] suggested that system entropy (S) should be constrained by an IR (L) cutoff, leading to proposed relation involving the IR cutoff and UV (Λ) as

$$L^3 \Lambda^3 \leq (S)^{3/4} \quad (2)$$

which combining with eqn. (1) leads to [9]

$$\Lambda^4 \leq (\gamma(4\pi)^\delta)L^{2\delta-4} \quad (3)$$

where, Λ^4 denotes the vacuum energy density. Employing the aforementioned inequality, we can suggest the THDE density as follows

$$\rho_t = BL^{2\delta-4} \quad (4)$$

where B is unknown parameter [35, 36, 37] and IR cutoff is taken as Hubble radius which leads to $L = H^{-1}$, where H is hubble parameter [10]. The density of THDE model along with its derivative by using eqn. (4) becomes

$$\rho_t = BH^{4-2\delta} \quad (5)$$

$$\dot{\rho}_t = B(4 - 2\delta)H^{3-2\delta}\dot{H} \tag{6}$$

where, \dot{H} is the derivative of Hubble parameter w.r.t t [10].

3. METRIC AND FIELD EQUATIONS

We consider the Marder’s space-time in the form [38]

$$ds^2 = M_1^2(dx^2 - dt^2) + M_2^2dy^2 + M_3^2dz^2 \tag{7}$$

where, M_1^2, M_2^2, M_3^2 are functions of cosmic time t . In recent years, M. Vijaya Santhi et al. [39] have conducted research on the dynamics of a Marder’s space-time cosmological model, which is grounded in the concept of bulk viscous strings within the framework of $f(R)$ gravity. Sezgin AYGÜN [40] has explored a homogenous and anisotropic Marder space-time model within the framework of (R, T) gravity, where the space-time is filled with a bulk viscous string matter distribution. D. D. Pawar and S. P. Shahre [38] have explored Marder’s space-time within the framework of (R, T) gravity, integrating a perfect fluid under a tilted congruence.

In this work we study the Marder’s space-time in (R, T) gravity with THDE. Here, the energy-momentum tensor for matter (T'_{ij}) and THDE (\bar{T}_{ij}) are given as follows:

$$T'_{ij} = \text{diag}[1, 0, 0, 0]\rho_m \tag{8}$$

$$\bar{T}_{ij} = \text{diag}[1, -\omega_t, -\omega_t, -\omega_t]\rho_t \tag{9}$$

it can be parameterized as

$$\bar{T}_{ij} = \text{diag}[1, -\omega_t, -\omega_t, -(\omega_t + \alpha)]\rho_t \tag{10}$$

where ρ_t and ρ_m are energy densities of THDE, and matter respectively and p_t and p_m is pressure of THDE and matter respectively. $\omega_t = \frac{p_t}{\rho_t}$ is an EoS parameter. Here, α the deviation from the EoS parameter in the z -direction, commonly referred to as the skewness parameter. We have an energy conservation equation as

$$(T'_{ij} + \bar{T}_{ij})_{;j} = 0 \tag{11}$$

The exploration of diverse cosmological models within the framework of (R, T) theory of gravity depends on the characteristics of the matter source under consideration. Harko et al. [41] introduced following class of $f(R, T)$ gravity:

$$f(R, T) = \begin{cases} R + 2f(T) \\ f_1(R) + f_2(T) \\ f_1(R) + f_2(R)f_3(T) \end{cases} \tag{12}$$

In this study, we have adopted a specific functional form, expressed as $f(R, T) = R + 2f(T)$. Here, $f(T)$ is a function of the trace of the energy-momentum tensor. By using this functional, the field equation can be rewritten as

$$R_{ij} - \frac{1}{2}Rg_{ij} = (T'_{ij} + \bar{T}_{ij})_{;j} + 2f_T(T'_{ij} + \bar{T}_{ij})_{;j} + [f(T) + 2pf_T]g_{ij} \tag{13}$$

where f_T is a partial derivative of f w.r.t T . We designate the function $f(T)$ to be contingent upon the trace of the energy-momentum tensor of matter, specifically as

$$f(T) = \lambda T \tag{14}$$

where λ is arbitrary constant. So $f_T = \lambda$. In metric (7), the Ricci scalar R can be represented in terms of metric potentials as [38]

$$R = -2 \left(\frac{\ddot{M}_1}{M_1^3} + \frac{\ddot{M}_2}{M_1^2 M_2} + \frac{\ddot{M}_3}{M_1^2 M_3} - \frac{\dot{M}_1^2}{M_1^4} + \frac{\dot{M}_2 \dot{M}_3}{M_1^2 M_2 M_3} \right) \tag{15}$$

In this analysis, we investigate the cosmological implications of the arbitrary function suggested by Harko et al. [41], which is represented by the expression

$$f(R, T) = R + 2f(T) \tag{16}$$

where R is the Ricci scalar and T is the trace of the energy-momentum tensor.

The field eqn. (13) for the metric (7), utilizing eqns. (8), (10), and (14) from modified $f(R, T)$ gravity, results in the following system of eqns:

$$\frac{1}{M_1^2} \left(\frac{\ddot{M}_2}{M_2} + \frac{\ddot{M}_3}{M_3} + \frac{\dot{M}_2 \dot{M}_3}{M_2 M_3} - \frac{\dot{M}_1 \dot{M}_2}{M_1 M_2} - \frac{\dot{M}_1 \dot{M}_3}{M_1 M_3} \right) = -(8\pi + 2\lambda)(\omega_t + \alpha)\rho_t + [2p_t - 3\omega_t \rho_t - \alpha\rho_t + \rho_m + \rho_t]\alpha \quad (17)$$

$$\frac{1}{M_1^2} \left(\frac{\ddot{M}_1}{M_1} + \frac{\ddot{M}_3}{M_3} - \frac{\dot{M}_1^2}{M_1^2} \right) = -(8\pi + 2\lambda)\omega_t \rho_t + [2p_t - 3\omega_t \rho_t - \alpha\rho_t + \rho_m + \rho_t]\alpha \quad (18)$$

$$\frac{1}{M_1^2} \left(\frac{\ddot{M}_1}{M_1} + \frac{\ddot{M}_2}{M_2} - \frac{\dot{M}_1^2}{M_1^2} \right) = -(8\pi + 2\lambda)\omega_t \rho_t + [2p_t - 3\omega_t \rho_t - \alpha\rho_t + \rho_m + \rho_t]\alpha \quad (19)$$

$$\frac{1}{M_1^2} \left(\frac{\dot{M}_1 \dot{M}_2}{M_1 M_2} + \frac{\dot{M}_1 \dot{M}_3}{M_1 M_3} + \frac{\dot{M}_2 \dot{M}_3}{M_2 M_3} \right) = -(8\pi + 2\lambda)(\rho_m + \rho_t) + [2p_t - 3\omega_t \rho_t - \alpha\rho_t + \rho_m + \rho_t]\alpha \quad (20)$$

We express the energy conservation eqn. (11) for both matter and THDE as follows,

$$(\dot{\rho}_m + \dot{\rho}_t) + \left(\frac{\dot{M}_1}{M_1} + \frac{\dot{M}_2}{M_2} + \frac{\dot{M}_3}{M_3} \right) [\rho_m + (1 + \omega_t)\rho_t] + \frac{\dot{M}_1}{M_1} \alpha \rho_t = 0 \quad (21)$$

where overhead ($\dot{}$) denotes for ordinary differentiation w.r.t t .

4. SOLUTION OF FIELD EQUATIONS AND COSMOLOGICAL MODELS

The set of field eqns. (17)-(20) represents a set of four independent eqns. with seven unknowns $M_1, M_2, M_3, \rho_m, \rho_t, \omega_t, \alpha$. From eqns. (18) and (19), we get

$$\frac{\dot{M}_2}{M_2} - \frac{\dot{M}_3}{M_3} = 0 \quad (22)$$

on integration gives,

$$\frac{M_2}{M_3} = c_2 \exp(c_1 \int dt) \quad (23)$$

To simplify matters, we decide that $M_1 = M_2$. The dynamical parameters for Marder’s space-time cosmological model are delineated as follows: The spatial volume of the metric is

$$V = a^3(t) = M_2^2 M_3 \quad (24)$$

The directional Hubble parameters

$$\begin{aligned} H_x = H_y &= \frac{\dot{M}_2}{M_2}, \\ H_z &= \frac{\dot{M}_3}{M_3} \end{aligned} \quad (25)$$

The generalized mean Hubble’s parameter H is expressed as

$$H = \frac{1}{3}(H_x + H_y + H_z) = \frac{1}{3} \left(\frac{2\dot{M}_2}{M_2} + \frac{\dot{M}_3}{M_3} \right) \quad (26)$$

The expansion scalar

$$\theta = 3H = 2\frac{\dot{M}_2}{M_2} + \frac{\dot{M}_3}{M_3} \quad (27)$$

The mean anisotropic parameter

$$A_m = \frac{1}{3} \sum_{i=1}^4 \left(\frac{H_i - H}{H} \right)^2 \quad (28)$$

The Shear scalar

$$\sigma^2 = \frac{3}{2} A_m H^2 \quad (29)$$

The deceleration parameter

$$q = -1 + \frac{d}{dt} \left(\frac{1}{H} \right) \tag{30}$$

From eqns. (23) and (24), we get

$$M_2 = V^{1/3} c_2^{1/3} \exp \left(\frac{c_1}{3} t \right) \tag{31}$$

$$M_3 = V^{1/3} c_2^{-2/3} \exp \left(-\frac{2}{3} c_1 t \right) \tag{32}$$

where c_1 and c_2 are integrating constants. From eqns. (31) and (32), metric (7) becomes

$$ds^2 = \left[V^{1/3} c_2^{1/3} \exp \left(\frac{c_1}{3} t \right) \right]^2 (dx^2 + dy^2 - dt^2) + \left[V^{1/3} c_2^{-2/3} \exp \left(-\frac{2}{3} c_1 t \right) \right]^2 dz^2 \tag{33}$$

To obtain the complete solution, we require two different volumetric expansion laws, both the power law expansion and exponential law expansion i.e. $V = t^m$ and $V = e^{AH_0 t}$ respectively [42].

5. MODEL FOR POWER LAW EXPANSION

We are contemplating a volumetric expansion by a power law relation as

$$V = t^m \tag{34}$$

where m is a positive constant. The positive value of the exponent m aligns with observational evidence that anticipates the universe.

The metric potentials (31) and (32) becomes

$$M_2 = t^{m/3} c_2^{1/3} \exp \left(\frac{c_1}{3} t \right) \tag{35}$$

$$M_3 = t^{m/3} c_2^{-2/3} \exp \left(-\frac{2}{3} c_1 t \right) \tag{36}$$

As the time t approaches zero, the analysis suggests that metric potentials (35) and (36) tend toward zero. Consequently, the model exhibits an initial singularity. Eqn. (33) with the help of eqns. (35) and (36) can be written as

$$ds^2 = \left[t^{m/3} c_2^{1/3} \exp \left(\frac{c_1}{3} t \right) \right]^2 (dx^2 + dy^2 - dt^2) + \left[t^{m/3} c_2^{-2/3} \exp \left(-\frac{2}{3} c_1 t \right) \right]^2 dz^2 \tag{37}$$

From eqns. (25), (35), and (36), the directional Hubble parameters are

$$H_x = H_y = \frac{m}{3t} + \frac{c_1}{3} \tag{38}$$

$$H_z = \frac{m}{3t} - \frac{2c_1}{3} \tag{39}$$

From eqns. (26), (35), and (36), the mean Hubble parameter is given by

$$H = \frac{m}{3t} \tag{40}$$

From eqns. (27) and (40), the expansion scalar is given by

$$\theta = \frac{m}{t} \tag{41}$$

From eqns. (28), (38), (39), and (40), the mean anisotropic parameter is given by

$$A_m = \frac{2c_1^2 t^2}{m^2} \tag{42}$$

From eqns. (29), (40), and (42), the Shear scalar is

$$\sigma^2 = \frac{c_1^2}{3} \tag{43}$$

From eqns. (30) and (40), the deceleration parameter is

$$q = \frac{3}{m} - 1 \tag{44}$$

The energy conservation eqn. (21) results in the derivation of the subsequent separate conservation eqn. as

$$\dot{\rho}_m + 3H\rho_m = 0 \tag{45}$$

$$\dot{\rho}_t + 3H(1 + \omega_t)\rho_t + \frac{\dot{M}_2}{M_2}\alpha\rho_t = 0 \tag{46}$$

On integrating eqn. (45), we get matter density as

$$\rho_m = \frac{c_3}{t^m} \tag{47}$$

where c_3 is an integrating constant.

The DM is pressure less [29] i.e.

$$p_m = 0 \tag{48}$$

From eqns. (5), (6), and (40), the density of THDE is given as

$$\rho_t = B \left(\frac{m}{3t}\right)^{4-2\delta} \tag{49}$$

$$\dot{\rho}_t = -B(4 - 2\delta) \left(\frac{m}{3t}\right)^{3-2\delta} \left(\frac{m}{3t^2}\right) \tag{50}$$

For Λ -CDM model, the DE EoS is

$$\omega_t = -1 \tag{51}$$

we get THDE pressure as

$$p_t = -B \left(\frac{m}{3t}\right)^{4-2\delta} \tag{52}$$

From eqns. (40), (46), (49), (50), and (51), the skewness parameter is given as

$$\alpha = \left(\frac{4 - 2\delta}{t}\right) \left(\frac{m}{3t} + \frac{c_1}{3}\right)^{-1} \tag{53}$$

The density parameter for THDE and the energy density parameter for matter are defined and calculated as follows:

$$\Omega_t = B \left(\frac{m}{3t}\right)^{4-2\delta} \left(\frac{m^2}{3t^2}\right)^{-1} \tag{54}$$

$$\Omega_m = \left(\frac{c_3}{t^m}\right) \left(\frac{m^2}{3t^2}\right)^{-1} \tag{55}$$

Hence,

$$\Omega_t + \Omega_m = \left[B \left(\frac{m}{3t}\right)^{4-2\delta} + \frac{c_3}{t^m} \right] \left(\frac{m^2}{3t^2}\right)^{-1} \tag{56}$$

6. MODEL FOR EXPONENTIAL LAW EXPANSION

The exponential law expansion is

$$V = e^{4H_0t} \tag{57}$$

Typically, this results in a universe resembling de Sitter space-time. In this scenario, H_0 represents the Hubble Parameter during the current epoch. We have delved into the dynamics of the universe within the framework of the $f(R, T)$ gravity, specifically emphasizing exponential law. This exploration is aimed at offering a thorough grasp of the dynamics of the model and contrasting it with those observed in the power law model.

The metric potentials (31) and (32) becomes

$$M_2 = (e^{4H_0t})^{1/3} c_2^{1/3} \exp\left(\frac{c_1}{3}t\right) \tag{58}$$

$$M_3 = (e^{4H_0t})^{1/3} c_2^{-2/3} \exp\left(-\frac{2c_1}{3}t\right) \tag{59}$$

Eqn. (33) with the help of eqns. (58) and (59) can be written as

$$ds^2 = \left[(e^{4H_0t})^{1/3} c_2^{1/3} \exp\left(\frac{c_1}{3}t\right) \right]^2 (dx^2 + dy^2 - dt^2) + \left[(e^{4H_0t})^{1/3} c_2^{-2/3} \exp\left(-\frac{2c_1}{3}t\right) \right]^2 dz^2 \tag{60}$$

From eqns. (25), (58), and (59), the directional Hubble parameters are

$$H_x = H_y = \frac{4}{3}H_0 + \frac{c_1}{3} \tag{61}$$

$$H_z = \frac{4}{3}H_0 - \frac{2c_1}{3} \tag{62}$$

From eqns. (26), (58) and (59), the mean Hubble parameter is given by

$$H = \frac{4}{3}H_0 \tag{63}$$

From eqns. (27) and (63), the expansion scalar is given by

$$\theta = 4H_0 \tag{64}$$

From eqns. (28), (61), (62) and (63), the mean anisotropic parameter is given by

$$A_m = \frac{c_1^2}{8} \tag{65}$$

From eqns. (29), (64) and (65), the Shear scalar is

$$\sigma^2 = \frac{c_1^2 H_0^2}{3} \tag{66}$$

From eqns. (30) and (63), the deceleration parameter is

$$q = -1 \tag{67}$$

On integrating eqn. (45), we get the matter density for the model as

$$\rho_m = -c_4 e^{-4H_0t} \tag{68}$$

where c_4 is an integrating constant. The DM is pressure less [29] i.e.

$$p_m = 0 \tag{69}$$

From eqns. (5), (6), and (63), the density of THDE is given as

$$\rho_t = B \left(\frac{4}{3}H_0 \right)^{4-2\delta} \tag{70}$$

$$\dot{\rho}_t = 0 \tag{71}$$

For Λ -CDM model, we get THDE pressure as

$$p_t = -B \left(\frac{4}{3}H_0 \right)^{4-2\delta} \tag{72}$$

From eqns. (46), (63), (70) and (71), skewness parameter is becomes

$$\alpha = 0 \tag{73}$$

The density parameter for THDE and the energy density parameter for matter are defined and calculated as follows:

$$\Omega_t = B \left(\frac{4}{3}H_0 \right)^{4-2\delta} \left(\frac{16}{9}H_0^2 \right)^{-1} \tag{74}$$

$$\Omega_m = (-c_4 e^{-4H_0t}) \left(\frac{16}{9}H_0^2 \right)^{-1} \tag{75}$$

Hence,

$$\Omega_t + \Omega_m = \left[B \left(\frac{4}{3}H_0 \right)^{4-2\delta} + (-c_4 e^{-4H_0t}) \right] \left(\frac{16}{9}H_0^2 \right)^{-1} \tag{76}$$

7. DISCUSSION

In the preceding section, we endeavored to unravel the precise solution of the THDE cosmological model within Marder’s space-time framework. To do so, we postulated both a power law expansion and an exponential expansion law as plausible scenarios for the evolution of the universe. We have discovered that,

In section 5, for power law model.

- From Figure 1, both the Hubble parameter and the expansion scalar are approaching infinity as $t = 0$ signifies that at the inception of the universe, it was characterized by an infinitely dense and hot state. This characteristic behavior aligns with the concept of the Big Bang singularity, marking the beginning of cosmic expansion. As time progresses, both the Hubble parameter and the expansion scalar show a decrease. This pattern implies a diminishing rate of universal expansion over time. Despite the ongoing expansion, the momentum of this process gradually diminishes over time. As the cosmic time approaches infinity, both the Hubble parameter and the expansion scalar tend toward zero. This suggests that the rate of expansion of the universe is approaching a constant value. Such a scenario hints at a future phase where the rate of expansion of the universe becomes nearly constant, known as the de Sitter phase.
- Item From Figure 1, as cosmic time increases, the anisotropic parameter grows at an increasing rate. From eqn. (42), it is evident that the behavior of the anisotropic parameter is contingent upon the constants c_1 and m . Under this circumstance, the anisotropic parameter escalates as cosmic time t increases, yet diminishes with higher values of m .
- From eqn. (44),
 1. If $m = 3$ the deceleration parameter becomes zero. It indicates that the expansion of the universe is neither accerlerating, but rather proceeding at a constant rate. This scenario is consistent with a universe in which the gravitational effects of matter and energy are exactly balanced by the expansion itself.
 2. If $m > 3$ then the deceleration parameter is positive ($q > 0$), it indicates that the expansion of the universe is decelerating. In this scenario, the gravitational forces exerted by matter and energy within the universe are sufficiently strong to slow down the rate of expansion over time.
 3. If $m < 3$ then the deceleration parameter is negative ($q < 0$), it indicates that the expansion of the universe is accelerating. In this scenario, the gravitational effects of matter and energy are not sufficient to counteract the expansion, causing it to accelerate over time.
- From Figure 2(a), at the beginning of cosmic time $t = 0$ the density of THDE is significantly high, implying a phase of rapid expansion similar to cosmic inflation. As cosmic time progresses, the density of THDE decreases, indicating a corresponding reduction in the rate of expansion of the universe over time.
- From Figure 2(b), at the beginning of cosmic time ($t = 0$) the density goes to zero, which signifies a crucial epoch.

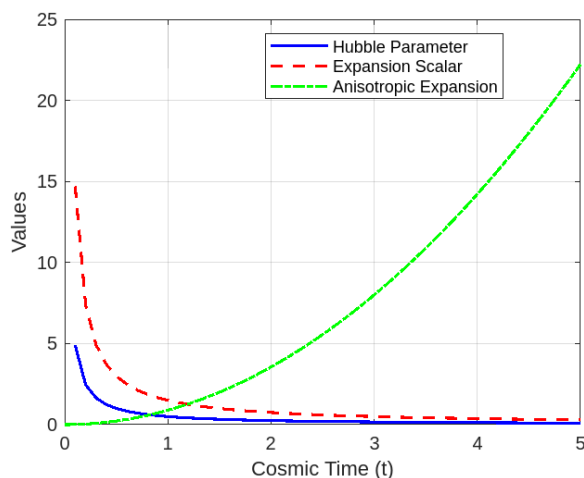


Figure 1. Hubble parameter, expansion scalar and anisotropic parameter versus cosmic time (t) for the particular choice of constants $c_1 = 1, m = 1.5$ in power law model

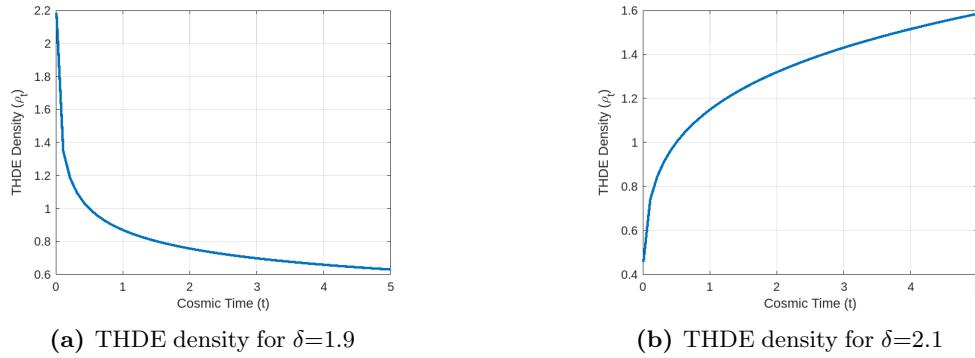


Figure 2. THDE density versus cosmic time (t) for the particular choice of constant $m = 1.5$ in power law model

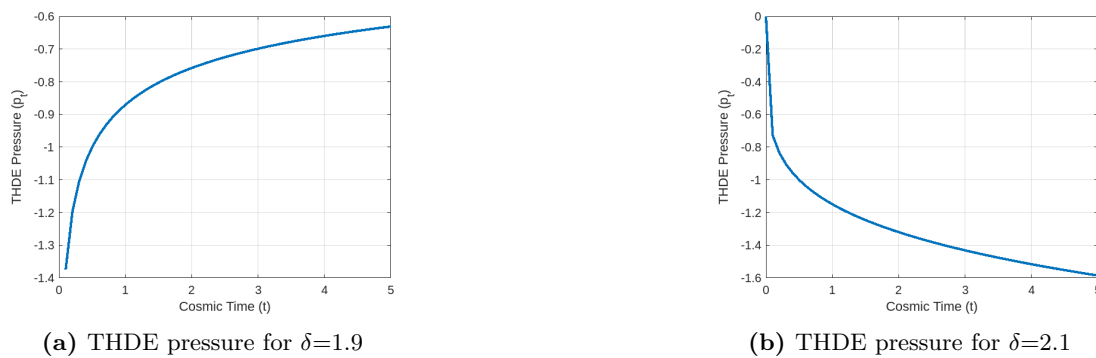


Figure 3. THDE pressure versus cosmic time (t) for the particular choice of constant $m = 1.5$ in power law model

- From Figure 2(a) (with $\delta = 1.9$), as cosmic time extends towards infinity the THDE density appears to stabilize at a fixed value. This suggests a scenario where, in the distant future, THDE could potentially dominate the energy density of the universe.
- From Figure 2(b) (with $\delta = 2.1$), as the cosmic time approaches infinity, the THDE density asymptotically approaches a non-zero value. In this case, the THDE density does not diminish to zero but approaches a finite value.

In section 6, for the exponential law model.

- The deceleration parameter $q = -1$ for this model signifies that the universe undergoes an accelerated expansion [42]. The expansion scalar maintains a constant value indicating that the rate of expansion of the universe remains constant over time [43]. The anisotropic parameter is constant, it implies that the universe exhibits isotropy.
- We found that the Hubble parameter, density, and pressure are constant.

8. CONCLUSION

We investigated Marder’s space-time model incorporating THDE within the framework of $f(R, T)$ gravity. The volumetric expansion law is utilized to derive precise solutions for field equations. Both the power law model and exponential law model yield the following conclusions. We analyzed 2D graph of the parameter by using MATLAB.



In the power law model, many fascinating findings emerge from our investigation. When the Hubble parameter is positive (t), we observe a universe is expanding. As time progresses towards infinity, the expansion gradually decelerates and eventually approaches zero. Interestingly, we have obtained the value of the deceleration parameter that depends on constant ($m = [2, 4]$), i.e. whether the universe accelerating or decelerating. From Figure 2(a) and 2(b), ($\delta < 2, \delta > 2$) the behavior of the universe suggests an evolving state where THDE plays a significant role in the expansion dynamics, potentially leading to an indefinite expansion. However, slight variations in the value of δ may influence the specific details of the expansion dynamics. Additionally, our examination highlights the existence of negative pressure, as depicted in eqn. (52). This negative pressure

is a distinctive attribute of DE. The inclusion of DE within the model provides evidence supporting the idea that DE plays a crucial role in influencing the dynamics of our universe.

In the exponential law model, we have obtained all dynamics parameters such as Hubble parameter (H), expansion scalar (θ), Shear scalar (σ^2), anisotropic parameter (A_m) are constant. Hence, as the universe evolves over time, this model demonstrates behavior similar to that of a cosmological constant model in its later stages. Additionally, the negative sign of the deceleration parameter signifies the expansion of the universe is accelerating. The ratio of the Shear scalar to the expansion scalar is non-zero, indicating that the universe is anisotropic.

Our findings indicate that the universe exhibits anisotropy during its early stages, yet as time progresses, the anisotropic behavior diminishes, leading to an isotropic present day universe. This conclusion aligns with various observational data. The models proposed in this paper offer a suitable description of the evolutionary trajectory of the universe.

ORCID

 **Abhijeet Ompratap Dhore**, <https://orcid.org/0009-0003-9970-3960>;  **Mohini Ramrao Ugale**, <https://orcid.org/0000-0002-4795-1052>

REFERENCES

- [1] A.G.Riess, A.V. Filippenko, P. Challis, A. Clocchiatti, A. Diercks, P.M. Garnavich, et al., "Observational evidence from supernovae for an accelerating universe and a cosmological constant," *The astronomical journal*, **116**(3), 1009 (1998). <https://doi.org/10.1086/300499>.
- [2] S. Perlmutter, G. Aldering, M.D. Valle, S. Deustua, R.S. Ellis, S. Fabbro, "Discovery of a supernova explosion at half the age of the Universe," *Nature*, **391**(6662),51-54 (1998). <https://doi.org/10.1038/34124>.
- [3] C.L. Bennett, R.S. Hill, G. Hinshaw, M.R. Nolta, N. Odegard, et al., "First-year wilkinson microwave anisotropy probe (wmap)* observations: foreground emission," *The Astrophysical Journal Supplement Series*, **148**(1), 97 (2003). <https://doi.org/10.1086/377252>.
- [4] M. Tegmark, M.A. Strauss, M.R. Blanton, K. Abazajian, S. Dodelson, H. Sandvik, et al., "Cosmological parameters from SDSS and WMAP," *Physical review D*, **69**(10), 103501 (2004). <https://doi.org/10.1103/PhysRevD.69.103501>.
- [5] P.A. Ade, N. Aghanim, M.I.R. Alves, C. Armitage-Caplan, M. Arnaud, M. Ashdown, et al., "Planck 2013 results, I. Overview of products and scientific results," *Astronomy and Astrophysics*, **571**, A1 (2014). <https://doi.org/10.1051/0004-6361/201321529>.
- [6] S. Weinberg, "The cosmological constant problem," *Reviews of modern physics*, **61**(1), 1 (1989). <https://doi.org/10.1103/RevModPhys.61.1>.
- [7] J.M. Overduin, and F.I. Cooperstock, "Evolution of the scale factor with a variable cosmological term," *Physical Review D*, **58**(4), 043506 (1998). <https://doi.org/10.1103/PhysRevD.58.043506>.
- [8] A.Y. Shaikh, "Diagnosing renyi and tsallis holographic dark energy models with hubble's horizon cutoff," *Indian Journal of Physics*, **98**, 1155–1162 (2023). <https://doi.org/10.1007/s12648-023-02844-3>.
- [9] A.G. Cohen, D.B. Kaplan, and A.E. Nelson, "Effective field theory, black holes, and the cosmological constant," *Physical Review Letters*, **82**(25), 4971 (1999). <https://doi.org/10.1103/PhysRevLett.82.4971>.
- [10] M. Younas, A. Jawad, S. Qummer, H. Moradpour, and S. Rani, "Cosmological implications of the generalized entropy based holographic dark energy models in dynamical Chern-Simons modified gravity," *Advances in High Energy Physics*, **2019**, 1287932 (2019). <https://doi.org/10.1155/2019/1287932>.
- [11] Y. Aditya, S. Mandal, P.K. Sahoo, and D.R.K. Reddy, "Observational constraint on interacting Tsallis holographic dark energy in logarithmic Brans–Dicke theory," *The European Physical Journal C*, **79**(12), 1020 (2019). <https://doi.org/10.1140/epjc/s10052-019-7534-5>.
- [12] H. Moradpour, S.A. Moosavi, I.P. Lobo, J.M. Graça, A. Jawad, and I.G. Salako, "Thermodynamic approach to holographic dark energy and the Rényi entropy," *The European Physical Journal C*, **78**, 1-6 (2018). <https://doi.org/10.1140/epjc/s10052-018-6309-8>.
- [13] M. Tavayef, A. Sheykhi, K. Bamba, and H. Moradpour, "Tsallis holographic dark energy," *Physics Letters B*, **781**, 195-200 (2018). <https://doi.org/10.1016/j.physletb.2018.04.001>.
- [14] C. Tsallis, and L.J. Cirto, "Black hole thermodynamical entropy," *The European Physical Journal C*, **73**, 1-7 (2013). <https://doi.org/10.1140/epjc/s10052-013-2487-6>.
- [15] A.S. Jahromi, S.A. Moosavi, H. Moradpour, J.M. Graça, I.P. Lobo, I.G. Salako, and A. Jawad, "Generalized entropy formalism and a new holographic dark energy model," *Physics Letters B*, **780**, 21-24 (2018). <https://doi.org/10.1016/j.physletb.2018.02.052>.
- [16] M.A. Zadeh, A. Sheykhi, H. Moradpour, and K. Bamba, "Note on Tsallis holographic dark energy," *The European Physical Journal C*, **78**, 1-11 (2018). <https://doi.org/10.1140/epjc/s10052-018-6427-3>.

- [17] S. Basilakos, A. Lympersis, M. Petronikolou, and E.N. Saridakis, "Alleviating both H_0 and σ_8 tensions in Tsallis cosmology," *The European Physical Journal C*, **84**(3), 297 (2024). <https://doi.org/10.1140/epjc/s10052-024-12573-4>.
- [18] A. Mohammadi, T. Golanbari, K. Bamba, and I.P. Lobo, "Tsallis holographic dark energy for inflation," *Physical Review D*, **103**(8), 083505 (2021). <https://doi.org/10.1103/PhysRevD.103.083505>.
- [19] J. Bharali, and K. Das, "Modified Tsallis Holographic Dark Energy," *Astrophysics*, **66**(3), 366-382 (2023). <https://doi.org/10.1007/s10511-023-09797-9>.
- [20] A. Pradhan, and A. Dixit, "Tsallis holographic dark energy model with observational constraints in the higher derivative theory of gravity," *New Astronomy*, **89**, 101636 (2021). <https://doi.org/10.1016/j.newast.2021.101636>.
- [21] A.A. Mamon, A.H. Ziaie, and K. Bamba, "A generalized interacting Tsallis holographic dark energy model and its thermodynamic implications," *The European Physical Journal C*, **80**, 1-12 (2020). <https://doi.org/10.1140/epjc/s10052-020-08546-y>.
- [22] M.V. Santhi, and Y. Sobhanbabu, "Bianchi type-III Tsallis holographic dark energy model in Saez-Ballester theory of gravitation," *The European Physical Journal C*, **80**(12), 1198 (2020). <https://doi.org/10.1140/epjc/s10052-020-08743-9>.
- [23] Y. Sobhanbabu, and M.V. Santhi, "Kantowski-Sachs Tsallis holographic dark energy model with sign-changeable interaction," *The European Physical Journal C*, **81**(11), 1-10 (2021). <https://doi.org/10.1140/epjc/s10052-021-09815-0>.
- [24] B.D. Pandey, P.S. Kumar, Pankaj, and U.K. Sharma, "New Tsallis holographic dark energy," *The European Physical Journal C*, **82**(3), 233 (2022). <https://doi.org/10.1140/epjc/s10052-022-10171-w>.
- [25] R. Saleem, I. Shahid, and M. Sabir, "An exact solution approach to warm inflation using Tsallis and Barrow holographic dark energy entropy within Rastall gravity," *The European Physical Journal Plus*, **137**(2), 279 (2022). <https://doi.org/10.1140/epjp/s13360-022-02494-0>.
- [26] M.V. Santhi, and Y. Sobhanbabu, "Tsallis holographic dark energy models in Bianchi type space time," *New Astronomy*, **89**, 101648 (2021). <https://doi.org/10.1016/j.newast.2021.101648>.
- [27] M. Sharif, and S. Saba, "Tsallis holographic dark energy in $f(G, T)$ gravity," *Symmetry*, **11**(1), 92 (2019). <https://doi.org/10.3390/sym11010092>.
- [28] M. Zubair, and L.R. Durrani, "Exploring tsallis holographic dark energy scenario in $f(R, T)$ gravity," *Chinese Journal of Physics*, **69**, 153-171 (2021). <https://doi.org/10.1016/j.cjph.2020.11.024>.
- [29] A.A. Aly, "Study of $F(T)$ gravity in the framework of the Tsallis holographic dark energy model," *The European Physical Journal Plus*, **134**, 1-7 (2019). <https://doi.org/10.1140/epjp/i2019-12698-6>.
- [30] A. Pradhan, G. Varshney, and U.K. Sharma, "The scalar field models of Tsallis holographic dark energy with Granda-Oliveros cutoff in modified gravity," *Canadian Journal of Physics*, **99**(10), 866-874 (2021). <https://doi.org/10.1139/cjp-2020-0605>.
- [31] S.H. Shekh, V.R. Chirde, and P.K. Sahoo, "Energy conditions of the $f(T, B)$ gravity dark energy model with the validity of thermodynamics," *Communications in Theoretical Physics*, **72**(8), 085402 (2020). <https://doi.org/10.1088/1572-9494/ab95fd>.
- [32] S. Wang, Y. Wang, and M. Li, "Holographic dark energy," *Physics reports*, **696**, 1-57 (2017). <https://doi.org/10.1016/j.physrep.2017.06.003>.
- [33] B. Wang, E. Abdalla, F. Atrio-Barandela, and D. Pavon, "Dark matter and dark energy interactions: theoretical challenges, cosmological implications and observational signatures," *Reports on Progress in Physics*, **79**(9), 096901 (2016). <https://doi.org/10.1088/0034-4885/79/9/096901>.
- [34] G.T. Hooft, "Dimensional reduction in quantum gravity," (1993). <https://doi.org/10.48550/arXiv.gr-qc/9310026>.
- [35] B. Guberina, R. Horvat, and H. Nikolić, "Non-saturated holographic dark energy," *Journal of Cosmology and Astroparticle Physics*, **2007**(01), 012 (2007). <https://doi.org/10.1088/1475-7516/2007/01/012>.
- [36] S. Ghaffari, M.H. Dehghani, and A. Sheykhi, "Holographic dark energy in the DGP braneworld with Granda-Oliveros cutoff," *Physical Review D*, **89**(12), 123009 (2014). <https://doi.org/10.1103/PhysRevD.89.123009>.
- [37] A.S. Jahromi, S.A. Moosavi, H. Moradpour, J.M. Graça, I.P. Lobo, I.G. Salako, and A. Jawad, "Generalized entropy formalism and a new holographic dark energy model," *Physics Letters B*, **780**, 21-24 (2018). <https://doi.org/10.1016/j.physletb.2018.02.052>.
- [38] D.D. Pawar, and S.P. Shahare, "Anisotropic tilted cosmological model in $f(R, T)$ theory of gravity," *New Astronomy*, **75**, 101318 (2020). <https://doi.org/10.1016/j.newast.2019.101318>.
- [39] M.V. Santhi, A.S. Rao, T. Chinnappalanaidu, and S.S. Madhu, "Bulk viscous string cosmological model in a modified theory of gravity," *Mathematical Statistician and Engineering Applications*, **71**(3s2), 1056-1072 (2022). <https://doi.org/10.1142/S0219887819500051>.
- [40] S. Aygün, "Marder type universe with bulk viscous string cosmological model in $f(R, T)$ gravity," *Turkish Journal of Physics*, **41**(5), 436-446 (2017). <https://doi.org/10.3906/fiz-1704-14>.

- [41] T. Harko, F.S. Lobo, S.I. Nojiri, and S.D. Odintsov, " $f(R, T)$ gravity," Physical Review D, **84**(2), 024020 (2011). <https://doi.org/10.1103/PhysRevD.84.024020>.
- [42] P.K. Sahoo, B. Mishra, and S.K. Tripathy, "Kaluza–Klein cosmological model in $f(R, T)$ gravity with $\Lambda(T)$," Indian Journal of Physics, **90**, 485-493 (2016). <https://doi.org/10.1007/s12648-015-0759-8>.
- [43] V.R. Chirde, and S.H. Shekh, "Plane symmetric dark energy models in the form of wet dark fluid in $f(R, T)$ gravity," Journal of Astrophysics and Astronomy, **37**, 1-16 (2016). <https://doi.org/10.1007/s12036-016-9391-z>.

АНАЛІЗ КОСМОЛОГІЧНОЇ МОДЕЛІ ГОЛОГРАФІЧНОЇ ТЕМНОЇ ЕНЕРГІЇ ЦАЛЛІСА У ПРОСТОРІ-ЧАСІ МАРДЕРА В $f(R, T)$ ТЕОРІЇ ГРАВІТАЦІЇ

Абхіджит Омпрагап Доре^a, Мохіні Рамрао Угале^b

^a Департамент математики, Shri. Dr. R.G. Коледж мистецтв і науки Патод,
Муртізанпур, Округ Акола 444 107, Махараштра, Індія

^b Департамент науки та гуманітарних наук, Інженерно-технологічний коледж Сипна,
Амраваті 444 701, Махараштра, Індія

У цій роботі досліджується анізотропна космологічна модель, заснована на просторово-часовій голографічній темній енергії Цалліса (THDE) Мардера в рамках $f(R, T)$ теорії гравітації, де R представляє скаляр Річчі, а T означає слід тензора енергії-імпульсу напруги. Рівняння поля розв'язано для класу гравітації $f(R, T)$, тобто $f(R, T) = R + f(T)$. Щоб отримати точне рішення, ми використали щільність моделі THDE разом із законами об'ємного розширення, а саме степеневим і експоненціальним законом. Також досліджуються фізичні та геометричні аспекти моделі.

Ключові слова: $f(R, T)$ гравітація; простір-час Мардера; THDE; Об'ємне розширення

ANISOTROPIC BARROW HOLOGRAPHIC DARK ENERGY MODELS IN SCALAR-TENSOR THEORY OF GRAVITATION

Y. Sobhanbabu^{a*}, G. Satyanarayana^b, N.V.S. Swamy Chinamilli^a, P.V. Rambabu^a

^aSRKR Engineering College (A), Bhimavaram-534204, India

^bSasi Institute of Technology and Engineering College (A), Tadepalligudem, India

*Corresponding Author e-mail: sobhan.maths@gmail.com

Received April 8, 2024; revised May, 9, 2024; accepted May 14, 2024

In this research, we have derived the solution of the field equations of the scalar-tensor theory of gravitation, proposed by Saez and Ballester (Phys. Lett. A113, 467:1986) within the frame-work of Bianchi type-III Universe. We have analyzed the interacting and non-interacting anisotropic Barrow Holographic Dark Energy (BHDE) models by assuming the time dependent deceleration parameter ($q(t)$). Further, we have discussed the several cosmological parameters such as energy densities of pressureless dark matter and BHDE, skewness, deceleration, equation of state parameters, $\omega_{BH}-\omega'_{BH}$ plane and stability of the both interacting and non-interacting models. Also, we have observed that in our non-interacting and interacting models deceleration and equation of state parameters support the recent observational data.

Keywords: *Bianchi type-III Universe; Cosmology; Saez-Ballester theory*

PACS: 04.50.Kd, 04.50.+h

1. INTRODUCTION

Precision Cosmology [1] measurements have definitively shown that our Universe is experiencing an accelerated phase expansion [2, 3, 4, 5, 6, 7, 8, 9]. However, the fuel of this mechanism is not yet known, leaving room for disparate explanations. Tentative descriptions can be basically grouped into two classes: on one side, Extended Gravity Theories [10] aim at solving the puzzle by modifying the geometric part of Einstein–Hilbert action in General Relativity. On the other side, one can introduce new degrees of freedom in the matter sector, giving rise to dynamical Dark Energy models. In this context, a largely followed approach is the so called Holographic Dark Energy (HDE) model [11, 12, 13, 14, 15, 16, 17, 18, 19, 20, 21, 22, 23, 24, 25, 26, 27, 28, 29, 30, 31, 32] which is based on the use of the holographic principle at cosmological scales.

The holographic DE model (HDE) suggests, this model is originated from holographic principle and its energy density can be expressed by $\rho_{de} = \frac{3C^2 M_p^2}{L^2}$, here C^2 is a numerical constant, M_p^2 is the reduced Planck mass and L denotes the size of the current Universe such as the Hubble scale [33, 34]. In addition, the holographic DE has some problems and cannot explain the time line of a flat FRW Universe [35, 36]. One of the proposed solutions for the HDE problems is the consideration of various entropies. One of the considered entropy is Tsallis entropy which has been used in many papers [37, 38, 39, 40]. In recent years, various entropy formalism have been used to discuss the gravitational and cosmological setups. Also, some new holographic DE models are constructed such as Tsallis HDE [41], Renyi HDE (RHDE) [42] and Sharma-Mittal HDE [43]. Kaniadakis [44, 45, 46], Barrow [47, 48, 49, 50, 51, 52, 53, 54, 55] entropies, which arise from the effort to introduce non-extensive, relativistic and quantum gravity corrections in the classical Boltzmann–Gibbs statistics, respectively. While predicting a richer phenomenology comparing to the standard Cosmology, generalized HDE models suffer from the absence of an underlying Lagrangian. This somehow questions their relevance in improving our knowledge of Universe at fundamental level. Hence, with this motivation, in this research, we consider the HDE with Barrow entropy formalism i.e., Barrow HDE (BHDE).

Saridakis [56], constructed the BHDE, by using the usual HP, however applying the Barrow entropy instead of the BH entropy. Also, for the limiting case as $\Delta = 0$ the BHDE possesses standard HDE, although The BHDE, in general, is a new scenario with cosmological behavior and richer structure. While standard HDE is given by the inequality $\rho_{BH} \leq SL^{-4}$, here L denotes horizon length, and under the imposition [57] then $\rho_{BH} = C(\frac{1}{L})^{2-\Delta}$, here C is a parameter. If we take into consideration the IR cut off L as the Hubble horizon (i.e., $L = H^{-1}$), then the energy density of BHDE is obtained as

$$\rho_{BH} = CH^{2-\Delta} \quad (1)$$

Saridakis [58], using Barrow entropy presented a modified cosmological scenario besides the Bekenstein-Hawking one. For the evolution of the effective DE density parameter, the analytical expression was obtained

Cite as: Y. Sobhanbabu, G. Satyanarayana, N.V.S. Swamy Chinamilli, P.V. Rambabu, East Eur. J. Phys. 2, 48 (2024), <https://doi.org/10.26565/2312-4334-2024-2-04>

© Y. Sobhanbabu, G. Satyanarayana, N.V.S. Swamy Chinamilli, P.V. Rambabu, 2024; CC BY 4.0 license

and shown the DM to DE era of the Universe. Using the Barrow entropy on the horizon in place of the standard Bekenstein-Hawking one, the potency of the generalized second law of thermodynamics has also been examined [59]. Mamon et al. [60] studied interacting BHDE model and also the validity of the generalized second law by assuming dynamical apparent horizon as the thermodynamic boundary. Anagnostopoulos et.al. [61] have studied observational constraints on BHDE. Pradhan et al. [62] have analysed FRW cosmological models with BHDE in the back-ground of BD theory of gravitation.

Srivastava and Sharma [63] have studied BHDE with Hubble horizon as IR cut-off. Adhikary et al. [64] constructed a BHDE in the case of non-flat Universe in particular, considering closed and open spatial geometry and observed that the scenario can describe the thermal history of the Universe, with the sequence of matter and dark energy epochs. Sarkar and Chattopadhyay [65] have analysed BHDE reconstruct $f(R)$ gravity as the form of back-ground evolution and point out the equation of state can have a transition from quintessence to phantom with the possibility of little Rip singularity. Xu and Lu [66] have investigated the non-interacting HDE with the Hubble radius as IR cut-off cannot explain the current accelerated expansion of Universe in the BD theory. Aditya et al. [67] have discussed anisotropic new HDE model in the frame-work of SB scalar tensor theory of gravitation. Sadri [68] has studied observational constraints on interacting THDE model. Zadeh et al. [69] have investigated the cosmic evolution of THDE in Bianchi type- I model filled with DM and THDE interacting with each other throughout a sign-changeable interacting with different IR cut offs. Chandra et al. [70] have discussed THDE in Bianchi type- I by using hybrid expansion law with K-essence. Sobhanbabu and Santhi [71] have investigated Kantowski-Sachs THDE model with sign-changeable interaction with the back-ground of scalar tensor theory of gravitation. Priyanka et al. [72] have discussed generalized BHDE with Granda-Oliver (GO) cut-off. Aditya et al. [73] have studied observational constraint on interacting THDE in logarithmic BD theory. Ghaffari et al. [74] have investigated interacting and non-interacting THDE models by considering the Hubble horizon as the IR cutoff within BD scalar theory. Jawad et al. [75] have studied cosmological implications of THDE in BD scalar theory. Santhi and Sobhanbabu [76] have analyzed anisotropic interacting and non-interacting THDE models in the frame-work of SB theory of gravitation.

Abdulla et al.[77] have investigated Dynamics of an Interacting BHDE Model and its Thermodynamic Implications. Recently, Ghaffari et.al. [78] have analysed BHDE in the frame-work of BD cosmology. Koussor et al. [79] have studied anisotropic BHDE model in symmetric teleparallel gravity. Very recently, Sobhanbabu et al. [80] have investigated Kantowski-Sachs interacting and non-interacting BHDE models in SB theory of gravitation.

Hence, motivated with the above discussion and observations, in the current work, we have studied anisotropic BHDE models in the back-ground of SB theory. The plan of the work as follows: In Section- II , we have derived field equations of SB theory and its cosmological solution with the help of Bianchi type- III Universe in the presence of two minimally interacting fields: DM and BHDE components. In Section- III , we have constructed non-interacting and interacting BHDE models along with their physical discussions. Finally, we summarize our results in conclusion Section- IV .

2. METRIC AND COSMOLOGICAL SOLUTION OF SB FIELD EQUATIONS

In the current work, we consider the anisotropic Bianchi type- III in the form

$$ds^2 = dt^2 - X^2(t)dx^2 - Y^2(t)e^{-2x}dy^2 - Z^2(t)dz^2, \quad (2)$$

where $X(t)$, $Y(t)$ and $Z(t)$ are the metric potentials, as functions of cosmic time (t). The following are the some physical parameters which are useful to find the solution of the SB field equations for the Universe BT- III . The average scale factor and volume are defined as

$$a(t) = (XYZ)^{\frac{1}{3}}, \quad V(t) = a(t)^3 = XYZ \quad (3)$$

The average Hubble parameter $H(t)$ is defined as

$$H(t) = \frac{\dot{a}}{a} = \frac{1}{3} \left(\frac{\dot{X}}{X} + \frac{\dot{Y}}{Y} + \frac{\dot{Z}}{Z} \right) \quad (4)$$

The deceleration parameter q is given by

$$q(t) = -\frac{a\ddot{a}}{\dot{a}^2} \quad (5)$$

The SB field equations for matter and BHDE distribution are (with $8\pi G = C = 1$) [83] given by

$$G_{\mu\nu} - w\phi^n \left(\phi_{,\mu}\phi_{,\nu} - \frac{1}{2}g_{\mu\nu}\phi_{,\lambda}\phi^{,\lambda} \right) = -(T_{\mu\nu} + \bar{T}_{\mu\nu}), \quad (6)$$

and the scalar field ϕ satisfies the following equation

$$2\phi^n \phi_{,\mu}^{\mu} + n\phi^{n-1} \phi_{,\lambda}\phi^{,\lambda} = 0, \quad (7)$$

where $G_{\mu\nu}$ represents the Einstein tensor and $T_{\mu\nu}$ & $\bar{T}_{\mu\nu}$ are energy momentum tensors for pressure-less dark matter and BHDE respectively. For physical interpretation, the energy momentum tensors for matter and BHDE can be written as

$$T_{\mu\nu} = \text{diag}[1, 0, 0, 0]\rho_M, \tag{8}$$

and

$$\bar{T}_{\mu\nu} = \text{diag}[1, -\omega_{BH}, -(\omega_{BH} + \alpha_{BH}), -(\omega_{BH} + \alpha_{BH})]\rho_{BH}, \tag{9}$$

where ρ_{BH} , ρ_M are energy densities of BHDE and matter and p_{BH} is the pressure of BHDE. $\omega_{BH} = \frac{p_{BH}}{\rho_{BH}}$ is an equation of state (EoS) parameter and the skewness parameters α_{BH} are the deviations from y and z axes. So, the field equations for the discussed metric can be written as

$$\frac{\ddot{Y}}{Y} + \frac{\ddot{Z}}{Z} + \frac{\dot{Y}\dot{Z}}{YZ} - \frac{w}{2}\phi^n\dot{\phi}^2 = -\omega_{BH} \rho_{BH}, \tag{10}$$

$$\frac{\ddot{X}}{X} + \frac{\ddot{Z}}{Z} + \frac{\dot{X}\dot{Z}}{XZ} - \frac{w}{2}\phi^n\dot{\phi}^2 = -(\omega_{BH} + \alpha_{BH}) \rho_{BH}, \tag{11}$$

$$\frac{\ddot{X}}{X} + \frac{\ddot{Y}}{Y} + \frac{\dot{X}\dot{Y}}{XY} - \frac{1}{X^2} - \frac{w}{2}\phi^n\dot{\phi}^2 = -(\omega_{BH} + \alpha_{BH}) \rho_{BH}, \tag{12}$$

$$\frac{\dot{X}\dot{Y}}{XY} + \frac{\dot{Y}\dot{Z}}{YZ} + \frac{\dot{X}\dot{Z}}{XZ} - \frac{1}{X^2} + \frac{w}{2}\phi^n\dot{\phi}^2 = \rho_M + \rho_{BH}, \tag{13}$$

$$\frac{\dot{X}}{Y} - \frac{\dot{Z}}{Z} = 0, \tag{14}$$

$$\ddot{\phi} + \left(\frac{\dot{X}}{X} + \frac{\dot{Y}}{Y} + \frac{\dot{Z}}{Z}\right)\dot{\phi} + \frac{n}{2}\frac{\phi^2}{\phi} = 0, \tag{15}$$

and the continuity equation of the matter and BHDE as

$$\rho_M \dot{M} + \left(\frac{\dot{X}}{X} + \frac{\dot{Y}}{Y} + \frac{\dot{Z}}{Z}\right)\rho_M + \rho_{BH} \dot{B}H + \left(\frac{\dot{X}}{X} + \frac{\dot{Y}}{Y} + \frac{\dot{Z}}{Z}\right)(1 + \omega_{BH})\rho_{BH} + \left(\frac{\dot{Y}}{Y} + \frac{\dot{Z}}{Z}\right)\alpha_{BH}\rho_{BH} = 0. \tag{16}$$

On integration, Eq.(14) yields $Y = c_1Z$, where c_1 is an integration constant. It can be taken as unity, without loss of generality, so that we have

$$Y = Z. \tag{17}$$

In view of Eq.(17), the field equations (10)-(15) reduce to

$$\frac{\ddot{X}}{X} + \frac{\ddot{Z}}{Z} + \frac{\dot{X}\dot{Z}}{XZ} - \frac{w}{2}\phi^n\dot{\phi}^2 = -\omega_{BH} \rho_{BH}, \tag{18}$$

$$\frac{\ddot{X}}{X} + \frac{\ddot{Z}}{Z} + \frac{\dot{X}\dot{Z}}{XZ} - \frac{w}{2}\phi^n\dot{\phi}^2 = -(\omega_{BH} + \alpha_{BH}) \rho_{BH}, \tag{19}$$

$$2\frac{\ddot{X}}{X} + \frac{\dot{X}^2}{X^2} - \frac{1}{X^2} - \frac{w}{2}\phi^n\dot{\phi}^2 = -(\omega_{BH} + \alpha_{BH}) \rho_{BH}, \tag{20}$$

$$\frac{\dot{X}^2}{X^2} + 2\frac{\dot{X}\dot{Z}}{XZ} - \frac{1}{X^2} + \frac{w}{2}\phi^n\dot{\phi}^2 = \rho_M + \rho_{BH}, \tag{21}$$

$$\ddot{\phi} + \left(\frac{2\dot{X}}{X} + \frac{\dot{Y}}{Y}\right)\dot{\phi} + \frac{n\phi^2}{2\phi} = 0, \tag{22}$$

and

$$\rho_M \dot{M} + \left(2\frac{\dot{X}}{X} + \frac{\dot{Z}}{Z}\right)((1 + \omega_{BH}) + \rho_{BH})\rho_M + \rho_{BH} \dot{B}H + \left(\frac{\dot{X}}{X} + \frac{\dot{Z}}{Z}\right)\alpha_{BH}\rho_{BH} = 0. \tag{23}$$

The above SB field equations (18)-(22) constitute a system of five non-linear equations with seven unknowns: X , Z , ϕ , ω_{BH} , ρ_{BH} , ρ_M , and α_{BH} . In order to get a deterministic solution, we take the following plausible physical conditions: Here, we consider the fact that expansion scalar is directly proportional to shear scalar which leads [81] to a relation between the metric potentials:

$$X = Z^m, \tag{24}$$

$m \neq 1$ is a positive constant. In this paper, we assume a well-motivated ansatz considered by Abdusattat et al. [82] which puts a constraint on the function form of the deceleration parameter $q(t)$ as

$$q = -\frac{\beta}{t^2} + \gamma - 1, \tag{25}$$

here $\beta > 0$ and $\gamma > 1$.

Hence, from the Eqs. (5), (24), and (25), we find the metric potentials as

$$X = Y = \left[t^2 + \frac{\beta}{\gamma}\right]^{\frac{3m}{2\gamma(2m+1)}}, \quad Z = \left[t^2 + \frac{\beta}{\gamma}\right]^{\frac{3}{2\gamma(2m+1)}}. \tag{26}$$

Now through a proper choice of coordinates and constants the metric (2) with the help of Eq.(26) can be written as

$$ds^2 = dt^2 - \left[t^2 + \frac{\beta}{\gamma}\right]^{\frac{3m}{\beta(2m+2)}} dx^2 - \left[t^2 + \frac{\beta}{\gamma}\right]^{\frac{m}{\gamma(2m+2)}} e^{2x} dy^2 - \left[t^2 + \frac{\beta}{\gamma}\right]^{\frac{3}{\gamma(2m+2)}} e^{-2x} dz^2. \tag{27}$$

Thus, Eq. (27) describes BT-III BHDE model in SB scalar tensor theory of gravitation.

The average scale parameter and volume of the model respectively, given by

$$a = \left[t^2 + \frac{\beta}{\gamma}\right]^{\frac{1}{2\gamma}} \quad \& \quad V = \left[t^2 + \frac{\beta}{\gamma}\right]^{\frac{3}{2\gamma}} \tag{28}$$

The Hubble parameter(H) of the model can be obtained as

$$H = \frac{t}{\gamma(t^2 + \frac{\beta}{\gamma})} \tag{29}$$

The energy density of the BHDE model is given by

$$\rho_{BH} = CH^{4-2\Delta}, \tag{30}$$

where C is a parameter.

Now with help of Eqs.(29) and (30), the energy density of BHDE is obtained as

$$\rho_{BH} = C \left[\frac{t}{\gamma(t^2 + \frac{\beta}{\gamma})} \right]^{2-\Delta} \tag{31}$$

Using Eqs. (18), and (20) we get the skewness parameters as

$$\alpha_{BH} = \left[\frac{9mH^2}{(2m+1)^2} + \left(\frac{t}{\gamma H}\right)^{-\frac{3m}{2\gamma(2m+1)}} + 3\frac{(m+1)\dot{H}}{(2m+1)} - 9\frac{m^2H^2}{(2m+1)^2} \right] \left[CH^{2-\Delta} \right] \tag{32}$$

where $H = \frac{t}{\gamma(t^2 + \frac{\beta}{\gamma})}$

Now using Eqs. (22) & (26), we have the scalar field ϕ is

$$\phi^{\frac{n+2}{2}} = \frac{n+2}{2} \int \phi_0 \left(t^2 + \frac{\beta}{\gamma}\right)^{\frac{-3}{2\gamma}} dt + c_2, \tag{33}$$

where ϕ_0 and c_2 are integration constants.

Using Eqs. (21), (31), and (33), we get

$$\rho_M = 9\frac{m(m+2)H^2}{(2m+1)^2} - \left(\frac{\gamma H}{t}\right)^{\frac{3m}{\gamma(2m+1)}} + \frac{w}{2}\phi_0^2 \left(\frac{\gamma H}{t}\right)^{\frac{3}{\gamma}} - CH^{2-\Delta} \tag{34}$$

The behavior of skewness parameter (α_{BH}) versus cosmic time (t) is plotted in Fig. 1 for the various values of γ . It is observed that the skewness parameter is positive throughout the evolution and it is initially bouncing behavior later decreases as Universe evolves. Figs. 2 & 3 describe the behavior of energy density of dark matter and BHDE against cosmic time (t) for the different values of γ . It is observed that ρ_M is positive throughout the evolution. From Fig. 3, it is observed that at initial epoch ρ_{BH} increases, reaches a maximum value and decreases at late times.

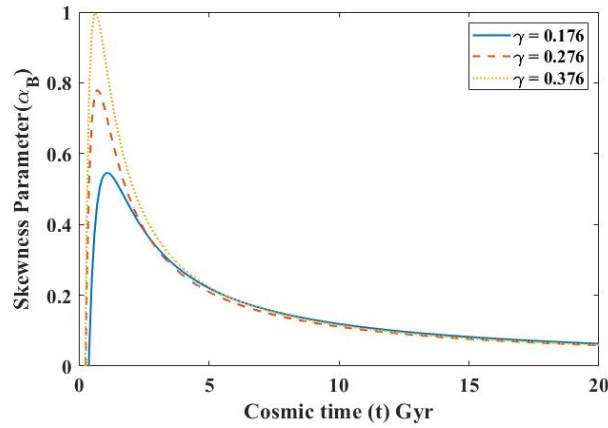


Figure 1. Plot of skewness parameter (α_B) versus cosmic time (t) for $n = 0.198$, $\xi_0 = 0.03$, $\xi_1 = 0.02$, $\xi_2 = 0.01$, $\alpha = 0.2904$, and $k = 0.593, 0.596$, and 0.599 .

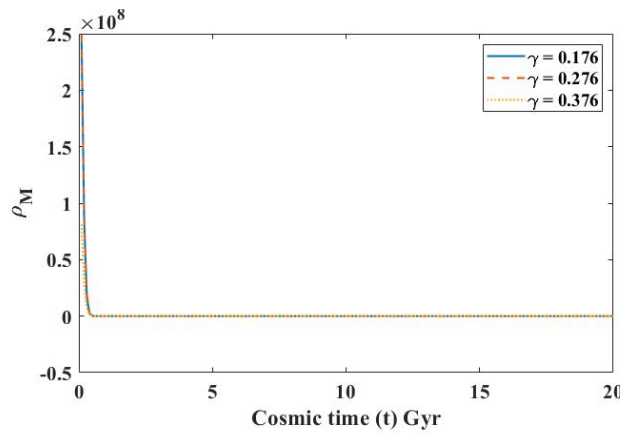


Figure 2. Plot of energy density (ρ_M) of matter versus cosmic time (t) for $m = 0.925$, $\beta = 0.798$, $\gamma = 0.376$, $\gamma = 0.476$, $\gamma = 0.576$, $w = 1000$.

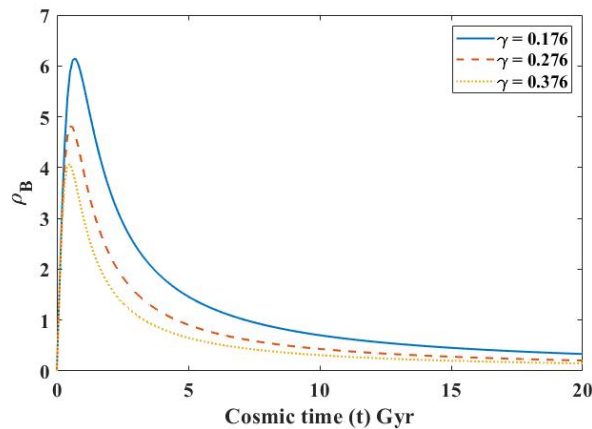


Figure 3. Plot of energy density (ρ_{BH}) of BHDE versus cosmic time (t) for $m = 0.925$, $\beta = 0.798$, $\gamma = 0.376$, $\gamma = 0.476$, $\gamma = 0.576$, $w = 1000$.

Non-interacting model

Here, we consider the non-interacting dark matter and BHDE. Hence, both of these conserve separately, so that we have from Eq. (16),

$$\rho_{\dot{M}} + \left(\frac{\dot{X}}{X} + \frac{\dot{Y}}{Y} + \frac{\dot{Z}}{Z} \right) \rho_M = 0, \tag{35}$$

$$\dot{\rho}_{BH} + \left(\frac{\dot{X}}{X} + \frac{\dot{Y}}{Y} + \frac{\dot{Z}}{Z}\right)(1 + \omega_{BH})\rho_{BH} + \alpha_B \left(\frac{\dot{Y}}{Y} + \frac{\dot{Z}}{Z}\right)\rho_{BH} = 0 \tag{36}$$

Using Eqs. (26), (31) and (33), we get the EoS parameter (ω_{BH}) of BHDE model

$$\omega_{BH} = -1 - \left[\frac{m+1}{2m+1} \left[\frac{9mH^2}{(2m+1)^2} + \left(\frac{t}{\gamma H}\right)^{-\frac{3m}{2\gamma(2m+1)}} + 3\frac{(m+1)\dot{H}}{(2m+1)} - 9\frac{m^2H^2}{(2m+1)^2} \right] \left[CH^{2-\Delta} \right] - \frac{(2-\Delta)\dot{H}}{3H^2} \right] \tag{37}$$

where $\dot{H} = \frac{\beta - \gamma t^2}{\gamma(\beta + \gamma t^2)^2}$

Fig. 4 represents the behavior of equation of state (EoS) parameter in terms of cosmic time (t) for the non-interacting model in different values of γ . It can be seen that EoS parameter completely varies in aggressive phantom region and finally tends to -1 .

Taking the derivative of Eq. (42) with respect to $\ln a$, we get

$$\omega'_{BH} = -\left\{ \frac{\alpha_{BH}}{(2m+1)H} - \frac{(2-\Delta)(H\ddot{H} - 2\dot{H}^2)}{3H^2} \right\} \tag{38}$$

where $\ddot{H} = \frac{2t(\gamma t^2 - 3\beta)}{(\beta + \gamma t^2)^3}$ and

$$\alpha_{BH} = \left\{ \begin{aligned} &\left[\frac{18mH\dot{H}}{(2m+1)^2} - \frac{3m(H-t\dot{H})}{2\gamma(2m+1)H^2} \left(\beta\right)^{\frac{3m}{2\gamma(2m+1)}} \left(\frac{t}{H}\right)^{-\frac{3m}{2\gamma(2m+1)-1}} + \frac{3m\ddot{H}}{2m+1} - \frac{18m^2H\dot{H}}{(2m+1)^2} \right] \\ &\times \left[C \left[\frac{t}{\gamma(t^2 + \frac{\beta}{\gamma})} \right]^{\Delta-2} \right] - \left[\frac{9mH^2}{(2m+1)^2} + \left(\frac{t}{\gamma H}\right)^{\frac{-3m}{2\gamma(2m+1)}} + \frac{3\dot{H}(m+1)}{(2m+1)} - \frac{9m^2H^2}{(2m+1)^2} \right] \\ &\times \left[(2-\Delta)H^{-1}\dot{H} \right] \end{aligned} \right\} \tag{39}$$

Fig. 5, represents the $\omega_{BH} - \omega'_{BH}$ plane for the non-interacting BHDE model for the different values of γ . It

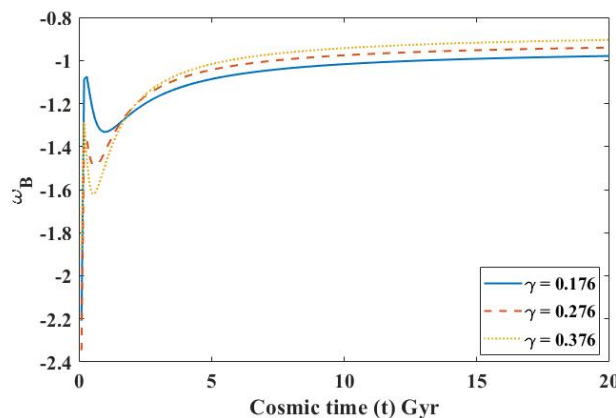


Figure 4. Plot of EoS parameter (ω_{BH}) versus cosmic time (t) for $m = 0.925$, $\beta = 0.798$, $\gamma = 0.376$, $\gamma = 0.476$, $\gamma = 0.576$, $w = 1000$.

is observed that the $\omega_{BH} - \omega'_{BH}$ plane corresponds to thawing region. The plot of squared speed of sound (v_s^2) versus cosmic time (t) is shown in Fig. 6. we can observe that squared speed of sound ($v_s^2 < 0$) represents our non-interacting BHDE model is unstable.

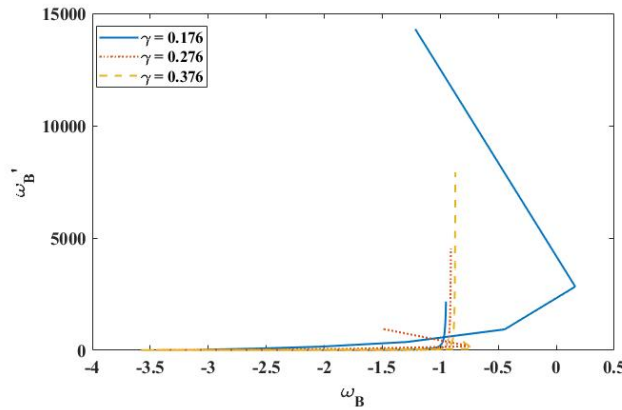


Figure 5. Plot of ω_{BH} versus ω'_{BH} for $m = 0.925, \beta = 0.798, \gamma = 0.376, \gamma = 0.476, \gamma = 0.576, w = 1000$.

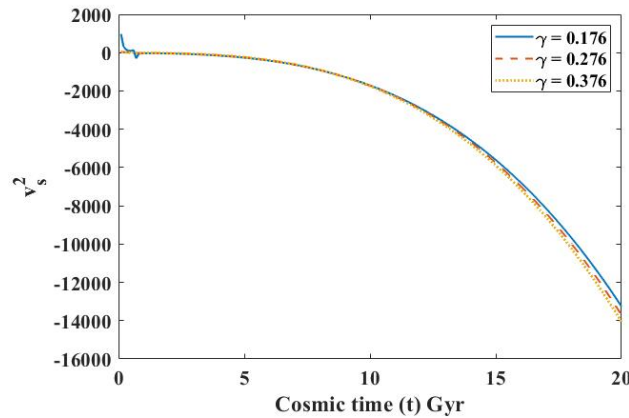


Figure 6. Plot of squared speed of sound (v_s^2) versus cosmic time (t) for $m = 0.925, \beta = 0.798, \gamma = 0.376, \gamma = 0.476, \gamma = 0.576, w = 1000$.

INTERACTING MODEL

In this case, we consider that both dark matter and BHDE are interacting with each other. Hence, we can write the energy conservation equation for matter and BHDE as

$$\rho_M \dot{M} + \left(\frac{\dot{X}}{X} + \frac{\dot{Y}}{Y} + \frac{\dot{Z}}{Z} \right) \rho_M = Q, \tag{40}$$

$$\dot{\rho}_{BH} + \left(\frac{\dot{X}}{X} + \frac{\dot{Y}}{Y} + \frac{\dot{Z}}{Z} \right) (1 + \omega_{BH}) \rho_{BH} + \alpha_B \left(\frac{\dot{Y}}{Y} + \frac{\dot{Z}}{Z} \right) \rho_{BH} = -Q \tag{41}$$

where the quantity Q denotes interaction between DE components. From the Eqs. (40) and (41), we can say that the total energy is conserved. Since there is no natural information from fundamental physics on the interaction term Q , one can only study it to a phenomenological level. Various forms of interaction term extensively considered in literature include $Q = 3d^2 H \rho_M, Q = 3d^2 H \rho_{BH}$ and $Q = 3d^2 H (\rho_M + \rho_{BH})$. Where, d is a coupling constant and positive c means that DE decays into DM, while negative d means DM decays into DE. Here we consider $Q = 3d^2 H \rho_{BH}$ as the interaction term with the coupling parameter d^2 .

From Eqs. (24), (29), and (44) we find the EoS parameter ω_{BH} as

$$\omega_{BH} = -1 - d^2 - \left[\frac{m+1}{2m+1} \left[\frac{9mH^2}{(2m+1)^2} + \left(\frac{t}{\gamma H} \right)^{-\frac{3m}{2\gamma(2m+1)}} + 3 \frac{(m+1)\dot{H}}{(2m+1)} - 9 \frac{m^2 H^2}{(2m+1)^2} \right] \left[CH^{2-\Delta} \right] - \frac{(2-\Delta)\dot{H}}{3H^2} \right] \tag{42}$$

Taking the derivative of Eq. (40) with respect to $\ln a$, we get

$$\omega'_{BH} = -\left\{ \frac{\alpha_{BH}}{(2m+1)H} - \frac{(2-\Delta)(H\ddot{H} - 2\dot{H}^2)}{3H^2} \right\}, \tag{43}$$

where $\ddot{H} = \frac{2t(\gamma t^2 - 3\beta)}{(\beta + \gamma t^2)^3}$ and

$$\alpha_{BH} = \left[\frac{18mH\dot{H}}{(2m+1)^2} - \frac{3m(H-t\dot{H})}{2\gamma(2m+1)H^2} \left(\beta\right)^{\frac{3m}{2\gamma(2m+1)}} \left(\frac{t}{H}\right)^{-\frac{3m}{2\gamma(2m+1)}-1} + \frac{3m\ddot{H}}{2m+1} - \frac{18m^2H\dot{H}}{(2m+1)^2} \right] \times \left[C \left[\frac{t}{\gamma(t^2 + \frac{\beta}{\gamma})} \right]^{\Delta-2} \right] - \left[\frac{9mH^2}{(2m+1)^2} + \left(\frac{t}{\gamma H}\right)^{\frac{-3m}{2\gamma(2m+1)}} + \frac{3\dot{H}(m+1)}{(2m+1)} - \frac{9m^2H^2}{(2m+1)^2} \right] \times \left[(2-\Delta)H^{-1}\dot{H} \right], \tag{44}$$

The plot of EoS parameter (ω_{BH}) against cosmic time (t) for various values of γ and d^2 are depicted in the

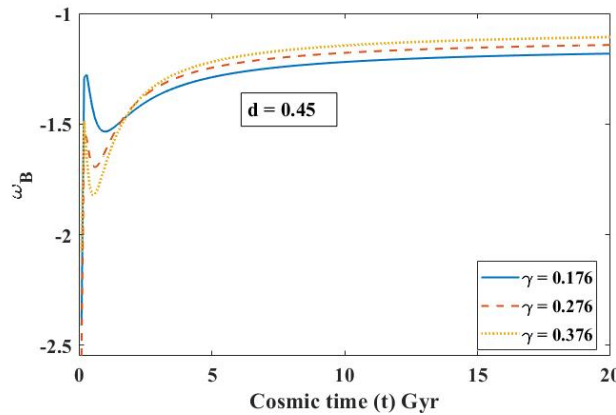


Figure 7. Plot of EoS parameter of BHDE versus cosmic time (t) for $m = 0.925$, $\beta = 0.798$, $\gamma = 0.376$, $\gamma = 0.476$, $\gamma = 0.576$, $w = 1000$ $d = 0.45$.

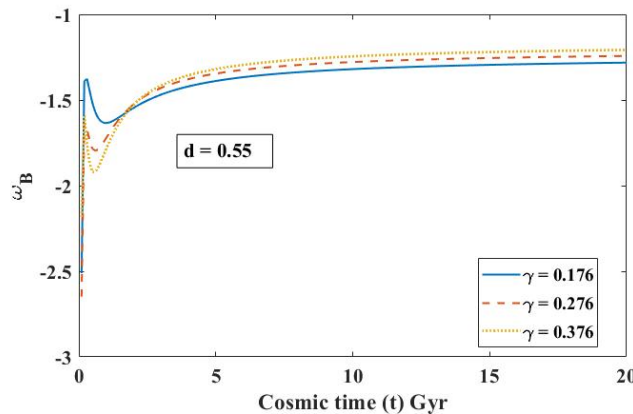


Figure 8. Plot of EoS parameter of BHDE versus cosmic time (t) for $m = 0.925$, $\beta = 0.798$, $\gamma = 0.376$, $\gamma = 0.476$, $\gamma = 0.576$, $w = 1000$ $d = 0.55$.

Fig. 7, 8 & 9 for the interacting model. It can be observed that the EoS parameter completely varies in aggressive phantom region for all values of coupling parameter d^2 and γ . The $\omega_{BH} - \omega'_{BH}$ plane is used to represents the dynamical property of dark models, where ω'_{BH} is the evolutionary form of ω_{BH} , here prime indicates derivative with respect to $\ln a$. In Figs. 10, 11, & 12, we plot the behavior of $\omega_{BH} - \omega'_{BH}$ plane for three different values

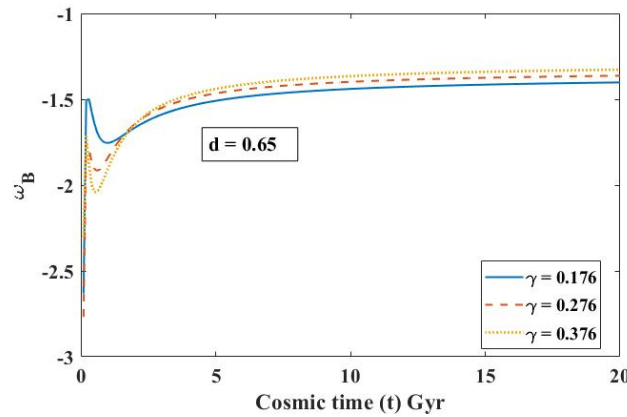


Figure 9. Plot of Plot of EoS parameter of BHDE versus cosmic time (t) for $m = 0.925$, $\beta = 0.798$, $\gamma = 0.376$, $\gamma = 0.476$, $\gamma = 0.576$, $w = 1000$ $d = 0.65$.

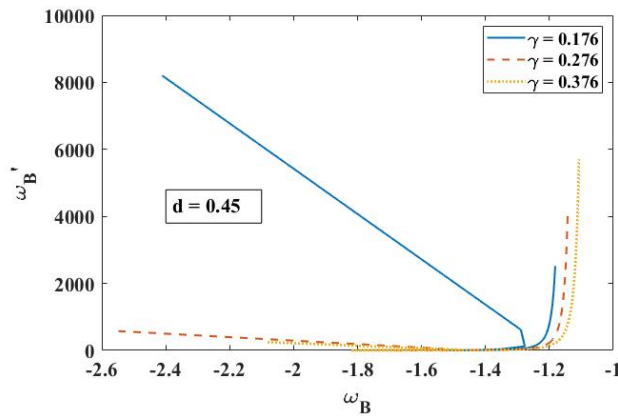


Figure 10. Plot of ω_{BH} versus ω'_{BH} for $m = 0.925$, $\beta = 0.798$, $\gamma = 0.376$, $\gamma = 0.476$, $\gamma = 0.576$, $w = 1000$ $d = 0.45$.

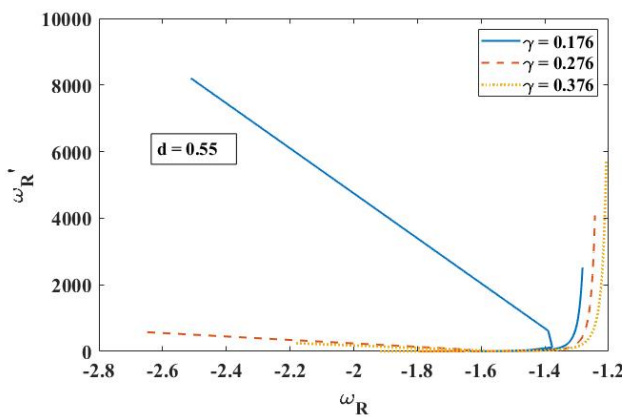


Figure 11. Plot of ω_{BH} versus ω'_{BH} for $m = 0.925$, $\beta = 0.798$, $\gamma = 0.376$, $\gamma = 0.476$, $\gamma = 0.576$, $w = 1000$ $d = 0.45$.

of d^2 and γ . It can be seen that the $\omega_{BH} - \omega'_{BH}$ plane, for interacting BHDE model corresponds to the thawing region ($\omega'_{BH} > 0$ and $\omega_{BH} < 0$) for all the three values of coupling parameter d^2 and γ . Figs. 13, 14, & 15 elaborates the plot of squared speed of sound (v_s^2) versus cosmic time t . The trajectories represents the negative behavior throughout evolution of the Universe which represents the interacting model is unstable for different values of d^2 and γ .

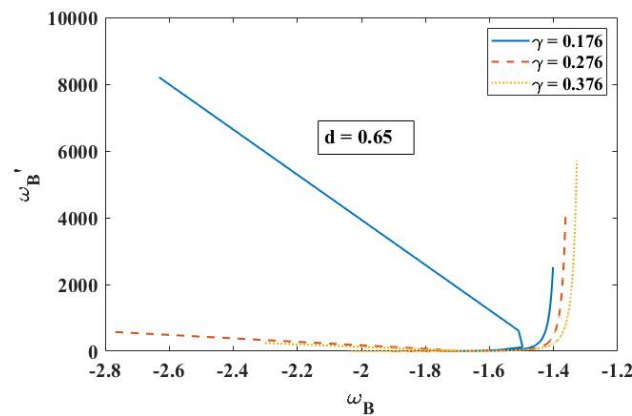


Figure 12. Plot of ω_{BH} versus ω'_{BH} for $m = 0.925, \beta = 0.798, \gamma = 0.376, \gamma = 0.476, \gamma = 0.576, w = 1000 d = 0.65$.

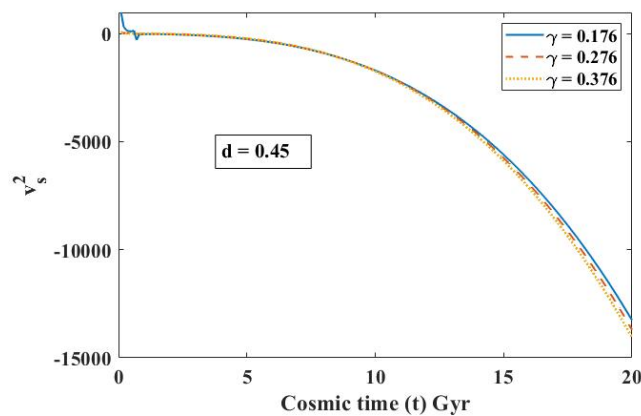


Figure 13. Plot of squared speed of sound v_s^2 versus cosmic time (t) for $m = 0.925, \beta = 0.798, \gamma = 0.376, \gamma = 0.476, \gamma = 0.576, w = 1000 d = 0.45$.

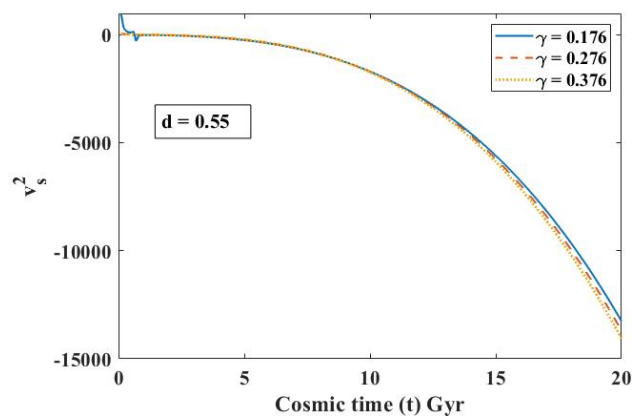


Figure 14. Plot of squared speed of sound v_s^2 versus cosmic time (t) for $m = 0.925, \beta = 0.798, \gamma = 0.376, \gamma = 0.476, \gamma = 0.576, w = 1000, \text{ and } d = 0.55$.

The nature of expansion of the model can be explained using the cosmological parameter called as deceleration parameter (DP). The DP for our both models (non-interacting and interacting) is same and given by

$$q = -\frac{\alpha}{t^2} + \beta - 1 \tag{45}$$

Fig. 16 depicts the behavior of DP versus cosmic time t for the different values of γ . We can observed that

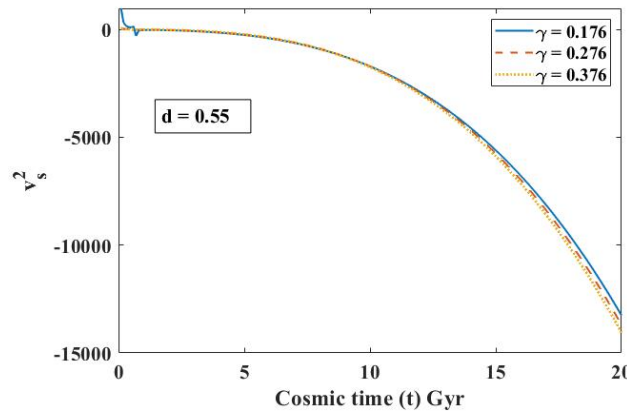


Figure 15. Plot of squared speed of sound v_s^2 versus cosmic time (t) for $m = 0.925$, $\beta = 0.798$, $\gamma = 0.376$, $\gamma = 0.476$, $\gamma = 0.576$, $w = 1000$ $d = 0.65$.

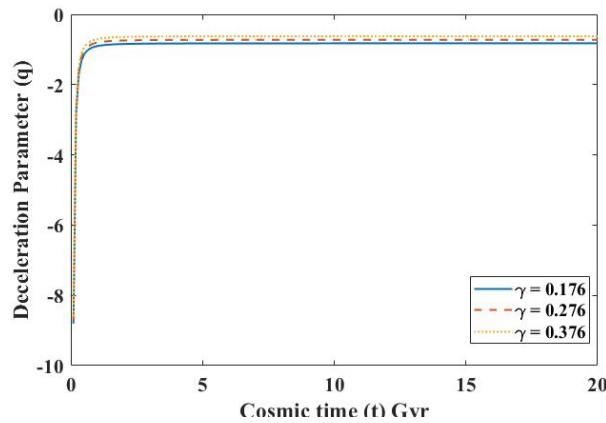


Figure 16. Plot of deceleration parameter (q) versus cosmic time (t) for $m = 0.925$, $\beta = 0.798$, $\gamma = 0.376$, $\gamma = 0.476$, $\gamma = 0.576$, and $w = 1000$.

our models (Interacting and non-interacting) exhibits negative behavior throughout the evolution and finally it tends to -1 , which represents our models accelerating behavior. Also, we can see that the models exhibit accelerated expansion at initial epoch and finally approaches to exponential expansion of the Universe.

In recent years there are many number of DE models have proposed to explain the accelerated expansion of the Universe. The two new parameters formulated by Sahni et al. [84] named as statefinder pair (r, s) by using the deceleration and Hubble parameters defined as follows:

$$r = \frac{\ddot{a}}{aH^3} = \frac{2\gamma(1 - 4\gamma)t + (1 + 2\gamma)(t^2 + \frac{\beta}{\gamma})\gamma t}{t^2} \tag{46}$$

$$s = \frac{r - 1}{3(q - \frac{1}{2})} = \frac{4\gamma t(1 - 4\gamma) + 2\gamma(1 + 2\gamma)(t^2 + \frac{\beta}{\gamma})t - t^2}{3((2\gamma - 3)t^2 - 2\beta)} \tag{47}$$

In Fig.17, we have plotted the trajectories of $r - s$ plane for the three values of γ . It is observe that $r - s$ plane for the three values $\gamma = 0.176$, 0.276 and 0.376 meets the Λ model. We also, observe that the $r - s$ plane belongs to the Chaplygin gas model ($s < 0$ and $r > 1$) for $\gamma = 0.176$ and 0.276 . For $\gamma = 0.376$ the $r - s$ plane corresponding to the dark energy models such as phantom ($s > 0$) and quintessence ($r < 1$).

The Om diagnostic parameter tool has been proposed by Sahni et al. [85] as a complementary to the statefinder parameter, which helps to distinguish the present matter density contrast Om in different models more effectively. This is also a geometrical diagnostic that explicitly depends on redshift (z) and the Hubble parameter (H). It is defined as follows:

$$Om(x) = \frac{h(x)^2 - 1}{x^3 - 1}, \tag{48}$$

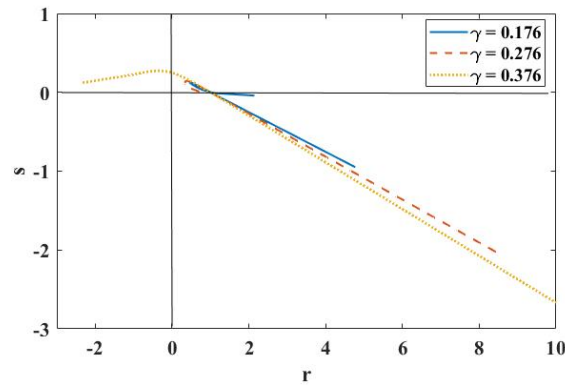


Figure 17. Plot of r versus s for $m = 0.925$, $\beta = 0.798$, $\gamma = 0.376$, $\gamma = 0.476$, $\gamma = 0.576$.

where $h(x) = \frac{H(x)}{H_0}$, $x = (1 + z)$ and H_0 is the present value of the Hubble parameter.

$$Om(x) = \frac{x^{4\gamma} \left(x^{-2\gamma} - \frac{\beta}{\gamma} \right)}{\gamma^2 (x^3 - 1)} \tag{49}$$

Fig. 18, we have plotted the evolution of Om diagnostic parameter versus cosmic time (t). It can be observed

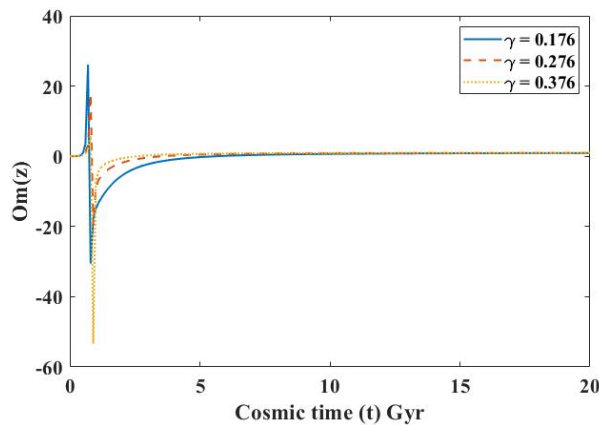


Figure 18. Plot of $Om(z)$ versus cosmic time (t) for $m = 0.925$, $\beta = 0.798$, $\gamma = 0.376$, $\gamma = 0.476$, $\gamma = 0.576$.

that the slope of Om diagnostic parameter is negativ, which represents the quintessence behavior of the Universe. This behavior is consistent with recent observational data.

3. CONCLUSIONS

In this paper, we have studied the accelerated expansion by assuming the BHDE in BT-III Universe within the frame-work of SB scalar-tensor theory of gravity. Using the relation between the metric potentials and the variable DP $q = -\frac{\beta}{t^2} + \gamma - 1$, we have obtained the solution of SB field equations with this solution, we have studied various cosmological parameters to analyze the viability of the non-interacting and non-interacting models and our conclusions are the following:

- The behavior of the skewness parameter is positive throughout the evolution and it is initially bouncing behavior later decreases as Universe evolves. The energy density of DM is observed that ρ_M is positive throughout the evolution. The energy density of BHDE is observed that at initial epoch ρ_{BH} increases, reaches a maximum value and decreases at late times.
- The trajectory of EoS parameter completely varies in aggressive phantom region and finally tends to -1 . The $\omega_{BH} - \omega_{BH}$ plane observed that the $\omega_{BH} - \omega_{Bh}$ plane corresponds to thawing region. The squared speed of sound ($v_s^2 < 0$) represents unstable for the non-interacting cosmological models for various values of γ .

- The plot of EoS parameter can be observed that the EoS parameter completely varies in aggressive phantom region for all values of coupling parameter d^2 and γ for interacting model. The $\omega_{BH} - \omega'_{BH}$ plane is used to represents the dynamical property of dark models, The behavior of $\omega_{BH} - \omega'_{BH}$ plane, for interacting BHDE model corresponds to the thawing region ($\omega'_{BH} > 0$ and $\omega_{BH} < 0$) for all the three values of coupling parameter d^2 and γ .
- The trajectories of v_s^2 represents the negative behavior throughout evolution of the Universe which represents the interacting model is unstable for different values of d^2 and γ . Also, it is worthwhile to mention here that the present values of EoS parameter of our modelS are in agreement with the modern Plank observational data given by Aghanim et al. [86]. It gives the constraints on EoS parameter of BHDE as follows:

$$\begin{aligned}\omega_{BH} &= -1.56_{-0.48}^{+0.60}(Planck + TT + lowE) \\ \omega_{BH} &= -1.58_{-0.41}^{+0.52}(Planck + TT, EE + lowE) \\ \omega_{BH} &= -1.57_{-0.40}^{+0.50}(Planck + TT, TE, EE + lowE + lensing)\end{aligned}$$

The EoS parameter ω_{BH} of our model lie within the above observational limits which shows the consistency of our results with the above cosmological observational data.





- The DP for the both Interacting and non-interacting models exhibits negative behavior throughout the evolution and finally it tends to -1 , which represents our models accelerating behavior of the Universe. The deceleration parameter q of our model is consistent with the observational data [87] given as

$$\begin{aligned}q &= -0.6401 \pm 0.187(BAO + Masers + TDSL + Panthelon + H_0) \\ q &= -0.930 \pm 0.218(BAO + Masers + TDSL + Panthelon + H_z).\end{aligned}$$

- The trajectories of $r - s$ plane for the different values of γ meets the Λ model. We also, observe that the $r - s$ plane belongs to the Chaplygin gas model ($s < 0$ and $r > 1$) for $\gamma = 0.176$ and 0.276 . For $\gamma = 0.376$ the $r - s$ plane corresponding to the dark energy models such as phantom ($s > 0$) and quintessence ($r < 1$).
- The Om diagnostic parameter is negative, which represents the quintessence behavior of the Universe for the different values of γ . This behavior is consistent with recent observational data.

Data Availability Statement: This manuscript has no associated data.

ORCID

 Y. Sobhanbabu, <https://orcid.org/0000-0003-0717-1323>;  G. Satyanarayana, <https://orcid.org/0000-0000-0000-0000>;  N.V.S. Swamy Chinamilli, <https://orcid.org/0000-0001-8565-633X>;  P.V. Rambabu, <https://orcid.org/0000-0003-4081-7739>

REFERENCES

- [1] J.R. Primack, Nucl. Phys. B Proc. Suppl. **173**, 1 (2007). <https://doi.org/10.1016/j.nuclphysbps.2007.08.152>
- [2]] A.G. Riess, et al., Astron. J. **116**, 1009 (1998). <https://doi.org/10.1086/300499>
- [3] S. Perlmutter, et al., Supernova Cosmology Project, Astrophys. J. **517**, 565 (1999). <https://doi.org/10.1086/307221>
- [4] D.N. Spergel, et al., WMAP, Astrophys. J. Suppl. **148**, 175 (2003). <https://doi.org/10.1086/377226>
- [5] M. Tegmark, et al., SDSS, Phys. Rev. D, **69**, 103501 (2004). <https://doi.org/10.1103/PhysRevD.69.103501>
- [6] P.A.R. Ade, et al., Planck, Astron. Astrophys. **571**, A16 (2014). <https://doi.org/10.1051/0004-6361/201321591>
- [7] P. Salucci, G. Esposito, et al., Front. Phys. **8**, 603190 (2020). <https://doi.org/10.3389/fphy.2020.603190>
- [8] S. Vagnozzi, L. Visinelli, et al., Phys. Rev. D, **104**, 063023 (2021). <https://doi.org/10.1103/PhysRevD.104.063023>
- [9] F. Ferlito, S. Vagnozzi, et al., Mon. Not. R. Astron. Soc. **512**, 1885 (2022). <https://doi.org/10.1093/mnras/stac649>
- [10] S. Capozziello, and M. De Laurentis, Phys. Rep. **509**, 167 (2011). <https://doi.org/10.1016/j.physrep.2011.09.003>
- [11] A.G. Cohen, D.B. Kaplan, et al., Phys. Rev. Lett. **82**, 4971 (1999). <https://doi.org/10.1103/PhysRevLett.82.4971>
- [12] P. Horava, and D. Minic, Phys. Rev. Lett. **85**, 1610 (2000). <https://doi.org/10.1103/PhysRevLett.85.1610>
- [13] S.D. Thomas, Phys. Rev. Lett. **89**, 081301 (2002). <https://doi.org/10.1103/PhysRevLett.89.081301>

- [14] M. Li, Phys. Lett. B, **603**, 1 (2004). <https://doi.org/10.1016/j.physletb.2004.10.014>
- [15] S.D.H. Hsu, Phys. Lett. B, **594**, 13 (2004). <https://doi.org/10.1016/j.physletb.2004.05.020>
- [16] Q.G. Huang, M. Li, J. Cosmol. Astropart. Phys. **08**, 013 (2004). <https://doi.org/10.1088/1475-7516/2004/08/013>
- [17] S. Nojiri, S.D. Odintsov, Gen. Relativ. Grav. **38**, 1285 (2006). <https://doi.org/10.1007/s10714-006-0301-6>
- [18] B. Wang, C.Y. Lin, et al., Phys. Lett. B, **637**, 357 (2006). <https://doi.org/10.1016/j.physletb.2006.04.009>
- [19] M.R. Setare, Phys. Lett. B **642**, 421 (2006). <http://dx.doi.org/10.1016/j.physletb.2006.09.027>
- [20] B. Guberina, R. Horvat, et al., J. Cosmol. Astropart. Phys. **01**, 012 (2007). <https://doi.org/10.1088/1475-7516/2007/01/012>
- [21] L.N. Granda, and A. Oliveros, Phys. Lett. B, **671275**, 199 (2009). <https://doi.org/10.1016/j.physletb.2008.12.025>
- [22] A. Sheykhi, Phys. Rev. D, **84**, 107302 (2011). <https://doi.org/10.1103/PhysRevD.84.107302>
- [23] K. Bamba, S. Capozziello, et al., Astrophys. Space Sci. **342**, 155 (2012). <https://doi.org/10.1007/s10509-012-1181-8>
- [24] S. Ghaffari, M.H. Dehghani, et al., Phys. Rev. D, **89**, 123009 (2014). <https://doi.org/10.1103/PhysRevD.89.123009>
- [25] S. Wang, Y. Wang, and M. Li, Phys. Rep. **696**, 1 (2017). <https://doi.org/10.1016/j.physrep.2017.06.003>
- [26] S. Nojiri, S.D. Odintsov, Eur. Phys. J. C, **77**, 528 (2017). <https://doi.org/10.1140/epjc/s10052-017-5097-x>
- [27] H. Moradpour, A.H. Ziaie, et al., Eur. Phys. J. C, **80**, 732 (2020). <https://doi.org/10.1140/epjc/s10052-020-8307-x>
- [28] X. Zhang, F.Q. Wu, Phys. Rev. D, **72**, 043524 (2005). <https://doi.org/10.1103/PhysRevD.72.043524>
- [29] M. Li, X.D. Li, et al., J. Cosmol. Astropart. Phys. **06**, 036 (2009). <https://doi.org/10.1088/1475-7516/2009/06/036>
- [30] X. Zhang, Phys. Rev. D, **79**, 103509 (2009). <https://doi.org/10.1103/PhysRevD.79.103509>
- [31] J. Lu, E.N. Saridakis, et al., J. Cosmol. Astropart. Phys. **03**, 031 (2010). <https://doi.org/10.1088/1475-7516/2010/03/031>
- [32] S. Nojiri, S.D. Odintsov, et al., Phys. Lett. B, **797**, 134829 (2019). <https://doi.org/10.1016/j.physletb.2019.134829>
- [33] P. Horava, and D. Minic, Phys. Rev. Lett. **85**, 1610 (2000). <https://doi.org/10.1103/PhysRevLett.85.1610>
- [34] S. Thomas, Phys. Rev. Lett. **89**, 081301 (2002). <https://doi.org/10.1103/PhysRevLett.89.081301>
- [35] S.D.H. Hsu, Phys. Lett. B **594**, 13 (2004). <https://doi.org/10.1016/j.physletb.2004.05.020>
- [36] M. Li, Phys. Lett. B, **603**, 1 (2004). <https://doi.org/10.1016/j.physletb.2004.10.014>
- [37] R. D'Agostino, Phys. Rev. D, **99**, 103524 (2019). <https://doi.org/10.1103/PhysRevD.99.103524>
- [38] A. Majhi, Phys. Lett. B, **775**, 32 (2017). <https://doi.org/10.1016/j.physletb.2017.10.043>
- [39] S. Abe, Phys. Rev. E, **63**, 061105 (2001). <https://doi.org/10.1103/PhysRevE.63.061105>
- [40] T.S. Biro, and P. Ván, Phys. Rev. E, **83**, 061147 (2011). <https://doi.org/10.1103/PhysRevE.83.061147>
- [41] M. Tavayef, A. Sheykhi, et al., Phys. Lett. B, **781**, 195 (2018). <https://doi.org/10.1016/j.physletb.2018.04.001>
- [42] C. Tsallis, and L.J.L. Cirto, Eur. Phys. J. C, **73**, 2487 (2013). <https://doi.org/10.1140/epjc/s10052-013-2487-6>
- [43] H. Moradpour, S.A. Moosavi, et al., Eur. Phys. J. C, **78**, 829 (2018). <https://doi.org/10.1140/epjc/s10052-018-6309-8>
- [44] N. Drepanou, A. Lymperis, et al., Eur. Phys. J. C, **82**, 449 (2022). <https://doi.org/10.1140/epjc/s10052-022-10415-9>
- [45] A. Hernández-Almada, G. Leon, et al., Mon. Not. R. Astron. Soc. **511**, 4147 (2022). <https://doi.org/10.1093/mnras/stac255>
- [46] G.G. Luciano, Eur. Phys. J. C, **82**, 314 (2022). <https://doi.org/10.1140/epjc/s10052-022-10285-1>
- [47] E.N. Saridakis, Phys. Rev. D, **102**, 123525 (2020). <https://doi.org/10.1103/PhysRevD.102.123525>
- [48] M.P. Dabrowski, and V. Salzano, Phys. Rev. D, **102**, 064047 (2020). <https://doi.org/10.1103/PhysRevD.102.064047>
- [49] A. Sheykhi, Phys. Rev. D, **103**, 123503 (2021). <https://doi.org/10.1103/PhysRevD.103.123503>
- [50] P. Adhikary, S. Das, et al., Phys. Rev. D, **104**, 123519 (2021). <https://doi.org/10.1103/PhysRevD.104.123519>
- [51] S. Nojiri, S.D. Odintsov, et al., Phys. Lett. B, **825**, 136844 (2022). <https://doi.org/10.1016/j.physletb.2021.136844>



- [52] G.G. Luciano, E.N. Saridakis, *Eur. Phys. J. C*, **82**, 558 (2022). <https://doi.org/10.1140/epjc/s10052-022-10530-7>
- [53] S. Ghaffari, G.G. Luciano, et al., *Eur. Phys. J. Plus*, **138**, 82 (2023). <https://doi.org/10.1140/epjp/s13360-022-03481-1>
- [54] G.G. Luciano, and J. Giné, (18 Oct. 2022). <https://doi.org/10.48550/arXiv.2210.09755>
- [55] N. Boulkaboul, *Phys. Dark Univ.* **40**, 101205 (2023). <https://doi.org/10.1016/j.dark.2023.101205>
- [56] E.N. Saridakis, (16 Dec. 2020). <https://doi.org/10.48550/arXiv.2005.04115>
- [57] M. Li, *Phys. Lett. B*, **603**, 1 (2004). <https://doi.org/10.1016/j.physletb.2004.10.014>
- [58] E.N. Saridakis, (4 Jun. 2020). <https://doi.org/10.48550/arXiv.2006.01105>
- [59] E.N. Saridakis, and S. Basilakos, (15 Sep. 2021). <https://doi.org/10.48550/arXiv.2005.08258>
- [60] A.A. Mamon, A. Paliathanasis et al., (22 Jan. 2021). <https://doi.org/10.48550/arXiv.2007.16020>
- [61] F.K. Anagnostopoulos, S. Basilakos et al., *Eur. Phys. J. C*, **80**, 826 (2020). <https://doi.org/10.1140/epjc/s10052-020-8360-5>
- [62] A. Pradhan, V.K. Bhardwaj, et al., *Int. J. Geom. Met. Mod. Phys.* **19**, 2250106 (2022). <https://doi.org/10.1142/S0219887822501067>
- [63] S. Srivastava, and U.K. Sharma, (6 Oct. 2020). <https://arxiv.org/abs/2010.09439v1>
- [64] P. Adhikary, S. Das, S. Basilakos, et al., *Phys. Rev. D*, **104**, 123519 (2021). <https://doi.org/10.1103/PhysRevD.104.123519>
- [65] A. Sarkar, and S. Chattopadhyay, *Int. J. of Geom. Meth. Modern Phys.* **1809**, 2150148 (2021). <https://doi.org/10.1142/S0219887821501486>
- [66] L. Xu, and J. Lu, *Eur. Phys. J. C*, **60**, 135 (2009). <https://doi.org/10.1140/epjc/s10052-008-0858-1>
- [67] Y. Aditya, and D.R.K. Reddy, *Astrophys. Space Sci.* **363**, 207 (2018). <https://doi.org/10.1007/s10509-018-3429-4>
- [68] E. Sadri, *Eur. Phys. J. C*, **79**, 762 (2019). <https://doi.org/10.1140/epjc/s10052-019-7263-9>
- [69] M.A. Zadeh, A. Sheykhi, et al., (11 Jan. 2019). <https://arxiv.org/abs/1901.05298>
- [70] V.C. Dubey, S. Srivastava, et al., *Pramana J. Phys.* **93**, 78 (2019). <https://doi.org/10.1007/s12043-019-1843-y>
- [71] Y. Sobhanbabu, and M.V. Santhi, *Eur. Phys. J. C*, **81**, 1040 (2021). <https://doi.org/10.1140/epjc/s10052-021-09815-0>
- [72] G. Priyanka, A. Pradhan, et al., *Int. J. Geom. Met. Mod. Phys.* **20**, 2350082 (2023). <https://doi.org/10.1142/S0219887823500822>
- [73] Y. Aditya, S. Mandal, et al., *Eur. Phys. J. C*, **79**, 1020 (2019). <https://doi.org/10.1140/epjc/s10052-019-7534-5>
- [74] S. Ghaffari, H. Moradpour, I.P. Lobo, et al., *Eur. Phys. J. C*, **78**, 706 (2018). <https://doi.org/10.1140/epjc/s10052-018-6198-x>
- [75] A. Jawad, A. Aslam, et al., *Int. J. Mod. Phys. D*, **28**, 1950146 (2019). <https://doi.org/10.1142/S0218271819501463>
- [76] M.V. Santhi, and Y. Sobhanbabu, *Eur. Phys. J. C*, **80**, 1198 (2020). <https://doi.org/10.1140/epjc/s10052-020-08743-9>
- [77] A. Al Mamon, A. Paliathanasis, et al., (22 Jan. 2021). <https://doi.org/10.48550/arXiv.2007.16020>
- [78] S. Ghaffari, G.G. Luciano, et al. (7 Nov. 2022). <https://arxiv.org/abs/2209.00903v2>
- [79] M. Koussour, S.H. Shekh, et al., (14 Oct. 2022). <https://arxiv.org/abs/2203.08181v2>
- [80] Y. Sobhanbabu, R.S. Rao, et al., *New Astronomy*, **104**, 102066 (2023). <https://doi.org/10.1016/j.newast.2023.102066>
- [81] C.B. Collins, et al. *Gen. Relativ. Gravit.* **12**, 805 (2011). <http://dx.doi.org/10.1007/BF00763057>
- [82] Abdussatter, and S.R. Prajapati, *Astrophys. Space Sci.* **331**, 657 (2011). <https://doi.org/10.1007/s10509-010-0461-4>
- [83] D. Saez, and V.J. Ballester, *J. Phys. Lett.* **113**, 467 (1986). [https://doi.org/10.1016/0375-9601\(86\)90121-0](https://doi.org/10.1016/0375-9601(86)90121-0)
- [84] V. Sahni, T.D. Saini, et al., *Phys. Lett.* **77**, 201 (2003). <https://doi.org/10.1134/1.1574831>
- [85] V. Sahni, A. Shaleloo, et al., *Phys. Rev. D*, **78**, 103502 (2008). <https://doi.org/10.1103/PhysRevD.78.103502>
- [86] N. Aghanim, Y. Akrami, et al., *Astronomy and Astrophys.* **641**, A6 (2020). <https://doi.org/10.1051/0004-6361/201833910>
- [87] S. Capozziello, et al. *Mon. Not. R. Astron. Soc.* **484**, 4484 (2019). <https://doi.org/10.1093/mnras/stz176>

АНІЗОТРОПНІ ГОЛОГРАФІЧНІ МОДЕЛІ ТЕМНОЇ ЕНЕРГІЇ БАРРОУ В
СКАЛЯРНО-ТЕНЗОРНОЇ ТЕОРІЇ ГРАВІТАЦІЇЮ. Собханбабу^a, Г. Сатьянараяна^b, Н.В.С. Свами Чінаміллі^a, П.В. Рамбабу^a^a Факультет математики, Інженерний коледж SRKR (A), Бхімаварам-534204, Індія^b Технологічний інститут Сасі та інженерний коледж (A), Тадепаллігудем, Індія

У цьому дослідженні ми отримали розв'язок польових рівнянь скалярно-тензорної теорії гравітації, запропонованої Саезом і Баллестером (Phys. Lett. A113, 467:1986) у рамках типу Б'янкі III Всесвіт. Ми проаналізували взаємодіючі та не взаємодіючі анізотропні моделі голографічної темної енергії Барроу (BHDE), припустивши залежний від часу параметр уповільнення ($q(t)$). Крім того, ми обговорили кілька космологічних параметрів, таких як щільність енергії темної матерії без тиску та BHDE, асиметрія, уповільнення, рівняння параметрів стану, $\omega_{BH}-\omega'_{BH}$ площина та стабільність як взаємодіючі, так і не взаємодіючі моделі. Крім того, ми помітили, що в наших не взаємодіючих і взаємодіючих моделях уповільнення та рівняння параметрів стану підтверджують останні дані спостережень.

Ключові слова: Всесвіт типу Б'янкі-III; космологія; теорія Саеза-Баллестера

NUMERICAL APPROACH TO BURGERS' EQUATION IN DUSTY PLASMAS WITH DUST CHARGE VARIATION

 Harekrishna Deka^a,  Jnanjyoti Sarma^b

^a*K.K. Handiqui State Open University, Khanapara, Guwahati, 781022, India*

^b*R.G. Baruah College, Fatasil Ambari, Guwahati, 781025, India*

*Corresponding Author e-mail: harekrishnadeka11@gmail.com

Received February 6, 2024; revised March 6, 2024; accepted March 14, 2024

In this paper, the Crank-Nicolson method is applied to solve the one-dimensional nonlinear Burgers' equation in warm, dusty plasmas with dust charge variation. After obtaining numerical results, a thorough analysis is conducted and compared against analytical solutions. On the basis of the comparison, it is evident that the numerical results obtained from the analysis are in good agreement with the analytical solution. The error between the analytical and numerical solutions of the Burgers' equation is calculated by two error norms, namely L_2 and L_∞ . A Von-Neumann stability analysis is performed on the present method, and it is found to be unconditionally stable according to the Von-Neumann analysis.

Keywords: Warm Dusty plasmas; Burgers' equation; Crank-Nicolson method; von Neumann stability analysis

PACS: 02.70Bf, 52.27Lw, 52.35Fp, 52.35Tc

1. INTRODUCTION

Many real-life problems are represented by nonlinear partial differential equations, including plasma physics, acoustics, fluid mechanics, etc. One notable model equation is the nonlinear Burgers' equation, initially introduced by Bateman [1] and later recognized as a mathematical model for turbulence by Johannes Martinus Burgers [2]. The Burgers' equation is a partial differential equation that is used as a simplified version of the Navier-Stokes equation [3]. The Burgers' equation is a combination of convection and diffusion terms and has the same nonlinear and dissipative terms as the Navier-Stokes equation. This equation is primarily used for studying turbulence and shock wave theory in the context of nonlinear and dissipative phenomena. Burgers' equation in dusty plasmas that describes the nonlinear phenomenon of the shock structure formation on the acoustic wave originating from dust charge fluctuation dynamics.

The study of dusty plasmas, characterized by the presence of charged microparticles suspended in a plasma medium, has garnered significant attention in both experimental and theoretical research in recent years because dusty plasma plays an important role in studying the different types collective process in space environment, namely lower and upper mesosphere, radiofrequency, plasma discharge, planetary rings, plasma crystals, commentary tail, asteroid zones, planetary magnetosphere, interplanetary spaces, interstellar medium, earth's environment etc. [4, 5]. A dusty plasma is characterised by intense interactions between the dust particles and the nearby plasma species, which have a significant influence on plasma behaviour. Charged dust particles influence not only the equilibrium and stability of the plasma system but also exhibit fascinating dynamical properties, such as dust acoustic waves, dust ion-acoustic waves, and dust cyclotron waves. These waves have the potential to have a significant impact on the overall dynamics of a plasma due to the collective behaviour of dust particles. The Burgers' equation, which includes the effects of both convection and diffusion, is one of the fundamental equations used to describe the dynamics of dusty plasmas [6]. Researchers have been greatly interested in this equation since it was first presented because of its many practical applications, including gas dynamics, shock theory, traffic flows, viscous flow, and turbulence. Over the past few decades, numerous numerical methods have been developed and applied for solving Burgers' equation [7, 8, 9, 10, 11, 12, 13, 14]. These methods include finite element methods, finite difference methods, least-squares finite element methods, and spectral methods.

The Burgers' equation was studied by Wei and Gu in 2002, and they employed the Conjugate Filter Approach as a method for solving the equation [15]. Additionally, N.A. Mohamed [16] introduced new fully implicit schemes for solving the unsteady one-dimensional and two-dimensional equations. Singh and Gupta [17] have developed a new fourth order modified cubic B-spline (mCB) based upon collocation technique (mCBCT4) to determine approximate solution of Burgers' equation. Yusuf et al. [18] applied finite element collocation method with strang splitting to finding exact solutions of Burgers' type equation. Xu et al. [19] proposed a novel numerical scheme to solve Burgers' equation. Inan and Bahadir [20], developed implicit and fully implicit

exponential finite difference methods for numerical solution of the one-dimensional Burgers' equation. Inan and Bahadir [21] solved Burgers' equation numerically using a Crank-Nicolson exponential finite difference method. Mittal and Jain [22] have implemented modified cubic B-splines collocation method to solve nonlinear Burgers' equation. Wani and Thakar [23] developed a modified Crank-Nicolson type method for numerical solution of Burgers' equation. Mohamed [24] provided a new numerical scheme based on the finite difference method for solving the nonlinear one-dimensional Burgers' equation.

Yaghoobi and Najafi [25] constructed implicit non-standard finite difference scheme for solving the nonlinear Burgers' equation. An efficient numerical solution based on Milne method was presented in [26]. Shallal et al. [27] solved Burgers' Equation by a cubic Hermite finite element method. A numerical technique is formulated for solving the coupled viscous Burgers' equation (CVBE) by employing cubic B-spline and the Hermite formula [28]. Hussain [29] introduces a hybrid radial basis function (HRBF) approach for the numerical solution of the quasi-linear viscous Burgers' equation.

In this research article, the Crank-Nicholson method is applied to solve the Burgers' equation in warm dusty plasmas, taking dust charge fluctuations into account. The Crank-Nicholson method, a finite difference-based scheme, provides a robust and accurate numerical approach by employing an implicit midpoint rule, which combines the advantages of explicit and implicit schemes. This approach surpasses other numerical techniques in terms of precision. The behavior of plasma can be significantly impacted by the fluctuating charge levels of dust particles. Therefore, the inclusion of dust charge variation is crucial. The numerical method described in this paper aims to provide a comprehensive analysis of the influence of varying dust charge on the behavior of nonlinear waves and shock structures in dusty plasmas.

The manuscript is organized as follows: In Section 2, we introduce the governing equations for dusty plasmas with variable dust charge, and it provides a detailed discussion on the derivation of Burgers' equation within the context of dusty plasmas. In Section 3, we provide an overview of the Crank-Nicolson method used for the solution of the equation. Section 4 presents the stability analysis of the technique. In Section 5, we present the results and discussions, wherein we analyze the numerical solutions obtained and thoroughly discuss their implications.

2. BASIC EQUATIONS AND DERIVATION OF BURGERS' EQUATION

The fundamental equations governing the behavior of dust-charged grains in a fluid description consist of the equations of continuity and momentum, which can be expressed as follows[30]:

$$\frac{\partial n_d}{\partial t} + \frac{\partial}{\partial x} (n_d v_d) = 0 \tag{1}$$

$$\frac{\partial v_d}{\partial t} + v \frac{\partial v_d}{\partial x} + \frac{\zeta_d}{n_d} \frac{\partial p_d}{\partial x} = z_d \frac{\partial \psi}{\partial x} + \zeta \frac{\partial^2 v_d}{\partial x^2} \tag{2}$$

$$\frac{\partial p_d}{\partial t} + v \frac{\partial p_d}{\partial x} + 3p_d \frac{\partial v_d}{\partial x} = 0 \tag{3}$$

The Poisson's equation is given as

$$\frac{\partial^2 \psi}{\partial x^2} = z_d \lambda n_d + (1 - \lambda) n_e - n_i \tag{4}$$

The distribution of electron and ion density can be characterized using a Boltzmann distribution, that is.

$$n_e = n_{e0} \exp(\psi) \tag{5}$$

$$n_i = n_{i0} \exp(-\beta\psi) \tag{6}$$

In the given context, where n_d , n_e , n_i , v_d , p_d , ψ , x , and t represent the dust particle number density, electron number density, ion number density, dust fluid velocity, dust fluid pressure, electrostatic potential, spatial variable, and time, respectively, and they are normalized by n_{d0} (unperturbed dust particle number density), n_{e0} (unperturbed electron particle number density), and n_{i0} (unperturbed ion particle number density); $\lambda = \frac{n_{d0}}{n_{i0}}$, $\beta = \frac{T_e}{T_i}$, and $\zeta_d = \frac{T_d}{T_e}$, where T_d , T_e , and T_i are the temperatures for dust, electron, and ion. λ_d is the fluid velocity normalized to the dust acoustic speed $C_d = \left(\frac{z_d n_{d0} e \lambda + 3 \zeta_d K_B T_e q}{m_d q} \right)^{\frac{1}{2}}$ with $q = (1 - \lambda) n_{e0} + \beta n_{i0}$, and K_B , m_d , and z_d being the Boltzmann constant, dust acoustic mass, and charged number of dust particles. p_d is the pressure normalized to $n_{d0} K_B T_d$; ψ is the electrostatic wave potential normalized by $\left(\frac{K_B T_i}{e} \right)$, with e being the electron charge; the spatial variable is normalized to the dust Debye length $\vartheta_d = \left(\frac{3 \sigma_d K_B T_e m_d}{4 \pi n_{d0} (z_d^2 + qe)} \right)^{\frac{1}{2}}$,

and the time variable is normalized to the dust period $\varpi_{pd}^{-1} = \left(\frac{m_d}{4\pi n_{d_0} z_d^2 e^2}\right)^{\frac{1}{2}}$. The coefficient of viscosity ζ is a normalized quantity given by $\varpi_{pm} \vartheta_m^2 m_d n_{d_0}$.

The plasma system maintains overall charge neutrality through the following relationship:

$$z_d \lambda n_{d_0} + (1 - \lambda) n_{e_0} = n_{i_0} \tag{7}$$

The following stretched coordinates are taken into consideration in order to obtain the Burgers' equation:

$$\chi = \rho(x - \vartheta t); \zeta = \rho^2 t \tag{8}$$

Here, ϑ represents the phase velocity of the wave along the x direction, normalized by the acoustic velocity, while ρ serves as a dimensionless expansion parameter, quantifying the strength of dispersion. The equation of Burgers is formulated in [30] as:

$$\frac{\partial \psi^{(1)}}{\partial \zeta} + A \phi^{(1)} \frac{\partial \psi^{(1)}}{\partial \chi} = C \frac{\partial^2 \psi^{(1)}}{\partial \chi^2} \tag{9}$$

where

$$A = \frac{z_d \lambda \{ \vartheta^2 n_{i_0} - (1 - \lambda) n_{e_0} \} (\vartheta - 3\zeta_d) - 3 (\vartheta^2 + \zeta_d) \{ (1 - \lambda) n_{e_0} + \beta n_{i_0} \}^2}{2\vartheta z_d \lambda \{ (1 - \lambda) n_{e_0} + \beta n_{i_0} \}} \tag{10}$$

and

$$C = \frac{\zeta}{2\vartheta} \tag{11}$$

Employing the tanh-method [31], the solution for the shock wave is derived as

$$\psi^1(\chi, \zeta) = \psi_m \left\{ 1 - \tanh\left(\frac{\Omega}{\Upsilon}\right) \right\} \tag{12}$$

Where $\Omega = \chi - Mt$, $\psi_m = \frac{M}{A}$ and $\Upsilon = \frac{2B}{M}$. The variables ψ_m and Υ represent the amplitude and width of the shock waves, respectively, while M denotes the Mach number. The profile of the shock wave is influenced by the nonlinearity coefficient A and dissipation coefficient C, both of which are functions of plasma parameters.

3. CRANK-NICOLSON METHOD

Section 2 introduces the derivation of the Burgers equation within the context of dusty plasmas, considering variations in dust charge, and presents the solution for shock waves. Here, we proceed to apply the Crank-Nicolson method to solve the derived Burgers equation. The Crank-Nicolson method, proposed by Crank and Nicolson [24], is a numerical scheme and is a combination of the forward Euler method and the backward Euler method, which provides improved accuracy and stability. We simplify the equation 9 by introducing the transformations $\psi^1(\chi, \zeta) = u(x, t) \cong u_{i,x,j,t} \cong u_{i,j}$. The equation 9 can be expressed as

$$\frac{\partial u}{\partial t} + Au \frac{\partial u}{\partial x} = C \frac{\partial^2 u}{\partial x^2} \tag{13}$$

Let us consider the discretization of the Burgers' equation by using the Crank-Nicolson method:

$$\frac{\partial u}{\partial x} = \frac{u_{i+1,j+1} - u_{i-1,j+1}}{2h} + \frac{u_{i+1,j} - u_{i-1,j}}{2h} \tag{14}$$

$$\frac{\partial^2 u}{\partial x^2} = \frac{u_{i+1,j+1} - 2u_{i,j+1} + u_{i-1,j+1}}{2h^2} + \frac{u_{i+1,j} - 2u_{i,j} + u_{i-1,j}}{2h^2} \tag{15}$$

$$\frac{\partial u}{\partial t} = \frac{u_{i,j+1} - u_{i,j}}{k} \tag{16}$$

Now substituting eqs (26)-(28) into eq (25), we obtain

$$\begin{aligned} & \frac{u_{i,j+1} - u_{i,j}}{k} + Au_{i,j} \left(\frac{u_{i+1,j+1} - u_{i-1,j+1}}{2h} + \frac{u_{i+1,j} - u_{i-1,j}}{2h} \right) \\ & = C \left(\frac{u_{i+1,j+1} - 2u_{i,j+1} + u_{i-1,j+1}}{2h^2} + \frac{u_{i+1,j} - 2u_{i,j} + u_{i-1,j}}{2h^2} \right) \end{aligned} \tag{17}$$

Let $a = \frac{Ck}{2h^2}$, $r = \frac{Ak}{2h}$, the equation (29) will become

$$\begin{aligned} (1 + 2a) u_{i,j+1} - a(u_{i-1,j+1} + u_{i+1,j-1}) &= (1 - 2a) u_{i,j} + a(u_{i-1,j} + u_{i+1,j}) \\ -r [u_{i,j} (u_{i+1,j+1} - u_{i-1,j+1}) + u_{i,j} (u_{i+1,j} - u_{i-1,j})] & \end{aligned} \tag{18}$$

4. STABILITY ANALYSIS OF THE CRANK-NICHOLSON METHOD

The stability analysis was developed by the mid-twentieth century Hungarian mathematician and father of the electronic computer John von Neumann. The Von Neumann stability theory in which the growth factor of a Fourier mode is defined as

$$u_{i,j} = \xi^j e^{Ikh_i} = \xi^j e^{I\theta i} \tag{19}$$

Where $I = \sqrt{-1}$, ξ^j is the amplitude at time level k is the wave number and $h = \Delta x$. To investigate the stability of the numerical scheme, the Burgers' equation has been linearized by ignoring the nonlinear term and then obtained the differential equation by applying the Crank-Nicholson method to the linearized Burgers' equation. The linearized Burgers' equation is given as below:

$$\frac{\partial u}{\partial t} = C \frac{\partial^2 u}{\partial x^2} \tag{20}$$

Applying the Crank-Nicolson method to equation 20, we get

$$(1 + 2a) u_{i,j+1} - a (u_{i-1,j+1} + u_{i+1,j+1}) = (1 - 2a) u_{i,j} + a (u_{i-1,j} + u_{i+1,j}) \tag{21}$$

Substitute 19 in 21, we get

$$(1 + 2a) \xi^j e^{I\theta i} \xi - a (\xi^j e^{I\theta i} \xi e^{-I\theta} + \xi^j e^{I\theta i} \xi e^{I\theta}) = (1 - 2a) \xi^j e^{I\theta i} + a (\xi^j e^{I\theta i} e^{-I\theta} + \xi^j e^{I\theta i} e^{I\theta}) \tag{22}$$

$$(1 + 2a) \xi - a (\xi e^{-I\theta} + \xi e^{I\theta}) = (1 - 2a) + a (e^{-I\theta} + e^{I\theta}) \tag{23}$$

$$(1 + 2a) \xi - a \xi \cos\theta = (1 - 2a) + a \cos\theta \tag{24}$$

$$\xi = \frac{1 - 2a + a \cos\theta}{1 + 2a - a \cos\theta} \tag{25}$$

Where the quantity ξ in equation 19 is called the amplification factor. Since $0 \leq \cos\theta \leq 1$ When $\cos\theta = 0, \xi = \frac{1-2a}{1+2a} \leq 1$ When $\cos\theta = 1, \xi = \frac{1-2a+a}{1+2a-a} = \frac{1-a}{1+a} \leq 1$ Hence, $\xi \leq 1$ is always satisfied for any value of a where 1 is the upper limit for ξ . For stability, we must have $|\xi| \leq 1$, which means $-1 \leq \xi \leq 1$. Now, we consider the lower limit for ξ .

$$-1 \leq \xi \tag{26}$$

$$-1 \leq \frac{1 - 2a + a \cos\theta}{1 + 2a - a \cos\theta} \tag{27}$$

$$-1 (1 + 2a - a \cos\theta) \leq 1 - 2a + a \cos\theta \tag{28}$$

$$a \cos\theta - 1 - 2a \leq 1 - 2a + a \cos\theta \tag{29}$$

$$-1 - 2a \leq 1 - 2a \tag{30}$$

$$2a - 2a \leq 1 + 1 \tag{31}$$

$0 \leq 2$ which is always true.

It implies that the lower limit for ξ is satisfied for any value of a . Thus the Crank-Nicholson method is unconditionally stable according to the linear analysis.

5. RESULTS AND DISCUSSION

The analytical solution 12 can be rewritten as ,

$$u(x, t) = \frac{M}{A} \left\{ 1 - \tanh \frac{M}{2C} (x - Mt) \right\} \tag{32}$$

To proceed the numerical solution of Burgers' equation, we consider the initial condition as

$$u(x, 0) = \frac{M}{A} \left\{ 1 - \tanh \frac{Mx}{2C} \right\} \tag{33}$$

and the boundary conditions

$$u(0, t) = \frac{M}{A} \left\{ 1 + \tanh \frac{M^2 t}{2C} \right\} \tag{34}$$

$$u(1, t) = \frac{M}{A} \left\{ 1 - \tanh \frac{M}{2C} (1 - Mt) \right\} \tag{35}$$

Due to the dependence of the nonlinear coefficient A and dissipation coefficient C on different plasma parameters, we have considered a range of values for A and C, corresponding to the various plasma parameters. The validity of the present technique is evaluated using the absolute error which is defined by

$$\left| u_i^{Analytical} - u_i^{Numerical} \right| \tag{36}$$

Also, L_2 and L_∞ error norms, defined by

$$L_2 = \sqrt{h \sum_{j=1}^N \left| u_j^{analytical} - u_j^{numerical} \right|^2} \tag{37}$$

$$L_\infty = \max \left| u_j^{analytical} - u_j^{numerical} \right| \tag{38}$$

are presented graphically for various values of nonlinear coefficient and dissipation coefficient for chosen space and time steps to check the accuracy and effectiveness of the method.

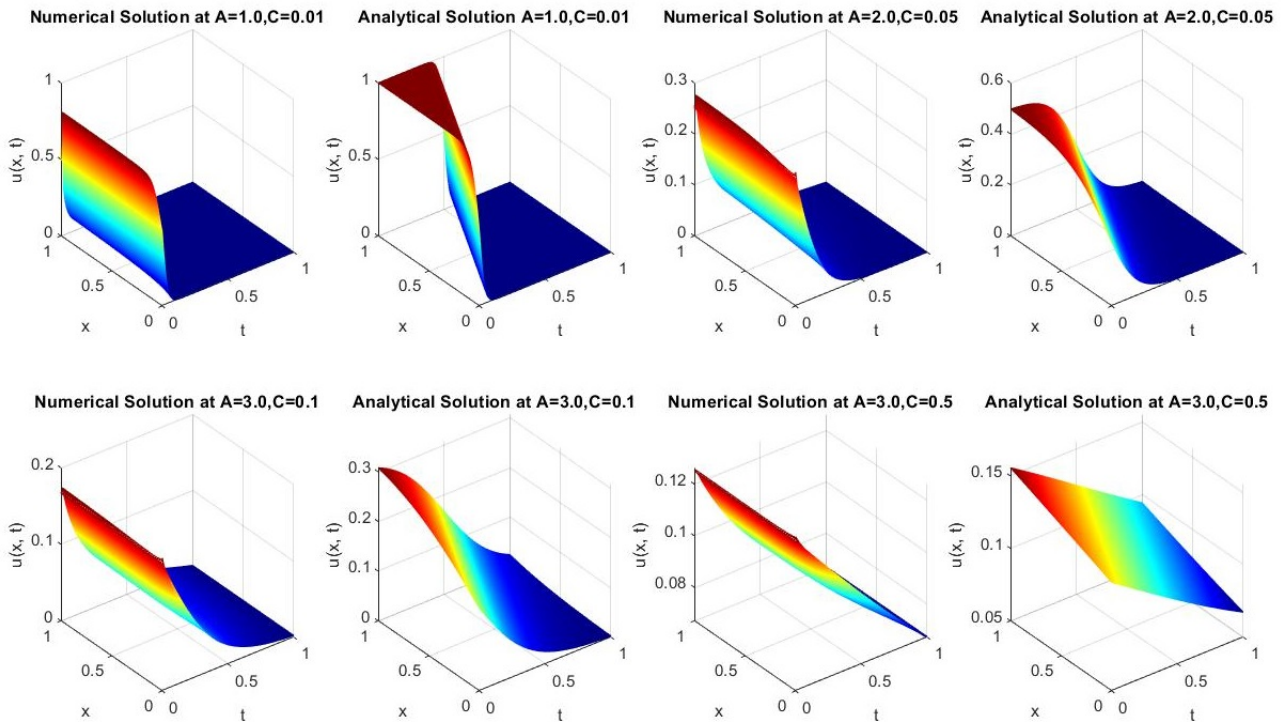


Figure 1. Comparison of Analytical and numerical solution of Burgers' equation at various values of A and C.

The comparison between the analytical and numerical solutions of the Burgers' equation in dusty plasma using the Crank-Nicholson method has been presented in Figure 1. It has been observed that the numerical solution obtained through the Crank-Nicholson method demonstrates good agreement with the analytical solution. The figure clearly illustrates that the presence of shock wave structures is observed when the dissipation coefficient is reduced to a smaller value. As C becomes larger, the diffusive behavior becomes more prominent and suppress the formation of shocks and maintain a more diffusive behavior. The wavefronts become smoother and propagate slower as C increases. When the nonlinear coefficient (A) is increased, the advection term becomes dominant, leading to the formation of steep gradients and shock waves in the solution.

Table 1. Absolute error between the numerical and analytical values at $A = 1.0$, $C = 0.01$

x	t	Numerical value	Analytical value	Absolute error
0	0	0.5000	1.0000	0.5000
0.1	0.1	0.071419	1.0000	0.9286
0.2	0.2	0.022251	1.0000	0.9777
0.3	0.3	0.0059356	0.99995	0.9940
0.4	0.4	0.0011129	0.99331	0.9922
0.5	0.5	0.0001371	0.5000	0.4999
0.6	0.6	1.0961e-05	0.0066929	0.0067
0.7	0.7	5.7353e-07	4.5398e-05	4.4824e-05
0.8	0.8	1.9973e-08	3.059e-07	2.8593e-07
0.9	0.9	4.7392e-10	2.0612e-09	1.5872e-09
1.0	1.0	0.0	1.3888e-11	1.3888e-11
L_2				0.442952
L_∞				0.996807

Table 2. Absolute error between the numerical and analytical values at $A = 2.0$, $C = 0.05$

x	t	Numerical value	Analytical value	Absolute error
0	0	0.25	0.49665	0.2467
0.1	0.1	0.12951	0.49101	0.3615
0.2	0.2	0.075079	0.47629	0.4012
0.3	0.3	0.047618	0.4404	0.3928
0.4	0.4	0.030846	0.36553	0.3347
0.5	0.5	0.019766	0.25	0.2302
0.6	0.6	0.012283	0.13447	0.1222
0.7	0.7	0.0072688	0.059601	0.0523
0.8	0.8	0.0039561	0.023713	0.0198
0.9	0.9	0.0017256	0.0089931	0.0073
1.0	1.0	2.2699e-05	0.0033464	0.0033
L_2				0.155768
L_∞				0.403353

Table 3. Absolute error between the numerical and analytical values at $A = 3.0$, $C = 0.1$

x	t	Numerical value	Analytical value	Absolute error
0	0	0.16667	0.30805	0.1414
0.1	0.1	0.11332	0.2936	0.1803
0.2	0.2	0.079198	0.27252	0.1933
0.3	0.3	0.0585	0.24369	0.1852
0.4	0.4	0.044279	0.20749	0.1632
0.5	0.5	0.033691	0.16667	0.1330
0.6	0.6	0.025343	0.12585	0.1005
0.7	0.7	0.018454	0.089647	0.0712
0.8	0.8	0.012529	0.060809	0.0483
0.9	0.9	0.0072105	0.039734	0.0325
1.0	1.0	0.002231	0.025286	0.0231
L_2				0.077955
L_∞				0.193327

Table 4. Absolute error between the numerical and analytical values at $A = 4.0, C = 0.5$

x	t	Numerical value	Analytical value	Absolute error
0	0	0.125	0.15561	0.0306
0.1	0.1	0.11556	0.14967	0.0341
0.2	0.2	0.1064	0.14361	0.0372
0.3	0.3	0.098681	0.13746	0.0388
0.4	0.4	0.09209	0.13124	0.0392
0.5	0.5	0.0864	0.125	0.0386
0.6	0.6	0.081442	0.11876	0.0373
0.7	0.7	0.077087	0.11254	0.0355
0.8	0.8	0.073233	0.10639	0.0332
0.9	0.9	0.069802	0.10033	0.0305
1.0	1.0	0.067235	0.094385	0.0271
L_2				0.021960
L_∞				0.039163

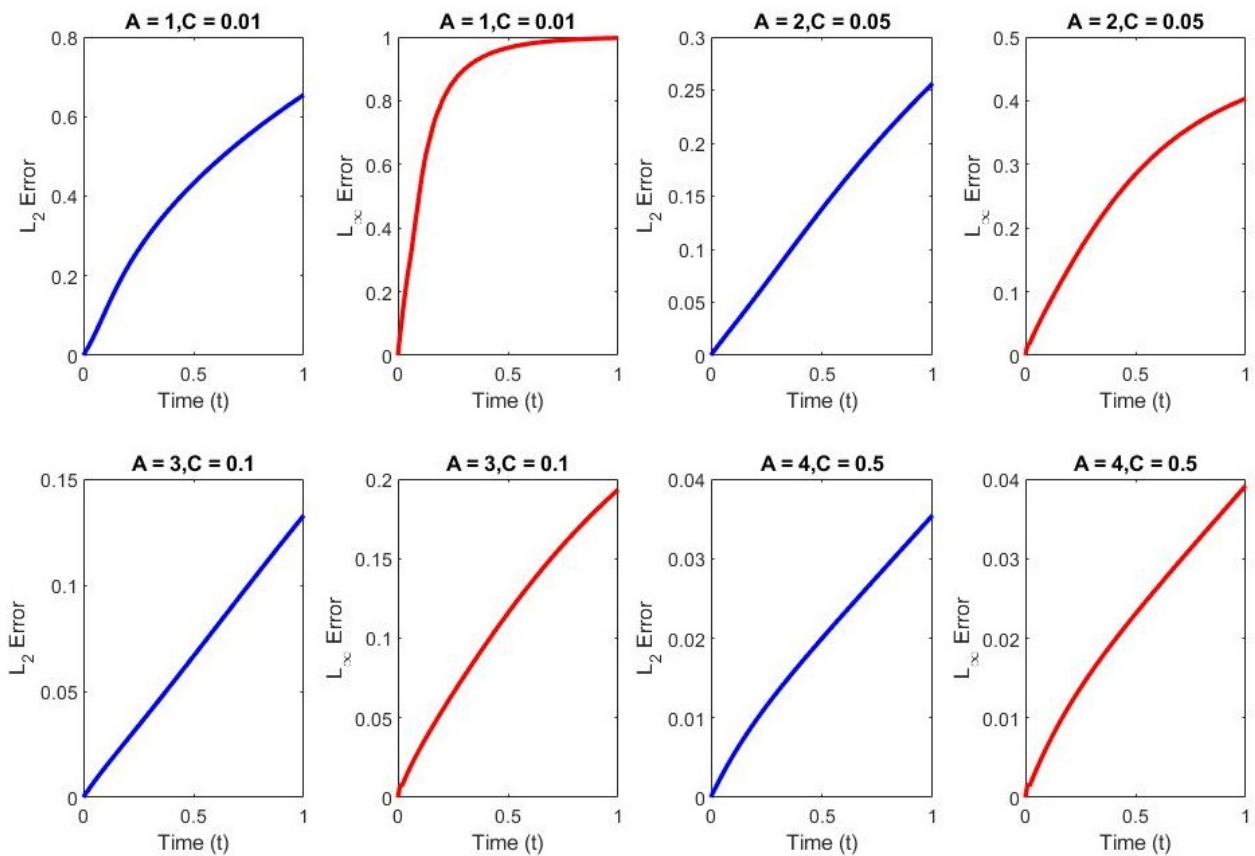


Figure 2. L_2 and L_∞ error norms at various values of A and C.

It has been observed from the Table 1-4 and Figure 2 that the value of L_2 and L_∞ decrease as the value nonlinear coefficient A and the dissipation coefficient C increases. As it is seen from the Table 1-4, the error norms L_2 and L_∞ are sufficiently small and satisfactorily acceptable. A decreasing trend in the L_2 and L_∞ error norm as the mesh size or time step is refined indicates improved accuracy and convergence of the numerical scheme. A lower L_2 and L_∞ error norm indicates better accuracy and convergence of the numerical scheme.

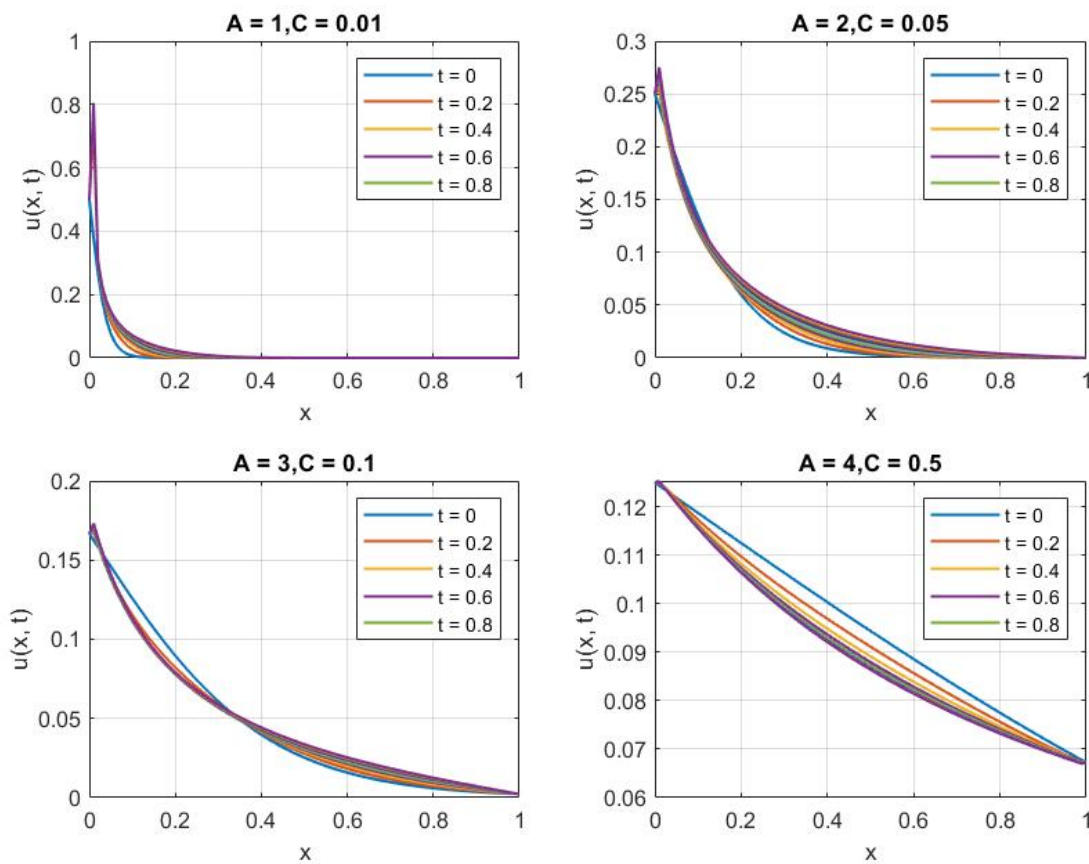


Figure 3. Numerical solutions at different times for (a) $A = 1, C = 0.01$, (b) $A = 2, C = 0.05$, (c) $A = 3, C = 0.1$ and (d) $A = 4, C = 0.5$.

The graphs of the numerical solution at different times for increasing values of the nonlinear coefficient will show more pronounced changes in the solution profile, with sharper transitions and larger gradients. The graphs of the numerical solution at different times for increasing values of the dissipation coefficient will exhibit smoother profiles with reduced oscillations and less pronounced sharp transitions.

6. CONCLUSION

In this study, one dimensional Burgers' equation is numerically solved using the Crank-Nicholson method and the behavior of shock wave profiles are investigated in warm dusty plasmas considering dust charge variation. The graphs of the numerical results are plotted to compare with the analytical results and it is clear from the comparison that the graphs of numerical results are close with the results obtained by analytically and better than numerical solutions obtained by some other methods in literature. The propagation of the shock waves for various values of nonlinear coefficient and dissipation coefficient have been observed and it is found that the wave front become more sharper as the dissipation coefficient decreases. The absolute error is computed for checking the accuracy and efficiency of the present technique. From the study, it has been noted that the accuracy and efficiency of the technique depends on the value of dissipation coefficient and the result will get better when the dissipation coefficient takes smaller value.

ORCID

Harekrishna Deka, <https://orcid.org/0000-0003-4280-3728>; Jnanjyoti Sarma, <https://orcid.org/0000-0002-0793-5680>

REFERENCES

[1] H. Bateman, "Some recent researches on the motion of fluids," Monthly Weather Review, **43**, 163-170 (1915). [https://doi.org/10.1175/1520-0493\(1915\)43%3C163:SRR0TM%3E2.0.CO;2](https://doi.org/10.1175/1520-0493(1915)43%3C163:SRR0TM%3E2.0.CO;2)

- [2] J.M. Burgers, "Mathematical examples illustrating relations occurring in the theory of turbulent fluid motion," in *Selected Papers of J.M. Burgers*, edited by F.T.M Nieuwstadt, and J.A. Steketee, (Springer Science + Business Mwdia, B.V., Netherlands, 1995). pp. 281-334. https://doi.org/10.1007/978-94-011-0195-0_10
- [3] S. Dhawan, S. Kapoor, S. Kumar, and S. Rawat, "Contemporary review of techniques for the solution of nonlinear Burgers equation," *Journal of Computational Science*, **3**, 405-419 (2012). <https://doi.org/10.1016/j.jocs.2012.06.003>
- [4] M. Horányi, "Charged dust dynamics in the solar system," *Annual review of astronomy and astrophysics*, **34**, 383-418 (1996). <https://doi.org/10.1146/annurev.astro.34.1.383>
- [5] M. Horányi, and D.A. Mendis, "The dynamics of charged dust in the tail of comet Giacobini Zinner," *Journal of Geophysical Research: Space Physics*, **91**, 355-361 (1986). <https://doi.org/10.1029/JA091iA01p00355>
- [6] B.P. Pandey, "Thermodynamics of a dusty plasma," *Physical Review E*, **69**, 026410 (2004). <https://doi.org/10.1103/PhysRevE.69.026410>
- [7] J. Caldwell, P. Caldwell, and A.E. Cook, "A finite element approach to Burgers' equation," *Applied Mathematical Modelling*, **5**, 189-193 (1981). [https://doi.org/10.1016/0307-904X\(81\)90043-3](https://doi.org/10.1016/0307-904X(81)90043-3)
- [8] N. Bressan, and A. Quarteroni, "An implicit/explicit spectral method for Burgers' equation," *Calcolo*, **23**, 265-284 (1986). <https://doi.org/10.1007/BF02576532>
- [9] S. Kutluay, A.R. Bahadır, and A. Özdeş, "Numerical solution of one-dimensional Burgers equation: explicit and exact-explicit finite difference methods," *Journal of computational and applied mathematics*, **108**, 251-261 (1999). ([https://doi.org/10.1016/S0377-0427\(98\)00261-1](https://doi.org/10.1016/S0377-0427(98)00261-1))
- [10] T. Öziş, E.N. Aksan, and A. Özdeş, "A finite element approach for solution of Burgers' equation," *Journal of computational and applied mathematics*, **139**, 417-428 (2003). [https://doi.org/10.1016/S0096-3003\(02\)00204-7](https://doi.org/10.1016/S0096-3003(02)00204-7)
- [11] Y. Duan, and R. Liu, "Lattice Boltzmann model for two-dimensional unsteady Burgers' equation," *Journal of Computational and Applied Mathematics*, **206**, 432-439 (2007). <https://doi.org/10.1016/j.cam.2006.08.002>
- [12] M.M. Cecchi, R. Nociforo, and P.P. Grego, "Space-time finite elements numerical solutions of Burgers Problems," *Le Matematiche*, **51**, 43-57 (1996). <https://lematematiche.dmi.unict.it/index.php/lematematiche/article/view/425/398>
- [13] I.A. Hassanien, A.A. Salama, and H.A. Hosham, "Fourth-order finite difference method for solving Burgers' equation," *Applied Mathematics and Computation*, **170**, 781-800 (2005). <https://doi.org/10.1016/j.amc.2004.12.052>
- [14] J. Zhao, H. Li, Z. Fang, and X. Bai, "Numerical solution of Burgers' equation based on mixed finite volume element methods," *Discrete dynamics in nature and society*, **2020**, 6321209 (2020). <https://doi.org/10.1155/2020/6321209>
- [15] G.W. Wei, and Y. Gu, "Conjugate filter approach for solving Burgers' equation," *Journal of Computational and Applied mathematics*, **149**, 439-456 (2002). [https://doi.org/10.1016/S0377-0427\(02\)00488-0](https://doi.org/10.1016/S0377-0427(02)00488-0)
- [16] N.A. Mohamed, "Solving one-and two-dimensional unsteady Burgers' equation using fully implicit finite difference schemes," *Arab Journal of Basic and Applied Sciences*, **26**, 254-268 (2019). <https://doi.org/10.1080/25765299.2019.1613746>
- [17] B.K. Singh, and M. Gupta, "A new efficient fourth order collocation scheme for solving Burgers' equation," *Applied Mathematics and Computation*, **399**, 126011 (2021). <https://doi.org/10.1016/j.amc.2021.126011>
- [18] Y. Uçar, M. Yağmurlu, and İ. Çelikkaya, "Numerical solution of Burger's type equation using finite element collocation method with strang splitting," *Mathematical Sciences and Applications E-Notes*, **8**, 29-45 (2009). <https://doi.org/10.36753/mathenot.598635>
- [19] M. Xu, R.H. Wang, J.H. Zhang, and Q. Fang, "A novel numerical scheme for solving Burgers' equation," *Applied mathematics and computation*, **217**, 4473-4482 (2011). <https://doi.org/10.1016/j.amc.2010.10.050>
- [20] B. Inan, and A.R. Bahadır, "Numerical solution of the one-dimensional Burgers' equation: Implicit and fully implicit exponential finite difference methods," *Pramana*, **81**, 547-556 (2013). <https://doi.org/10.1007/s12043-013-0599-z>
- [21] B. Inan, and A.R. Bahadır, "A numerical solution of the Burgers' equation using a Crank-Nicolson exponential finite difference method," *Math. Comput. Sci.* **4**, 849-860 (2014). <https://scik.org/index.php/jmcs/article/download/1853/984>
- [22] R.C. Mittal, and R.K. Jain, "Numerical solutions of nonlinear Burgers' equation with modified cubic B-splines collocation method," *Applied Mathematics and Computation*, **218**, 7839-7855 (2012). <https://doi.org/10.1016/j.amc.2012.01.059>
- [23] S.S. Wani, and S.H. Thakar, "Crank-Nicolson type method for Burgers' equation," *International Journal of Applied Physics and Mathematics*, **3**, 324-328 (2013). <https://doi.org/10.7763/IJAPM.2013.V3.230>
- [24] N.A. Mohamed, "Fully implicit scheme for solving Burgers' equation based on finite difference method," *The Egyptian International Journal of Engineering Sciences and Technology*, **26**, 38-44 (2018).

- [25] A. Yaghoobi, and H.S. Najafi, "A fully implicit non-standard finite difference scheme for one dimensional Burgers' equation," Journal of Applied Research on Industrial Engineering, **7**, 301-312 (2020). <https://doi.org/10.22105/jarie.2021.244715.1188>
- [26] S. Chonladed, and K. Wuttanachamsri, "A numerical solution of Burger's equation based on milne method," IAENG International Journal of Applied Mathematics, **51**, 411-415 (2021). https://www.iaeng.org/IJAM/issues_v51/issue_2/IJAM_51_2_20.pdf
- [27] M.A. Shallal, A.H. Taqi, B.F. Jumaa, H. Rezazadeh, and M. Inc, "Numerical solutions to the 1D Burgers' equation by a cubic Hermite finite element method," Indian J. Phys, **96**, 3831-3836 (2022). <https://doi.org/10.1007/s12648-022-02304-4>
- [28] M. Abdullah, M.Yaseen, and M. De la Sen, "Numerical simulation of the coupled viscous Burgers equation using the Hermite formula and cubic B-spline basis functions," Phys. Scr. **95**, 115216 (2020). <https://doi.org/10.1088/1402-4896/abbf1f>
- [29] M. Hussain, "Hybrid radial basis function methods of lines for the numerical solution of viscous Burgers' equation," Computational and Applied Mathematics, **40**, 107-156 (2021). <https://doi.org/10.1007/s40314-021-01505-7>
- [30] J. Sarma, and A.N. Dev, "Dust acoustic waves in warm dusty plasmas," Indian Journal of Pure & Applied Physics, **52**, 747-754 (2014). [https://nopr.niscpr.res.in/bitstream/123456789/29598/1/IJPAP%2052\(11\)%20747-754.pdf](https://nopr.niscpr.res.in/bitstream/123456789/29598/1/IJPAP%2052(11)%20747-754.pdf)
- [31] G.C. Das, C.B. Dwivedi, M. Talukdar, and J. Sarma, "A new mathematical approach for shock-wave solution in a dusty plasma," Physics of Plasmas, **4**, 4236-4239 (1997). <https://doi.org/10.1063/1.872586>

ЧИСЕЛЬНИЙ ПІДХІД ДО РІВНЯННЯ БЮРГЕРСА В ЗАПИЛЕНІЙ ПЛАЗМІ ЗІ ЗМІНОЮ ЗАРЯДУ ПИЛУ

Харекрішна Дека^a, Джнанджьоті Сарма^b

^a К.К. Державний відкритий університет Хандікі, Хананара, Гувахаті, 781022, Індія

^b Коледж Р.Г. Баруа, Фатасил Амбарі, Гувахаті, 781025, Індія

У цій статті застосовано метод Кренка-Ніколсона для вирішення одновимірного нелінійного рівняння Бюргерса в теплій заповненій плазмі зі змінюючим зарядом пилу. Проведено аналіз отриманих чисельних результатів та порівняння з аналітичними результатами. На основі порівняння очевидно, що числові результати, отримані в результаті аналізу, добре узгоджуються з аналітичним рішенням. Похибка між аналітичним і чисельним розв'язками рівняння Бюргерса обчислюється за двома нормами похибки, а саме L_2 і L_∞ . Аналіз стабільності виконується за методом фон-Неймана, і він виявляється безумовно стабільним згідно з аналізом.

Ключові слова: гаряча пилова плазма; рівняння Бюргерса; метод Кренка-Ніколсона; аналіз стійкості фон Неймана

EXISTENCE OF SMALL AMPLITUDE KdV AND MKdV SOLITONS IN A MAGNETIZED DUSTY PLASMA WITH q -NONEXTENSIVE DISTRIBUTED ELECTRONS

 Muktarul Rahman^{a*},  Satyendra Nath Barman^b

^aDepartment of Mathematics, Gauhati University, Guwahati-781014, Assam, India

^bB. Borooah College, Guwahati-781007, Assam, India

*Corresponding Author e-mail: mrahman23.math@gmail.com

Received March 2, 2024; revised April 8, 2024; accepted April 19, 2024

The existence and propagating characteristics of small amplitude dust-ion-acoustic (DIA) Korteweg-de Vries (KdV) and modified KdV solitons in a three component magnetized plasma composed of positive inertial ions with pressure variation, noninertial electrons and negative charged immobile dust grains are theoretically and numerically investigated when the electrons obey a q -nonextensive velocity distribution. Utilizing the reductive perturbation method, to derive KdV and modified KdV equations and obtain the DIA soliton solutions along with the corresponding small amplitude potentials. This study shows that there are compressive and/or rarefactive solitons and no soliton at all, due to the parametric dependency on the first-order nonlinear coefficient through the number density of positive ions and negative dust grains and the electron nonextensivity. The coexistence of compressive and rarefactive solitons appears by raising the measure of nonlinearity coefficient to the second-order using the modified KdV equation. The properties such as speed, amplitude, width etc. of the propagating soliton are numerically discussed.

Keywords: *Dust ion acoustic wave; Magnetized plasma; q -nonextensive distribution; Reductive perturbation method; KdV equation*

PACS: 52.27.Lw; 52.25.Xz; 52.35.Fp; 52.35.Qz; 52.35.Sb

1. INTRODUCTION

The propagation of nonlinear electrostatic waves in many physical situation is an fascinating and recently growing field of research in plasma dynamics; however its exploration had started in the long past. During last few decades, the discovery of dust charged grains in the plasma medium have opened a great deal of interest in the minds of modern plasma workers, because its presence is drastically change in the characteristics of waves in plasma. The role and influence of dust particles are beautifully explained by several experts in space and astrophysical plasmas such as in Saturn's rings, Earth's ionosphere and magnetosphere, in Planetary rings and magnetosphere, in Cometary tails, interstellar medium as well as in laboratory plasmas (not mentioned here). The formation and existence of nonlinear electrostatic waves in a magnetized plasma consisting of charged dust particles has been extensively investigated theoretically [1–4] and experimentally [5–8]. DIA waves are weak-frequency waves which involve in the movement of massive ions and form compression and rarefaction region just like in travelling sound waves; in which, the inertia is attributed to the number density of ions, whereas the thermal pressure of electrons is assumed to establish the restoring force which is responsible for initiating the plasma waves, and the negatively charged dust grains are expected to remain stationary in this realism. The understanding of the nonlinear propagation of DIA solitons in an unmagnetized plasma having three components namely, positive ions, electrons, and negatively charged dust grains is now theoretically [9–12] and experimentally [13, 14] well-established. The presence of an external magnetic field in a plasma is not only affects the existence and direction of DIA modes, but also introduces new approach of propagation and inherent oscillations. Many studies have published into how the magnetic field influences the dynamic characteristics of DIA waves, considering both linear and nonlinear properties. For instance, Ghosh et al. [15] conducted theoretical investigations into DIA wave propagation in a magnetized dusty plasma with charge fluctuations using the reductive perturbation method. Anowar and Mamun [16] derived a KdV equation to describe the oblique propagation of solitary waves in an adiabatic magnetized dusty plasma. While the oblique propagation of large amplitude DIA solitary waves in a magnetized dusty plasma are studied by Saha and Chatterjee [17]. Besides, it has been established by many researchers in various relevant scenarios that the presence of a magnetic field significantly alters the inherent characteristics of DIA waves as they propagate through plasmas. [18–22]. Recently, Abdus et al. [23] employed the reductive perturbation approach to theoretically investigate the influence of higher-order nonlinear and dispersive effects on the fundamental characteristics of DIA solitary waves in a magnetized dusty plasma.

Nonlinear electrostatic waves in plasmas can be treated mathematically in a variety of ways, but two main approaches are commonly employed. The most popular method involves employing the Sagdeev pseudo-potential method to study the arbitrary amplitude of waves in plasmas. On the other hand, the evolution equation for the small amplitude electrostatic waves may be extracted using a reductive perturbation method. The velocity distribution function of plasma particle plays a crucial role in influencing the nonlinear behavior of plasma waves. In many instances, the Maxwellian velocity distribution function is the standard choice for describing electron's behavior. However, in recent years, there has been a notable increase in interest regarding the study of particle distribution in plasma using the Boltzmann Gibbs Shannon entropy. This concept was originally introduced by Renyi [24] and has garnered significant attention. The generalization of Boltzmann-Gibbs entropy in the non-equilibrium states with the q -nonextensive entropy suggested by Tsallis [25]. By citing this approach many researchers have paid more attention to employ the nonextensive distribution for the number density of particles in plasma [26–32]. The q -nonextensive distribution function shows distinct behaviors based on the values of q , which determines the quantity of the nonextensivity of the system being studied. For $q < 1$, the distribution function indicates the plasma with higher number of superthermal particles compared to that of Maxwellian case (superextensivity), whereas for $q > 1$, the distribution function shows the plasma with large number of low-speed particles compared to that of Maxwellian case (subextensivity). Moreover, if $q = 1$, the distribution function is then reduced to common Maxwell-Boltzmann velocity distribution [33].

The main objective of the paper is to investigate the propagating behavior of nonlinear DIA solitary waves in a three component magnetized plasma consisting of inertial ions, nonextensive electrons and charged dust grains. For this work, the reductive perturbation method is used to investigate the nonlinear DIA waves and we emphasize the DIA solitary waves of small amplitude. The paper is organized as follows: in Section-1, we have given the usual introduction; in Section-2, we give the basic set governing equations for describing the plasma model; in Section-3 and Section-4, we derivation of the KdV and modified KdV equation respectively, where the result and discussion are made and Finally we summarize our work in Section-5. At the end, the references are included.

2. THE BASIC EQUATIONS FOR PLASMA SYSTEM

We consider a magnetized collisionless plasma system consisting of positively charged inertial ions, negatively charged dust grains and noninertial electrons which obey q -nonextensive distributions. Therefore, at equilibrium $z_i n_{i0} = n_{e0} + z_d n_{d0}$, where n_{i0} , n_{e0} and n_{d0} are the particle number densities of ion, electron and dust respectively at equilibrium, while z_i and z_d are the ion and dust charge numbers. An uniform external magnetic field is assumed along z -direction in the plasma, *i.e.* $\vec{B} = B_0 \hat{z}$. The charges carried by the dust grains are considered to remain constant, and their effects on the dynamics of DIA waves is ignored. As the plasma possesses a finite ion temperature, we keep the ion pressure gradient term in our considerations. The dynamics of nonlinear waves structures in such a plasma system are governed by the following unnormalized fluid equations

$$\frac{\partial N}{\partial T} + \vec{\nabla}' \cdot (N \vec{V}) = 0, \quad (1)$$

$$\frac{\partial \vec{V}}{\partial T} + (\vec{V} \cdot \vec{\nabla}') \vec{V} = -\frac{z_i e}{m} \vec{\nabla}' \Phi + \frac{z_i e}{m} (\vec{V} \times \vec{B}) - \frac{1}{mN} \vec{\nabla}' P, \quad (2)$$

$$\frac{\partial P}{\partial T} + (\vec{V} \cdot \vec{\nabla}') P + \gamma P (\vec{\nabla}' \cdot \vec{V}) = 0, \quad (3)$$

$$\nabla'^2 \Phi = 4\pi e [N_e + z_d n_{d0} - z_i N]. \quad (4)$$

where N , \vec{V} , m , P , e , N_e and Φ are respectively the ion number density, ion fluid velocity, mass of an ion, ion fluid pressure, electronic charge, electron number density and electrostatic potential. And $\gamma = C_{ip}/C_{iv}$ is the adiabatic index, where C_{ip} (C_{iv}) is the specific heat of ion at constant pressure (volume). We have taken adiabatic index, $\gamma = 3$. To normalize the set of equations (1)-(4), we consider the dimensionless variables as follows:

$$t = \frac{T}{\omega_{pi}^{-1}}, \quad n = \frac{N}{n_{i0}}, \quad n_e = \frac{N_e}{n_{e0}}, \quad \vec{v} = \frac{\vec{V}}{c_i}, \quad \phi = \frac{e\Phi}{k_b T_e}, \quad \vec{\nabla} = \frac{\vec{\nabla}'}{\lambda_D^{-1}}, \quad p = \frac{P}{p_{i0}}.$$

with the characteristic ion plasma frequency ω_{pi} , the electron Debye length λ_D and equilibrium ion pressure p_{i0} are given by

$$\omega_{pi} = \sqrt{\frac{4\pi n_{i0} e^2 z_i^2}{m}}; \quad \lambda_D = \sqrt{\frac{k_b T_e}{4\pi n_{i0} e^2 z_i}} \quad \text{and} \quad p_{i0} = n_{i0} k_b T_i.$$

Thus, the ion acoustic speed $c_i = \omega_{pi} \lambda_D = \sqrt{z_i k_b T_e / m}$. Where T_e (T_i) and k_b are the characteristic electron (ion) temperature and the Boltzmann constant respectively. As the electron velocity distribution is assumed to

be q -nonextensive, so the normalized expression for the number density of electron is given by [34–36]

$$n_e = [1 + (q - 1)\phi]^{\frac{(q+1)}{2(q-1)}}. \quad (5)$$

Where the parameter q stands for the strength of electrons nonextensivity and it is a real number greater than -1 . The normalized form of the set of equations (1)-(4) can be written in the component form as

$$\frac{\partial n}{\partial t} + \frac{\partial(nu)}{\partial x} + \frac{\partial(nv)}{\partial y} + \frac{\partial(nw)}{\partial z} = 0, \quad (6)$$

$$\frac{\partial u}{\partial t} + u \frac{\partial u}{\partial x} + v \frac{\partial u}{\partial y} + w \frac{\partial u}{\partial z} = -\frac{\partial \phi}{\partial x} + \Omega v - \frac{\sigma}{n} \frac{\partial p}{\partial x}, \quad (7)$$

$$\frac{\partial v}{\partial t} + u \frac{\partial v}{\partial x} + v \frac{\partial v}{\partial y} + w \frac{\partial v}{\partial z} = -\frac{\partial \phi}{\partial y} - \Omega u - \frac{\sigma}{n} \frac{\partial p}{\partial y}, \quad (8)$$

$$\frac{\partial w}{\partial t} + u \frac{\partial w}{\partial x} + v \frac{\partial w}{\partial y} + w \frac{\partial w}{\partial z} = -\frac{\partial \phi}{\partial z} - \frac{\sigma}{n} \frac{\partial p}{\partial z}, \quad (9)$$

$$\frac{\partial p}{\partial t} + u \frac{\partial p}{\partial x} + v \frac{\partial p}{\partial y} + w \frac{\partial p}{\partial z} + 3p \left(\frac{\partial u}{\partial x} + \frac{\partial v}{\partial y} + \frac{\partial w}{\partial z} \right) = 0, \quad (10)$$

$$\frac{\partial^2 \phi}{\partial x^2} + \frac{\partial^2 \phi}{\partial y^2} + \frac{\partial^2 \phi}{\partial z^2} = 1 - n + a_1 \phi + a_2 \phi^2 + a_3 \phi^3 + \dots, \quad (11)$$

with the coefficients a_1, a_2, a_3, \dots appear in the last equation are expressed by

$$a_1 = \frac{(1 - \mu)(1 + q)}{2}, \quad a_2 = \frac{a_1(3 - q)}{4}, \quad a_3 = \frac{a_2(5 - 3q)}{6} \quad (12)$$

In the above equations $\vec{V} = (u, v, w)$, where u, v , and w are the ion fluid velocities along x, y and z axes. We have defined $\Omega = \frac{\omega_{ci}}{\omega_{pi}}$, in which $\omega_{ci} = \frac{ez_i B_0}{m}$ is ion gyrofrequency, $\sigma = \frac{T_i}{z_i T_e}$ is ion-to-electron temperature ratio and $\mu = \frac{z_d n_{d0}}{z_i n_{i0}} < 1$ is dust-to-ion number density ratio.

3. THE KDV EQUATION AND SMALL AMPLITUDE WAVES

3.1. Derivation Of KdV Equation:

To investigate the dynamics of propagating DIA waves of small amplitude, the reductive perturbation method is applied to the equations (6)-(11) to derive nonlinear KdV equation for the present plasma model. For this, the independent space variables (x, y, z, t) are stretched to (ξ, τ) by

$$\xi = \epsilon^{1/2}(l_x x + l_y y + l_z z - U_p t), \quad \tau = \epsilon^{3/2} t. \quad (13)$$

Where ϵ ($0 < \epsilon \ll 1$) is a dimensionless expansion parameter, is represents the level of the perturbation, U_p is the phase velocity of the waves, and l_x, l_y and l_z are the direction cosines of the wave vector \vec{k} along the x, y and z axes respectively so that $l_x^2 + l_y^2 + l_z^2 = 1$. We now write all the dependent variables in the power series of ϵ about their equilibrium state as

$$\left. \begin{aligned} n &= 1 + \epsilon n_1 + \epsilon^2 n_2 + \epsilon^3 n_3 + \dots, \\ p &= 1 + \epsilon p_1 + \epsilon^2 p_2 + \epsilon^3 p_3 + \dots, \\ u &= \epsilon^{3/2} u_1 + \epsilon^2 u_2 + \epsilon^{5/2} u_3 + \dots, \\ v &= \epsilon^{3/2} v_1 + \epsilon^2 v_2 + \epsilon^{5/2} v_3 + \dots, \\ w &= \epsilon w_1 + \epsilon^2 w_2 + \epsilon^3 w_3 + \dots, \\ \phi &= \epsilon \phi_1 + \epsilon^2 \phi_2 + \epsilon^3 \phi_3 + \dots, \end{aligned} \right\} \quad (14)$$

As a result of drift $\vec{E} \times \vec{B}$ in a magnetized plasma causes u_1 and v_1 to be smaller [37]. Now, on substituting the transformations (13) and the expansions (14) into the equations (6)-(11) and then equating the lowest order terms of ϵ , we get the first order perturbed quantities as

$$-U_p \frac{\partial n_1}{\partial \xi} + l_z \frac{\partial w_1}{\partial \xi} = 0, \quad (15)$$

$$l_x \frac{\partial \phi_1}{\partial \xi} + \sigma l_x \frac{\partial p_1}{\partial \xi} - \Omega v_1 = 0, \quad (16)$$

$$l_y \frac{\partial \phi_1}{\partial \xi} + \sigma l_y \frac{\partial p_1}{\partial \xi} + \Omega u_1 = 0, \quad (17)$$

$$-U_p \frac{\partial w_1}{\partial \xi} + l_z \frac{\partial \phi_1}{\partial \xi} + \sigma l_z \frac{\partial p_1}{\partial \xi} = 0, \quad (18)$$

$$-U_p \frac{\partial p_1}{\partial \xi} + 3l_z \frac{\partial w_1}{\partial \xi} = 0, \quad (19)$$

$$n_1 - a_1 \phi_1 = 0. \quad (20)$$

Integrating (15),(18) and (19) by using the boundary conditions: $n_1 = p_1 = w_1 = 0$ and $\phi_1 = 0$ as $|\xi| \rightarrow \infty$, and then we express above first-order quantities as a function of ϕ_1 , namely

$$\left. \begin{aligned} n_1 &= \frac{l_z}{U_p} w_1 = a_1 \phi_1, \\ u_1 &= -\frac{l_y}{\Omega} (1 + 3\sigma a_1) \frac{\partial \phi_1}{\partial \xi}, \\ v_1 &= \frac{l_x}{\Omega} (1 + 3\sigma a_1) \frac{\partial \phi_1}{\partial \xi}, \\ w_1 &= -\frac{l_z}{U_p} (1 + 3\sigma a_1) \phi_1, \\ p_1 &= 3n_1 = \frac{3l_z}{U_p} w_1 = 3a_1 \phi_1. \end{aligned} \right\} \quad (21)$$

Moreover, the expression for phase velocity can be obtained as

$$U_p = l_z \sqrt{\frac{1}{a_1} + 3\sigma}. \quad (22)$$

From expression (22), the phase velocity U_p of DIA waves depends on ions and electrons temperature by σ , the dust and ion number density by μ , nonextensive parameter q and the direction cosine $l_z = \cos \theta$, where θ is the obliqueness angle between \vec{B} and the wave vector \vec{k} .

In Figure[1a], we showed the variation of phase velocity U_p versus nonextensive parameter q with varying obliqueness angle θ , while the variation of U_p versus dust-to-ion number density ratio μ with varying ion-to-electron temperature ratio σ as depicted in Figure[1b]. Where we found that the phase velocity of propagating DIA waves drops (Figure[1a]) with the increasing of q and also with the increasing of θ . That means the phase velocity is advanced for the parallel propagating and more superthermal electrons than the obliquely propagating and large low-speed electrons. On the other hand, the phase velocity grows (Figure[1b]) with the increasing of μ as well as σ . That is the the phase velocity is higher for the increase in ion temperature and more populated negative dust particles than the increase in electron temperature and less populated negative dust particles.

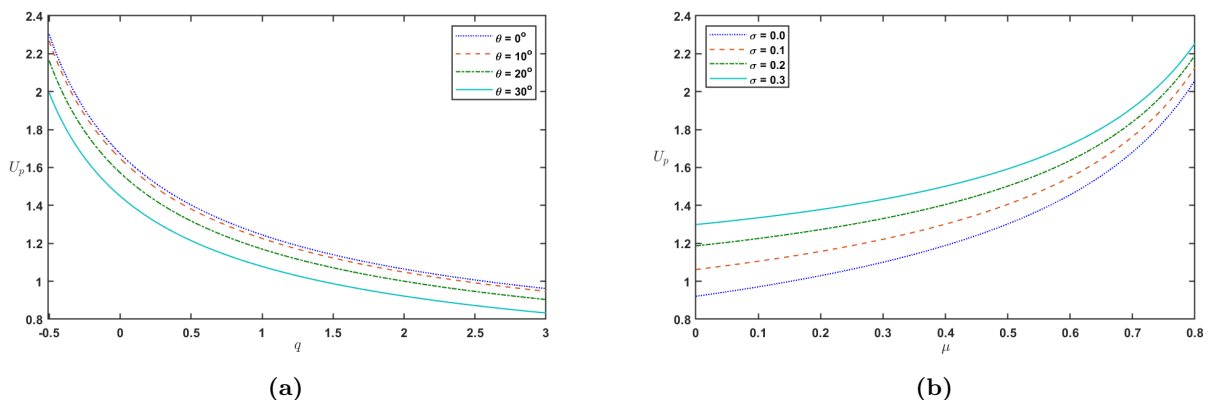


Figure 1. The variation of phase velocity U_p (a) versus nonextensive parameter q with varying obliqueness angle θ , with fixed ion-to-electron temperature $\sigma = 0.1$ and dust-to-ion number density $\mu = 0.2$; and (b) versus μ with varying σ and fixed $\theta = 15^\circ$, $q = 1.2$.

Now, for the second-order perturbed quantities, we equate the coefficients of next higher order terms in ϵ from the equations (6)-(11), we obtain the following equations

$$-U_p \frac{\partial n_2}{\partial \xi} + \frac{\partial n_1}{\partial \tau} + l_x \frac{\partial u_2}{\partial \xi} + l_y \frac{\partial v_2}{\partial \xi} + l_z \frac{\partial w_2}{\partial \xi} + l_z \frac{\partial (n_1 w_1)}{\partial \xi} = 0, \quad (23)$$

$$-U_p \frac{\partial u_1}{\partial \xi} - \Omega v_2 = 0 \implies v_2 = -\frac{U_p}{\Omega} \frac{\partial u_1}{\partial \xi}, \tag{24}$$

$$-U_p \frac{\partial v_1}{\partial \xi} + \Omega u_2 = 0 \implies u_2 = \frac{U_p}{\Omega} \frac{\partial v_1}{\partial \xi}, \tag{25}$$

$$-U_p \frac{\partial w_2}{\partial \xi} - U_p n_1 \frac{\partial w_1}{\partial \xi} + \frac{\partial w_1}{\partial \tau} + w_1 l_z \frac{\partial w_1}{\partial \xi} + l_z \frac{\partial \phi_2}{\partial \xi} + n_1 l_z \frac{\partial \phi_1}{\partial \xi} + \sigma l_z \frac{\partial p_2}{\partial \xi} = 0, \tag{26}$$

$$-U_p \frac{\partial p_2}{\partial \xi} + \frac{\partial p_1}{\partial \tau} + l_z w_1 \frac{\partial p_1}{\partial \xi} + 3l_x \frac{\partial u_2}{\partial \xi} + 3l_y \frac{\partial v_2}{\partial \xi} + 3l_z \frac{\partial w_2}{\partial \xi} + l_z p_1 \frac{\partial w_1}{\partial \xi} = 0, \tag{27}$$

$$-\frac{\partial^2 \phi_1}{\partial \xi^2} - n_2 + a_1 \phi_2 + a_2 \phi_1^2 = 0 \implies n_2 = a_1 \phi_2 + a_2 \phi_1^2 - \frac{\partial^2 \phi_1}{\partial \xi^2}. \tag{28}$$

Eliminating w_2 and p_2 from (23), (26) and (27) and then putting the values of v_2 , u_2 and n_2 from (24), (25) and (28) and using the values of first-order quantities from (21), the KdV equation is obtained as

$$\frac{\partial \varphi}{\partial \tau} + \mathcal{A} \varphi \frac{\partial \varphi}{\partial \xi} + \mathcal{B} \frac{\partial^3 \varphi}{\partial \xi^3} = 0. \tag{29}$$

with $\phi_1 = \varphi$ and the the nonlinear coefficient \mathcal{A} and dispersion coefficient \mathcal{B} are given by

$$\mathcal{A} = \frac{1}{2a_1 U_p} \left\{ 4a_1^2 U_p^2 - a_1 l_z^2 - 2l_z^2 \left(\frac{a_2}{a_1} \right) \right\}, \tag{30}$$

$$\mathcal{B} = \frac{1}{2a_1 U_p} \left\{ \frac{l_z^2}{a_1} + (1 - l_z^2) \frac{a_1 U_p^4}{l_z^2 \Omega^2} \right\}. \tag{31}$$

The nonlinear term \mathcal{A} (causing wave steepening) and the dispersion term \mathcal{B} (causing wave broadening) are crucial factors not only for the structure of the propagation of DIA solitary waves but also for specifying the soliton's characteristics. So it is important to analysed on the the parametric dependence of these two terms

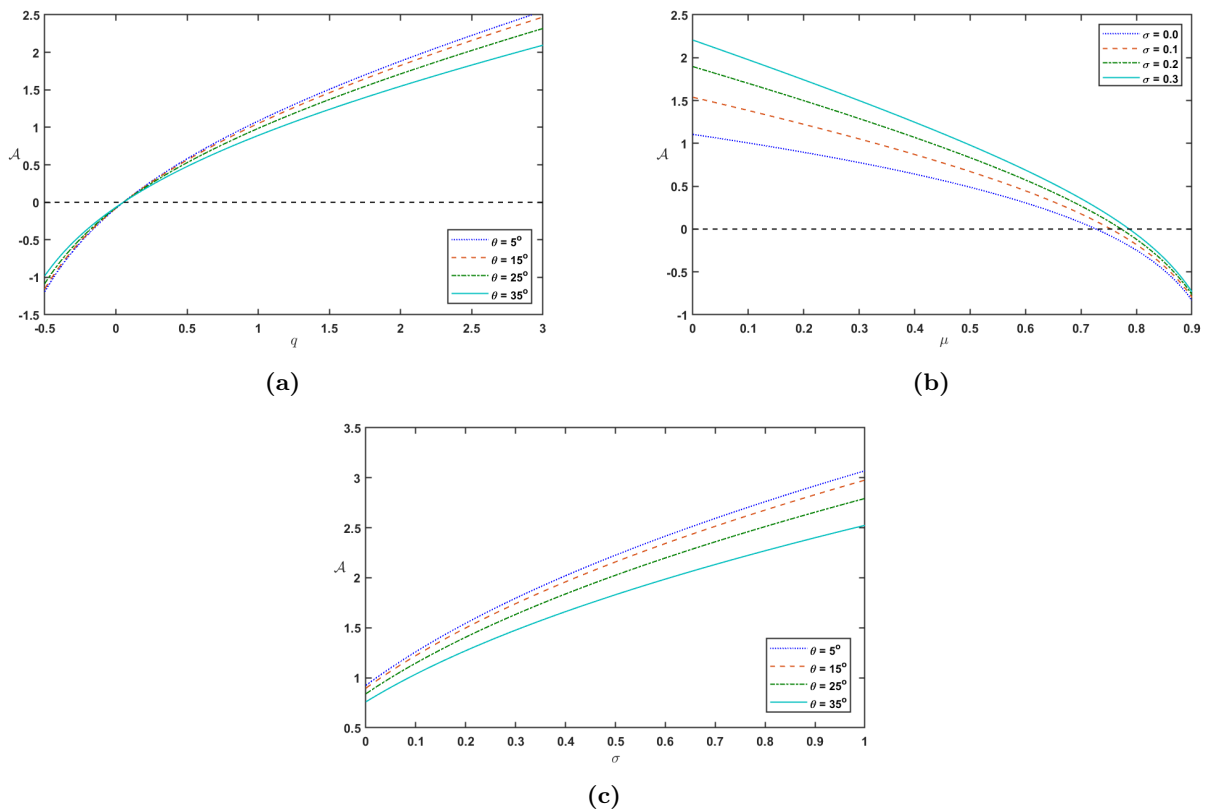


Figure 2. The variation of nonlinear term \mathcal{A} (a) versus nonextensive parameter q with varying obliqueness angle θ , with fixed ion-to-electron temperature $\sigma = 0.1$ and dust-to-ion number density $\mu = 0.2$; (b) versus μ with varying σ and fixed $\theta = 15^\circ$, $q = 1.2$; and (c) versus σ with varying θ and fixed $\mu = 0.2$, $q = 1.2$.

in our considered plasma system. From expressions (30) and (31), both \mathcal{A} and \mathcal{B} are the functions obliqueness

angle θ , nonextensive parameter q , ion-to-electron temperature ratio σ and dust-to-ion number density ratio μ . Besides, the dispersion term \mathcal{B} is also a function of external magnetic field strength B_0 through Ω but the nonlinearity is unaffected at all. Interestingly, we can see that both \mathcal{A} and \mathcal{B} become zero for limiting $\theta \rightarrow 90^\circ$, in this case the propagating DIA solitons does not exist, that is the waves are electrostatic is abolished for the larger values of θ , and they should instead be electromagnetic in nature [38]. Again, the influences of the external magnetic field disappears for $\theta = 0^\circ$, in this case the terms \mathcal{A} and \mathcal{B} become to the condition for unmagnetized plasma system. Thus, we have consider small value for obliqueness angle θ ($0 < \theta < 55^\circ$) in this investigation. It is seen from the expression(31) that the dispersion \mathcal{B} acquires only positive values in varying different physical parameters under consideration and it increases with θ , σ and μ and decreases with q and Ω (figures not shown here). In order to inspect the parametric effects on the nonlinear term \mathcal{A} , we have plotted the variation of \mathcal{A} versus nonextensive parameter q with varying obliqueness angle θ ; \mathcal{A} versus dust-to-ion number density ratio μ with varying ion-to-electron temperature ratio σ and \mathcal{A} versus σ with varying θ in Figure[2]. Where, we find that the nonlinearity increases with the increase of q and also increase of σ , while it decreases with the increase of μ and also increase of θ . Form first two panels of Figure[2], we have found that the nonlinear term \mathcal{A} changes its sign from positive to negative or vice versa and it become zero for a critical composite value of nonextensive parameter (say q_c) for a fixed value of μ , or a critical composite value of dust-to-ion number density ratio (say μ_c), for a fixed value of q . That means the KdV soliton can changed its types from compressive to rarefactive or vice versa in the considered plasma system. Now, by solving the equation $A(q, \sigma, \mu, l_z) = 0$ for μ and q separately, both q_c and μ_c are found as

$$q_c = \frac{-[3(1-\mu)\{4\sigma(1-\mu)+1\}+1]}{12\sigma(1-\mu)^2} \pm \frac{\sqrt{[3(1-\mu)\{4\sigma(1-\mu)+1\}+1]^2 - 24\sigma(1-\mu)^2 [3(1-\mu)\{2\sigma(1-\mu)+1\} - 3]}}{12\sigma(1-\mu)^2}, \quad (32)$$

$$\mu_c = \frac{3\{4\sigma(1+q)+1\}}{12\sigma(1+q)} \pm \frac{\sqrt{9\{4\sigma(1+q)+1\}^2 - 24\sigma\{6\sigma(1+q)^2 + 4q\}}}{12\sigma(1+q)}, \quad (33)$$

Since these critical values are identifies the polarity of DIA solitary waves, so it is important to analysed them. From expressions (32) and (33), we seen that q_c (μ_c) is a explicit function of σ and μ (q), and both q_c and μ_c are undefined when $\sigma = 0$. For $-1 < q < q_c$ (or $1 > \mu > \mu_c$) with fixed μ (or q), $\mathcal{A} < 0$; And for $q > q_c$ (or $0 \leq \mu < \mu_c$) with fixed μ (or q), $\mathcal{A} > 0$. The variation of q_c versus μ and μ_c versus q with different values of σ are shown in Figure[3], and we found that the value of q_c (μ_c) increases with μ (q). We have also predicted the value of q_c is reduced while μ_c is raised as the increase ion-to-electron temperature ratio σ in our considered plasma system.

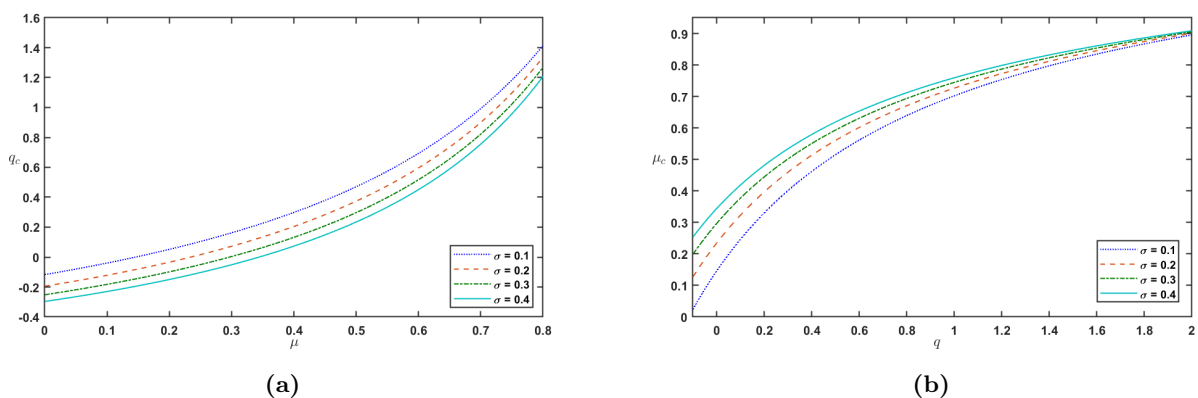


Figure 3. The variation of critical value (a) q_c versus μ and (b) μ_c versus q with varying $\sigma > 0$

3.2. Solitary Wave Solution

To obtain the stationary wave solutions of the KdV equation (29), we introduce a new transformation variable $\chi = \xi - \nu\tau$, where ν is the travelling wave velocity in the linear χ - space. Then, the KdV equation (29) becomes the ordinary differential equation,

$$-\nu \frac{d\varphi}{d\chi} + \mathcal{A}\varphi \frac{d\varphi}{d\chi} + \mathcal{B} \frac{d^3\varphi}{d\chi^3} = 0 \quad (34)$$

This equation is known the reduced KdV equation and its well-known solution (*i.e.*, solitary wave solution) is given by

$$\varphi = \varphi_m \operatorname{sech}^2\left(\frac{\chi}{\delta}\right) \quad (35)$$

where $\varphi_m = \frac{3\nu}{\mathcal{A}}$ and $\delta = \sqrt{\frac{4\mathcal{B}}{\nu}}$, represents the peak amplitude and the width of the pulse of solitary waves respectively and here both ν and \mathcal{B} are positive values.

Now, integrating twice equation(32) over χ , and using the boundary conditions: $\varphi = \frac{d\varphi}{d\chi} = \frac{d^2\varphi}{d\chi^2} = 0$ as $|\chi| \rightarrow \infty$, we have

$$\frac{1}{2} \left(\frac{d\varphi}{d\chi} \right)^2 + P(\varphi) = E_c \quad (36)$$

This is the form of law of conservation of energy, in which E_c is the integration constant and is acted as the entire energy of the system. The term $\frac{1}{2}(d\varphi/d\chi)^2$ is presumed as kinetic energy while $P(\psi)$ indicates the potential energy that is defined as

$$P(\varphi) = \left[\frac{\mathcal{A}}{6\mathcal{B}} \right] \varphi^3 - \left[\frac{\nu}{2\mathcal{B}} \right] \varphi^2 \quad (37)$$

The properties of this potential as **(i)** $P(\varphi) = P'(\varphi) = 0$ and $P''(\varphi) < 0$, for $\varphi = 0$; **(ii)** $P(\varphi) = 0$, $P'(\varphi) \neq 0$, for $\varphi = \varphi_m$ and $P(\varphi) < 0$ in between 0 and φ_m . That is the potential $P(\varphi)$ has double roots, one root is $\psi = 0$, at which $P(\psi)$ reaches its highest value value also and other root is $\varphi = \varphi_m$. Thus, we can also analysed the dynamical characteristics of DIA solitary waves in the considered magnetized plasma system through the amplitude potential $P(\varphi)$ for different core plasma parameters under consideration.

3.3. Numerical Discussions for Parametric effects

In order to discuss the parametric effects on the dynamical characteristics of DIA solitons for small amplitude limit by plotting both the solitary wave profile $\varphi(\chi)$ given in equation (35) against the linear parameter χ and the amplitude potential $P(\varphi)$ given in equation (37) against the electrostatic potential φ are as depicted in Figures[4-9]. It is important to notice one thing that, where the curve of the potential $V(\varphi)$ crosses the φ -axis from below at some point of φ , from that point we predicted the soliton's amplitude φ_m .

In Figures[4a-4b], we showed the variation of $\varphi(\chi)$ versus χ and the variation of $P(\varphi)$ versus φ with different values of travelling wave velocity ν for fixed other parameters, where we observed only one type of solitons *i.e.*, compressive solitons propagates and the amplitude of the pulse of compressive DIA soliton increase while width decrease with the increases in ν . In Figures[5a-5b], we showed the variation of $\varphi(\chi)$ versus χ and also $P(\varphi)$ versus φ with different values of obliqueness angle θ and fixed other parameters, where we found that the propagating DIA soliton is compressive and both the amplitude and width of the compressive solitary pulse to increase with obliqueness angle θ . For the wave propagates along the external magnetic field (*i.e.*, $\theta = 0^\circ$), the values of the amplitude and width gets smaller and as θ increases, both the amplitude and width increases. That means, we predicts that the energy of the propagating DIA soliton is directly influenced by the obliqueness propagating angle. Likewise, the variation of $\varphi(\chi)$ versus χ and also $P(\varphi)$ versus φ with different values of ion-to-electron temperature ratio σ and fixed other parameters are shown in Figures[6a-6b], where we observed the compressive DIA soliton and its amplitude of the solitary pulse is seen to decrease, while width to increase as the value of σ gets higher. That is, in the considered plasma system by increasing (decreasing) the temperature of ion (electron) species with keeping the electron (ion) temperature fixed, will typically change the geometrical structure of the propagating DIA soliton.

In Figures[7a-7b], we showed the variation of $\varphi(\chi)$ versus χ and also the variation of $P(\varphi)$ versus φ with different values of parameters q and fixed other parameters: $\theta = 15^\circ$, $\sigma = 0.1$, $\mu = 0.2$, $\Omega = 0.3$ and $\nu = 0.02$, where we found that the soliton type transformed from rarefactive (negative potential) to compressive (positive potential), which is obvious from our results that the sign of nonlinearity \mathcal{A} changes from negative to positive for varying q . It is observed that both amplitude and width of the rarefactive DIA solitary pulse to increase as the value of q increases in between -1 and q_c , whereas both amplitude and width of the compressive DIA solitary pulse to decrease as the value of $q > q_c$. For the chosen parametric values, we obtain $q_c = 0.0516$. Thus, it is predicting that the electron nonextensivity makes a noticeable impact on the dynamics of DIA soliton in the present plasma system. An analogous result is obtained due to the variation of dust-to-ion number density ratio μ with fixed other parameters: $\theta = 15^\circ$, $\sigma = 0.1$, $q = 1.2$, $\Omega = 0.3$ and $\nu = 0.02$, as shown in the Figures[8a-8b]. That is, the propagating DIA solitons can transits from compressive to rarefactive with varying μ . Both the amplitude and width of the compressive DIA solitary pulse are seen to increases for the increase of μ in between 0 and μ_c ; while the amplitude and width of the rarefactive DIA solitary pulse are seen to decreases for the increase of $\mu > \mu_c$, in which $\mu_c = 0.7539$. That is, increasing the population of negatively charged dust grains with fixing the ion number density in our considered plasma system can leads to the transformation of soliton type from compressive to rarefactive. Lastly, in Figures[9a-9b], we showed the variation of $\varphi(\chi)$ versus

χ and also the variation of $P(\varphi)$ versus φ with different values of external magnetic field strength B_0 by Ω and fixed other parameters, where we have found that the propagating DIA soliton is compressive and the width of the solitary pulse is to reduces, while the amplitude is seen to remain constant as the value of Ω get increased. Hence, the amplitude of DIA solitons is unaffected by the external magnetic field B_0 , but their width is significantly affected.

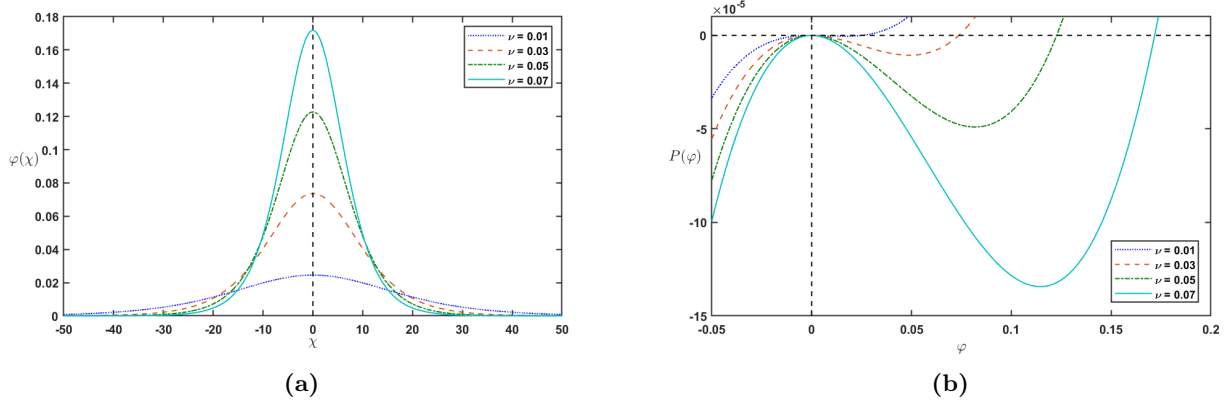


Figure 4. The variation of (a) solitary wave profile $\varphi(\chi)$ versus χ , and (b) small amplitude potential $P(\varphi)$ versus φ with varying ν . where $\theta = 15^\circ$, $\sigma = 0.1$, $q = 1.2$, $\mu = 0.2$ and $\Omega = 0.3$.

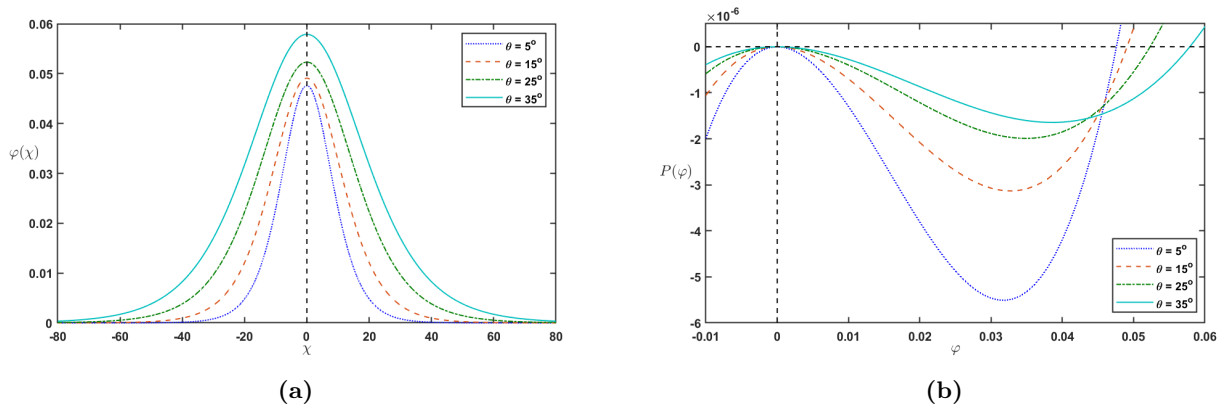


Figure 5. The variation of (a) solitary wave profile $\varphi(\chi)$ versus χ , and (b) small amplitude potential $P(\varphi)$ versus φ with varying θ . where $\sigma = 0.1$, $q = 1.2$, $\mu = 0.2$, $\Omega = 0.3$ and $\nu = 0.02$.

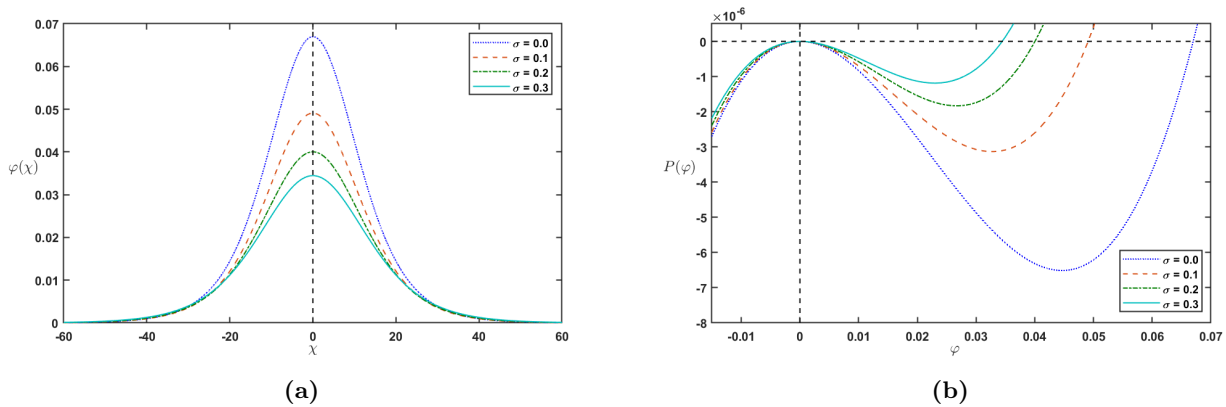


Figure 6. The variation of (a) solitary wave profile $\varphi(\chi)$ versus χ , and (b) small amplitude potential $P(\varphi)$ versus φ with varying σ . where $\theta = 15^\circ$, $q = 1.2$, $\mu = 0.2$, $\Omega = 0.3$ and $\nu = 0.02$.

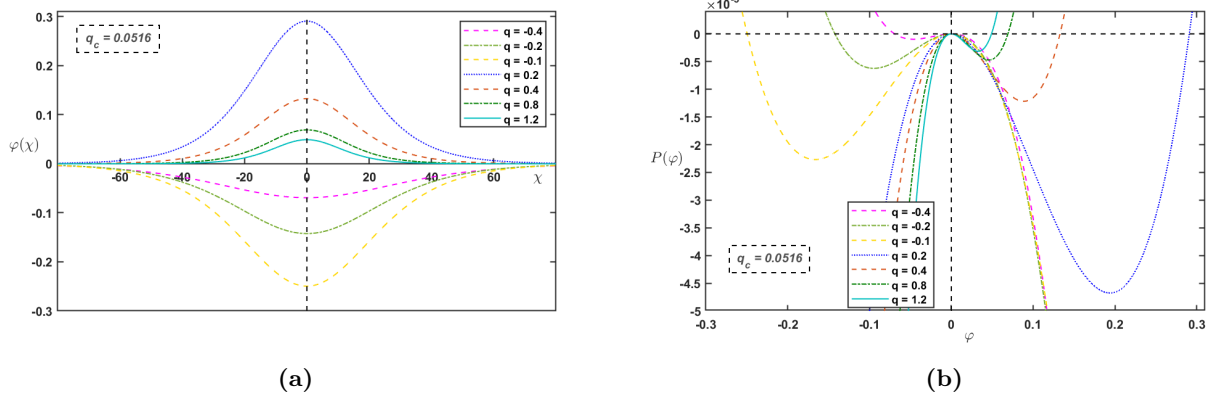


Figure 7. The variation of (a) solitary wave profile $\varphi(\chi)$ versus χ , and (b) small amplitude potential $P(\varphi)$ versus φ with varying q . where $\theta = 15^\circ$, $\sigma = 0.1$, $\mu = 0.2$, $\Omega = 0.3$ and $\nu = 0.02$.

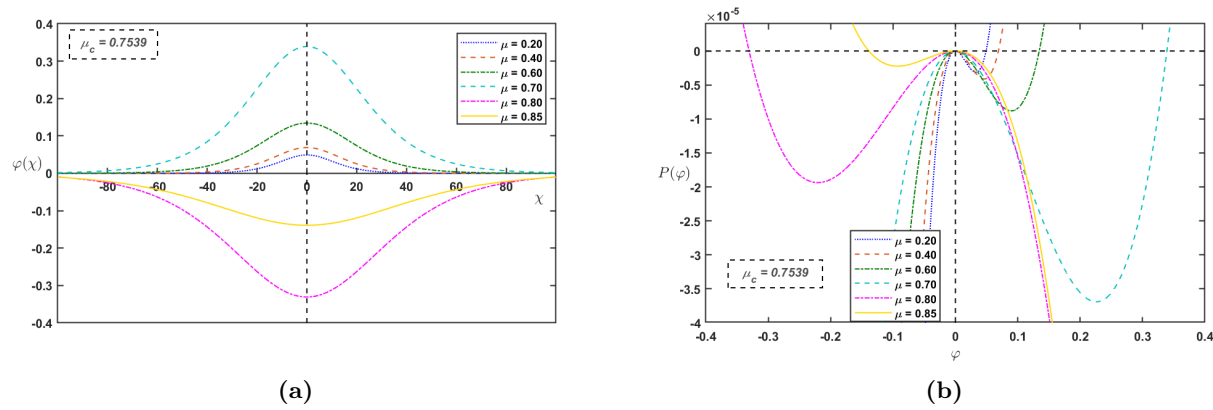


Figure 8. The variation of (a) solitary wave profile $\varphi(\chi)$ versus χ , and (b) small amplitude potential $P(\varphi)$ versus φ with varying μ . where $\theta = 15^\circ$, $\sigma = 0.1$, $q = 1.2$, $\Omega = 0.3$ and $\nu = 0.02$.

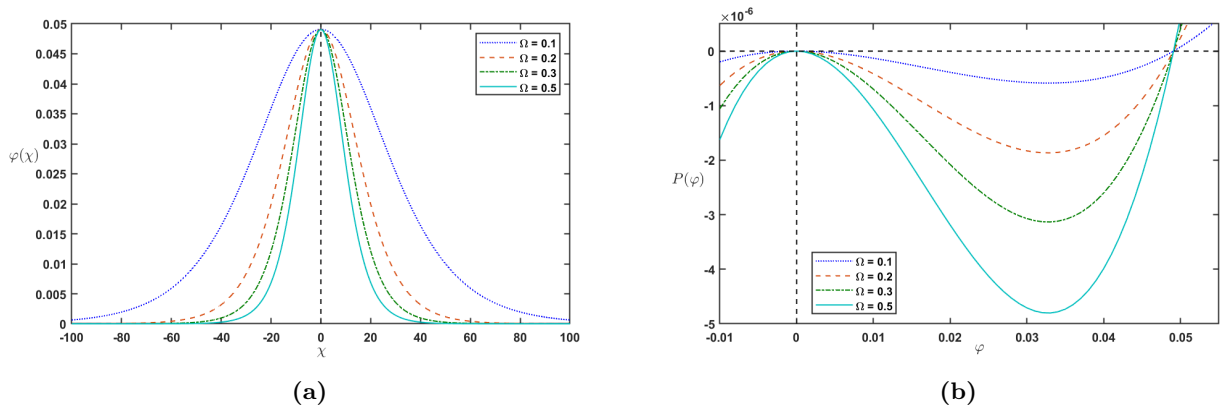


Figure 9. The variation of (a) solitary wave profile $\varphi(\chi)$ versus χ , and (b) small amplitude potential $P(\varphi)$ versus φ with varying Ω . where $\theta = 15^\circ$, $\sigma = 0.1$, $q = 1.2$, $\mu = 0.2$ and $\nu = 0.02$.

From the observation mentioned above, it has been evidently noted that the propagating DIA soliton represented by KdV equation (29) is shifts from a positive potential to a negative potential as a result of changes in electron nonextensivity q and dust and ion number density via μ in the considered plasma system. The amplitude of the soliton becomes infinite nearly at either $q = q_c$ or $\mu = \mu_c$, for which $\mathcal{A} = 0$. In this context, the KdV equation (29) fails to described the model. In order to explore dynamics of DIA solitary waves in this critical scenario, we must considered the evolution equation having second higher order nonlinearity as modified KdV equation and will be described in the next following section.

4. THE MKDV EQUATION AND SMALL AMPLITUDE WAVES

4.1. Derivation Of mKdV Equation

To study the solitary waves at the critical number density region μ_c , we derive the modified kdV (mKdV) equation, for small but finite amplitude DIA solitary waves. For this, we again use the reductive perturbation method and introduce a modified stretching of independent variables as

$$\xi = \epsilon(l_x x + l_y y + l_z z - U_p t), \quad \tau = \epsilon^3 t \quad (38)$$

For this approach, we use the following dependent variables in the power series of ϵ as

$$\left. \begin{aligned} n &= 1 + \epsilon n_1 + \epsilon^2 n_2 + \epsilon^3 n_3 + \dots \\ p &= 1 + \epsilon p_1 + \epsilon^2 p_2 + \epsilon^3 p_3 + \dots \\ u &= \epsilon^2 u_1 + \epsilon^3 u_2 + \epsilon^4 u_3 + \dots \\ v &= \epsilon^2 v_1 + \epsilon^3 v_2 + \epsilon^4 v_3 + \dots \\ w &= \epsilon w_1 + \epsilon^2 w_2 + \epsilon^3 w_3 + \dots \\ \phi &= \epsilon \phi_1 + \epsilon^2 \phi_2 + \epsilon^3 \phi_3 + \dots \end{aligned} \right\} \quad (39)$$

Now, using (38) and (39) into the equations (6)-(9) and equating the coefficients of smallest order of ϵ (i.e., ϵ^2 from (6)-(8) and ϵ from (9)), we obtain the first order terms which are same as (21)-(22) given in Subsection[3.1]. For second order terms of ϵ , we equate the coefficients of ϵ^3 from (6)-(8) and ϵ^2 from (9) and we obtain

$$-U_p \frac{\partial n_2}{\partial \xi} + l_x \frac{\partial u_1}{\partial \xi} + l_y \frac{\partial v_1}{\partial \xi} + l_z \frac{\partial w_2}{\partial \xi} + l_z n_1 \frac{\partial w_1}{\partial \xi} + l_z w_1 \frac{\partial n_1}{\partial \xi} = 0 \quad (40)$$

$$-U_p \frac{\partial u_1}{\partial \xi} + l_x \frac{\partial \phi_2}{\partial \xi} + l_x n_1 \frac{\partial \phi_1}{\partial \xi} + \sigma l_x \frac{\partial p_2}{\partial \xi} - \Omega(v_2 + n_1 v_1) = 0 \quad (41)$$

$$-U_p \frac{\partial v_1}{\partial \xi} + l_y \frac{\partial \phi_2}{\partial \xi} + l_y n_1 \frac{\partial \phi_1}{\partial \xi} + \sigma l_y \frac{\partial p_2}{\partial \xi} + \Omega(u_2 + n_1 u_1) = 0 \quad (42)$$

$$-U_p \frac{\partial w_2}{\partial \xi} - U_p n_1 \frac{\partial w_1}{\partial \xi} + l_z w_1 \frac{\partial w_1}{\partial \xi} + l_z \frac{\partial \phi_2}{\partial \xi} + l_z n_1 \frac{\partial \phi_1}{\partial \xi} + \sigma l_z \frac{\partial p_2}{\partial \xi} = 0 \quad (43)$$

$$-U_p \frac{\partial p_2}{\partial \xi} + 3l_x \frac{\partial u_1}{\partial \xi} + 3l_y \frac{\partial v_1}{\partial \xi} + 3l_z \frac{\partial w_2}{\partial \xi} + 3l_z p_1 \frac{\partial w_1}{\partial \xi} + l_z w_1 \frac{\partial p_1}{\partial \xi} = 0 \quad (44)$$

$$n_2 - a_2 \phi_2 - a_1 \phi_1^2 = 0 \quad (45)$$

Integrating (40),(43) and (44) by using the boundary conditions $n_1 = n_2 = p_1 = p_2 = w_1 = w_2 = u_1 = v_1 = 0$ as $|\xi| \rightarrow \infty$ and then using the first-order quantities from (21), we write the second-order quantities in terms of ϕ 's, we get

$$\left. \begin{aligned} n_2 &= a_2 \phi_2 + a_1 \phi_1^2 \\ u_2 &= \frac{U_p l_x}{\Omega^2} (1 + 3\sigma a_1) \frac{\partial^2 \phi_1}{\partial \xi^2} - \frac{l_y}{\Omega} \left\{ (1 + 3\sigma a_1) \frac{\partial \phi_2}{\partial \xi} + 3\sigma (a_1 + 2a_2) \phi_1 \frac{\partial \phi_1}{\partial \xi} \right\} \\ v_2 &= \frac{U_p l_y}{\Omega^2} (1 + 3\sigma a_1) \frac{\partial^2 \phi_1}{\partial \xi^2} + \frac{l_x}{\Omega} \left\{ (1 + 3\sigma a_1) \frac{\partial \phi_2}{\partial \xi} + 3\sigma (a_1 + 2a_2) \phi_1 \frac{\partial \phi_1}{\partial \xi} \right\} \\ w_2 &= \frac{l_z}{U_p} \left\{ (1 + 3\sigma a_1) \phi_2 + \left(\frac{a_1}{2} + 3\sigma (a_2 + a_1^2) \right) \phi_1^2 \right\} \\ p_2 &= 3n_2 + 3n_1^2 = 3a_1 \phi_2 + 3(a_2 + a_1^2) \phi_1^2 \end{aligned} \right\} \quad (46)$$

Similarly, for third order terms of ϵ , we equate the coefficients ϵ^4 from (6) and (8) and ϵ^3 from (9), we obtain

$$-U_p \frac{\partial n_3}{\partial \xi} + \frac{\partial n_1}{\partial \tau} + l_x \frac{\partial (u_2 + n_1 u_1)}{\partial \xi} + l_y \frac{\partial (v_2 + n_1 v_1)}{\partial \xi} + l_z \frac{\partial (n_1 w_2 + n_2 w_1)}{\partial \xi} + l_z \frac{\partial w_3}{\partial \xi} = 0 \quad (47)$$

$$-U_p \frac{\partial u_2}{\partial \xi} - U_p n_1 \frac{\partial u_1}{\partial \xi} + l_x \frac{\partial \phi_3}{\partial \xi} + l_x n_1 \frac{\partial \phi_2}{\partial \xi} + l_x n_2 \frac{\partial \phi_1}{\partial \xi} + \sigma l_x \frac{\partial p_3}{\partial \xi} + l_z w_1 \frac{\partial u_1}{\partial \xi} - \Omega(v_3 + n_1 v_2 + n_2 v_1) = 0 \quad (48)$$

$$-U_p \frac{\partial v_2}{\partial \xi} - U_p n_1 \frac{\partial v_1}{\partial \xi} + l_y \frac{\partial \phi_3}{\partial \xi} + l_y n_1 \frac{\partial \phi_2}{\partial \xi} + l_y n_2 \frac{\partial \phi_1}{\partial \xi} + \sigma l_y \frac{\partial p_3}{\partial \xi} + l_z w_1 \frac{\partial v_1}{\partial \xi} + \Omega(u_3 + n_1 u_2 + n_2 u_1) = 0 \quad (49)$$

$$-U_p \frac{\partial w_3}{\partial \xi} - U_p n_1 \frac{\partial w_2}{\partial \xi} - U_p n_2 \frac{\partial w_1}{\partial \xi} + l_z \frac{\partial \phi_3}{\partial \xi} + l_z n_1 \frac{\partial \phi_2}{\partial \xi} + l_z n_2 \frac{\partial \phi_1}{\partial \xi} + \sigma \frac{\partial p_3}{\partial \xi} + \frac{\partial w_1}{\partial \tau} + l_x u_1 \frac{\partial w_1}{\partial \xi} + l_y v_1 \frac{\partial w_1}{\partial \xi} + l_z w_1 n_1 \frac{\partial w_1}{\partial \xi} + l_z \frac{\partial(w_1 w_2)}{\partial \xi} = 0 \quad (50)$$

$$-U_p \frac{\partial p_3}{\partial \xi} + l_x u_1 \frac{\partial p_1}{\partial \xi} + l_y v_1 \frac{\partial p_1}{\partial \xi} + l_z w_1 \frac{\partial p_2}{\partial \xi} + +3l_x \frac{\partial u_2}{\partial \xi} + 3l_y \frac{\partial v_2}{\partial \xi} + 3l_z \frac{\partial w_3}{\partial \xi} + \frac{\partial p_1}{\partial \tau} + 3l_x p_1 \frac{\partial u_1}{\partial \xi} + 3l_y p_1 \frac{\partial v_1}{\partial \xi} + 3l_z p_1 \frac{\partial w_2}{\partial \xi} + l_z w_2 \frac{\partial p_1}{\partial \xi} + 3l_z p_2 \frac{\partial w_1}{\partial \xi} = 0 \quad (51)$$

$$- \frac{\partial^2 \phi_1}{\partial \xi^2} + a_1 \phi_3 + 2a_2 \phi_1 \phi_2 + a_3 \phi_1^3 - n_3 = 0 \quad (52)$$

Now, eliminating p_3 , w_3 and n_3 from equations (47), (49)-(52) and substituting the values of first and second order terms given in (21) and (46), and using the expression (22), we found a nonlinear equation of the form,

$$\frac{\partial \phi_1}{\partial \tau} + \mathcal{A}' \phi_1^2 \frac{\partial \phi_1}{\partial \xi} + B' \frac{\partial^3 \phi_1}{\partial \xi^3} + C' \frac{\partial(\phi_1 \phi_2)}{\partial \xi} = 0 \quad (53)$$

where the coefficient \mathcal{A}' is given by

$$\mathcal{A}' = \frac{1}{2a_1 U_p} \left[12a_1 a_2 U_p^2 - 13l_z^2 (a_1^2 + a_2) + 14a_1^3 U_p^2 + \frac{2a_1 l_z^4}{a_1 U_p^2} (a_1^2 + 2a_2) - 3l_z^2 \left(\frac{a_3}{a_1} \right) \right] \quad (54)$$

and the coefficients B' and C' are exactly same as that of \mathcal{B} and \mathcal{A} respectively given in (30) and (31) in the Subsection-3.1. But at the critical regime, *i.e.*, at $\mu = \mu_c$ or $q = q_c$, $\mathcal{A} = C' = 0$. Thus, if we consider $\mathcal{B} = B'$, and $\phi_1 = \psi$, equation (53) becomes the standard mKdV equation as

$$\frac{\partial \psi}{\partial \tau} + \mathcal{A}' \psi^2 \frac{\partial \psi}{\partial \xi} + \mathcal{B} \frac{\partial^3 \psi}{\partial \xi^3} = 0 \quad (55)$$

with the second order nonlinear coefficient \mathcal{A}' and the dispersion coefficient \mathcal{B} . From the definition of the expression (31), we have $\mathcal{B} > 0$ for all plasma parametric values. Therefore, here we analyse the the parametric dependence of the term \mathcal{A}' in our considered plasma system. For this, we showed the variation of \mathcal{A}' versus μ for varying σ at $q = q_c$ and also versus q for varying σ at $\mu = \mu_c$ in the Figures[10a-10b], where we observed that when $q = q_c$, the second order nonlinearity increases for an increase of μ and also an increase of σ ; moreover when $\mu = \mu_c$, the second order nonlinearity increases for an increase of q in between -1 and 1.7 and after $q \approx 1.7$ it gets decreases. Thus, in both the cases the value of \mathcal{A}' is seen to be positive.

4.2. Solitary Wave Solution

To obtain the stationary wave solution of (55), we use the same transformation given in Subsection-3.2. So, mKdV equation(55) is transformed into the reduced mKdV equation as

$$-\nu \frac{d\psi}{d\chi} + \mathcal{A}' \psi^2 \frac{d\psi}{d\chi} + \mathcal{B} \frac{d^3 \psi}{d\chi^3} = 0 \quad (56)$$

and we obtain two stationary solitary wave solution as

$$\psi = \pm \psi_m \operatorname{sech} \left(\frac{\chi}{\Delta} \right) \quad (57)$$

where $\psi_m = \sqrt{6\nu/\mathcal{A}'}$ and $\Delta = \sqrt{\mathcal{B}/\nu}$ are respectively the amplitude and width of solitary waves represented by the mKdV equation(55) and ν is the travelling wave velocity in the linear χ -space. And the positive and negative indicators are respectively associated to the compressive and rarefactive DIA soliton.

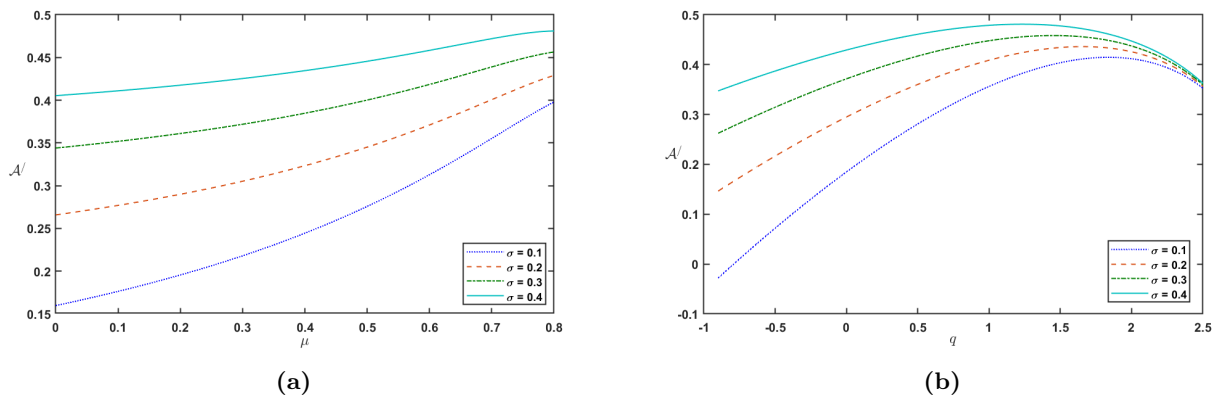


Figure 10. The variation of second order nonlinearity \mathcal{A}' (a) versus dust-to-ion number density μ when $q = q_c$ and (b) versus nonextensive parameter q when $\mu = \mu_c$, with varying σ and $\theta = 15^\circ$.

Integrating equation(56) twice with the boundary conditions: $\psi = \frac{d\psi}{d\chi} = \frac{d^2\psi}{d\chi^2} = 0$ as $|\chi| \rightarrow \infty$ and proceeding the same way as given in Subsection-3.2, we obtain the small amplitude potential energy equation as

$$P_m(\psi) = \left[\frac{\mathcal{A}'}{12\mathcal{B}} \right] \psi^4 - \left[\frac{\nu}{2\mathcal{B}} \right] \psi^2 \quad (58)$$

This potential has also the same characteristics that of the potential $P(\varphi)$ given in (37), *i.e.*, at $\psi = 0$, both its value and its first derivative vanish, while the second derivative is negative. This indicates that $P_m(\psi)$ has a maximum value and a root at origin. Also, $\psi = \psi_m$ is the other root of the potential $P_m(\psi)$, which is the amplitude of the mKdV solitons. In the region of the vanishing first order nonlinear term \mathcal{A} , two types of solitons compressive and rarefactive appear to coexist in the expressions (57) and (58).

4.3. Numerical Discussions for Parametric effects

We have analysed the parametric effects (mainly the effects of obliqueness angle θ , the ion-to-electron temperatures via σ , the electron nonextensive parameter q , dust-to-ion number density via μ and external magnetic field strength B_0 via Ω , at when q_c or μ_c) on the geometrical behaviour of DIA soliton represented by the mKdV equation (55) in the considered magnetized plasma system by plotting both the modified solitary wave profile $\psi(\chi)$ given in equation (57) against the linear parameter χ and the corresponding small amplitude potential $P_m(\psi)$ given in equation (58) against the electrostatic potential ψ .

In the Figure[11], we showed the variation of $\psi(\chi)$ versus χ and also $P_m(\psi)$ versus ψ with varying σ and μ in separate panels when $q = q_c$. And also we depicted the variation of $\psi(\chi)$ versus χ and also $P_m(\psi)$ versus ψ with varying σ and q separately in different panels in the Figure[12] when $\mu = \mu_c$. Where we find that in both the situations, the amplitude decreases while width increases of the pulse of compressive and rarefactive (DIA) modified solitons (as shown in Figures [11a-11b] & [12a-12b]) for an increase in ion temperature. The similar result is to visible with the variation of μ (or q) at fixed $q = q_c$ (or $\mu = \mu_c$), that is the amplitude reduces whereas the width raises of both the pulse of compressive and rarefactive (DIA) modified solitons with an increasing values of μ (or $q < 1.7$) as seen in Figures[11c-11d] (Figures[12c-12d]). However, in the case of the variation of electron nonextensivity q at the critical scenario μ_c , it is worth to noticed that the propagating modified DIA solitons show opposite characteristics for $q \geq 1.7$ in the considered plasma system, for which both the amplitude and width of the pulse compressive and rarefactive DIA solitons are seen to enhanced in this particular case (Figure is not included here). By this numerical examination, we can predict that the solitary waves in the critical region $q = q_c$ are to form more taller and wider than in the critical region $\mu = \mu_c$ for any other plasma parametric values.

5. RESULTS & CONCLUSIONS

In this manuscript, we have theoretically investigated the existence and propagation characteristics of DIA solitary waves in a magnetized plasma in presence of inertial ions, noninertial electrons which obey q -nonextensive velocity distribution and negative dust grains. The ion pressure as a variable is taken into consideration and the Poisson's equation is taken to making the plasma system self-consistent. The nonlinear KdV and modified KdV equations are derives by adopting reductive perturbation method that describes the existence of the small amplitude DIA waves in the considered system. The solution of these two equations and the corresponding small amplitude Sagdeev type virtual potential is obtained to analyse the characteristics

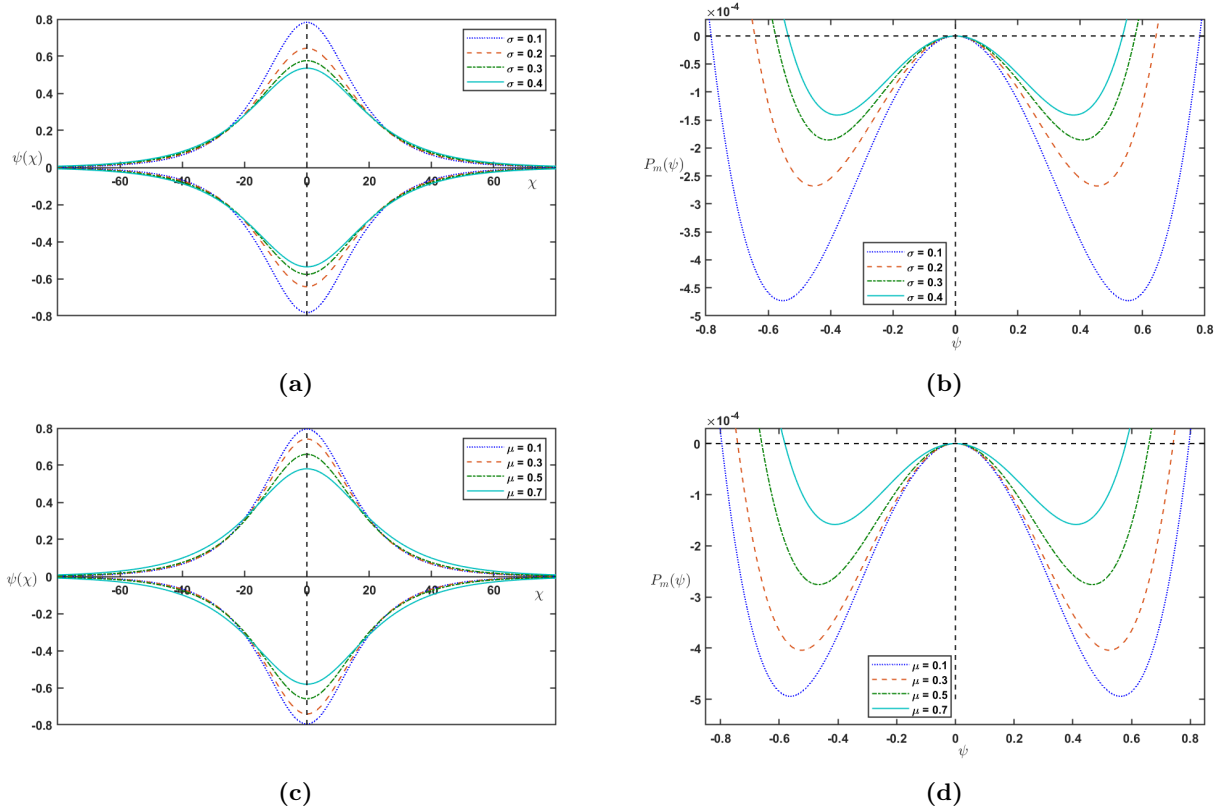


Figure 11. The variation of modified solitary wave profile $\psi(\chi)$ versus χ and small amplitude potential $P_m(\psi)$ versus ψ (a)-(b) with varying σ and $\theta = 15^\circ$, $\mu = 0.2$, $\Omega = 0.3$ and (c)-(d) with varying μ and $\theta = 15^\circ$, $\sigma = 0.1$, $\Omega = 0.3$. In all the panels, $q = q_c$ and $\nu = 0.02$.

of the DIA solitons in such a plasma system. The effects of different plasma parameters such as obliqueness angle (θ), electron nonextensivity (q), dust-to-ion number density ratio (μ), ion temperature (via ion-to-electron temperature ratio σ), external magnetic field (via Ω) etc. on the dynamical characteristics of propagating DIA solitary waves are studied. The results that have been noticed in our theoretical investigation can be succinctly summarized as follows.

1. The basic nature of the propagating DIA solitons that is amplitude, width and speed, are virtually affected by the core plasma parameters viz θ , σ , μ , q and Ω .
2. The phase velocity (U_p) of the waves advances for the parallel propagating than for the obliquely propagating along the magnetic field. While the phase velocity is lower in plasma having large low-speed electrons than the superthermal electrons.
3. The phase velocity is faster in a dusty plasma owning hot ions than in a dusty plasma with cold ion. Besides, the phase velocity achieves higher (lower) values in a plasma having more (less) number of negative dusts than in a plasma having less (more) number of positive ions.
4. The dispersion coefficient \mathcal{B} is a positive quantity, while the nonlinear coefficient \mathcal{A} can be a positive and a negative quantity, depending on the plasma parametric values. Therefore, in our considered plasma system the existence of compressive and/or rarefactive DIA solitary structures possible.
5. The change in the soliton types from compressive to rarefactive or vice-versa is predicting mainly through the deviation of electron nonextensivity by q and also the dust and ion number density by μ . At an appropriate value of nonextensive parameter q (i.e., q_c) with fixed other parameters or dust-to-ion number density ratio μ (i.e., μ_c) with fixed other parameters, the coefficient $\mathcal{A} = 0$, consequently the amplitude of the pulse of solitary structure become infinite. That is, it can be say that there does not exist any soliton for this condition.
6. Both the width and amplitude of pulse of soliton is found to increase with the obliqueness propagation angle $\theta \leq 55^\circ$, But the width decreases for $\theta \geq 55^\circ$ and the amplitude (width) of the DIA soliton is seen to be infinity (zero) as $\theta \rightarrow 90^\circ$, which implying the possibility for the of DIA solitary waves propagation for $0 \leq \theta \leq 55^\circ$.
7. The increasing of ion temperature (by σ) in the plasma, lead to increase the amplitude and decrease the width of the pulses of the propagating DIA soliton.

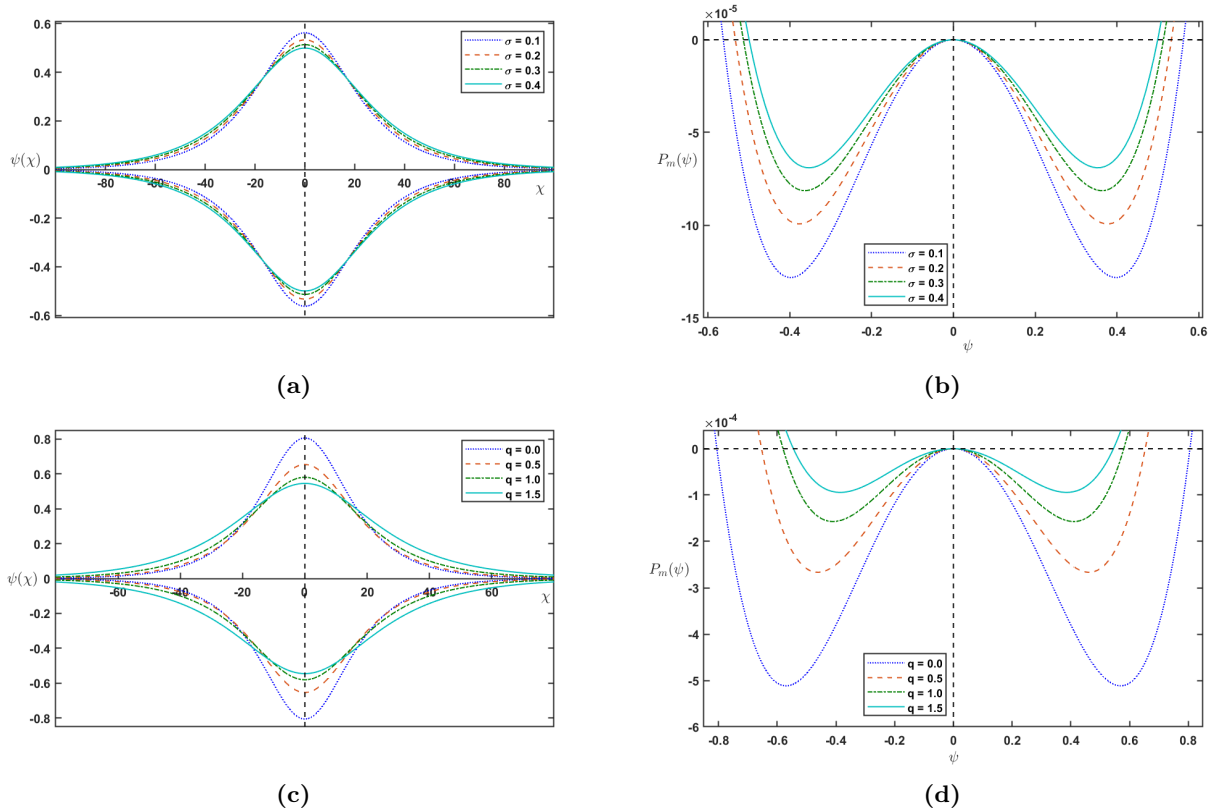


Figure 12. The variation of modified solitary wave profile $\psi(\chi)$ versus χ and small amplitude potential $P_m(\psi)$ versus ψ (a)-(b) with varying σ and $\theta = 15^\circ$, $q = 1.2$, $\Omega = 0.3$ and (e)-(f) with varying q and $\theta = 15^\circ$, $\sigma = 0.1$, $\Omega = 0.3$. In all the panels, $\mu = \mu_c$ and $\nu = 0.02$.

8. The strength of external magnetic field has a significant impact on the width of the propagating DIA soliton and width reduces with increasing the strength of the magnetic field, but it does not have any effect on the amplitude of the soliton.
9. Both the amplitude and width of pulse of propagating compressive (rarefactive) soliton is found to decrease (increase) with the increases of electron nonextensivity. Compressive soliton is obtained after the point q_c and rarefactive soliton is obtained before that point. However, the same but opposite characteristics is found with increase (decrease) of the number density of dust (ion) in the plasma.
10. At the critical q_c or μ_c , a second order nonlinearity \mathcal{A}' which is a positive quantity, is obtained via mKdV equation. And it is predicted that the coexistence of compressive and rarefactive solitons are feasible in the considered plasma system.
11. The amplitude of both compressive and rarefactive modified soliton decreases, while width increases with ion temperature and also with dust-to-ion number density, μ (electron nonextensivity q) at fixed $q = q_c$ ($\mu = \mu_c$). However, the amplitude is seen to higher in the region q_c compared to the region μ_c .

Finally, we draw the conclusion that our present theoretical findings should be useful for better understanding the dynamical nature of small but finite amplitude DIA solitons in both astrophysical and space contexts as well as in future laboratory investigations in which the considered plasma model are existed.

ORCID

Muktarul Rahman, <https://orcid.org/0009-0000-3523-8412>; Satyendra Nath Barman, <https://orcid.org/0000-0003-1136-8364>

REFERENCES

- [1] C. Thompson, A. Barkan, N. D'angelo, and R. L. Merlino, "Dust acoustic waves in a direct current glow discharge," *Phys. Plasmas*, **4**(7), 2231-2353 (1997). <https://doi.org/10.1063/1.872238>
- [2] N.N. Rao, P.K. Shukla, and M.Y. Yu, "Dust-acoustic waves in dusty plasmas." *Planet. Space Sci.* **38**(4), 543-546 (1990). [https://doi.org/10.1016/0032-0633\(90\)90147-I](https://doi.org/10.1016/0032-0633(90)90147-I)
- [3] P.K. Shukla, and V.P. Silin, "Dust ion-acoustic wave". *Phys. Scr.* **45**(5), 508 (1992). <https://dx.doi.org/10.1088/0031-8949/45/5/015>

- [4] P.V. Bliokh, and V.V. Yaroshenko, "Electrostatic waves in saturns rings," *Soviet Astron.* **29**, 330–336 (1985). <https://adsabs.harvard.edu/full/1985SvA....29..330B>
- [5] M. Rosenberg, "On dust wave instabilities in collisional magnetized plasmas," *IEEE Trans. Plasma Sci.* **44**(4), 451–457 (2016). <https://doi.org/10.1109/TPS.2015.2499119>
- [6] P.K. Shukla, M.Y. Yu, and R. Bharuthram, "Linear and nonlinear dust drift waves," *J. Geophys. Res.: Space Sci.* **96**(A12), 21343–21346 (1991). <https://doi.org/10.1029/91JA02331>
- [7] F. Melandso, "Lattice waves in dust plasma crystals," *Phys. Plasmas*, **3**(11), 3890–3901 (1996). <https://doi.org/10.1063/1.871577>
- [8] R.L. Merlino, A. Barkan, C. Thompson, and N. D'Angelo, "Laboratory studies of waves and instabilities in dusty plasmas," *Phys. Plasmas*, **5**(5), 1607–1614 (1998). <https://doi.org/10.1063/1.872828>
- [9] S. Ghosh, S. Sarkar, M. Khan, and M.R. Gupta, "Nonlinear properties of small amplitude dust ion acoustic solitary waves," *Phys. Plasmas*, **7**(9), 3594–3599 (2000). <https://doi.org/10.1063/1.1287140>
- [10] B.C. Kalita, S. Das, and D. Bhattacharjee, "Determination of the measure of size (amplitude) of perturbation and its role in the process of enforcing discrete Korteweg-de Vries solitons to modified Korteweg-de Vries solitons as means of continuum hypothesis in a multi-component dusty plasma," *Phys. Plasmas*, **24**(10), 102121 (2017). <https://doi.org/10.1063/1.5005535>
- [11] S. Das, and D.C. Das, "Compressive and rarefactive dust ion-acoustic korteweg–de vries and modified korteweg–de vries solitons in a multi-component dusty plasma," *J. Korean Phys. Soc.* **83**, 328 (2023). <https://doi.org/10.1007/s40042-023-00892-w>
- [12] R. Khanam, M. Rahman, and S.N. Barman, "Nonlinear propagation of ion acoustic solitary waves in weakly relativistic plasmas with positive and negative ions: The effect of electron inertia," *Adv. Appl. Fluid Mech.* **30**(2), 169–185 (2023). <https://doi.org/10.17654/0973468623010>
- [13] Y. Nakamura, and A. Sarma, "Observation of ion-acoustic solitary waves in a dusty plasma," *Phys. Plasmas*, **8**(9), 3921–3926 (2001). <https://doi.org/10.1063/1.1387472>
- [14] X. Liang, J. Zheng, J.X. Ma, W.D. Liu, J. Xie, G. Zhuang, and C.X. Yu, "Experimental observation of ion-acoustic waves in an inhomogeneous dusty plasma," *Phys. Plasmas*, **8**(5), 1459–1462 (2001). <https://doi.org/10.1063/1.1362530>
- [15] S. Ghosh, S. Sarkar, M. Khan, and M.R. Gupta, "Small amplitude nonlinear dust ion acoustic waves in a magnetized dusty plasma with charge fluctuation," *Phys. Scr.* **63**(5), 395 (2001), <https://dx.doi.org/10.1238/Physica.Regular.063a00395>
- [16] M.G.M. Anowar, and A.A. Mamun, "Dust ion-acoustic solitary waves in a hot adiabatic magnetized dusty plasma," *Phys. Lett. A*, **372**(37), 5896–5900 (2008). <https://doi.org/10.1016/j.physleta.2008.07.056>
- [17] T. Saha, and P. Chatterjee, "Obliquely propagating ion acoustic solitary waves in magnetized dusty plasma in the presence of nonthermal electrons," *Phys. Plasmas*, **16**(1), 013707 (2009). <https://doi.org/10.1063/1.3067824>
- [18] M. Shahmansouri, and H. Alinejad, "Arbitrary amplitude dust ion acoustic solitary waves in a magnetized suprathermal dusty plasma," *Phys. Plasmas*, **19**(12), 123701 (2012). <https://doi.org/10.1063/1.4769850>
- [19] A.P. Misra, and A. Barman, "Oblique propagation of dust ion-acoustic solitary waves in a magnetized dusty pair-ion plasma," *Phys. Plasmas*, **21**(7), 073702 (2014). <https://doi.org/10.1063/1.4886125>
- [20] A. Atteya, S. Sultana, and R. Schlickeiser, "Dust-ion-acoustic solitary waves in magnetized plasmas with positive and negative ions: The role of electrons superthermality," *Chinese J. Phys.* **56**(5), 1931–1939 (2018). <https://doi.org/10.1016/j.cjph.2018.09.002>
- [21] N. Zerglaine, K. Aoutou, and T.H. Zerguini, "Propagation of dust ion acoustic wave in a uniform weak magnetic field," *Astrophys. Space Sci.* **364**, 84 (2019). <https://doi.org/10.1007/s10509-019-3573-5>
- [22] Md.R. Hassan, and S. Sultana, "Damped dust-ion-acoustic solitons in collisional magnetized nonthermal plasmas," *Contr. Plasma Phys.* **61**(9), e202100065 (2021). <https://doi.org/10.1002/ctpp.202100065>
- [23] S.Md. Abdus, A.Md. Ali, and A.Md. Zulfikar, "Higher-order nonlinear and dispersive effects on dust-ion-acoustic solitary waves in magnetized dusty plasmas," *Results Phys.* **32**, 105114, (2022). <https://doi.org/10.1016/j.rinp.2021.105114>
- [24] A. Rényi, "On a new axiomatic theory of probability," *Acta Mathematica Academiae Scientiarum Hungaricae*, **6**(3-4), 285–335 (1955). <https://doi.org/10.1007/BF02024393>
- [25] C. Tsallis, "Possible generalization of boltzmann-gibbs statistics," *J. Stat. Phys.* **52**, 479–487 (1988). <https://doi.org/10.1007/BF01016429>
- [26] M. Tribeche, L. Djebarni, and R. Amour, "Ion-acoustic solitary waves in a plasma with a q-nonextensive electron velocity distribution," *Phys. Plasmas*, **17**(4), 042114 (2010). <https://doi.org/10.1063/1.3374429>
- [27] H.R. Pakzad, "Effect of q-nonextensive electrons on electron acoustic solitons," *Phys. Scr.* **83**(1), 015505 (2010). <https://dx.doi.org/10.1088/0031-8949/83/01/015505>
- [28] U.K. Samanta, A. Saha, and P. Chatterjee, "Bifurcations of dust ion acoustic travelling waves in a magnetized dusty plasma with a q-nonextensive electron velocity distribution," *Phys. Plasmas*, **20**(2), 022111 (2013). <https://doi.org/10.1063/1.4791660>

- [29] A.A. Mahmoud, E.M. Abulwafa, A.F. Al-Araby, and A.M. Elhanbaly, "Plasma parameters effects on dust acoustic solitary waves in dusty plasmas of four components," *Adv. Math. Phys.* **11**, 7935317 (2018). <https://doi.org/10.1155/2018/7935317>
- [30] F. Araghi, S. Miraboutalebi, and D. Dorrnian, "Effect of variable dust size, charge and mass on dust acoustic solitary waves in nonextensive magnetized plasma," *Indian J. Phys.* **94**, 547–554 (2020). <https://doi.org/10.1007/s12648-019-01488-6>
- [31] P. Eslami, M. Mottaghizadeh, and H.R. Pakzad, "Nonplanar dust acoustic solitary waves in dusty plasmas with ions and electrons following a q -nonextensive distribution," *Phys. Plasmas*, **18**(10), 102303 (2011). <https://doi.org/10.1063/1.3642639>
- [32] A. Saha, and P. Chatterjee, "Propagation and interaction of dust acoustic multi-soliton in dusty plasmas with q -nonextensive electrons and ions," *Astrophys. Space Sci.* **353**, 169–177 (2014). <https://doi.org/10.1007/s10509-014-2028-2>
- [33] P. Chatterjee, K. Roy, and U.N. Ghosh, *Waves and Wave Interactions in Plasmas*, (World Scientific Publishing Co. Pte. Ltd., 2022), pp. 25–28.
- [34] M. Tribeche, L. Djebarni, and R. Amour, "Ion-acoustic solitary waves in a plasma with a q -nonextensive electron velocity distribution," *Phys. Plasmas*, **17**(4), 042114 (2010). <https://doi.org/10.1063/1.3374429>
- [35] U.N. Ghosh, P. Chatterjee, and S.K. Kundu, "The effect of q -distributed ions during the head-on collision of dust acoustic solitary waves," *Astrophys. Space Sci.* **339**, 255–260 (2012). <https://doi.org/10.1007/s10509-012-1009-6>
- [36] G. Ullah, M. Saleem, M. Khan, M. Khalid, A. Rahman, and S. Nabi, "Ion acoustic solitary waves in magnetized electron–positron–ion plasmas with tsallis distributed electrons," *Contr. Plasma Phys.* **60**(10), e202000068 (2020). <https://doi.org/10.1002/ctpp.202000068>
- [37] J. Tamang, A. Abdikian, and A. Saha, "Phase plane analysis of small amplitude electronacoustic supernonlinear and nonlinear waves in magnetized plasmas," *Phys. Scr.* **95**(10), 105604 (2020). <https://dx.doi.org/10.1088/1402-4896/abb05b>
- [38] F. Verheest, "Oblique propagation of solitary electrostatic waves in multispecies plasmas," *J. Phys. A: Math. Theor.* **42**(28), 285501 (2009). <https://dx.doi.org/10.1088/1751-8113/42/28/285501>

ІСНУВАННЯ СОЛІТОНІВ KdV ТА mKdV МАЛОЇ АМПЛІТУДИ В НАМАГНІЧЕНІЙ ЗАПИЛЕНІЙ ПЛАЗМІ З q -НЕЕКСТЕНСИВНИМИ РОЗПОДІЛЕНИМИ ЕЛЕКТРОНАМИ

Муктарул Рахман^a, Сатъендра Нат Барман^b

^a *Департамент математики, Університет Гаухаті, Гувахаті-781014, Ассам, Індія*

^b *Коледж Б. Бороа, Гувахаті-781007, Асам, Індія*

Існування та характеристики поширення пилово-іонно-акустичних (DIA) солітонів Кортевега-де Фріза (KdV) і модифікованих KdV солітонів малої амплітуди в трикомпонентній намагніченій плазмі, що складається з позитивних інерційних іонів зі зміною тиску, неінерційних електронів і негативно заряджених нерухомих частинок пилу теоретично та чисельно досліджено, коли електрони підкоряються q -неекстенсивному розподілу швидкостей. Використовуючи метод редуکتивних збурень, отримати KdV і модифіковані рівняння KdV і отримати солітонні рішення DIA разом із відповідними потенціалами малої амплітуди. Це дослідження показує, що існують стискаючі та/або розріджені солітони та відсутні солітони взагалі через параметричну залежність від нелінійного коефіцієнта першого порядку через щільність позитивних іонів і негативних частинок пилу та неекстенсивність електронів. Співіснування стискаючих і розріджених солітонів з'являється шляхом підвищення міри коефіцієнта нелінійності до другого порядку за допомогою модифікованого рівняння KdV. Чисельно обговорюються такі властивості, як швидкість, амплітуда, ширина тощо.

Ключові слова: *пилова іонна акустична хвиля; намагнічена плазма; q -неекстенсивний розподіл; редуکتивний метод збурень; рівняння KdV*

REFLECTIONLESS INCIDENCE OF THE *p*-POLARIZED ELECTROMAGNETIC WAVE THROUGH SOLID-STATE STRUCTURE “COATING-UNIAXIAL PLASMONIC METASURFACE-DIELECTRIC-METAL”

✉ Mykola M. Biletskiy*, ✉ Ivan D. Popovych

*O.Ya. Usikov Institute for Radiophysics and Electronics of NASU
12, Acad. Proskury St., Kharkiv, 61085, Ukraine*

*Corresponding Author e-mail: bmbeletski@gmail.com

Received February 26, 2024; revised March 29, 2024; accepted April 10, 2024

In this work we studied the effects which occur during the incidence of *p*-polarized electromagnetic wave on the solid-state structure “coating-uniaxial plasmonic metasurface-dielectric-metal”. The purpose of this work is researching how the coating influences the effect of reflectionless incidence of the *p*-polarized electromagnetic waves on the solid-state structure “uniaxial plasmonic metasurface-dielectric-metal”. Numerical modelling was used to find the conditions that lead to reflectionless incidence of the *p*-polarized electromagnetic wave on the solid-state structure under consideration. Using this method we determined the parameters of the coating which are required to observe incidence of *p*-polarized waves with no reflection. It was found that dielectric coating of the solid state structure significantly changes the behavior of the effect. We showed that dielectric permittivity of the coating changes the frequencies at which reflectionless *p*-polarized waves occur. The dependency was established between permittivity and thickness of the coating which causes the effect of the reflectionless incidence of *p*-polarized waves. The conducted research has a great scientific and practical interest. The solid-state structure that was studied can be applied for designing conceptually new types of nanoelectronic and optical devices.

Keywords: *Dielectric coating; p-polarized electromagnetic waves; Uniaxial plasmonic metasurface; Reflectionless incidence*

PACS: 41.20.Jb

1. INTRODUCTION

The presence of two-dimensional material (metasurface) at the boundary of the dielectric layer causes some interesting and important effects to take place [1–6]. The articles [4–6] studied uniaxial plasmonic metasurfaces consisting of a periodical array of conductive ellipsoids. Such plasmonic metasurfaces can be described using a two-dimensional non-diagonal conductivity tensor, which depends on the frequency and the angle of electromagnetic wave propagation relative to the principal axis of the ellipsoids. Of particular interests are the effects based on the *p*-polarized electromagnetic waves that incident on the metasurface placed on top of the dielectric layer [4–6]. One of these effects is reflectionless propagation of *p*-polarized electromagnetic waves through the metasurface. Such behavior can be observed in case the symmetry axis of plasmonic metasurface is in fact the plane of incidence of the electromagnetic wave [4, 6]. Another interesting observation is full transformation of the *p*-polarized electromagnetic wave into the *s*-polarized one [5, 6], which occurs when the plane of incidence forms an acute angle with the great symmetry axis of the metasurface. It’s important to note that both aforementioned effects take place in case coating of the dielectric layer is either metal or dielectric itself. In addition, in [4–6] the conditions were established which lead to reflectionless incidence and full transformation and how they depend on the frequency of *p*-polarized wave and the angle of incidence on the plasmonic metasurface.

In this paper, we are proceeding further with theoretical research of the described in [4, 6] effect of *p*-polarized electromagnetic wave incidence through solid-state structure with no reflection [6] assuming, that plasmonic metasurface has protective dielectric layer. Here, we studied how this new dielectric layer impacts the conditions of reflectionless incidence.

2. PROBLEM STATEMENT

The geometry of the problem is shown in Figure 1. Let the area $z < 0$ be a dielectric with permittivity ε_1 . The first layer (area $0 < z < d_1$) – dielectric layer with permittivity ε_2 covers uniaxial plasmonic metasurface ($z = d_1$), which is located on top of the second dielectric layer (scope between $d_1 < z < d_1 + d_2$) that has permittivity ε_3 . Perfectly conductive metal substrate occupies the area $z > d_1 + d_2$. Uniaxial plasmonic metasurface was regarded as two-dimensional (2D) array of conductive ellipsoids [4–6].

We assumed that an electric field of the *p*-polarized electromagnetic wave lies in a plane which makes an angle φ with the major symmetry axis of the plasmonic metasurface. Moreover, let electromagnetic wave with frequency ω fall on the dielectric structure with angle θ .

As in [4–6] to describe electromagnetic properties of the plasmonic metasurface within the solid-state structure under consideration, we incorporated two-dimensional effective conductivity tensor.

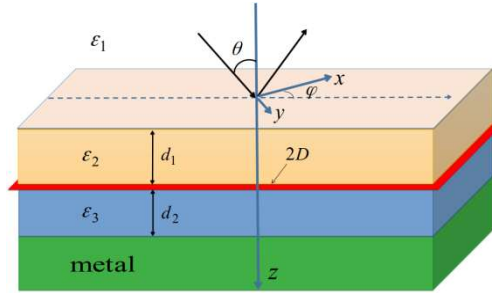


Figure 1. Geometry of the problem

In the coordinate frame making an angle φ with the principle axis of the plasmonic metasurface (assuming that the plane of incidence of the electromagnetic wave is identical to the XZ plane) effective conductivity tensor of the plasmonic metasurface takes the following form [4-6]:

$$\sigma_{\varphi} = \begin{pmatrix} \sigma_{xx} & \sigma_{xy} \\ \sigma_{yx} & \sigma_{yy} \end{pmatrix}, \quad (1)$$

where

$$\sigma_{xx} = \sigma_{\parallel} \cos^2 \varphi + \sigma_{\perp} \sin^2 \varphi, \quad (2)$$

$$\sigma_{yy} = \sigma_{\parallel} \sin^2 \varphi + \sigma_{\perp} \cos^2 \varphi, \quad (3)$$

$$\sigma_{xy} = \sigma_{yx} = (\sigma_{\perp} - \sigma_{\parallel}) \sin \varphi \cos \varphi. \quad (4)$$

In the formulas (2–4) diagonal components of the effective conductivity tensor describing uniaxial plasmonic metasurface $\sigma_{\parallel, \perp}$, normalized by $c/4\pi$, can be expressed using (c is the speed of light):

$$\sigma_{\parallel, \perp} = \sigma_{\parallel, \perp}^{\infty} + i \frac{\omega A_{\parallel, \perp}}{\omega^2 - \Omega_{\parallel, \perp}^2 + i\omega\gamma_{\parallel, \perp}} = \sigma'_{\parallel, \perp} + i\sigma''_{\parallel, \perp}. \quad (5)$$

The indices « \parallel » and « \perp » here correspond respectively to the along and across directions of the plasmonic metasurface principal symmetry axis, $\Omega_{\parallel, \perp}$ and $\gamma_{\parallel, \perp}$ are the resonant frequencies and half-widths of the lines, $A_{\parallel, \perp}$ are the oscillator forces magnitudes and $\sigma_{\parallel, \perp}^{\infty}$ are the background conductivities. In addition, $\sigma'_{\parallel, \perp}$ and $\sigma''_{\parallel, \perp}$ are the real and imaginary parts of the conductivity tensor for the corresponding components. We assumed that $\sigma_{\parallel, \perp}^{\infty} = 0.2i$, $A_{\parallel, \perp} = 0.2$, $\gamma_{\parallel, \perp} = 0.02$, $\Omega_{\parallel} = 1.0$, $\Omega_{\perp} = 1.2$ [4].

It should be noted that the presence of non-zero non-diagonal conductivity tensor components σ_{xy} , σ_{yx} in case $\varphi \neq 0$ and $\varphi \neq 90^\circ$ cause reflective s-polarized electromagnetic waves to be created. As a result, when p -polarized wave propagates through uniaxial plasmonic metasurface reflected waves will have all the electromagnetic field components and will be elliptically polarized in the general case. In the chosen coordinate system, electromagnetic field of p -polarized waves has the following components: $\vec{E}_p = \{E_x, 0, E_z\}$, $\vec{H}_p = \{0, H_y, 0\}$. Similarly for the s-polarized electromagnetic waves we have: $\vec{E}_s = \{0, E_y, 0\}$, $\vec{H}_s = \{H_x, 0, H_z\}$.

The wave vectors for each layer have the following components $\vec{k}_j = (k_x, 0, k_{zj})$, $j = 1, 2, 3$. Moreover, the longitudinal wave number equals $k_x = \frac{\omega}{c} \sqrt{\varepsilon_1} \sin \theta$. For the transverse wave number the formula is $k_{zj} = \sqrt{\frac{\omega^2}{c^2} \varepsilon_j - k_x^2}$.

Let's write down non-zero tangential components of the electromagnetic field in each medium of the established above solid-state structure. We will omit multiplier $\exp(ik_x x - \omega t)$. In the equations below index « p » relates to the p -polarized waves, and « s » – to s -polarized ones.

Medium 1 (layer $z < 0$).

$$H_{y1}^p(z) = e^{ik_{z1}z} + r_{pp} e^{-ik_{z1}z}, \quad (6)$$

$$E_{x1}^p(z) = \frac{ck_{z1}}{\omega\epsilon_1} (e^{ik_{z1}z} - r_{pp}e^{-ik_{z1}z}), \quad (7)$$

$$E_{y1}^s(z) = r_{ps}e^{-ik_{z1}z}, \quad (8)$$

$$H_{x1}^s(z) = \frac{ck_{z1}}{\omega} r_{ps}e^{-ik_{z1}z}. \quad (9)$$

Medium 2 (layer $0 < z < d_1$).

$$H_{y2}^p(z) = H_{p2}^+e^{ik_{z2}z} + H_{p2}^-e^{-ik_{z2}z}, \quad (10)$$

$$E_{x2}^p(z) = \frac{ck_{z2}}{\omega\epsilon_2} (H_{p2}^+e^{ik_{z2}z} - H_{p2}^-e^{-ik_{z2}z}), \quad (11)$$

$$E_{y2}^s(z) = E_{s2}^+e^{ik_{z2}z} + E_{s2}^-e^{-ik_{z2}z}, \quad (12)$$

$$H_{x2}^s(z) = -\frac{ck_{z2}}{\omega} (E_{s2}^+e^{ik_{z2}z} - E_{s2}^-e^{-ik_{z2}z}). \quad (13)$$

Medium 3 (layer $d_1 < z < d_1 + d_2$).

$$H_{y3}^p(z) = H_{p3}^+e^{ik_{z3}z} + H_{p3}^-e^{-ik_{z3}z}, \quad (14)$$

$$E_{x3}^p(z) = \frac{ck_{z3}}{\omega\epsilon_3} (H_{p3}^+e^{ik_{z3}z} - H_{p3}^-e^{-ik_{z3}z}), \quad (15)$$

$$E_{y3}^s(z) = E_{s3}^+e^{ik_{z3}z} + E_{s3}^-e^{-ik_{z3}z}, \quad (16)$$

$$H_{x3}^s(z) = -\frac{ck_{z3}}{\omega} (E_{s3}^+e^{ik_{z3}z} - E_{s3}^-e^{-ik_{z3}z}). \quad (17)$$

Here r_{pp} and r_{ps} are the amplitudes of p - and s -polarized waves, reflected from the uniaxial plasmonic metasurface. The magnitudes H_{p2}^+ , E_{s2}^+ and H_{p2}^- , E_{s2}^- are the amplitudes of the forward and backward p - and s -polarized waves in a medium with dielectric permittivity ϵ_2 . Likewise, H_{p23}^+ and E_{s3}^+ are the amplitudes of the forward, while H_{p3}^- and E_{s3}^- – amplitudes of the backward p - and s -polarized waves within the layer characterized by permittivity ϵ_3 .

To get both r_{pp} and r_{ps} we incorporated boundary conditions near the $z = 0$, $z = d_1$ and $z = d_1 + d_2$.

For $z = 0$ tangential components of the electric and magnetic fields in adjacent mediums are equal.

However, when $z = d_1$, tangential components of the electric fields are continuous, unlike tangential components of magnetic fields:

$$E_{x2}^p(d_1) = E_{x3}^p(d_1), \quad (18)$$

$$E_{y2}^s(d_1) = E_{y3}^s(d_1), \quad (19)$$

$$H_{y3}^p(d_1) - H_{y2}^p(d_1) = -\frac{4\pi}{c} (\sigma_{xx}E_{x2}^p(d_1) + \sigma_{xy}E_{y2}^s(d_1)), \quad (20)$$

$$H_{x3}^s(d_1) - H_{x2}^s(d_1) = \frac{4\pi}{c} (\sigma_{yx}E_{x2}^p(d_1) + \sigma_{yy}E_{y2}^s(d_1)). \quad (21)$$

On the metal boundary $z = d_1 + d_2$ tangential components of the electric fields equal to zero.

The reflection coefficient of the p -polarized electromagnetic wave from the plasmonic metasurface is a sum of $|r_{pp}|^2$ and $|r_{ps}|^2$:

$$R_p = |r_{pp}|^2 + |r_{ps}|^2, \quad (22)$$

where

$$r_{pp} = \frac{P_- S + Q_-}{P_+ S + Q_+}, \quad (23)$$

$$r_{ps} = 2\sigma_{yx} \frac{\sin^2(k_3 \delta_2)}{P_+ S + Q_+}, \quad (24)$$

$$P_{\pm} = \left(\frac{\varepsilon_3}{k_3} \cos(k_3 \delta_2) - i\sigma_{xx} \sin(k_3 \delta_2) \right) \left(\cos(k_2 \delta_1) \mp i \frac{\varepsilon_1 k_2}{\varepsilon_2 k_1} \sin(k_2 \delta_1) \right) - \sin(k_3 \delta_2) \left(\frac{\varepsilon_2}{k_2} \sin(k_2 \delta_1) \pm i \frac{\varepsilon_1}{k_1} \sin(k_2 \delta_1) \right), \quad (25)$$

$$S = \left(k_3 \cos(k_3 \delta_2) - i\sigma_{yy} \sin(k_3 \delta_2) \right) \left(\cos(k_2 \delta_1) - i \frac{k_1}{k_2} \sin(k_2 \delta_1) \right) - i \sin(k_3 \delta_2) (k_1 \cos(k_2 \delta_1) - ik_2 \sin(k_2 \delta_1)), \quad (26)$$

$$Q_{\pm} = \sigma_{xy}^2 \sin^2(k_3 \delta_2) \left(\cos(k_2 \delta_1) \mp i \frac{\varepsilon_1 k_2}{\varepsilon_2 k_1} \sin(k_2 \delta_1) \right) \left(\cos(k_2 \delta_1) - i \frac{k_1}{k_2} \sin(k_2 \delta_1) \right). \quad (27)$$

Note that in equations above we used dimensionless quantities: $k_j = \frac{ck_{zj}}{\omega}$ $j = 1, 2, 3$ and $\delta_{1,2} = \frac{d_{1,2}\omega}{c}$.

3. THE AFFECT OF THE COATING COVERING THE UNIAXIAL PLASMONIC METASURFACE ON THE REFLECTIONLESS INCIDENCE OF THE P-POLARIZED ELECTROMAGNETIC WAVE

We were trying to identify the conditions under which $R_p = 0$ is the case. Let's consider either $\varphi = 0^\circ$ or $\varphi = 90^\circ$. Then $\sigma_{xy} = \sigma_{yx} = 0$ and $r_{ps} = 0$. It's clear, that under such circumstances the reflected electromagnetic wave becomes p-polarized and $R_p = |r_{pp}|^2$. Seeing that $Q_{\pm} = 0$, from the expression (23) we can conclude that $r_{pp} = 0$, when $P_- = 0$. Since quantity P_- is a complex number, the equation $r_{pp} = 0$ satisfied in case the following conditions are met simultaneously:

$$\left(\frac{\varepsilon_3}{k_3} \cos(k_3 \delta_2) + \sigma_{\parallel, \perp}'' \sin(k_3 \delta_2) \right) \cos(k_2 \delta_1) - \left(\frac{\varepsilon_2}{k_2} - \frac{\varepsilon_1 k_2}{\varepsilon_2 k_1} \sigma_{\parallel, \perp}' \right) \sin(k_2 \delta_1) \sin(k_3 \delta_2) = 0, \quad (28)$$

$$\left(\frac{\varepsilon_3}{k_3} \cos(k_3 \delta_2) + \sigma_{\parallel, \perp}'' \sin(k_3 \delta_2) \right) \frac{\varepsilon_1 k_2}{\varepsilon_2 k_1} \sin(k_2 \delta_1) + \left(\frac{\varepsilon_1}{k_1} - \sigma_{\parallel, \perp}' \right) \cos(k_2 \delta_1) \sin(k_3 \delta_2) = 0, \quad (29)$$

From the equations (28), (29) we have:

$$\tan(k_2 \delta_1) = \frac{\frac{\varepsilon_3}{k_3} \cos(k_3 \delta_2) + \sigma_{\parallel, \perp}'' \sin(k_3 \delta_2)}{\left(\frac{\varepsilon_2}{k_2} - \frac{\varepsilon_1 k_2}{\varepsilon_2 k_1} \sigma_{\parallel, \perp}' \right) \sin(k_3 \delta_2)}, \quad (30)$$

$$\tan(k_2 \delta_1) = - \frac{\left(\frac{\varepsilon_1}{k_1} - \sigma_{\parallel, \perp}' \right) \sin(k_3 \delta_2)}{\left(\frac{\varepsilon_3}{k_3} \cos(k_3 \delta_2) + \sigma_{\parallel, \perp}'' \sin(k_3 \delta_2) \right) \frac{\varepsilon_1 k_2}{\varepsilon_2 k_1}}. \quad (31)$$

Comparing the right side of the equations (30) and (31) we obtain the following expression:

$$\frac{\frac{\varepsilon_3}{k_3} \cos(k_3 \delta_2) + \sigma''_{\parallel, \perp} \sin(k_3 \delta_2)}{\left(\frac{\varepsilon_2}{k_2} - \frac{\varepsilon_1 k_2}{\varepsilon_2 k_1} \sigma'_{\parallel, \perp} \right) \sin(k_3 \delta_2)} + \frac{\left(\frac{\varepsilon_1}{k_1} - \sigma'_{\parallel, \perp} \right) \sin(k_3 \delta_2)}{\left(\frac{\varepsilon_3}{k_3} \cos(k_3 \delta_2) + \sigma''_{\parallel, \perp} \sin(k_3 \delta_2) \right) \frac{\varepsilon_1 k_2}{\varepsilon_2 k_1}} = 0. \quad (32)$$

With fixed values of ε_3 and δ_2 the equation (32) allows us to find the relation $\omega(\varepsilon_2)$, which causes the effect of reflectionless incidence of the p -polarized electromagnetic wave through composed solid-state structure. The relevant dependencies $\delta_1(\varepsilon_2)$ can be simply established from one of the equations (30) or (31).

It should be mentioned that for the solid-state structure uniaxial plasmonic metasurface – dielectric layer – metal ($\delta_1 = 0$) [6] the effect of propagation of the p -polarized electromagnetic waves with no reflection with the fixed angle of incidence θ can be observed at the two frequencies ω_1 and ω_2 , that are symmetrically located relative to Ω_{\parallel} (for $\varphi = 0^\circ$) and Ω_{\perp} ($\varphi = 90^\circ$). These frequencies correspond to the different values of dielectric layer thickness δ_2 . The reason is that for uniaxial plasmonic metasurface functions $\sigma'_{\parallel, \perp}(\omega)$ are symmetric, and $\sigma''_{\parallel, \perp}(\omega)$ are asymmetric relative to the resonant frequencies Ω_{\parallel} and Ω_{\perp} .

We are interested in the situation when the angle of incidence of the p -polarized waves on the structure under consideration equals $\theta = 45^\circ$ and permittivity is $\varepsilon_3 = 2.0$. Assuming that there is no coating covering dielectric structure ($\delta_1 = 0$) and $\varphi = 0^\circ$ the effect of the incidence with no reflection of the p -polarized waves arise at the frequency $\omega_1 \approx 0.976$ and the thickness $\delta_2 \approx 0.377$ as well as when $\omega_2 \approx 1.025$ and $\delta_2 \approx 2.224$. In case $\varphi = 90^\circ$ reflectionless behavior can be observed for the following pairs of frequencies and thicknesses $\omega_1 \approx 1.176$, $\delta_2 \approx 0.377$ and $\omega_2 \approx 1.225$, $\delta_2 \approx 2.224$.

Let's now try to understand how the coating ($\delta_1 \neq 0$) affects the propagation behavior of the p -polarized electromagnetic waves in particular case when there is no reflection. We considered the following parameters $\varphi = 0^\circ$, $\theta = 45^\circ$ and $\varepsilon_3 = 2.0$. The general idea was to find how frequencies $\omega_{1,2}$ and thickness δ_1 depend on the dielectric layer permittivity ε_2 .

Figure 2 shows relation $\omega_1(\varepsilon_2)$ (left-hand ordinate axis, solid line) and $\delta_1(\varepsilon_2)$ (right-hand ordinate axis, dashed line) in case $R_p = 0$ and $\varphi = 0^\circ$, $\theta = 45^\circ$, $\varepsilon_3 = 2.0$, $\delta_2 \approx 0.377$. From the Figure 2 we can observe that the function $\omega_1(\varepsilon_2)$ is monotonically increasing unlike $\delta_1(\varepsilon_2)$ which decreases in the same way. Horizontal dotted line from the Figure 2 corresponds to the quantity ω_1 when there is no coating covering the uniaxial plasmonic metasurface.

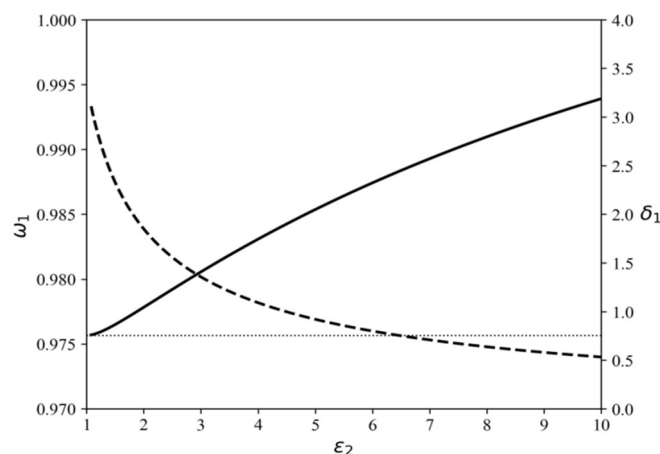


Figure 2. Dependencies $\omega_1(\varepsilon_2)$ (left-hand ordinate axis, solid line) and $\delta_1(\varepsilon_2)$ (right-hand ordinate axis, dashed line) corresponding to the situation $R_p = 0$ for $\varphi = 0^\circ$, $\theta = 45^\circ$, $\varepsilon_3 = 2.0$, $\delta_2 \approx 0.377$

Therefore, when $\delta_1 \neq 0$ the frequency ω_1 shifts closer to resonant frequency Ω_{\parallel} . The quantity of displacement is directly proportional to the permittivity value ε_2 . We also can discover another dependency. The thickness value δ_1 that is necessary to observe the effect of electromagnetic wave reflectionless incidence propagation when ε_2 goes up.

The way that coating affects the reflection coefficient R_p of the p -polarized electromagnetic wave can be seen on the Figure 3. In this graph the solid line correspond to the dependency $R_p(\omega)$ for the situation when $\phi = 0, \theta = 45^\circ, \varepsilon_2 = 1.5, \varepsilon_3 = 2.0, \delta_1 = 2.329, \delta_2 = 0.377$. The figure also contains a dashed line showing the same dependency between the frequency and reflection coefficient for the solid-state structure with no coating ($\delta_1 = 0$).

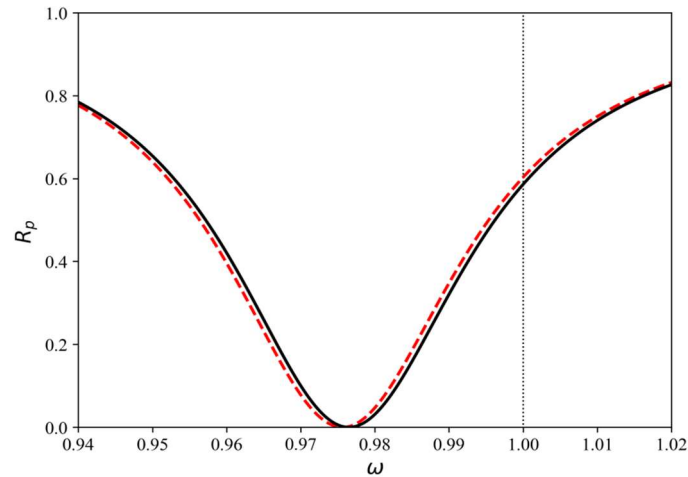


Figure 3. Dependency $R_p(\omega)$ for $\phi = 0^\circ, \theta = 45^\circ, \varepsilon_2 = 1.5, \varepsilon_3 = 2.0, \delta_2 = 0.377$ and $\delta_1 = 2.329$ (solid line), $\delta_1 = 0$ (dashed line)

From the Figure 3 we can deduce that adding the coating ($\delta_1 \neq 0$) leads to the shifting of zero value of reflection coefficient R_p (displacement of ω_1) closer to the resonant frequency $\Omega_{||} = 1.0$.

It is known that in the regular situation with no coating, the effect of the reflectionless incidence of the p -polarized electromagnetic waves takes place when the frequency value is either close to $\omega_1 \approx 0.976$ or $\omega_2 \approx 1.025$ [6]. The thickness value should be also shifted to $\delta_2 \approx 2.224$.

Let us now consider what happens with ω_2 after introducing the coating for the metasurface. The Figure 4 describes the relation $\omega_2(\varepsilon_2)$ (left-hand ordinate axis, solid lines) and $\delta_1(\varepsilon_2)$ (right-hand ordinate axis, dashed lines) that met $R_p = 0$ condition for $\phi = 0^\circ, \theta = 45^\circ, \varepsilon_3 = 2.0, \delta_2 \approx 2.224$. It can be discovered from the graph that both $\omega_2(\varepsilon_2)$ and $\delta_1(\varepsilon_2)$ are monotonically decreasing functions. Horizontal dashed line on the Figure 4 corresponds to the value ω_2 when no coating covering metasurface. Thus, by increasing ε_2 the frequency value ω_2 at which reflectionless propagation of the p -polarized electromagnetic waves takes place is approaching to the resonant frequency $\Omega_{||} = 1.0$.

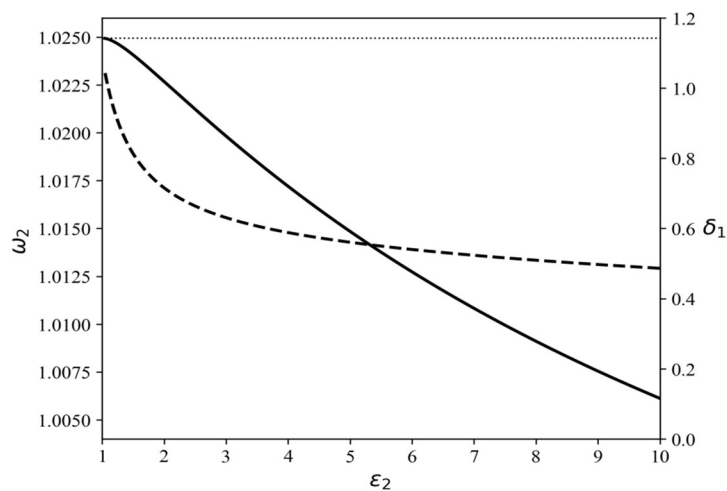


Figure 4. Dependencies $\omega_2(\varepsilon_2)$ (left-hand ordinate axis solid lines) and $\delta_1(\varepsilon_2)$ (right-hand ordinate axis, dashed lines) corresponding to $R_p = 0$ for $\phi = 0^\circ, \theta = 45^\circ, \varepsilon_3 = 2.0, \delta_2 \approx 2.224$

Figure 5 using a solid line describes dependency $R_p(\omega)$ for the particular situation when $\phi = 0^\circ, \theta = 45^\circ, \varepsilon_2 = 2.0, \varepsilon_3 = 2.0, \delta_1 \approx 0.716, \delta_2 \approx 2.224$. Similarly to the figures above, the graph also shows same dependency $R_p(\omega)$ for the case with no coating $\delta_1 = 0$.

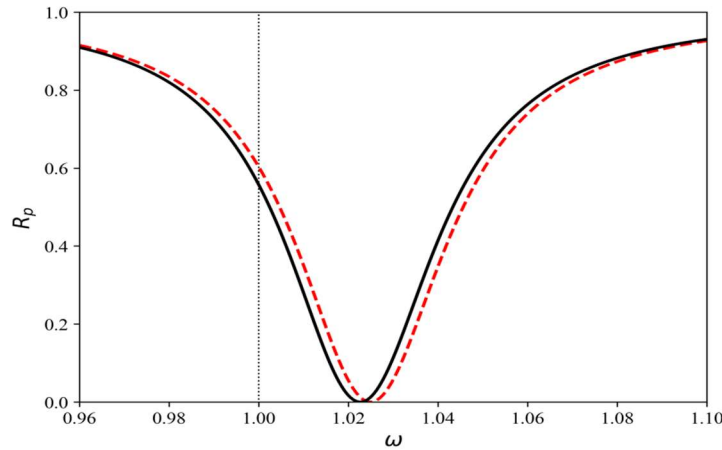


Figure 5. Dependency $R_p(\omega)$ for $\phi = 0^\circ, \theta = 45^\circ, \varepsilon_2 = 2.0, \varepsilon_3 = 2.0, \delta_2 = 2.224$ for $\delta_1 = 0.716$ (solid line) and $\delta_1 = 0$ (dashed line)

By using the Figure 5 we can deduce that incorporating the coating causes shifting of zero value of R_p closer to the resonant frequency $\Omega_{||}$. By increasing the dielectric permittivity of the ε_2 effect of non-reflective incidence of the p -polarized electromagnetic waves arise on the lower frequencies ω_2 and higher thicknesses δ_1 of the dielectric layer.

We also studied the changes introduced by adding coating for the case when the plane of incidence of the p -polarized electromagnetic waves makes the right angle with the principal axis of plasmonic metasurface ($\phi = 90^\circ$). Similarly to the previous cases we considered the following: $\theta = 45^\circ, \varepsilon_3 = 2.0$. If $\delta_2 \approx 0.377$ and the coating is absent the effect of the reflectionless propagation of p -polarized electromagnetic waves takes place at the frequency $\omega_1 \approx 1.176$. Extending the solid-state structure with the coating leads to the change of ω_1 . Figure 6 shows dependencies $\omega_1(\varepsilon_2)$ (left-hand ordinate axis, solid line) and $\delta_1(\varepsilon_2)$ (right-hand ordinate axis, dashed line) for $R_p = 0$ when $\phi = 90^\circ, \theta = 45^\circ, \varepsilon_3 = 2.0, \delta_2 \approx 0.377$. It can be seen from the graph that the dependency $\omega_1(\varepsilon_2)$ is monotonically increasing function. However, $\delta_1(\varepsilon_2)$ monotonically decreases. Horizontal dotted line on the Figure 6 corresponds to the $\omega_1 \approx 1.176$, when there is no coating. It should be noted, that by increasing ε_2 the value ω_1 approached to the resonant frequency $\Omega_{\perp} = 1.2$, unlike δ_1 which is decreasing.

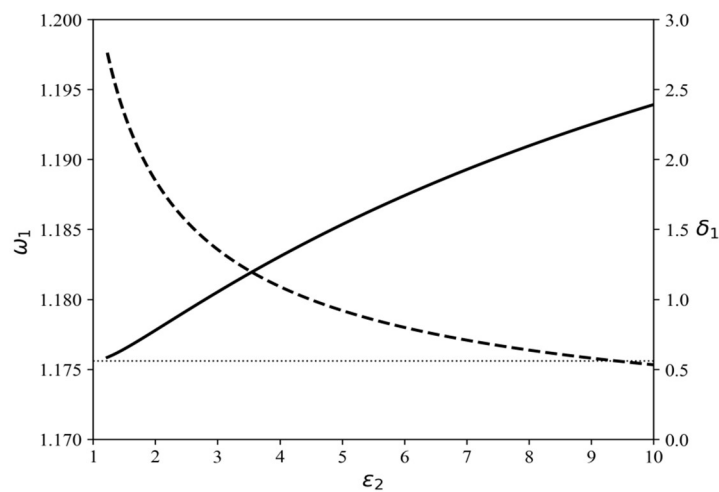


Figure 6. Dependencies $\omega_1(\varepsilon_2)$ (left-hand coordinate axis, solid lines) and $\delta_1(\varepsilon_2)$ (right-hand ordinate axis, dashed lines) corresponding to $R_p = 0$ for $\phi = 90^\circ, \theta = 45^\circ, \varepsilon_3 = 2.0, \delta_2 \approx 0.377$

Let's set $\delta_2 \approx 2.224$. Then for solid-state structure with no coating reflectionless incidence can be observed at the frequency $\omega_2 \approx 1.225$. Figure 7. shows the dependencies $\omega_2(\varepsilon_2)$ (left-handed ordinate axis, solid line) and $\delta_1(\varepsilon_2)$ (right-handed ordinate axis, dashed line). From the graph we can deduce that both dependencies $\omega_2(\varepsilon_2)$ and $\delta_1(\varepsilon_2)$ are monotonically decreasing functions. Also, it's possible to see that by increasing ε_2 the quantity of ω_2 advances to the resonant frequency $\Omega_{\perp} = 1.2$.

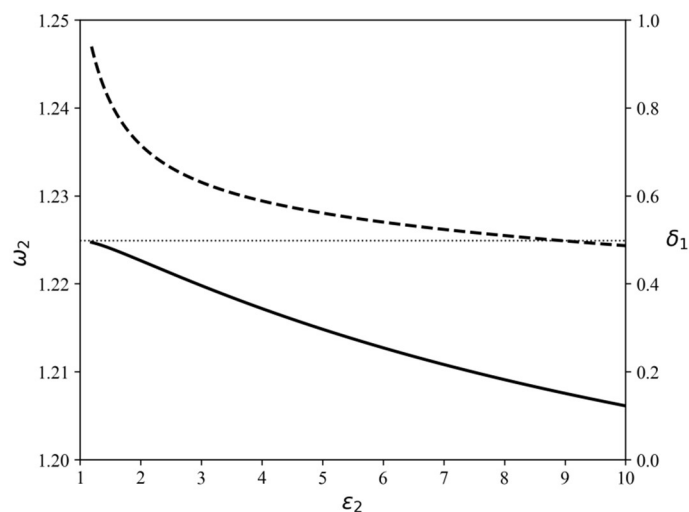


Figure 7. Dependencies $\omega_2(\varepsilon_2)$ (left-handed ordinate axis, solid line) and $\delta_1(\varepsilon_2)$ (right-handed ordinate axis dashed lines) corresponding to $R_p = 0$ for $\phi = 90^\circ$, $\theta = 45^\circ$, $\varepsilon_3 = 2.0$, $\delta_2 \approx 2.224$

4. CONCLUSIONS

It was shown that the dielectric coating of the solid-state structure uniaxial-plasmonic metasurface-dielectric-metal significantly influence the effect of reflectionless incidence of the p -polarized electromagnetic waves. The conditions were studied under which the effect of the non-reflective incidence of p -polarized wave can be observed depending on the dielectric permittivity of the coating. We established that increasing coating permittivity causes the frequency at which the effect arising to shift closer to the resonant frequency Ω_{\parallel} (for $\varphi = 0^\circ$) or to the frequency Ω_{\perp} (for $\varphi = 90^\circ$).

In addition, the thicknesses of the coating δ_1 were founded required for the reflectionless incidence of p -polarized wave. We also analysed dependency between δ_1 and dielectric permittivity of the coating ε_2 . It was determined that by increasing the permittivity of the coating ε_2 , we end up with lower thickness δ_1 , that is required to observe the effect of non-reflective incidence. Moreover, we found that, this holds true not only for the case when the plane of incidence of the electromagnetic wave is parallel to the principal symmetry axis of plasmonic metasurface ($\varphi = 0^\circ$), but also if the plane of incidence is perpendicular to the principal symmetry axis ($\varphi = 90^\circ$).

Studied effects can be applied for designing conceptually new types of optical and nanoelectronic equipment with unique practical characteristics.

ORCID

Mykola M. Biletskiy, <https://orcid.org/0000-0002-3194-7251>; Ivan D. Popovych, <https://orcid.org/0009-0000-2539-0373>

REFERENCES

- [1] K. Sakoda, *Electromagnetic Metamaterials. Modern Insights into Macroscopic Electromagnetic Fields*, (Springer, 2019). <https://doi.org/10.1007/978-981-13-8649-7>
- [2] B.E.A. Saleh, and M.C. Teich, *Fundamentals of Photonics*, (Wiley, 2019).
- [3] J. Hao, Y. Yuan, L. Ran, T. Jiang, J.A. Kong, C.T. Chan, and L. Zhou, "Manipulating Electromagnetic Wave Polarizations by Anisotropic Metamaterials," *Phys. Rev. Lett.* **99**, 063908 (2007). <https://doi.org/10.1103/PhysRevLett.99.063908>
- [4] N.N. Beletskii, and I.D. Popovich, "Influence of uniaxial plasmon metasurface on antireflection properties of dielectric layer," *Radio Physics and Radio Astronomy*, **27**(1), 75-80 (2022). <https://doi.org/10.15407/rpra22.01.075> (in Ukrainian).
- [5] M.M. Beletskii, and I.D. Popovych, "Changes in Electromagnetic Wave Polarization Resulting from its Reflection at a Uniaxial Plasmonic Metasurface on Top of a Dielectric Layer," *Radio Physics and Radio Astronomy*, **27**(2), 73-80 (2022). <https://doi.org/10.15407/rpra22.02>
- [6] M.M. Beletskii, and I.D. Popovych, "Non-reflective incidence of p -polarized electromagnetic waves on the solidstate structure "uniaxial plasmonic metasurface-dielectric layer-metal",," *Radio Physics and Radio Astronomy*, **28**(2), 166-173 (2023). <https://doi.org/10.15407/rpra28.02.166>

ПАДІННЯ БЕЗ ВІДОБРАЖЕННЯ *p*-ПОЛЯРИЗОВАНОЇ ЕЛЕКТРОМАГНІТНОЇ ХВИЛІ НА ТВЕРДОТІЛЬНУ СТРУКТУРУ “ПОКРИТТЯ-ОДНОВІСНА-ПЛАЗМОННА МЕТАПОВЕРХНЯ-ДІЕЛЕКТРИК МЕТАЛ”

Микола М. Білецький, Іван Д. Попович

Інститут радіофізики та електроніки ім. О.Я. Усикова НАН України, 12, вул. Акад. Проскури, Харків, 61085, Україна

У роботі досліджені ефекти, що виникають при падінні *p*-поляризованої електромагнітної хвилі на твердотіlnу структуру “покриття-одновісна плазмонна метаповерхня-діелектрик-метал”. Метою роботи є дослідження впливу покриття твердотіlnої структури “одновісна плазмонна метаповерхня-діелектрик-метал” на ефект падіння *p*-поляризованих електромагнітних хвиль без відображення. Для знаходження умов виникнення ефекту падіння без відображення *p*-поляризованої електромагнітної хвилі на структуру “покриття-одновісна плазмонна метаповерхня-діелектрик-метал” було використано чисельне моделювання. За допомогою цього методу було визначено параметри покриття, що дають змогу спостерігати ефект падіння без відображення *p*-поляризованих електромагнітних хвиль. Було знайдено, що діелектричне покриття твердотіlnої структури, яка розглядалася, має істотний вплив на ефект безвідбівного падіння *p*-поляризованих хвиль. Показано, що діелектрична проникність покриття змінює частоту спостереження цього ефекту. Визначена залежність між проникністю та товщиною покриття, яка необхідна для виникнення ефекту падіння без відображення *p*-поляризованих електромагнітних хвиль. Проведене в роботі дослідження має великий науковий та практичний інтерес. Досліджені в роботі структури можна використати для створення принципово нових пристроїв оптики та наноелектроніки.

Ключові слова: діелектричне покриття; *p*-поляризовані електромагнітні хвилі; одновісна плазмонна метаповерхня; падіння без відображення

A SIMPLISTIC ANALYTICAL MODEL FOR HYDROGEN SURFACE COVERAGE UNDER THE INFLUENCE OF VARIOUS SURFACE-RELATED PROCESSES AND ION BOMBARDMENT

 Ivan I. Okseniuk*,  Viktor O. Litvinov,  Dmytro I. Shevchenko,  Inna O. Afanasieva,  Valentyn V. Bobkov

V.N. Karazin Kharkiv National University, 4, Svobody Sq., Kharkiv, 61022, Ukraine

*Corresponding Author, e-mail: ivanokseniuk@karazin.ua

Received April 1, 2024; revised April 22, 2024; accepted May 7, 2024

The paper describes a simple analytical model that allows the calculation of hydrogen surface coverage under the influence of several processes that can co-occur during the ion-beam bombardment/sputter analysis of a sample surface, in particular during analysis by secondary ion mass spectrometry (SIMS). The model considers processes of dissociative adsorption, desorption, absorption from the surface into the sample volume, and removal by ion bombardment. After describing the model, we provide some examples of its practical applications for interpretation of the experimental results obtained during *in situ* SIMS studies of hydrogen interaction with the hydrogen-storage alloys TiFe, Zr₂Fe, and with nickel. In the examples, some quantitative characteristics of surface-related processes involving hydrogen, such as hydrogen sputtering rate, activation energy of hydrogen desorption and absorption, have been successfully determined using various model approaches.

Keywords: Secondary ion mass spectrometry; Hydrogen storage; Sputtering; Adsorption; Desorption; Ion bombardment; Kinetics

PACS: 34.35.a, 68.43.-h, 68.49.Sf, 79.20.Rf

1. INTRODUCTION

Among rather few other surface analysis techniques, secondary ion mass spectrometry (SIMS) is capable of direct detection and imaging of hydrogen isotopes with high sensitivity. Hydrogen analysis with SIMS can sometimes be complicated by the occurrence of such processes as adsorption of hydrogen-containing molecules on the surface, diffusion, segregation, and desorption of hydrogen directly during the analysis [1–9]. Although the ease of occurrence of such processes constitutes an obstacle for hydrogen quantification and localization, it can be exploited to study those processes themselves since they are of great importance in certain fields: hydrogen interaction with hydrogen-storage materials [10] being one of such fields.

In our previous studies [11–15] of the interaction of hydrogen-storage alloys with hydrogen and oxygen using SIMS, it was found that the emission intensity of hydrogen-containing secondary ions can be used to monitor the presence and changes in concentration of hydrogen on the surface in a fairly wide range of experimental conditions. In earlier studies [16–19], SIMS had been already utilized to determine the characteristics of hydrogen interaction with metals. Papers [12,13,16–18,20] exemplify that the SIMS technique indeed provides good opportunities for *in situ* characterization of hydrogen interaction processes with metals and alloys.

However, difficulties in the analysis of such experimental results arise when several processes affecting hydrogen concentration on the surface occur simultaneously during the measurements. Therefore, to understand how hydrogen surface concentration is affected by the action and characteristics of each such process, an analytical model was developed that considers the influence of several processes that can occur within the range of experimental conditions of SIMS studies [12,13]. The analysis with the developed model allows distinguishing and predicting (to a certain extent) the results of action of each process, which, ultimately, provides grounds for appropriate interpretation of the experimental results.

The model considers processes of hydrogen dissociative adsorption, recombinative desorption, dissolution/absorption from surface chemisorption sites into the bulk, and processes of ion beam removal/sputtering. One quite commonly occurring process, that we omitted from consideration in the model, is hydrogen segregation on the surface. To include the surface segregation, hydrogen in the bulk has to be considered and characterized, which is generally a rather complex task when real samples (apart from near perfect single-crystals) are studied [2,4,5,21,22]. In our studies, the samples are usually polycrystalline alloys, often with complex constitution and numerous uncharacterized bulk defects/features what may influence hydrogen in the bulk. Other than our SIMS instrument we don't have other means to characterize bulk-hydrogen at small concentrations (as relevant for our experimental conditions), and without having the details about bulk hydrogen we don't attempt describing it. Therefore, the model considers only a comparably small presence of bulk hydrogen and its appearance on the surface mainly as a result of the ion beam etching of the sample. A very limited approach to segregation is described in **Section 3.5**.

Although the model was intended mainly to help with *in situ* SIMS studies of hydrogen interaction with a sample as exemplified in **Section 3**, recent studies [23–25] reported that the use of H₂ flooding might be also beneficial in SIMS multilayer depth profiling and elemental quantification. In such measurements the balance between hydrogen adsorption

and beam-etching will be of main focus although other processes can co-occur as well, therefore the usage of such a model can be fruitful in this application. Besides that, the model may also have some relevance for vacuum devices operation where hydrogen adsorption and desorption from surfaces are important factors affecting vacuum conditions and operation. In particular, accelerators and plasma devices have surfaces exposed to energetic irradiation by ions, electrons, or photons. If in accelerators the ion-stimulated desorption is a known and actively studied issue [26], there are plasma devices for which irradiation-stimulated hydrogen desorption is an essential part of their operation [27–29]. Recently, a similar but much more sophisticated and material-specific model was developed for hydrogen interaction with tungsten in relevance to magnetic confinement plasma fusion devices [30]. For such applications, the presented here model, one way or another, has to be complemented by an appropriate consideration of hydrogen within the solid's bulk.

2. DESCRIPTION OF THE MODEL

2.1. Main Model Equation and Processes Representation

The basis of the model is an equation that establishes the relation of the hydrogen concentration changes on surface over time under the influence of a number of possible processes. Each considered process has its representative term in equation (1).

$$\frac{d\theta}{dt} = 2aF(1 - \theta)^2 - 2b\theta^2 - D\theta - s_1j_p\theta - 2s_2j_p\theta^2 + s_0j_p\theta_0. \quad (1)$$

Here $\theta = c_H/c_{H_{\max}}$ is the relative coverage of the surface by chemisorbed hydrogen atoms, defined as a ratio of the hydrogen concentration (c_H) to a certain maximal value of the concentration ($c_{H_{\max}}$).

The first term is responsible for the increase of coverage due to dissociative adsorption of hydrogen molecules. It takes into account the decrease in the sticking coefficient with increasing coverage $(1-\theta)^2$ [31], which arises from the necessity for two unoccupied adsorption sites according to Langmuir's model of dissociative adsorption of diatomic molecules. a is the initial sticking probability, F is the flow of hydrogen molecules into the area of one adsorption site. F is calculated by:

$$F = \frac{1}{n_{\text{at}}} \times \frac{p_{\text{H}_2}}{\sqrt{2\pi m_{\text{H}_2} k_B T_{\text{H}_2}}}, \quad (2)$$

where p_{H_2} is hydrogen partial pressure near the sample surface, n_{at} is the density of hydrogen adsorption sites on the surface. It is commonly assumed that n_{at} is roughly equal (it may differ by 2-3 times) to the density of substrate surface atoms. m_{H_2} is the mass of a hydrogen molecule, T_{H_2} is the hydrogen gas temperature, k_B is Boltzmann constant. If the presence of surface roughness is presumed, a coefficient-multiplier should be introduced for this term (and, perhaps, for the other terms too).

The second term of equation (1) is responsible for removing hydrogen from the surface by thermally-stimulated recombinative desorption. Hence, b is the rate coefficient of desorption, which in the simplest form can be described similarly to the Polanyi-Wigner equation, widely used in the temperature-programmed desorption (TPD) analysis. So b can be expressed as:

$$b = \frac{b_0}{2} \exp \left\{ \frac{-E_a}{RT} \right\}, \quad (3)$$

where $b_0/2$ is the pre-exponential factor, E_a is the activation energy of desorption, T is the sample temperature.

The next term ($-D\theta$) describes the dissolution/absorption of hydrogen from the surface into the bulk of the sample. Accordingly, D is the frequency of hydrogen atoms absorption from the surface into the volume. In our experimental SIMS practice, some diffusion of hydrogen atoms from the outmost surface layer inward of the sample occurred for practically every studied intermetallic alloy: LaNi₅ and its Al-, Mn-modified variants [32], TiFe [12], Zr-based non-evaporable getter alloys [13]. The degree of such absorption below the surface was different based on alloy characteristics. For three Zr-based alloys, the absorbed amount was roughly proportional to hydrogen exposure ($p\{\text{H}_2\} \times t$), was seemingly unlimited at studied hydrogen pressures (below 10⁴ Torr, 1 Torr = 133.322Pa), and was regarded as true bulk-absorption. For other studied alloys, only a limited amount of hydrogen migrated to subsurface. Estimated amount of such subsurface-migrated hydrogen was comparable to or few times higher than the amount of surface-chemisorbed hydrogen, and it could not be increased by increasing hydrogen exposure. Such limited absorption was characteristic to the alloys which had relatively small enthalpies of their hydrides or hydrogen solid solution, which equilibrium pressure are of order of the atmospheric pressure that is many orders of magnitude higher than the studied $p\{\text{H}_2\}$ range. Whereas, Zr-based getter alloys which absorbed hydrogen in bulk are characterized by large-value negative enthalpies, resulting in the high stability of hydrides/dissolved hydrogen at room temperature-UHV conditions. For most of the alloys dissolution/migration rate increased with temperature indicating the presence of the activation barrier.

The following two terms ($-s_1j_p\theta$ and $-2s_2j_p\theta^2$) describe the removal of hydrogen from the surface as a result of ion beam bombardment. Therefore, these terms are proportional to the ion beam current density (j_p). The term $-s_1j_p\theta$ represents all mechanisms of ion beam induced removal the rate of which is proportional to hydrogen coverage: collision cascade sputtering would be one of such mechanisms. The term $-2s_2j_p\theta^2$ represents the removal by ion beam induced

recombinative desorption (i.e. in the form of H_2 molecules), therefore it is proportional to hydrogen coverage squared: such removal may occur at high hydrogen coverage since the energy needed to form and remove an H_2 molecule from the surface is substantially smaller than the energy needed to remove an alone H atom. The coefficients s_1 and s_2 represent the effectiveness of the corresponding removal rates.

Regarding the ion beam sputtering of hydrogen, the authors of paper [33] provided theoretical argumentation for ineffectiveness of the collision cascade sputtering in the case of chemisorbed hydrogen atoms on the surface of metals. According to the argumentation, the amount of kinetic energy transferred to a hydrogen atom in a collision with a metal atom having typical values of the kinetic energy in the cascade is not enough to overcome the bonding of hydrogen atom to the surface. The transferred energy is reduced due to the large mass difference between hydrogen and metal atoms. However, the experimental findings about the ion beam removal rates of chemisorbed hydrogen at small surface coverages indicate that the rate of hydrogen removal is instead 20-30% higher than the removal rate of chemisorbed oxygen² [12], and these rates are practically of the same order as the sputtering rate of metal atoms. Such rather high effectiveness of hydrogen removal may be a result of hydrogen sputtering in the form of molecules MeH formed with sputtered metal atoms Me, as proposed for the case of sputtering of oxygen-metal systems [34]. In such a case, there is no need to transfer the kinetic energy to hydrogen atoms to detach them from the surface, instead, hydrogen atoms only need to replace the bond with the surface by a bond with a metal atom that leaves the surface during a sputtering event. Known data indicate [35] that the binding energy values are comparable for the case of hydrogen atoms on metal surfaces and for the case of hydrogen atoms within a molecule with a metal atom. The existence of such a mechanism is confirmed by the presence of hydrogen molecules with metal and semiconductor atoms in the mass spectra of neutral sputtered particles from surfaces with the hydrogen presence [36,37], and also confirmed by the presence of polyatomic hydrogen-containing secondary ions in the mass spectra obtained in [11–14].

Regarding the removal of hydrogen by recombinative desorption of H_2 molecules induced by ion bombardment, such a removal may occur within very short time after an ion impact on the surface as a result of electrons excitation around the impact place. Such electronic excitations (if ~ 10 keV ions can induce them) are known [38,39] to desorb hydrogen molecules from surfaces including surfaces that adsorb hydrogen dissociatively, although such desorption can deviate from the second-order kinetics [38,39]. Another pathway of ion-induced H_2 desorption might be provided at the ‘late’ stages of collision cascades. At these stages, the energy of an impacting ion becomes distributed among many target atoms in the vicinity of the impact, and although individual atoms no longer have enough energy for knock-off sputtering, the activation energy of the order of 1 eV may still be supplied for associative desorption of H_2 molecules. Studies [40,41] show that the ‘effective temperature’ of the near-surface region excited by an impact of ions with the energy of an order of 10 keV can reach thousands of K, which can promote the thermal-like hydrogen desorption.

The last term $s_0 j_p \theta$ introduces the hydrogen contained in the sample volume and its appearance on the surface as a result of the sample material removal by ion beam sputtering, i.e. as a result of sample erosion/etching and gradual ‘shifting’ of the surface into the depth of the sample. Small amount of homogeneously distributed immobile hydrogen in the sample bulk is assumed by this term. If $s_0 j_p$ represents the frequency of ion beam removal of one monolayer of the sample atoms then θ_0 represents the coverage-equivalent hydrogen content per one monolayer in the sample volume.

2.2. The Steady State Solution

Under conditions of dynamic equilibrium, i.e. when hydrogen concentration on the surface is constant, the sum of all components in (1) is zero. Considering all process rate constants as independent of time and coverage, expression (1) is a quadratic equation for θ . Therefore, it is possible to obtain a solution (4) that expresses the coverage dependence on all coefficients present in (1).

$$\theta = \frac{D+4aF+s_1 j_p - \sqrt{(D+4aF+s_1 j_p)^2 + 8(b-aF+s_2 j_p)(2aF+s_0 j_p \theta_0)}}{4(-b+aF-s_2 j_p)} \quad (4)$$

If there is no absorption into the bulk ($D=0$) and also there is no thermally-stimulated desorption ($b=0$), expression (4) can be rewritten as:

$$\theta = \frac{4a \frac{F}{j_p} + s_1 - \sqrt{8a \frac{F}{j_p} (s_1 + 2s_2 - s_0 \theta_0) + s_1^2 + 8s_2 s_0 \theta_0}}{4a \frac{F}{j_p} - 4s_2}, \quad (5)$$

in which, the current density of the ion beam and hydrogen partial pressure are present only in a form of the ratio F/j_p . That is, if an x-fold change in the current density is accompanied by the same x-fold change in the hydrogen partial pressure, then the coverage remains unchanged. Such a result was indeed obtained more than once for some of the studied alloys [12,13] if not heated.

² Note that the mass of oxygen atoms is only several times smaller than the mass of metal atoms, not dozen times smaller as in the case of hydrogen atoms.

2.3. Calculated Effects of Different Processes on Steady State Surface Coverage

Fig. 1 (a-d) shows the dependences of surface coverage on hydrogen pressure, as calculated using expression (4). To illustrate the influence of various processes, calculations were done with a set of parameters values that characterize the processes included in equation (4). Fig. 1a shows how the residual/bulk hydrogen concentration affects the coverage dependence on hydrogen pressure.

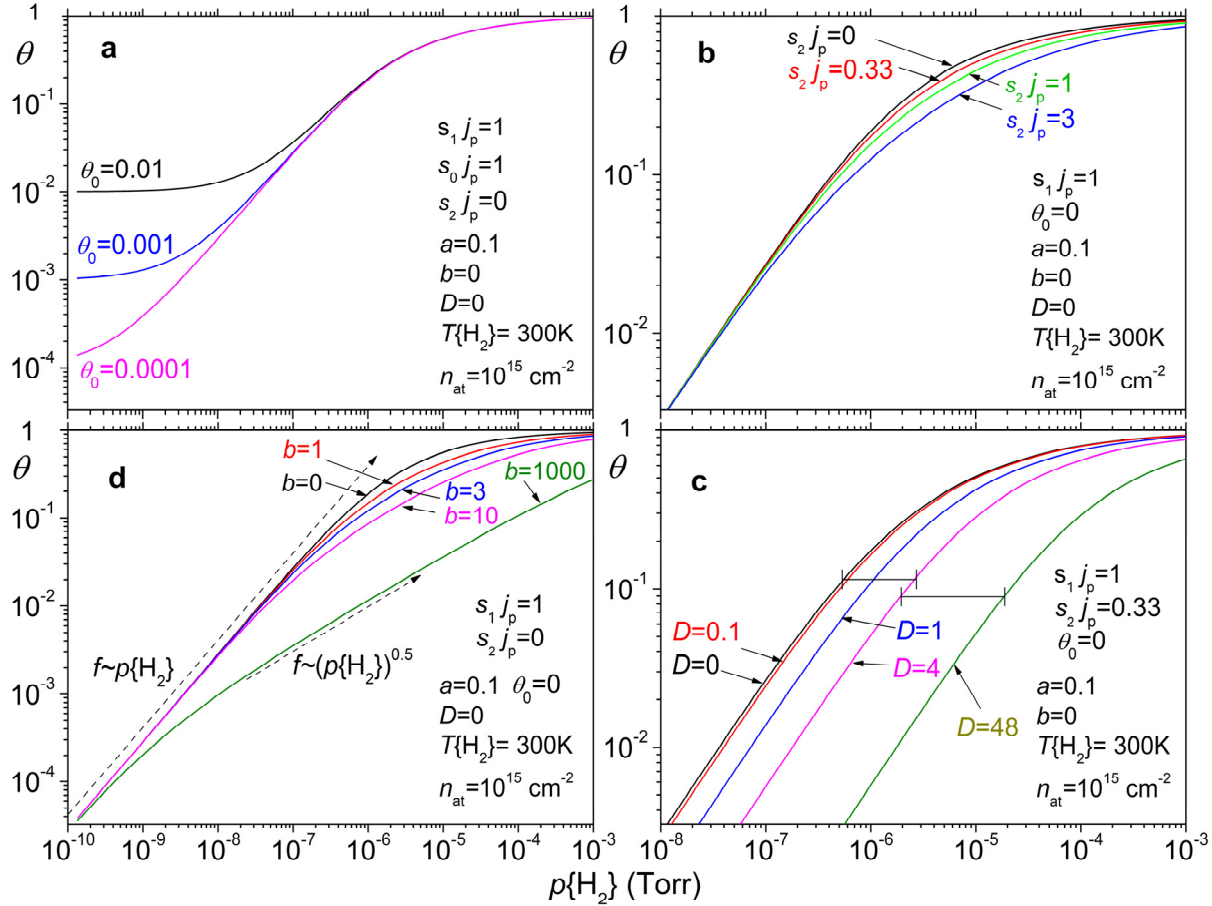


Figure 1. The dependences of surface coverage by adsorbed hydrogen atoms on the hydrogen gas pressure as calculated using expression (4) for a set of values of the parameters that characterize the processes included in the model. **a:** influence of the residual hydrogen presence, **b:** influence of the ion-induced recombinative desorption, **c:** influence of the absorption rate from the surface into the bulk, **d:** influence of the rate of thermally-stimulated recombinative desorption.

Fig. 1b illustrates how the rate of hydrogen removal by ion-induced recombinative desorption influences the coverage dependence on pressure. The influence of ion-induced desorption manifests as a decrease of the rate with which the concentration increases: It slows down the asymptotic approaching to ‘the saturation’, but its influence diminishes at low coverages due to the second order kinetics of the desorption.

The main effect of the presence of absorption from surface to bulk is the decrease in surface coverage at the same hydrogen pressure (Fig. 1c). As the rate of absorption increases, the dependence curves shift toward higher pressures, since to achieve a certain concentration, the part of hydrogen which is removed from the surface due to absorption must be compensated by an increase in the amount of adsorbed hydrogen, which is achieved when the pressure is increased.

The influence of the rate of thermally-stimulated desorption is illustrated in Fig. 1d. Relatively small values of the desorption rate produce the effect which has been already described above in the explanation for Fig. 1b. However, the values of the desorption rate at high temperatures can be very large compared to the ion sputtering rate (the curve for $b=1000$ in Fig. 1d is an example). In such a case, the dependence of coverage on the pressure at middle-to-small coverages becomes proportional to the square root of the pressure instead of the linear dependence on the pressure, which is in accordance with Sievert's law. This change from the linear to the square root dependence can be used to identify the recombinative desorption process when it dominates over other hydrogen removal processes.

3. PRACTICAL APPLICATIONS IN SIMS MEASUREMENTS

The main aim of the development of the model was its application for interpretation of experimental results of hydrogen interaction with alloys or metals obtained during *in situ* SIMS measurements. Therefore, practical application of the model for processes analysis as well as for obtaining quantitative estimates of the characteristics of hydrogen interaction with few studied samples are described below.

3.1. A Time-Dependent Solution Characterizing Ion Beam Sputtering

At low coverages, the rate coefficient of linear hydrogen removal by ion bombardment $j_p s_1$ can be determined experimentally. In the absence of desorption ($b=0$), the other terms in (1) proportional to θ^2 can be neglected at low coverages. Besides that, if there is no absorption into the bulk ($D=0$), then equation (1) can be simplified to the form:

$$\frac{d\theta}{dt} = -\theta(4aF + s_1 j_p) + 2aF + s_0 j_p \theta_0. \tag{6}$$

If only θ depends on time, then the solution of (6) is:

$$\theta = C_0 \exp\{-(4aF + s_1 j_p)t\} + \frac{2aF + s_0 j_p \theta_0}{4aF + s_1 j_p}. \tag{7}$$

At low adsorption rates (at low hydrogen pressures) compared to the sputtering rate, expression (7) can be represented in the form:

$$\theta \approx C_0 \exp\{-s_1 j_p t\} + C_1, \tag{8}$$

that is, in the form of an exponential decay function, where C_0+C_1 is the initial value of the coverage at the beginning of sputtering, while C_1 is the residual coverage after prolonged sputtering. Using this function for fitting the dependences of H^- emission intensity on time measured during the sputtering of the chemisorbed hydrogen that was beforehand adsorbed at small exposures (<0.3 Langmuir), it is possible to determine the value of $s_1 j_p$, or the value of characteristic removal time $\tau = (s_1 j_p)^{-1}$, as shown in Fig. 2.

It should be noted that it is potentially possible to experimentally characterize also the quadratic removal rate $s_2 j_p$ in similar experiments if the coverage (exposure) is not limited to low amounts but extended to the saturation. However, the experiment results with the TiFe and few other alloys indicated that some amount of hydrogen can diffuse into subsurface sites or into the bulk, and this diffusion is facilitated by sample temperature or by high surface coverage [13,14,32]. Therefore, in such cases, the assumption that hydrogen is adsorbed only within the topmost surface monolayer is not valid anymore. Another possible complication is the nonlinearity of secondary ion yield relation to hydrogen coverage [12]. Due to these factors, the analysis of hydrogen removal was not attempted at high coverages.

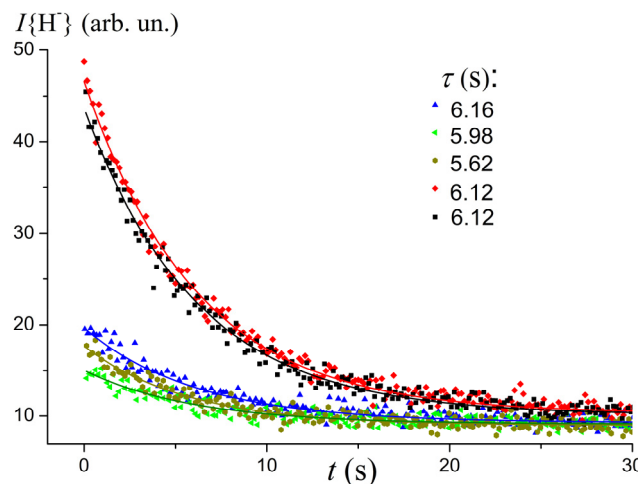


Figure 2. Points: dependences of the emission intensity of H^- secondary ions on sputtering time as measured after various small exposures of the TiFe alloy surface in hydrogen atmosphere. **Lines:** curves of the exponential decay function (8) used to approximate the measured dependences. The values of characteristic removal time τ obtained from the approximations are also listed.

3.2. Applications for Adsorption, Sputtering, and Desorption Characterization

Fig. 3 shows examples of the approximations of experimental data using expressions (2-4) for the dependences of hydrogen-containing secondary ions emission intensity on hydrogen pressure (Fig. 3a) and the sample temperature (Fig. 3b) which were measured with the TiFe alloy sample. Fig. 3a shows the measured points and the fitting curves for two types of secondary ions: $^{48}\text{TiH}^+$ and H^- . The corresponding values of adsorption and sputtering parameters determined from their approximations are also listed. To compare the emission intensities of the secondary ions with the amount of hydrogen coverage, the correspondence of $\theta = 1$ to intensity values of ~ 7700 relative units was used for $^{48}\text{TiH}^+$ and ~ 600 relative units for H^- . Such values were determined by measuring the intensities after high ($>10^4$ Langmuir) surface exposures in hydrogen atmosphere without ion bombardment just after the beginning of bombardment. The ion bombardment was initiated with substantially reduced beam current density to minimize hydrogen removal, thus appropriate normalization of intensity values using the ratio between the nominal and the reduced beam current densities was done.

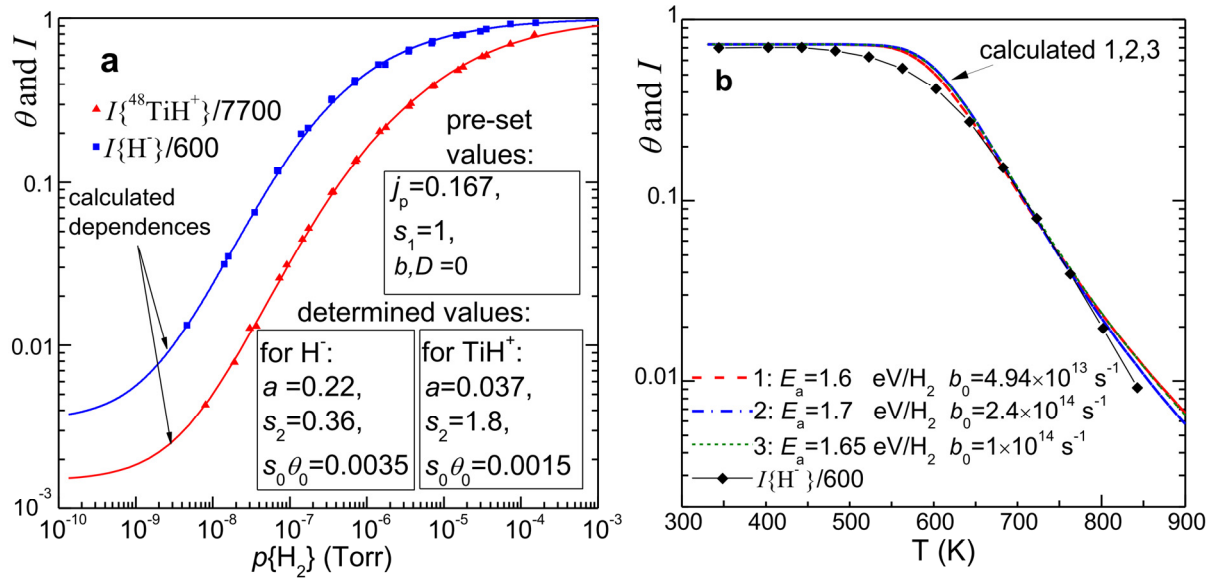


Figure 3. Approximations of the measured dependences for the TiFe alloy. **a:** secondary ion emission intensity dependences $I\{^{48}\text{TiH}^+\}$ and $I\{\text{H}^-\}$ on hydrogen pressure and their fits using formula (4), **b:** $I\{\text{H}^-\}$ dependence on the sample temperature at hydrogen pressure $p\{\text{H}_2\} = 7.1 \times 10^{-6}$ Torr and its fits using formulae (2-4), (assuming $D=0$).

Besides the intensity scale factors, other pre-set parameters in the approximations were the rate coefficient of hydrogen removal: $s_1 j_p = 0.167 \text{ s}^{-1}$ as determined from the results shown in Fig. 2, and the value $n_{\text{at}} = 1.8 \times 10^{15} \text{ cm}^{-2}$ used in expression (2) (it was calculated using the density of TiFe alloy $6.5 \text{ g} \times \text{cm}^{-3}$ [42]), assuming that it is equal to the density of possible hydrogen atom chemisorption sites on the alloy surface. Other parameters values included in equation (4), namely the sticking probability, the rate coefficient of ion-stimulated H_2 desorption, the contribution of hydrogen content in the sample bulk to the surface coverage, were determined when approximating the measured dependences on hydrogen pressure by formula (4), as shown in Fig. 3a, provided that absorption ($D=0$) and desorption ($b=0$) are effectively absent.

The parameters values determined by the approximation differ quite substantially when using $I\{^{48}\text{TiH}^+\}$ or $I\{\text{H}^-\}$ dependences. Nevertheless, both values of the sticking probability correspond to the range of typical values for many transition metals [35,43]. The relatively large value of s_2/s_1 determined from the approximation using $I\{^{48}\text{TiH}^+\}$ may indicate that, starting from the coverage $\theta \geq 0.278$, most of the hydrogen is removed from the surface by ion-stimulated recombinative desorption.

The difference in the measured pressure dependences for TiH^+ and H^- is because the yields of secondary ions either TiH^+ or H^- (or both of them) nonlinearly depend on the hydrogen surface concentration when the concentration is high. The possible reasons for the nonlinearity are discussed in [12]. Since the secondary ion emission intensity values corresponding to the coverage saturation (7700 rel. units for TiH^+ and 600 rel. units for H^-) were determined at ‘maximal’ coverage, the nonlinearity is included in the dynamic range of the ion emission intensity and therefore affects the values resulting from the fittings, including the residual hydrogen concentration (θ_0) and sticking probability (a), even that the dependence lines for $I\{\text{TiH}^+\}$ and $I\{\text{H}^-\}$ in Fig. 3a are parallel (can match each other when shifted) at low concentrations. Unfortunately, it is not possible to determine whether the yield dependences of these secondary ions on the concentration are linear or not with the available experimental data. In order to obtain reliable parameters values by doing such approximations as shown in Fig. 3, the knowledge of the exact relationship between the secondary ion emission intensities and the hydrogen concentration is required. To obtain such knowledge, it is necessary either to know the value of the sticking probability of hydrogen and its precise dependence on coverage or to use another quantitative method for in situ calibration, such as temperature programmed desorption (TPD) or nuclear reaction analysis (NRA) [16,17,44–46].

Fig. 3b shows the measured points of the temperature dependence of secondary ion emission intensity and several variants of their approximation using expressions (2-4) in the presence of thermally-stimulated hydrogen desorption from the surface. The values of the desorption activation energy E_a and the pre-exponential factor b_0 are also given for each approximation variant. At coverages $\theta \leq 0.2$, the calculated dependences of the coverage on the temperature coincide quite well with the measured points. However, at higher coverages, experimental results indicate that desorption begins at significantly lower temperatures than predicted by the calculations. Most probably this is a result of a reduction of the desorption activation energy at high coverages, which has not been accounted for in (3). This reduction may be related to the desorption from less strongly bound states on the surface, or related to the existence of repulsive interaction between the adsorbed hydrogen atoms [47–49]. Another problem concerning specifically the approximation in Fig. 3b is the presence of a ‘compensation effect’ [47,50], which consists in that different combinations of the values of desorption activation energy E_a and of the pre-exponential factor b_0 produce very similar calculated desorption rate dependences. The accuracy of the experimental data, therefore, allows fitting the data by a certain range of different combinations of E_a and b_0 , as illustrated by curves 1-3. In addition, possible non-linearity of the secondary ion yield relation to the coverage

can also contribute to the mismatch of desorption rate at high coverages. Thus, unfortunately, in the absence of an accurately calibrated relation between the ion yield and hydrogen coverage/concentration, the estimates of the parameters obtained with the approximations in Fig.3 are not reliable.

3.3. Constant-Coverage Approach to Characterize Thermally-Activated Desorption Process

A possible approach that can bypass the mentioned earlier ‘compensation effect’ and determine the value of the desorption activation energy separately is realized by setting up the desorption experiment in the constant coverage mode. The calibration of secondary ion yield is also unnecessary unless the activation energy needs to be tied to a specific coverage value. Although, one should make sure the relationship between the ion yield and hydrogen concentration on the surface is not affected by the sample temperature.

When a dynamic equilibrium is established among the action of a number of processes, which results in a certain surface coverage by chemisorbed hydrogen, and when only the desorption rate coefficient depends on temperature³, the hydrogen pressure near the surface can be expressed using relations (1-3) as follows:

$$p = c_1 \exp\left\{\frac{-E_a}{RT}\right\} + p_0, \quad (9)$$

where, E_a is the desorption activation energy, T is the surface temperature, c_1, p_0 are constants that depend on the coverage and the parameters values in (1-3). Formula (9) expresses the necessity to increase pressure exponentially with temperature in order to compensate for the increasing desorption rate while maintaining the same coverage.

The experiments testing such approach were performed with a polycrystalline nickel sample under experimental conditions similar to those described in [12]. During the experiments, hydrogen pressure was adjusted and measured following each stepwise increase of the sample temperature, in order to maintain constant coverage. The $^{58}\text{Ni}_2\text{H}^+$ emission intensity was used as the main indicator of coverage. The examples of the measured dependences of hydrogen gas pressure on the sample temperature are shown in Fig. 4a.

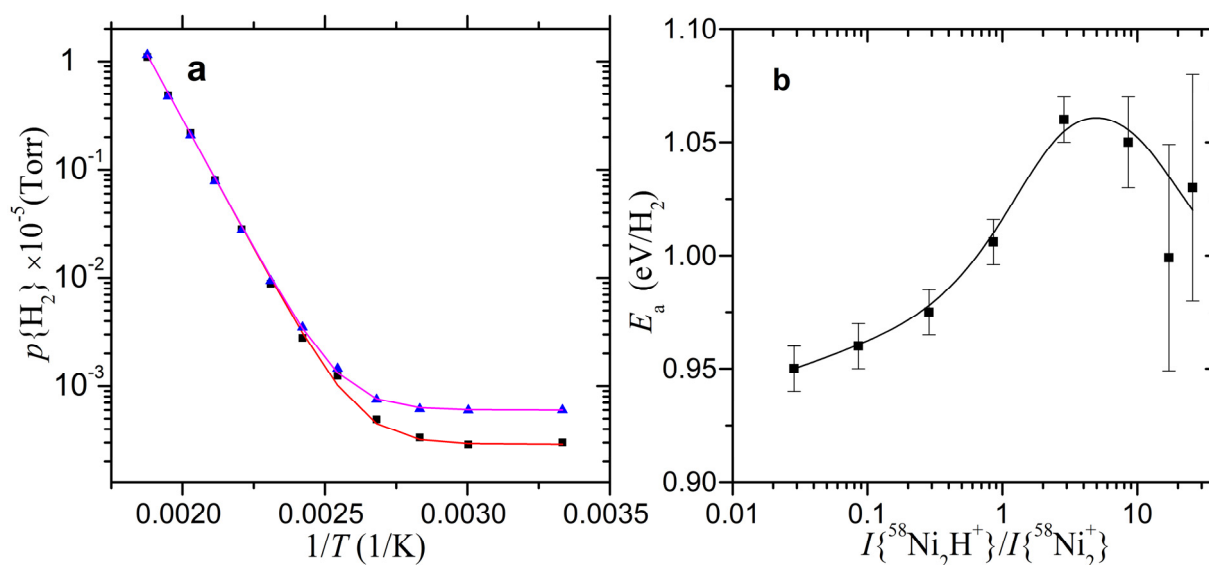


Figure 4. a: Dependences of the hydrogen gas pressure needed to maintain the same surface coverage with chemisorbed hydrogen on the reciprocal temperature of the nickel sample. Points denote experimental data, lines correspond to its fit with formula (9). **b:** Dependence of the obtained hydrogen desorption activation energy E_a on the ratio of secondary ion emission intensity $I\{^{58}\text{Ni}_2\text{H}^+\}/I\{^{58}\text{Ni}_2^+\}$, serving as a relative measure of the surface coverage with hydrogen.

The plotted two sets of data were obtained at twofold-different values of ion beam current density but the same coverage. The logarithmic scale plot of hydrogen pressure on the reciprocal sample temperature gives a straight line indicating the existence of exponential dependence in the temperature range where the desorption rate dominates over the ion-induced removal. Fitting the data (see the lines in Fig. 4a) with function (9) allows one to determine the desorption activation energy E_a . Such measurements and approximations were carried out at different hydrogen coverages, which thereby provided information on how E_a changes over about two orders of the coverage amount. Fig. 4b shows the dependence of E_a on the secondary ion emission intensity ratio $I\{^{58}\text{Ni}_2\text{H}^+\}/I\{^{58}\text{Ni}_2^+\}$, which serves as an instrument-independent measure of the relative surface coverage by chemisorbed hydrogen [17,18]. The obtained values are close to the known values of $E_a = 1 \text{ eV}/\text{H}_2$ for Ni(111), Ni(100) [43], whereas the increase of H_2 adsorption heat (which is related to the measured here E_a) from small to moderate coverages was also observed for Ni(110) [51].

³ if there is effectively no absorption, and neither the rate of ion-induced hydrogen removal nor the chemisorption sticking probability depend on the sample temperature, which is valid for the TiFe alloy, at least in the range of 300-500 K [12]

3.4. Characterizing Thermally-Activated Absorption/Dissolution Processes

The developed model was also applied to characterize hydrogen absorption/dissolution process, i.e. the transition of hydrogen atoms from the surface chemisorbed sites into the volume of the Zr_2Fe getter alloy sample [13]. In the studies series with Zr_2Fe , the dependences of emission intensities of several types of negative secondary ions on hydrogen pressure were measured at three sample temperatures. The bombarding ion beam current density j_p was reduced fivefold from the nominal during those measurements. Such measured dependences are shown in Fig. 5 for the secondary ions H^- , $^{56}FeH^-$, and $^{90}ZrH_2^-$. It was also found [13] that increasing the sample temperature above 300 K leads to a progressive increase in the efficiency of hydrogen absorption into the bulk of the alloy.

Following the model predictions, a substantial increase in the rate of hydrogen absorption from the surface into the depth of a sample causes a shift of the coverage dependence on the pressure towards higher pressures (Fig. 1c). Similar shift of the curves towards higher pressures is observed in the experimental results in Fig. 5 with increasing the sample temperature. For comparative purposes, the dependences measured at 513 K are additionally plotted in Fig. 5 with their hydrogen pressure values multiplied by 10 (hollow point symbols). These ‘shifted’ dependences approximately coincide with the dependences measured at 627 K, thus the dependences measured at 513 and 627 K are approximately parallel with ten times difference in the hydrogen pressure between them, which is similar to the parallel shifts predicted in Fig. 1c.

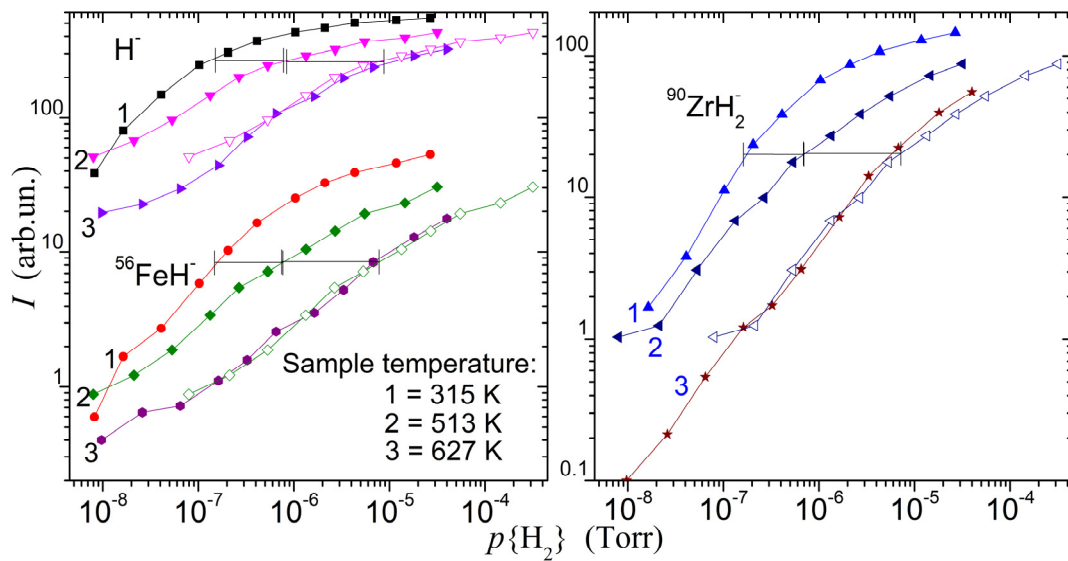


Figure 5. Dependences of the secondary ion emission intensity of negative hydrogen-containing secondary ions on hydrogen partial pressure measured at several temperatures of the Zr_2Fe alloy sample. For these measurements, the current density of the primary ion beam was fivefold-reduced ($s_{I_p} \sim 0.05 \text{ s}^{-1}$) from its nominal value.

Considering that the absorption of hydrogen from the surface chemisorption states into the bulk of the alloy is a thermally-activated process, it is possible to estimate the effective value of its activation energy from the available experimental results. Besides the desorption, expression (9) can be used for the evaluation of the absorption activation energy too. The values of c_1 , p_0 , and E_a can be found after selecting three hydrogen pressure values at each sample temperature that correspond to the same coverage. At 315 K, the hydrogen coverage is mostly limited by the ion beam removal, and the rate of hydrogen outflow into the bulk is comparatively small [13], thus in expression (9), the contribution from p_0 is dominant. At 513 and 627 K, the rate of hydrogen removal from the surface by absorption already exceeds several times the rate of its sputtering by ion beam, thus in expression (9), the contribution of $c_1 \exp\{-E_a/(RT)\}$ is dominant, which allows determining c_1 and E_a . The found value of the absorption activation energy is $E_a=0.61 \text{ eV}$ at hydrogen coverage around the middle of the investigated range. Since based on only three available points of hydrogen pressure it is impossible to confirm the presence of a straight-line segment on a logarithmic plot, similar to that in Fig. 4a, the found E_a value can be considered only as an estimate.

3.5. Characterizing the Surface Stage of Desorption of Bulk Absorbed Hydrogen

In such process, hydrogen atoms migrate from the volume of a metal/alloy to its surface (let's call it the bulk stage) where they recombine into H_2 molecules and desorb (the surface stage). The bulk stage can consist of other sub-stages such as H-detraping, hydride phase decomposition, diffusion and we won't consider the details of the bulk stage due to its general complexity and our inability to control/study it with SIMS. The surface stage is assumed to be the same as for the desorption of chemisorbed hydrogen, although the exceptions from this are possible. The hydrogen atoms migrating from the bulk to the surface are ‘segregating’ on the surface before the desorption in the same states as chemisorbed hydrogen. Therefore, in SIMS conditions, the processes included in equation (1) apply. Essentially, the surface receives a flow of ‘segregating’ hydrogen atoms from the bulk. This flow, in one of most simple ways, can be modelled by a term (10) equivalent to atomic (first order) adsorption and be added to the equation (1).

$$+k_s(1 - \theta). \quad (10)$$

Here k_s is the segregation frequency which depends on all of the bulk sub-stages, $(1-\theta)$ is the surface site availability factor. This process in isolation should produce increase of the coverage up to the saturation. In our SIMS experimental practice, it was never observed in isolation, but only simultaneously with other processes which makes it difficult to study. However, there had been experiments where it helped in studying the surface desorption stage.

Hydrogen absorbed in the bulk of the Zr_2Fe alloy could be desorbed by high-temperature heating of the sample. The desorption rate could be measured by gas mass spectrometer (TDS/TPD technique) and hydrogen coverage on the surface could be simultaneously monitored with H-containing secondary ion signal. Such experiments were presented in [13], although a round of similar experiments was conducted later with slightly modified technique. Briefly, in these experiments the sample was exposed to various hydrogen pressures for 175 seconds, at $T \approx 473$ K. The Ar^+ beam bombardment was started simultaneously with heating of the sample to generate secondary ions for monitoring of hydrogen coverage changes on the surface. The intensity changes of ZrH^+ secondary ions and the hydrogen pressure in the sample chamber, reflecting desorption of the absorbed hydrogen during the temperature ramp (1.45 K/s) after exposures, are shown in Fig. 6.

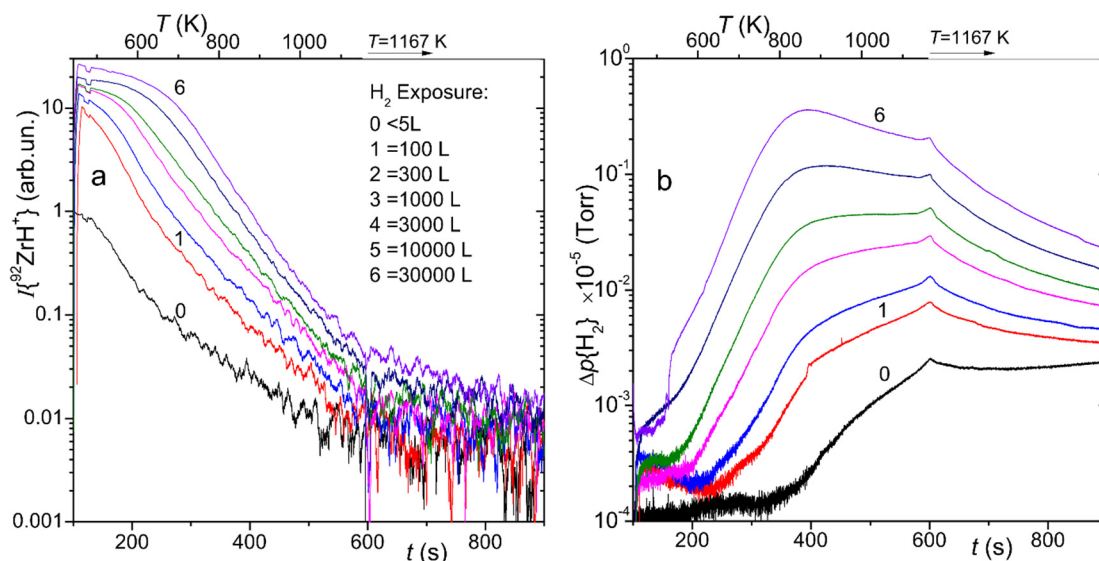


Figure 6. Dependences of emission intensity of $^{92}ZrH^+$ secondary ions on time (a) and dependences of hydrogen pressure in the sample chamber on time (b) during the heating and desorption of hydrogen from the Zr_2Fe alloy sample exposed to hydrogen atmosphere (exposures: <5 to 3×10^4 Langmuir). The $I\{^{92}ZrH^+\}$ dependences are smoothed by a moving average filter with a window size of 8 s for better visibility, and the background hydrogen pressure in the sample chamber is subtracted from the hydrogen pressure dependences.

During the analysis of these results, we hypothesized that in these experiments surface hydrogen coverage might be in an effective equilibrium between the segregation of hydrogen and hydrogen removal processes (its thermal desorption and sputtering by ion beam) since the surface was not saturated with hydrogen when substantial desorption occurred. At high temperatures, the rate of (thermal) recombinative desorption can be much higher than that of the beam sputtering. Therefore, the main processes that determine the hydrogen surface coverage are its segregation on surface and recombinative desorption, whereas impacts of other processes are comparably small. The segregation flow in such conditions is approximately equal to the desorption flow (when neglecting all other processes and neglecting the change of actual amount of hydrogen on the surface), hence the measured pressure rise due to the desorbing hydrogen $\Delta p\{H_2^{desorb.}\}$ can be used as a measure of the segregation flow. In the dynamic equilibrium corresponding to such conditions, from (1) we can find:

$$2b\theta^2 \approx C_2 \Delta p\{H_2^{desorb.}\}, \quad (11)$$

where C_2 is an instrument-sample-characteristic constant. Relation (11) is similar to the main relation of conventional TDS-analysis for second order desorption, but the crucial difference here is that in case of the desorption from bulk Polyani-Wigner equation generally cannot be used to find the surface coverage. The relation (11) can also be expressed as

$$\frac{\Delta p\{H_2^{desorb.}\}}{\theta^2} \approx C_3 b, \quad (12)$$

where C_3 is another instrument-sample-characteristic constant. From the experiments in Fig.6, we have both the desorbing hydrogen pressure and ZrH^+ ion intensity which reflects the surface coverage. According to (12), the ratio

$\Delta p\{H_2^{desorb.}\}/(I\{ZrH^+\})^2$ should be proportional to the desorption frequency constant, which (if not dependent on coverage) should be a function of temperature only and, in these experiments, should be the same at the same sample temperature. The ratio is plotted versus desorption time/sample temperature in Fig. 7a. Indeed, the ratio curves constructed from different hydrogen absorption-desorption experiments coincide at higher temperatures, demonstrate seemingly exponential growth when the sample temperature increases linearly, and demonstrate plateau when temperature is stabilized at 1167K, which is the expected behavior for the desorption frequency constant. This validates the hypothesis and the assumptions above. Plotting the ratio curves using a logarithmic scale versus inverse temperature Fig. 7b produces a straight line in the region where the individual curves coincide, confirming the exponential dependence on temperature. Fitting the line with exponential function similar to (3) allows extraction of the activation energy $E_a=1,85$ eV of hydrogen desorption from the surface of the studied Zr_2Fe alloy sample.

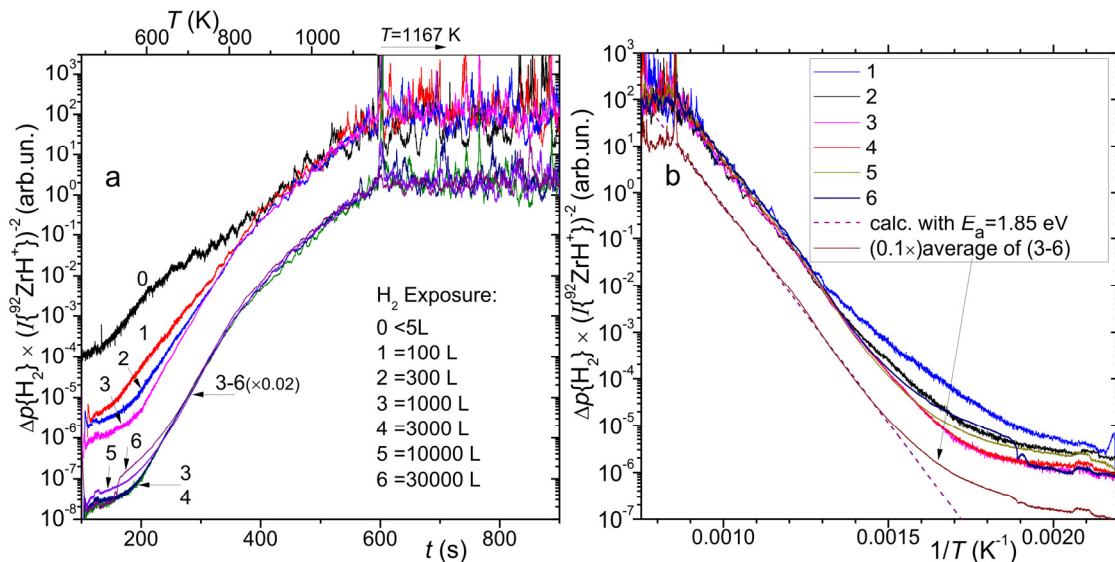


Figure 7. Dependences of the ratio of desorbing hydrogen pressure (from Fig.6b) to hydrogen-containing secondary ion emission intensity $I\{^{92}ZrH^+\}$ squared (from Fig.6a) on the sample heating/desorption time (a) and on the inverse sample temperature (b). Note that some dependence curves are manually shifted on Y-scale for better visibility.

4. CONCLUSIONS

The developed model is a simple and useful tool for practical analysis and characterization of hydrogen interaction processes with metal samples using the dynamic SIMS technique as demonstrated by the examples of extraction of the quantitative process parameters of hydrogen sputtering, absorption, and desorption. At the same time, the simplified reflection of the processes, characteristic parameters of which often depend on the amount of coverage, can limit the model's applicability. Regardless of that, in the case of analysis of SIMS measurements, the major obstacle preventing the full-potential realization of the model capabilities to quantitatively characterize the interaction processes occurring during the experiments was the lack of experimental data on the exact correspondence of the yields of secondary ions to the hydrogen concentration on the surface and the yields nonlinearities, which is a problem of the experimental technique rather than of the model and should be addressed in future studies.

ORCID

© Ivan I. Okseniuk, <https://orcid.org/0000-0002-8139-961X>; © Viktor O. Litvinov, <https://orcid.org/0000-0003-2311-2817>
 © Inna O. Afanasieva, <https://orcid.org/0000-0002-9523-9780>; © Dmytro I. Shevchenko, <https://orcid.org/0000-0002-4556-039X>
 © Valentyn V. Bobkov, <https://orcid.org/0000-0002-6772-624X>

Acknowledgments

The developments described in this paper are a preparatory work for the EURIZON project, which is funded by the European Union under grant agreement No.871072.

REFERENCES

- [1] Z. Zhu, V. Shutthanandan, and M. Engelhard, "An investigation of hydrogen depth profiling using ToF-SIMS", *Surface and Interface Analysis*, **44**(2), 232–237 (2012). <https://doi.org/10.1002/sia.3826>
- [2] F.A. Stevie, "Analysis of hydrogen in materials with and without high hydrogen mobility", *Surface and Interface Analysis*, **48**(5), 310–314 (2016). <https://doi.org/10.1002/sia.5930>
- [3] S. Pal, J. Barrirero, M. Lehmann, Q. Jeangros, N. Valle, F.-J. Haug, A. Hessler-Wyser, C.N. Shyam Kumar, F. Mücklich, T. Wirtz, and S. Eswara, "Quantification of hydrogen in nanostructured hydrogenated passivating contacts for silicon photovoltaics combining SIMS-APT-TEM: A multiscale correlative approach", *Applied Surface Science*, **555**, 149650 (2021). <https://doi.org/10.1016/j.apsusc.2021.149650>

- [4] M. Riedel, and H. Düsterhöft, “Hydrogen outgassing of ZrNiCu(H) amorphous alloy studied by secondary ion mass spectrometry”, *Rapid Communications in Mass Spectrometry*, **12**(20), 1510–1514 (1998). [https://doi.org/10.1002/\(SICI\)1097-0231\(19981030\)12:20<1510::AID-RCM334>3.0.CO;2-2](https://doi.org/10.1002/(SICI)1097-0231(19981030)12:20<1510::AID-RCM334>3.0.CO;2-2)
- [5] A. Nishimoto, M. Koyama, S. Yamato, Y. Oda, T. Awane, and H. Noguchi, “Detection of Charged Hydrogen in Ferritic Steel through Cryogenic Secondary Ion Mass Spectrometry”, *ISIJ International*, **55**(1), 335–337 (2015). <https://doi.org/10.2355/isijinternational.55.335>
- [6] T. Asakawa, D. Nagano, S. Denda, and K. Miyairi, “Influence of primary ion beam irradiation conditions on the depth profile of hydrogen in tantalum film”, *Applied Surface Science*, **255**(4), 1387–1390 (2008). <https://doi.org/10.1016/j.apsusc.2008.05.042>
- [7] X. Lin, A. Fucsko, K. Noehring, E. Gabriel, A. Regner, S. York, and D. Palsulich, “New SIMS method to characterize hydrogen in polysilicon films”, *Journal of Vacuum Science & Technology B*, **40**(1), (2022). <https://doi.org/10.1116/6.0001472>
- [8] J. Sameshima, and S. Numao, “Behavior and process of background signal formation of hydrogen, carbon, nitrogen, and oxygen in silicon wafers during depth profiling using dual-beam TOF-SIMS”, *Surface and Interface Analysis*, **54**(2), 165–173 (2022). <https://doi.org/10.1002/sia.7035>
- [9] D. Andersen, H. Chen, S. Pal, L. Cressa, O. De Castro, T. Wirtz, G. Schmitz, and S. Eswara, “Correlative high-resolution imaging of hydrogen in Mg₂Ni hydrogen storage thin films”, *International Journal of Hydrogen Energy*, **48**(37), 13943–13954 (2023). <https://doi.org/10.1016/j.ijhydene.2022.12.216>
- [10] M.V. Lototskyy, B.P. Tarasov, and V.A. Yartys, “Gas-phase applications of metal hydrides”, *Journal of Energy Storage*, **72**, 108165 (2023). <https://doi.org/10.1016/j.est.2023.108165>
- [11] V.A. Litvinov, I.I. Okseniuk, D.I. Shevchenko, and V.V. Bobkov, “Secondary-ion mass spectrometry study of LaNi₅-hydrogen-oxygen system”, *Ukrainian Journal of Physics*, **66**(8), 723–735 (2021). <https://doi.org/10.15407/ujpe66.8.723>
- [12] I. Okseniuk, and D. Shevchenko, “SIMS studies of hydrogen interaction with the TiFe alloy surface: hydrogen influence on secondary ion yields”, *Surface Science*, **716**, 121963 (2022). <https://doi.org/10.1016/j.susc.2021.121963>
- [13] I.I. Okseniuk, V.O. Litvinov, D.I. Shevchenko, R.L. Vasilenko, S.I. Bogatyrenko, and V.V. Bobkov, “Hydrogen interaction with Zr-based getter alloys in high vacuum conditions: In situ SIMS-TPD studies”, *Vacuum*, **197**, 110861 (2022). <https://doi.org/10.1016/J.VACUUM.2021.110861>
- [14] V.A. Litvinov, I.I. Okseniuk, D.I. Shevchenko, and V. V. Bobkov, “SIMS Study of Hydrogen Interaction with the LaNi₅ Alloy Surface”, *Journal of Surface Investigation*, **12**(3), 576–583 (2018). <https://doi.org/10.1134/S1027451018030321>
- [15] V.O. Litvinov, I.I. Okseniuk, D.I. Shevchenko, and V. V. Bobkov, “The Role of Surface in Hydride Formation Processes”, *East European Journal of Physics*, (3), 10–42 (2023). <https://doi.org/10.26565/2312-4334-2023-3-01>
- [16] C.S. Zhang, B. Li, and P.R. Norton, “The study of hydrogen segregation on Zr(0001) and Zr(1010) surfaces by static secondary ion mass spectroscopy, work function, Auger electron spectroscopy and nuclear reaction analysis”, *Journal of Alloys and Compounds*, **231**(1–2), 354–363 (1995). [https://doi.org/10.1016/0925-8388\(95\)01847-6](https://doi.org/10.1016/0925-8388(95)01847-6)
- [17] X.Y. Zhu, and J.M. White, “Hydrogen interaction with nickel(100): a static secondary ion mass spectroscopy study”, *The Journal of Physical Chemistry*, **92**(13), 3970–3974 (1988). <https://doi.org/10.1021/j100324a056>
- [18] A. Benninghoven, P. Beckmann, D. Greifendorf, K.H. Müller, and M. Schemmer, “Hydrogen detection by secondary ion mass spectroscopy: Hydrogen on polycrystalline nickel”, *Surface Science*, **107**(1), 148–164 (1981). [https://doi.org/10.1016/0039-6028\(81\)90618-X](https://doi.org/10.1016/0039-6028(81)90618-X)
- [19] T. Asakawa, D. Nagano, H. Miyazawa, and I. Clark, “Absorption, discharge, and internal partitioning behavior of hydrogen in the tantalum and tantalum oxide system investigated by in situ oxidation SIMS and ab initio calculations”, *Journal of Vacuum Science & Technology B*, **38**(3), 034008 (2020). <https://doi.org/10.1116/6.0000100>
- [20] A. Röhsler, O. Sobol, H. Hänninen, and T. Böllinghaus, “In-situ ToF-SIMS analyses of deuterium re-distribution in austenitic steel AISI 304L under mechanical load”, *Scientific Reports*, **10**(1), 3611 (2020). <https://doi.org/10.1038/s41598-020-60370-2>
- [21] P. Kesten, A. Pundt, G. Schmitz, M. Weisheit, H.U. Krebs, and R. Kirchheim, “H- and D distribution in metallic multilayers studied by 3-dimensional atom probe analysis and secondary ion mass spectrometry,” *Journal of Alloys and Compounds*, (2002), pp. 225–228. [https://doi.org/10.1016/S0925-8388\(01\)01596-1](https://doi.org/10.1016/S0925-8388(01)01596-1)
- [22] C.S. Zhang, B. Li, and P.R. Norton, “The initial stages of interaction of hydrogen with the Zr(1010) surface”, *Surface Science*, **346**(1–3), 206–221 (1996). [https://doi.org/10.1016/0039-6028\(95\)00904-3](https://doi.org/10.1016/0039-6028(95)00904-3)
- [23] J. Ekar, P. Panjan, S. Drev, and J. Kovač, “ToF-SIMS Depth Profiling of Metal, Metal Oxide, and Alloy Multilayers in Atmospheres of H₂, C₂H₂, CO, and O₂”, *Journal of the American Society for Mass Spectrometry*, **33**(1), 31–44 (2022). <https://doi.org/10.1021/jasms.1c00218>
- [24] J. Ekar, and J. Kovač, “AFM Study of Roughness Development during ToF-SIMS Depth Profiling of Multilayers with a Cs⁺ Ion Beam in a H₂ Atmosphere”, *Langmuir*, **38**(42), 12871–12880 (2022). <https://doi.org/10.1021/acs.langmuir.2c01837>
- [25] J. Ekar, S. Kos, and J. Kovač, “Quantitative Aspects of ToF-SIMS Analysis of Metals and Alloys in a UHV, O₂ and H₂ Atmosphere”, Preprint (at <https://www.ssrn.com>), (2024). <https://doi.org/10.2139/ssrn.4683611>
- [26] O.B. Malyshev, *Vacuum in Particle Accelerators* (Wiley, 2019)
- [27] I. Sereda, Y. Hrechko, I. Babenko, and M. Azarenkov, “The emission of H⁻ ions from Penning-type ion source with metal hydride cathode in pulsating regime”, *Vacuum*, **200**, 111006 (2022). <https://doi.org/10.1016/j.vacuum.2022.111006>
- [28] I. Sereda, Y. Hrechko, I. Babenko, and M. Azarenkov, “The Features of Intense Electron Flow Impact on Metal Hydride Electrode”, *East European Journal of Physics*, (2), 99–102 (2022). <https://doi.org/10.26565/2312-4334-2022-2-12>
- [29] I. Sereda, Y. Hrechko, and I. Babenko, “The Plasma Parameters of Penning Discharge with Negatively Biased Metal Hydride Cathode at Longitudinal Emission of H⁻ Ions”, *East European Journal of Physics*, (3), 81–86 (2021). <https://doi.org/10.26565/2312-4334-2021-3-12>
- [30] E.A. Hodille, S. Markelj, M. Pecovnik, M. Ajmalghan, Z.A. Piazza, Y. Ferro, T. Schwarz-Selinger, and C. Grisolia, “Kinetic model for hydrogen absorption in tungsten with coverage dependent surface mechanisms”, *Nuclear Fusion*, **60**(10), 106011 (2020). <https://doi.org/10.1088/1741-4326/aba454>
- [31] K.E. Lu, and R.R. Rye, “Flash desorption and equilibration of H₂ and D₂ on single crystal surfaces of platinum”, *Surface Science*, **45**(2), 677–695 (1974). [https://doi.org/10.1016/0039-6028\(74\)90197-6](https://doi.org/10.1016/0039-6028(74)90197-6)

- [32] V.A. Litvinov, I.I. Okseniuk, D.I. Shevchenko, and V. V. Bobkov, "SIMS study of the surface of lanthanum-based alloys", *Ukrainian Journal of Physics*, **62**(10), 845–857 (2017). <https://doi.org/10.15407/ujpe62.10.0845>
- [33] V.T. Cherepin, M.O. Vasylyev, I.M. Makeeva, V.M. Kolesnik, and S.M. Voloshko, "Secondary Ion Emission during the Proton Bombardment of Metal Surfaces", *Uspehi Fiziki Metallov*, **19**(1), 49–69 (2018). <https://doi.org/10.15407/ufm.19.01.049>
- [34] A. Wucher, "Formation of atomic secondary ions in sputtering", *Applied Surface Science*, **255**(4), 1194–1200 (2008). <https://doi.org/10.1016/j.apsusc.2008.05.252>
- [35] K. Christmann, "Adsorption of Hydrogen," in *Surface and Interface Science, Volume 5 and 6: Volume 5 - Solid Gas Interfaces I; Volume 6 - Solid Gas Interfaces II*, edited by K. Wandelt, (John Wiley & Sons, 2016), pp. 255–357
- [36] J. Sopka, and H. Oechsner, "Determination of hydrogen concentration depth profiles in a-Si:H by Secondary Neutral Mass Spectrometry (SNMS)", *Journal of Non-Crystalline Solids*, **114**, 208–210 (1989). [https://doi.org/10.1016/0022-3093\(89\)90115-4](https://doi.org/10.1016/0022-3093(89)90115-4)
- [37] J. Scholz, H. Züchner, H. Paulus, and K.-H. Müller, "Ion bombardment induced segregation effects in VDx studied by SIMS and SNMS", *Journal of Alloys and Compounds*, **253–254**, 459–462 (1997). [https://doi.org/10.1016/S0925-8388\(96\)03000-9](https://doi.org/10.1016/S0925-8388(96)03000-9)
- [38] D.N. Denzler, C. Frischkorn, C. Hess, M. Wolf, and G. Ertl, "Electronic Excitation and Dynamic Promotion of a Surface Reaction", *Physical Review Letters*, **91**(22), 226102 (2003). <https://doi.org/10.1103/PhysRevLett.91.226102>
- [39] F. Le Pimpec, O. Gröbner, and J.M. Laurent, "Electron stimulated molecular desorption of a non-evaporable Zr–V–Fe alloy getter at room temperature", *Nuclear Instruments and Methods in Physics Research Section B: Beam Interactions with Materials and Atoms*, **194**(4), 434–442 (2002). [https://doi.org/10.1016/S0168-583X\(02\)01034-0](https://doi.org/10.1016/S0168-583X(02)01034-0)
- [40] Y. Kudriavtsev, R. Asomoza, A. Hernandez, D.Y. Kazantsev, B.Y. Ber, and A.N. Gorokhov, "Nonlinear effects in low-energy ion sputtering of solids", *Journal of Vacuum Science & Technology A*, **38**(5), 053203 (2020). <https://doi.org/10.1116/6.0000262>
- [41] V. V Ovchinnikov, F.F. Makhin'ko, and V.I. Solomonov, "Thermal-spikes temperature measurement in pure metals under argon ion irradiation ($E = 5-15$ keV)", *Journal of Physics: Conference Series*, **652**, 012070 (2015). <https://doi.org/10.1088/1742-6596/652/1/012070>
- [42] L.O. Williams, *Hydrogen Power: An Introduction to Hydrogen Energy and Its Applications* (Pergamon press, 2013)
- [43] K. Christmann, "Interaction of hydrogen with solid surfaces", *Surface Science Reports*, **9**(1–3), 1–163 (1988). [https://doi.org/10.1016/0167-5729\(88\)90009-X](https://doi.org/10.1016/0167-5729(88)90009-X)
- [44] G. Ross, "Analysis of hydrogen isotopes in materials by secondary ion mass spectrometry and nuclear microanalysis", *Vacuum*, **45**(4), 375–387 (1994). [https://doi.org/10.1016/0042-207X\(94\)90306-9](https://doi.org/10.1016/0042-207X(94)90306-9)
- [45] M. Wilde, M. Matsumoto, L. Gao, T. Schwarz-Selinger, A. Manhard, and W. Jacob, "Cross section of ^{15}N - ^{2}D nuclear reactions from 3.3 to 7.0 MeV for simultaneous hydrogen and deuterium quantitation in surface layers with ^{15}N ion beams", *Nuclear Instruments and Methods in Physics Research Section B: Beam Interactions with Materials and Atoms*, **478**, 56–61 (2020). <https://doi.org/10.1016/j.nimb.2020.05.020>
- [46] M. Wilde, S. Ohno, S. Ogura, K. Fukutani, and H. Matsuzaki, "Quantification of Hydrogen Concentrations in Surface and Interface Layers and Bulk Materials through Depth Profiling with Nuclear Reaction Analysis", *Journal of Visualized Experiments*, (109), (2016). <https://doi.org/10.3791/53452>
- [47] V.P. Zhdanov, "Arrhenius parameters for rate processes on solid surfaces", *Surface Science Reports*, **12**(5), 185–242 (1991). [https://doi.org/10.1016/0167-5729\(91\)90011-L](https://doi.org/10.1016/0167-5729(91)90011-L)
- [48] H.J. Kreuzer, S.H. Payne, and Y.K. Tovbin, "Equilibria and Dynamics of Gas Adsorption on Heterogeneous Solid Surfaces," in *Studies in Surface Science and Catalysis*, edited by G.Z. Edited by W. Rudziński, W.A. Steele, (Elsevier, 1997), pp. 153–284
- [49] K. Christmann, "Kinetics, energetics and structure of hydrogen adsorbed on transition metal single crystal surfaces", *Bulletin Des Sociétés Chimiques Belges*, **88**(7–8), 519–539 (2010). <https://doi.org/10.1002/bscb.19790880706>
- [50] D.L.S. Nieskens, A.P. van Bavel, and J.W. Niemantsverdriet, "The analysis of temperature programmed desorption experiments of systems with lateral interactions; implications of the compensation effect", *Surface Science*, **546**(2–3), 159–169 (2003). <https://doi.org/10.1016/j.susc.2003.09.035>
- [51] K. Christmann, O. Schober, G. Ertl, and M. Neumann, "Adsorption of hydrogen on nickel single crystal surfaces", *The Journal of Chemical Physics*, **60**(11), 4528–4540 (1974). <https://doi.org/10.1063/1.1680935>

ПРОСТА АНАЛІТИЧНА МОДЕЛЬ ПОКРИТТЯ ПОВЕРХНІ ВОДНЕМ ПІД ВПЛИВОМ РІЗНИХ ПРОЦЕСІВ НА ПОВЕРХНІ ТА ІОННОГО БОМБАРДУВАННЯ

Іван І. Оксенюк, Віктор О. Літвінов, Дмитро І. Шевченко, Інна О. Афанасьєва, Валентин В. Бобков

Харківський національний університет імені В. Н. Каразіна, майдан Свободи 4, 61022, Харків, Україна

У статті описано просту аналітичну модель, яка дозволяє розрахувати покриття поверхні воднем під дією декількох процесів, що можуть відбуватися одночасно під час бомбардування/розпилення поверхні зразка іонним пучком, зокрема під час аналізу за допомогою вторинної іонної мас-спектрометрії (ВІМС). Модель розглядає процеси дисоціативної адсорбції, десорбції, поглинання з поверхні в об'єм зразка та видалення водню іонним бомбардуванням. Після опису моделі наведено низку прикладів її практичного застосування для інтерпретації експериментальних результатів, отриманих під час *in situ* ВІМС-досліджень взаємодії водню з гідродуотворюючими сплавами, TiFe, Zr₂Fe та з нікелем. У наведених прикладах, із застосуванням різних апроксимацій моделі було успішно визначено низку кількісних характеристик поверхневих процесів за участю водню, зокрема швидкість розпилення водню, величини енергії активації десорбції та абсорбції водню.

Ключові слова: вторинна іонна мас-спектрометрія; іонне бомбардування; розпилення; накопичення водню; адсорбція; десорбція; кінетика

TRANSITION PROBABILITIES, OSCILLATOR AND LINE STRENGTHS IN Sc XIX

Muhammad Kaleem^a, Saba Javaid^b, Roohi Zafar^b,  Zaheer Uddin^{a*}

^aDepartment of Physic, University of Karachi, Karachi, Pakistan

^bDepartment of Physic, NED University of Engineering & Technology, Karachi, Pakistan

*Corresponding Author email: zuddin@uok.edu.pk

Received February 6, 2024; revised March 27, 2024; accepted March 30, 2024

Scandium XIX ion is a member of the isoelectronic sequence of Li-like ions. Numerical coulomb approximation and quantum defect theory have been used to calculate energies, quantum defects & transition probabilities, oscillator, and line strengths of Sc XIX ion for the transitions $ns \rightarrow mp$, $np \rightarrow ms$, $np \rightarrow md$, and $nd \rightarrow mp$ Rydberg series. The energies of Sc XIX ions up to $n = 5$ are given in the NIST database and the literature. We used quantum defect theory and determined the energies and quantum defects up to $n = 30$. The energies and quantum defects of 125 levels are reported for the first time. Sc XIX ion's transition probabilities, oscillator, and line strengths were compared with the corresponding values in the NIST database of spectral lines. The NIST database contains data of only seventy-six spectral lines. Only six spectra lines have percent uncertainties of more than 10%. The results of the remaining seventy spectral lines agree well with the NIST values. Almost 1800 transition probabilities, oscillators, and line strengths are new.

Keywords: Scandium; Li-like; Rydberg Level; Quantum Defect theory; Transition Probability; Oscillator strength; Line Strength

PACS: 31.10.+z, 31.15.-p, 31.15.Ct, 31.90.+s, 32.30-r

INTRODUCTION

The knowledge of the composition of stars plays an important role in understanding the galaxies. Different stars have different compositions of elements, giving different physical and chemical properties to the stars. Scandium, Vanadium, and Yttrium are observed in galactical centers [1]. It is believed that atomic diffusion below the superficial convection region is the cause of abundance anomalies in AmFm stars. Scandium is a key element to understanding this cause of abundance, as it is one of the underabundant elements at the surface of AmFm stars [2]. The nucleosynthesis theory and the chemical evolution of the Galaxy of long-lived F and G stars can be understood by scandium abundance [3]. The hyperfine structure studies data were used to determine the Scandium abundance in Sun and Arcturus [4].

The calculation of the ionization potential of Sc XIX to Zn XXVIII by the R-matrix method was compared with the full core plus correlation method. The R-matrix method was also used to calculate the quantum defects of the series $1s2nh$ [5]. An improved theoretical prediction of the g factor of Li-like ions was performed using QED corrections. The calculations were compared with three different methods, including QED, and the results were consistent [6]. With the help of full-core-plus-correlation, the energies of Li-like Sc XIX to Zn XXVIII ions were calculated for the series $1s2ng$ ($n = 5$ to 8). An effective nuclear charge formula was used to reduce the uncertainties, and first-order perturbation calculations were done to assess the mass and relativistic polarization effects [7]. The energies and fine structure intervals of $1s2l2l'$ for Li-like ions from Ar to U were calculated using the relativistic configuration interaction method. The calculations include QED corrections, nuclear recoil effect, and Breit interaction [8]. The g factor of Li-like ions was calculated, and the effect of nuclear recoil was evaluated for $Z = 3$ -92; using Breit interaction, the recoil term for two electrons is calculated for low and middle Z ions [9]. The energy, electron impact excitation, and transition rates were calculated for an isoelectronic sequence of Li-like ions from $21 \leq Z \leq 28$. The energy and transition probabilities were calculated using the General-Purpose Relativistic Atomic Structure Package (GPRASP) for the lowest 24 levels. The r-matrix method was used to calculate the excitation rates. The transition probabilities were used to calculate the lifetimes of the levels [10]. The spectra of the isoelectronic sequence of lithium are determined using the QED approach [11]. The full core plus correlation method is employed to determine the transition energies and the dipole oscillator strengths $1s^2 2s-1s^2 np$ ($2 \leq n \leq 9$) and $1s^2 2p-1s^2$ and ($3 \leq n \leq 9$) of lithium-like Sc 18+ ion. The expectation values of spin-orbit and spin-other-orbit interaction operators were used to obtain the fine structure splittings of $1s 2np$ and $1s2nd$ ($n \leq 9$). The quantum defects of the above series, as a function of the principal quantum number n , are determined. The agreement between the values obtained from three alternative formulae is excellent [12].

Compared with quantum defects for high-Z ions, the energy level data recommendation by the screening constant is more effective and accurate. The quantum defect converges to a small value as Z increases, whereas the screening constant decreases monotonically. The dependency of the screening constant on Z is approximately Z^3 for values of $Z=10$ to $Z=40$, and $Z^{3.5}$ for values of $Z=40$ to $Z=70$, and Z^4 for $Z > 70$. The dependence of the screening constant on Z^3 could be explained in terms of the spin-orbit interaction of the hydrogenic wavefunction in the Coulomb potential [13]. By considering the differences between calculated ab initio values of the ionization potentials and the NIST-evaluated for Li through the Ar isoelectronic series, new ionization potentials are extracted for several light ions for $Z=3$ to $Z=50$. The relativistic multiconfiguration Dirac-Fock method has been applied to calculate the ionization energies' ab initio

values [14]. Energies of lithium 1s 2s 2S and 1s2 2p2P isoelectronic sequence for values of Z up to Z=40 are calculated using a variational method. The oscillator strengths, finite nuclear mass effects, and the associated lifetimes for the transitions 1s2 2s2S→1s22p2P are determined for Z up to 20 [15]. The fine structure levels ($n \leq 12, l \leq 5$) for $Ca^{17+}, Sc^{18+}, Ti^{19+}, V^{20+}, Cr^{21+}$ and Mn^{22+} and the radiative transition probabilities between them are calculated in the multiconfiguration Dirac-Fock scheme [16].

THEORY

For non-relativistic calculations of energy and wavefunctions of Li atom and Li-like ions the Schrödinger equation in atomic unit in the following forms can be used.

$$H = \sum_{i=1}^N \left(-\frac{1}{2} \nabla_i^2 - \frac{Z}{r_i} \right) + \sum_{i>j}^N \frac{1}{r_{ij}} \quad (1)$$

The Li atom and Li-like ions, however, can be treated as hydrogen-like if the electrons other than the valence shell electron, i.e., the electrons in 1s orbital together with the nucleus, are considered core, around which the valence electron revolves. In such case, the radial part of the Schrödinger equation becomes;

$$\frac{d^2 R}{dr^2} + \frac{2}{r} \frac{dR}{dr} + 2 \left(E + \frac{Z^*}{r_i} - \frac{l^*(l^*+1)}{r_i^2} \right) = 0, \quad (2)$$

here $l^* = l - \delta_n, n^* = n - \delta_n, \delta_n$ is the quantum defect and is given as a function of n. The values of δ_n can be found using Quantum Defect Theory. The solution of equation (2) gives the radial wavefunction given by [17-18]

$$R = \left(\frac{2Z^*}{n^*} \right)^{l^* + \frac{3}{2}} \sqrt{\frac{(n^* - l^* - 1)!}{2n^* \Gamma(n^* + l^* + 1)}} \exp\left(-\frac{Z^* r}{n^*}\right) r^{l^*} L_{n^* - l^* - 1}^{2l^* + 1} \left(\frac{2Z^* r}{n^*} \right). \quad (3)$$

The energy (E_n), corresponds to the principal quantum number 'n', is given by the effective principal quantum number 'n* '.

$$E_n = I - \frac{RZ^2}{(n - \delta_n)^2}. \quad (4)$$

The value of δ_n is found by

$$\delta_n = a_0 + \frac{a_1}{(n - \delta_0)^2} + \frac{a_2}{(n - \delta_0)^4} + \frac{a_3}{(n - \delta_0)^6}. \quad (5)$$

The coefficients $a_0, a_1, a_2,$ and a_3 are known as spectral coefficients; the values of these constants depend on the nature of the orbital, i.e., penetrating and non-penetrating orbitals and their orbital angular momentum. The values can be found with the help of Rydberg levels' first few known energies.

The transition probability (A_{fi}) of a transition between fine levels is given by

$$A_{fi} = 2.0261 \times 10^{-6} \frac{(E_f - E_i)^3}{2l_i + 1} S, \quad (6)$$

E_f and E_i are the energies of upper and lower states; S is dipole line strength and is found by

$$S_{LS} = [J_f, J_i, L_f, L_i] \left(\left\{ \begin{matrix} L_f & S & J_f \\ J_i & 1 & L_i \end{matrix} \right\} \left\{ \begin{matrix} L_f & l_f & L_c \\ 1 & L_i & l_i \end{matrix} \right\} P_{l_i l_f}^{(1)} \right)^2. \quad (7)$$

The terms in the bracket contain two 6J symbols and the matrix element $P_{l_i l_f}^{(1)}$, which is given by [19-20].

$$P_{l_i l_f}^{(1)} = l_f \langle n_i, l_i | r | n_f, l_f \rangle = l_f \int_0^\infty r^3 R_{n_i l_i} R_{n_f l_f} dr. \quad (8)$$

Numerical coulomb approximation is used to calculate the matrix element.

RESULTS AND DISCUSSION

This study was devoted to calculating energies, quantum defects, transition probabilities, oscillator, and line strengths Sc XIX ion of isoelectronic sequence of Li-like ions. The energies and quantum defects of ns, np, and nd series are given in tables 1-3. The energies are compared with the available data in NIST [21] and Aggarwal's work [10]. A good match between calculated and available energies was found. Table 1 gives the energies of the 1s²ns (²S_{1/2}), and 1s²np (²P_{1/2}) series, table 2 gives the energies of 1s²np (²S_{3/2}) and 1s²nd (²D_{3/2}) series, and table 3 gives the energies of 1s²nd (²D_{5/2}) series. In each table, 1-3, the first, second, and third columns give the principal quantum number, quantum defects, and energies determined in this work, the fourth column gives corresponding NIST values, and the last two columns show

the energies from Aggarwal et al.'s work. Aggarwal et al. [10] calculations were based on the General-Purpose Relativistic Atomic Structure Package (GPRASP).

Four different series in spectral transition up to $n = 20$ were considered for calculating TP, OS, and LS of Sc XIX. This work presents eighteen hundred & sixty-two transitions in Rydberg ion Sc XIX, whose TP, OS, and LS are determined using numerical coulomb approximation and quantum defect theory. The results were compared with the NIST values for Sc XIX. Most of the results agree only six transitions differ significantly. Some of the results are shown in Table 5. (The complete results are available as a supplementary file on the Journal site.) There are eighteen columns; the first column gives the wavelength in Angstrom. Columns 2, 5, and 8 give the transition probabilities, oscillator, and line strengths calculated in this work, and columns 3, 6, and 9 give the corresponding values in the NIST database of spectral lines. Columns 4, 7, and 10 give the percent uncertainties between this work and NIST values. Columns 11 and 12 give the energies cm^{-1} of lower and upper levels, respectively. Columns 13, 14, and 15 show the configuration of the lower levels, term value, and angular momentum. The same for the upper level is given in columns 16-18. Most TP, OS, and LS are new and not found in the NIST data.

Table 1. The quantum defects and energies of $1s^2ns$ ($^2S_{1/2}$) and $1s^2np$ ($^2P_{1/2}$) up to $n = 3$ compared with NIST [21] and Aggarwal [10] results

n	QD	Energy (Rydberg)				n	QD	Energy (Rydberg)			
		This work	NIST [21]	GRASP1 [10]	GRASP2 [10]			This work	NIST [21]	GRASP1 [10]	GRASP2 [10]
2	0.149979	0.00000	0.00000	0	0	2	0.122049	2.79489	2.79489	2.80532	2.80715
3	0.201701	53.28798	53.28798	53.28735	53.25951	3	0.175645	54.04790	54.04790	54.0638	54.03701
4	0.253260	71.58441	71.58441	71.58356	71.54981	4	0.227392	71.89983	71.89983	71.90314	71.8698
5	0.304049	79.97183	79.97183	79.97088	79.93505	5	0.283215	80.10133	80.10133	80.1325	80.09689
6	0.338553	84.55576				6	0.321839	84.61518	84.49369		
7	0.361442	87.31243				7	0.347657	87.34287	87.26398		
8	0.377025	89.08862				8	0.365304	89.10572			
9	0.387991	90.29572				9	0.377754	90.30608			
10	0.395955	91.15158				10	0.386810	91.15826			
11	0.401899	91.77961				11	0.393577	91.78414			
12	0.406444	92.25370				12	0.398756	92.25690			
13	0.409993	92.62017				13	0.402802	92.62250			
14	0.412813	92.90918				14	0.406019	92.91094			
15	0.415090	93.14108				15	0.408617	93.14243			
16	0.416953	93.32995				16	0.410745	93.33102			
17	0.418498	93.48580				17	0.412508	93.48665			
18	0.419791	93.61588				18	0.413985	93.61657			
19	0.420885	93.72558				19	0.415235	93.72615			
20	0.421819	93.81893				20	0.416301	93.81940			
21	0.422621	93.89902				21	0.417218	93.89942			
22	0.423316	93.96826				22	0.418012	93.96860			
23	0.423922	94.02851				23	0.418705	94.02880			
24	0.424453	94.08127				24	0.419312	94.08152			
25	0.424921	94.12772				25	0.419847	94.12794			
26	0.425336	94.16884				26	0.420322	94.16903			
27	0.425706	94.20540				27	0.420744	94.20557			
28	0.426036	94.23807				28	0.421122	94.23822			
29	0.426333	94.26736				29	0.421461	94.26750			
30	0.426600	94.29374				30	0.421766	94.29386			

Table 2. The quantum defects and energies of $1s^2np$ ($^2P_{3/2}$) and $1s^2nd$ ($^2D_{3/2}$) up to $n = 3$ compared with NIST [21] and Aggarwal [10] results

n	QD	Energy (Rydberg)				n	QD	Energy (Rydberg)			
		This work	NIST [21]	GRASP1 [10]	GRASP2 [10]			NIST [21]	GRASP1 [10]	GRASP2 [10]	NIST [21]
2	0.117309	3.25691	3.25691	3.28673	3.26772	3	0.160635	54.47620	54.47620	54.50117	54.46362
3	0.170880	54.18459	54.18459	54.206	54.206	4	0.212962	72.07298	72.07298	72.0855	72.04777
4	0.227118	71.90314	71.90314	71.96299	71.96299	5	0.268387	80.19246	80.19246	80.22533	80.1875
5	0.263005	80.22533	80.22533	80.16309	80.16309	6	0.327832	84.59393	84.59393		
6	0.284901	84.74466	84.49369			7	0.374674	87.28304	87.28220		
7	0.298813	87.44921	87.26398			8	0.409372	89.04100	88.97718		
8	0.308083	89.18812				9	0.434988	90.24765			
9	0.314530	90.36930				10	0.454152	91.10862			
10	0.319178	91.20707				11	0.468743	91.74288			
11	0.322632	91.82228				12	0.480053	92.22280			
12	0.325265	92.28711				13	0.488970	92.59428			
13	0.327316	92.64675				14	0.496110	92.88747			
14	0.328944	92.93065				15	0.501906	93.12279			
15	0.330258	93.15865				16	0.506672	93.31446			
16	0.331332	93.34450				17	0.510633	93.47259			
17	0.332222	93.49797				18	0.513961	93.60456			
18	0.332967	93.62616				19	0.516781	93.71581			
19	0.333597	93.73433				20	0.519191	93.81046			
20	0.334134	93.82645				21	0.521267	93.89163			
21	0.334596	93.90553				22	0.523066	93.96178			
22	0.334996	93.97392				23	0.524636	94.02280			
23	0.335345	94.03347				24	0.526014	94.07621			
24	0.335651	94.08563				25	0.527230	94.12322			
25	0.335921	94.13158				26	0.528308	94.16482			
26	0.336160	94.17227				27	0.529268	94.20181			
27	0.336373	94.20847				28	0.530127	94.23483			
28	0.336563	94.24082				29	0.530898	94.26444			
29	0.336734	94.26984				30	0.531593	94.29109			
30	0.336887	94.29598									

Table 3. The quantum defects and energies of $1s^2nd$ ($^2D_{5/2}$) up to $n = 3$ compared with NIST [21] and Aggarwal [10] results

n	QD	Energy (Rydberg)				n	QD	Energy (Rydberg)			
		This work	NIST [21]	GRASP1 [10]	GRASP2 [10]			This work	NIST [21]	GRASP1 [10]	GRASP2 [10]
3	0.159346	54.51265	54.51265	54.54433	54.50651	17	0.50956	93.47275			
4	0.212198	72.08209	72.08209	72.10374	72.06586	18	0.51286	93.60469			
5	0.268387	80.19246	80.19246	80.23467	80.19676	19	0.51565	93.71593			
6	0.327832	84.59393	84.59393			20	0.51805	93.81056			
7	0.374496	87.28343	87.28220			21	0.52010	93.89172			
8	0.409006	89.04154	88.97718			22	0.52189	93.96186			
9	0.434462	90.24819				23	0.52345	94.02287			
10	0.453495	91.10911				24	0.52481	94.07627			
11	0.467982	91.74330				25	0.52602	94.12328			
12	0.479210	92.22316				26	0.52709	94.16487			
13	0.488060	92.59458				27	0.52804	94.20185			
14	0.495145	92.88772				28	0.52889	94.23487			
15	0.500897	93.12300				29	0.52966	94.26448			
16	0.505625	93.31464				30	0.53035	94.29113			

Lifetimes of Sc XIX Rydberg Levels

The lifetime of the ns, np, and nd & some f and g upper levels of the Rydberg series are also determined using the transition probabilities. All possible transitions from the level are considered to calculate the lifetime of an upper level; the lifetime is the reciprocal of the sum of all the transitions from the upper level, i.e.

$$\tau_j = \frac{1}{\sum_i A_{ji}}$$

One thousand eighteen hundred and sixty-two transition probabilities were used to calculate the lifetimes of ninety-six levels belonging to ns, np, and nd series up to $n = 20$. The lifetimes were compared with the work of Aggarwal et al. [10]. Out of twenty-one lifetimes, twenty lifetimes have percent uncertainties less than 0.1%. Only one lifetime differs significantly.

Table 4. The lifetimes of the ns, np, nd, some f, and g Rydberg levels of Sc XIX ion

Configuration	Lifetime (s)		Configuration	Lifetime (s)		Configuration	Lifetime (s)	
	This work	Aggarwal [10]		This work	Aggarwal [10]		This work	Aggarwal [10]
1s ² 3s (² S _{1/2})	8.714E-13	8.86E-13	1s ² 16p (² P _{1/2})	1.636E-10		1s ² 11d (² D _{3/2})	4.248E-12	
1s ² 4s (² S _{1/2})	1.301E-12	1.31E-12	1s ² 17p (² P _{1/2})	1.860E-10		1s ² 12d (² D _{3/2})	5.185E-12	
1s ² 5s (² S _{1/2})	2.097E-12	2.07E-12	1s ² 18p (² P _{1/2})	1.722E-10		1s ² 13d (² D _{3/2})	6.227E-12	
1s ² 6s (² S _{1/2})	3.654E-12		1s ² 19p (² P _{1/2})	1.443E-10		1s ² 14 (² D _{3/2})	7.391E-12	
1s ² 7s (² S _{1/2})	6.683E-12		1s ² 20p (² P _{1/2})	1.190E-10		1s ² 15d (² D _{3/2})	8.695E-12	
1s ² 8s (² S _{1/2})	1.287E-11		1s ² 2p (² P _{3/2})	4.459E-10	4.46E-10	1s ² 16d (² D _{3/2})	1.016E-11	
1s ² 9s (² S _{1/2})	2.665E-11		1s ² 3p (² P _{3/2})	3.454E-13	3.52E-13	1s ² 17d (² D _{3/2})	1.179E-11	
1s ² 10s (² S _{1/2})	6.079E-11		1s ² 4p (² P _{3/2})	5.771E-13	5.93E-13	1s ² 18d (² D _{3/2})	1.362E-11	
1s ² 11s (² S _{1/2})	1.477E-10		1s ² 5p (² P _{3/2})	1.021E-12	1.00E-12	1s ² 19d (² D _{3/2})	1.565E-11	
1s ² 12s (² S _{1/2})	2.667E-10		1s ² 6p (² P _{3/2})	1.769E-12		1s ² 20d (² D _{3/2})	1.788E-11	
1s ² 13s (² S _{1/2})	2.256E-10		1s ² 7p (² P _{3/2})	2.993E-12		1s ² 3d (² D _{5/2})	1.135E-13	1.16E-13
1s ² 14s (² S _{1/2})	1.438E-10		1s ² 8p (² P _{3/2})	4.995E-12		1s ² 4d (² D _{5/2})	2.642E-13	2.70E-13
1s ² 15s (² S _{1/2})	9.876E-11		1s ² 9p (² P _{3/2})	8.319E-12		1s ² 5d (² D _{5/2})	5.113E-13	5.19E-13
1s ² 16s (² S _{1/2})	7.566E-11		1s ² 10p (² P _{3/2})	1.397E-11		1s ² 6d (² D _{5/2})	8.823E-13	
1s ² 17s (² S _{1/2})	6.331E-11		1s ² 11p (² P _{3/2})	2.381E-11		1s ² 7d (² D _{5/2})	1.378E-12	
1s ² 18s (² S _{1/2})	5.671E-11		1s ² 12p (² P _{3/2})	4.108E-11		1s ² 8d (² D _{5/2})	1.976E-12	
1s ² 19s (² S _{1/2})	5.362E-11		1s ² 13p (² P _{3/2})	6.987E-11		1s ² 9d (² D _{5/2})	2.660E-12	
1s ² 20s (² S _{1/2})	5.303E-11		1s ² 14 (² P _{3/2})	1.088E-10		1s ² 10d (² D _{5/2})	3.422E-12	
1s ² 2p (² P _{1/2})	7.107E-10	7.10E-10	1s ² 15p (² P _{3/2})	1.389E-10		1s ² 11d (² D _{5/2})	4.264E-12	
1s ² 3p (² P _{1/2})	3.401E-13	3.44E-13	1s ² 16p (² P _{3/2})	1.397E-10		1s ² 12d (² D _{5/2})	5.195E-12	
1s ² 4p (² P _{1/2})	5.768E-13	5.82E-13	1s ² 17p (² P _{3/2})	1.213E-10		1s ² 13d (² D _{5/2})	6.228E-12	
1s ² 5p (² P _{1/2})	9.714E-13	9.87E-13	1s ² 18p (² P _{3/2})	1.008E-10		1s ² 14 (² D _{5/2})	7.381E-12	
1s ² 6p (² P _{1/2})	1.606E-12		1s ² 19p (² P _{3/2})	8.479E-11		1s ² 15d (² D _{5/2})	8.673E-12	
1s ² 7p (² P _{1/2})	2.590E-12		1s ² 20p (² P _{3/2})	7.340E-11		1s ² 16d (² D _{5/2})	1.012E-11	
1s ² 8p (² P _{1/2})	4.097E-12		1s ² 3d (² D _{3/2})	1.124E-13	1.16E-13	1s ² 17d (² D _{5/2})	1.175E-11	
1s ² 9p (² P _{1/2})	6.429E-12		1s ² 4d (² D _{3/2})	2.613E-13	2.68E-13	1s ² 18d (² D _{5/2})	1.358E-11	
1s ² 10p (² P _{1/2})	1.011E-11		1s ² 5d (² D _{3/2})	5.046E-13	5.14E-13	1s ² 19d (² D _{5/2})	1.561E-11	
1s ² 11p (² P _{1/2})	1.607E-11		1s ² 6d (² D _{3/2})	8.721E-13		1s ² 20d (² D _{5/2})	1.786E-11	
1s ² 12p (² P _{1/2})	2.602E-11		1s ² 7d (² D _{3/2})	1.364E-12		1s ² 4f (² F _{5/2})	5.486E-13	5.54E-13
1s ² 13p (² P _{1/2})	4.298E-11		1s ² 8d (² D _{3/2})	1.959E-12		1s ² 5f (² F _{5/2})	1.057E-12	1.07E-12
1s ² 14 (² P _{1/2})	7.162E-11		1s ² 9d (² D _{3/2})	2.641E-12		1s ² 4f (² F _{7/2})	5.499E-13	5.55E-13
1s ² 15p (² P _{1/2})	1.153E-10		1s ² 10d (² D _{3/2})	3.403E-12		1s ² 5g (² G _{9/2})	4.854E-13	1.80E-12

Table 5. The transition probabilities, oscillator, and line strengths in Sc XIX compared with NIST line data [21].

λ	Transition Probability (s^{-1})			Oscillator Strength			Line Strength			Energy		Lower Level			Upper Level		
	This work	NIST	% Diff.	This work	NIST	% Diff.	This work	NIST	% Diff.	Lower Level	Upper level	Conf.	Term	J	Conf.	Term	J
10.4428	2.462E+11	2.530E+11	2.6911	0.003968	0.004136	4.0635	0.000271	0.0002844	4.6680	0	9576000	1s2.2s	2S	0.5	1s2.7p	2P	0.5
10.4428	2.462E+11	2.530E+11	2.6911	0.007936	0.008273	4.0751	0.000542	0.0005688	4.6680	0	9576000	1s2.2s	2S	1.5	1s2.7p	2P	0.5
10.5738	2.235E+11	2.400E+11	6.8762	0.007387	0.008046	8.1847	0.000511	0.0005601	8.7392	306700	9764000	1s2.2p	2P	1.5	1s2.8d	2P	0.5
10.6308	4.361E+10	4.600E+10	5.1865	0.000729	0.000779	6.4634	0.000101	0.000109	6.9908	357400	9764000	1s2.2p	2P	1.5	1s2.8d	2P	1.5
10.6308	2.617E+11	2.800E+11	6.5409	0.006558	0.007116	7.8436	0.000912	0.0009962	8.4099	357400	9764000	1s2.2p	2P	2.5	1s2.8d	2P	1.5
10.7852	4.002E+11	4.030E+11	0.6832	0.006884	0.007028	2.0550	0.000486	0.0004991	2.6519	0	9272000	1s2.2s	2S	0.5	1s2.6p	2P	0.5
10.7852	4.002E+11	4.030E+11	0.6832	0.013767	0.01406	2.0829	0.000972	0.0009981	2.6421	0	9272000	1s2.2s	2S	1.5	1s2.6p	2P	0.5
10.7860	3.688E+11	3.660E+11	0.7644	0.012687	0.01277	0.6474	0.000896	0.0009067	1.2264	306700	9578000	1s2.2p	2P	1.5	1s2.7d	2P	0.5
10.8453	7.208E+10	7.100E+10	1.5267	0.001254	0.00125	0.2935	0.000178	0.000179	0.5763	357400	9578000	1s2.2p	2P	1.5	1s2.7d	2P	1.5
10.8453	4.325E+11	4.310E+11	0.3489	0.011283	0.0114	1.0262	0.001602	0.001628	1.6146	357400	9578000	1s2.2p	2P	2.5	1s2.7d	2P	1.5
11.1404	5.956E+11	5.930E+11	0.4434	0.021868	0.02207	0.9144	0.001595	0.001619	1.5019	306700	9283000	1s2.2p	2P	1.5	1s2.6d	2P	0.5
11.2037	1.165E+11	1.200E+11	2.9472	0.002162	0.002258	4.2319	0.000317	0.0003332	4.8069	357400	9283000	1s2.2p	2P	1.5	1s2.6d	2P	1.5
11.2037	6.988E+11	7.010E+11	0.3167	0.019462	0.01979	1.6575	0.002855	0.002919	2.2045	357400	9283000	1s2.2p	2P	2.5	1s2.6d	2P	1.5
11.3766	6.772E+11	6.900E+11	1.8556	0.012967	0.01339	3.1579	0.000966	0.001003	3.7132	0	8790000	1s2.2s	2S	0.5	1s2.5p	2P	0.5
11.3766	6.772E+11	6.900E+11	1.8556	0.025934	0.02678	3.1579	0.001932	0.002006	3.7132	0	8790000	1s2.2s	2S	1.5	1s2.5p	2P	0.5
11.7740	1.109E+12	1.090E+12	1.7434	0.045508	0.0453	0.4588	0.003508	0.00351	0.0462	306700	8800000	1s2.2p	2P	1.5	1s2.5d	2P	0.5
11.8447	2.171E+11	2.200E+11	1.2970	0.004509	0.004627	2.5444	0.000699	0.0007218	3.0933	357400	8800000	1s2.2p	2P	1.5	1s2.5d	2P	1.5
11.8447	1.303E+12	1.290E+12	0.9984	0.040583	0.0407	0.2864	0.006295	0.00635	0.8621	357400	8800000	1s2.2p	2P	2.5	1s2.5d	2P	1.5
12.6743	1.303E+12	1.400E+12	6.9013	0.031013	0.034	8.7864	0.002575	0.0028	8.0458	0	7890000	1s2.2s	2S	0.5	1s2.4p	2P	0.5
13.1539	2.424E+12	2.200E+12	10.1755	0.124289	0.11	12.9899	0.010711	0.0099	8.1938	306700	7909000	1s2.2p	2P	1.5	1s2.4d	2P	0.5
13.2405	2.859E+12	2.800E+12	2.0958	0.111398	0.11	1.2707	0.019327	0.019	1.7234	357400	7910000	1s2.2p	2P	2.5	1s2.4d	2P	1.5
13.2422	4.757E+11	4.600E+11	3.4131	0.012361	0.01209	2.2451	0.002145	0.002109	1.7063	357400	7909000	1s2.2p	2P	1.5	1s2.4d	2P	1.5
16.8180	2.895E+12	2.850E+12	1.5678	0.243169	0.242	0.4830	0.026823	0.0268	0.0852	0	5946000	1s2.2s	2S	1.5	1s2.3p	2P	0.5
16.8606	2.940E+12	2.910E+12	1.0218	0.124105	0.124	0.0844	0.013724	0.0138	0.5495	0	5931000	1s2.2s	2S	0.5	1s2.3p	2P	0.5
17.6326	7.429E+12	7.210E+12	3.0365	0.686237	0.672	2.1186	0.079376	0.078	1.7646	306700	5982000	1s2.2p	2P	1.5	1s2.3d	2P	0.5
17.7790	8.809E+12	8.580E+12	2.6678	0.620496	0.61	1.7207	0.144741	0.143	1.2173	357400	5982000	1s2.2p	2P	2.5	1s2.3d	2P	1.5
17.7917	1.467E+12	1.400E+12	4.7761	0.068982	0.066	4.5185	0.016103	0.016	0.6419	357400	5978000	1s2.2p	2P	1.5	1s2.3d	2P	1.5
18.0203	3.680E+11	3.700E+11	0.5528	0.017753	0.018	1.3725	0.002099	0.0021	0.0581	306700	5856000	1s2.2p	2P	0.5	1s2.3s	2S	0.5
18.1864	7.548E+11	7.300E+11	3.3906	0.018546	0.018	3.0336	0.004426	0.0043	2.9224	357400	5856000	1s2.2p	2P	0.5	1s2.3s	2S	1.5
26.0892	8.274E+10	8.500E+10	2.6589	0.016772	0.0173	3.0495	0.002874	0.00298	3.5587	5931000	9764000	1s2.3p	2P	1.5	1s2.8d	2D	0.5
26.1917	1.633E+10	1.700E+10	3.9220	0.001669	0.00175	4.6546	0.000574	0.000603	4.7991	5946000	9764000	1s2.3p	2P	1.5	1s2.8d	2D	1.5
26.1917	9.800E+10	1.000E+11	2.0005	0.015017	0.01543	2.6773	0.005167	0.005321	2.9026	5946000	9764000	1s2.3p	2P	2.5	1s2.8d	2D	1.5
26.8817	7.786E+10	7.700E+10	1.1165	0.008380	0.00834	0.4739	0.001480	0.00148	0.0302	5856000	9576000	1s2.3s	2S	0.5	1s2.7p	2P	0.5
26.8817	7.786E+10	7.700E+10	1.1165	0.016759	0.0167	0.3535	0.002959	0.00295	0.3087	5856000	9576000	1s2.3s	2S	1.5	1s2.7p	2P	0.5
27.4198	1.302E+11	1.290E+11	0.9564	0.029169	0.02908	0.3047	0.005254	0.00525	0.0681	5931000	9578000	1s2.3p	2P	1.5	1s2.7d	2D	0.5
27.5330	2.577E+10	2.400E+10	7.3559	0.002909	0.00273	6.5676	0.001052	0.000989	6.4033	5946000	9578000	1s2.3p	2P	1.5	1s2.7d	2D	1.5
27.5330	1.546E+11	1.520E+11	1.7055	0.026184	0.02591	1.0562	0.009471	0.009395	0.8085	5946000	9578000	1s2.3p	2P	2.5	1s2.7d	2D	1.5
27.7932	6.851E+09	6.600E+09	3.8038	0.000394	0.00038	3.7249	0.000144	0.00014	2.8007	5978000	9576000	1s2.3d	2D	0.5	1s2.7p	2P	1.5

λ	Transition Probability (s^{-1})		Oscillator Strength		Line Strength		Energy		Lower Level		Upper Level					
27.7932	6.851E+08	6.800E+08	0.7507	0.000079	0.2141	0.000029	0.7441	5978000	9576000	1s2.3d	2D	1.5	1s2.7p	2P	1.5	
27.8242	6.219E+09	6.100E+09	1.9515	0.000478	1.7284	0.000262	0.8324	5982000	9576000	1s2.3d	2D	1.5	1s2.7p	2P	2.5	
29.2740	1.295E+11	1.200E+11	7.9573	0.016541	7.2700	0.003181	7.0377	5856000	9272000	1s2.3s	2S	0.5	1s2.6p	2P	0.5	
29.2740	1.295E+11	1.200E+11	7.9573	0.033082	7.3048	0.006362	7.0557	5856000	9272000	1s2.3s	2S	1.5	1s2.6p	2P	0.5	
29.8329	2.110E+11	2.100E+11	0.4816	0.055967	0.1309	0.010969	0.3685	5931000	9283000	1s2.3p	2P	1.5	1s2.6d	2P	0.5	
29.9670	4.179E+10	4.100E+10	1.9243	0.005592	1.3025	0.002202	1.0043	5946000	9283000	1s2.3p	2P	1.5	1s2.6d	2P	1.5	
29.9670	2.507E+11	2.470E+11	1.5117	0.050327	0.04988	0.019817	0.6963	5946000	9283000	1s2.3p	2P	2.5	1s2.6d	2P	1.5	
30.3582	1.425E+10	1.200E+10	18.7737	0.000979	18.0604	0.000390	17.9539	5978000	9272000	1s2.3d	2D	0.5	1s2.6p	2P	1.5	
30.3582	1.425E+09	1.100E+09	29.5713	0.000196	30.4961	0.000078	28.0090	5978000	9272000	1s2.3d	2D	1.5	1s2.6p	2P	1.5	
30.3951	1.292E+10	1.000E+10	29.1803	0.001186	28.4542	0.000710	28.2159	5982000	9272000	1s2.3d	2D	1.5	1s2.6p	2P	2.5	
34.0832	2.112E+11	2.040E+11	3.5348	0.036579	2.9532	0.008193	2.7616	5856000	8790000	1s2.3s	2S	0.5	1s2.5p	2P	0.5	
34.0832	2.112E+11	2.040E+11	3.5348	0.073159	2.9532	0.016386	2.7358	5856000	8790000	1s2.3s	2S	1.5	1s2.5p	2P	0.5	
34.8554	3.805E+11	3.770E+11	0.9386	0.137862	0.1373	0.031580	0.1896	5931000	8800000	1s2.3p	2P	1.5	1s2.5d	2P	0.5	
35.0385	7.558E+10	7.400E+10	2.1385	0.013836	0.0136	0.006372	1.4645	5946000	8800000	1s2.3p	2P	1.5	1s2.5d	2P	1.5	
35.0385	4.535E+11	4.460E+11	1.6805	0.124520	0.1231	0.057348	0.9465	5946000	8800000	1s2.3p	2P	2.5	1s2.5d	2P	1.5	
35.5619	2.320E+10	2.200E+10	5.4453	0.002187	0.00209	0.001022	4.6477	5978000	8790000	1s2.3d	2D	0.5	1s2.5p	2P	1.5	
35.5619	2.320E+09	2.100E+09	10.4665	0.000437	0.0004	0.000204	7.6219	5978000	8790000	1s2.3d	2D	1.5	1s2.5p	2P	1.5	
35.6125	2.106E+10	1.900E+10	10.8183	0.002655	0.00241	0.001864	10.2912	5982000	8790000	1s2.3d	2D	1.5	1s2.5p	2P	2.5	
49.1642	3.808E+11	3.900E+11	2.3625	0.137382	0.1413	0.044413	2.9222	5856000	7890000	1s2.3s	2S	0.5	1s2.4p	2P	0.5	
50.5561	7.725E+11	7.800E+11	0.9648	0.589444	0.5978	0.195959	1.5281	5931000	7909000	1s2.3p	2P	1.5	1s2.4d	2P	0.5	
50.9165	9.259E+11	9.000E+11	2.8782	0.537481	0.5247	0.359919	2.3078	5946000	7910000	1s2.3p	2P	2.5	1s2.4d	2P	1.5	
50.9424	1.545E+11	1.500E+11	2.9701	0.059835	0.05836	0.040088	2.3960	5946000	7909000	1s2.3p	2P	1.5	1s2.4d	2P	1.5	
52.3013	5.274E+10	5.100E+10	3.4029	0.010768	0.0105	0.007407	2.8710	5978000	7890000	1s2.3d	2D	0.5	1s2.4p	2P	1.5	
53.3618	3.880E+10	3.850E+10	0.7720	0.032986	0.0329	0.011576	0.6567	7890000	9764000	1s2.4p	2P	1.5	1s2.8d	2D	0.5	
59.2417	5.900E+10	5.850E+10	0.8513	0.061840	0.0616	0.024095	0.3959	7890000	9578000	1s2.4p	2P	1.5	1s2.7d	2D	0.5	
59.9880	7.862E+09	7.500E+09	4.8275	0.002112	0.002	0.001667	4.1849	7909000	9576000	1s2.4d	2D	0.5	1s2.7p	2P	1.5	
59.9880	7.862E+08	7.700E+08	2.1048	0.000422	0.00042	0.000333	1.0278	7909000	9576000	1s2.4d	2D	1.5	1s2.7p	2P	1.5	
60.0240	7.110E+09	6.800E+09	4.5575	0.002550	0.0024	0.003020	4.1518	7910000	9576000	1s2.4d	2D	1.5	1s2.7p	2P	2.5	
71.7875	9.511E+10	9.120E+10	4.2900	0.146446	0.141	0.069158	3.8408	7890000	9283000	1s2.4p	2P	1.5	1s2.6d	2D	0.5	
73.3676	1.667E+10	1.400E+10	19.0558	0.006702	0.00565	0.006469	18.4818	7909000	9272000	1s2.4d	2D	0.5	1s2.6p	2P	1.5	
73.3676	1.667E+09	1.400E+09	19.0558	0.001340	0.0011	0.001294	17.6202	7909000	9272000	1s2.4d	2D	1.5	1s2.6p	2P	1.5	
73.4214	1.506E+10	1.200E+10	25.5171	0.008087	0.00647	0.011718	24.9207	7910000	9272000	1s2.4d	2D	1.5	1s2.6p	2P	2.5	
102.6694	2.150E+10			0.067742		0.043765		8790000	9764000	1s2.5p	2P	1.5	1s2.8d	2D	0.5	
102.6694	4.300E+09			0.006774		0.009153		8790000	9764000	1s2.5p	2P	1.5	1s2.8d	2D	1.5	
102.6694	2.580E+10			0.060968		0.082377		8790000	9764000	1s2.5p	2P	2.5	1s2.8d	2D	1.5	
109.8901	1.603E+11	1.590E+11	0.8386	0.578840	0.5757	0.418571	0.4165	0.4972	7890000	8800000	1s2.4p	2P	1.5	1s2.5d	2D	0.5
113.5074	2.899E+10	2.700E+10	7.3693	0.027917	0.0261	0.041704	0.039	6.9338	7909000	8790000	1s2.4d	2D	0.5	1s2.5p	2P	1.5
113.5074	2.899E+09	2.700E+09	7.3693	0.005583	0.0052	0.008341	0.0078	6.9338	7909000	8790000	1s2.4d	2D	1.5	1s2.5p	2P	1.5
113.6364	2.623E+10	2.400E+10	9.2737	0.033750	0.031	0.075713	0.0695	8.9403	7910000	8790000	1s2.4d	2D	1.5	1s2.5p	2P	2.5
126.9036	3.142E+10			0.151301		0.126358			8790000	9578000	1s2.5p	2P	1.5	1s2.7d	2D	0.5
126.9036	6.284E+09			0.015130		0.025272			8790000	9578000	1s2.5p	2P	1.5	1s2.7d	2D	1.5

λ	Transition Probability (s ⁻¹)	Oscillator Strength		Line Strength		Energy	Lower Level		Upper Level				
126.9036	3.770E+10	0.136171		0.227444		8790000	1s2.5p	2P	2.5	1s2.7d	2D	1.5	
128.8660	7.548E+09	0.009370		0.015893		8800000	1s2.5d	2D	0.5	1s2.7p	2P	1.5	
128.8660	7.548E+08	0.001874		0.003179		8800000	1s2.5d	2D	1.5	1s2.7p	2P	1.5	
128.8660	6.793E+09	0.011244		0.028607		8800000	1s2.5d	2D	1.5	1s2.7p	2P	2.5	
202.8398	4.833E+10	0.597228		0.797376		8790000	1s2.5p	2P	1.5	1s2.6d	2D	0.5	
202.8398	9.705E+09	0.059723		0.159475		8790000	1s2.5p	2P	1.5	1s2.6d	2D	1.5	
202.8398	5.823E+10	0.537505		1.433276		8790000	1s2.5p	2P	2.5	1s2.6d	2D	1.5	
203.2520	1.288E+10	0.159199		0.212983		9272000	1s2.6p	2P	1.5	1s2.8d	2D	0.5	
203.2520	2.577E+09	0.015920		0.042597		9272000	1s2.6p	2P	1.5	1s2.8d	2D	1.5	
203.2520	1.546E+10	0.143279		0.383370		9272000	1s2.6p	2P	2.5	1s2.8d	2D	1.5	
211.8644	1.669E+10	0.056031		0.156277		8800000	1s2.5d	2D	0.5	1s2.6p	2P	1.5	
211.8644	1.669E+09	0.011206		0.031255		8800000	1s2.5d	2D	1.5	1s2.6p	2P	1.5	
211.8644	1.502E+10	0.067238		0.281299		8800000	1s2.5d	2D	1.5	1s2.6p	2P	2.5	
279.7985	2.242E+09	0.052522	0.0523	0.4246	0.0964	357400	1s2.2s	2S	1.5	1s2.2p	2P	0.5	
326.0515	1.407E+09	0.022377	0.0222	0.7984	0.0476	0	306700	1s2.2s	2S	0.5	1s2.2p	2P	0.5
326.7974	1.682E+10	0.537425		1.156163		9272000	1s2.6p	2P	1.5	1s2.7d	2D	0.5	
326.7974	3.364E+09	0.053742		0.231233		9272000	1s2.6p	2P	1.5	1s2.7d	2D	1.5	
326.7974	2.018E+10	0.483682		2.081093		9272000	1s2.6p	2P	2.5	1s2.7d	2D	1.5	
341.2969	6.925E+09	0.060340		0.271142		9283000	1s2.6d	2D	0.5	1s2.7p	2P	1.5	
341.2969	6.925E+08	0.012068		0.054228		9283000	1s2.6d	2D	1.5	1s2.7p	2P	1.5	
341.2969	6.233E+09	0.072408		0.488055		9283000	1s2.6d	2D	1.5	1s2.7p	2P	2.5	
531.9149	8.743E+09	0.740213		2.592120		9576000	1s2.7p	2P	1.5	1s2.8d	2D	0.5	
531.9149	1.749E+09	0.074021		0.518424		9576000	1s2.7p	2P	1.5	1s2.8d	2D	1.5	
531.9149	1.049E+10	0.666191		4.665816		9576000	1s2.7p	2P	2.5	1s2.8d	2D	1.5	
1111.1111	2.166E+08	0.080048		0.585590		5856000	1s2.3s	2S	1.5	1s2.3p	2P	0.5	
1333.3333	1.248E+08	0.033193		0.291391		5856000	1s2.3s	2S	0.5	1s2.3p	2P	0.5	
2127.6596	1.975E+07	0.026759		0.374856		5931000	1s2.3p	2P	1.5	1s2.3d	2D	0.5	
2777.7778	1.065E+07	0.018450		0.674890		5946000	1s2.3p	2P	2.5	1s2.3d	2D	1.5	
3125.0000	1.244E+06	0.001819		0.074843		5946000	1s2.3p	2P	1.5	1s2.3d	2D	1.5	
5263.1579	5.564E+06	0.046129		1.598534		7890000	1s2.4p	2P	1.5	1s2.4d	2D	0.5	
9090.9091	6.445E+06	0.159428		9.542886		9272000	1s2.6p	2P	1.5	1s2.6d	2D	0.5	
9090.9091	1.289E+06	0.015943		1.908577		9272000	1s2.6p	2P	1.5	1s2.6d	2D	1.5	
9090.9091	7.734E+06	0.143486		17.177195		9272000	1s2.6p	2P	2.5	1s2.6d	2D	1.5	
10000.0000	2.213E+06	0.066227		4.360551		8790000	1s2.5p	2P	1.5	1s2.5d	2D	0.5	
10000.0000	4.425E+05	0.006623		0.872110		8790000	1s2.5p	2P	1.5	1s2.5d	2D	1.5	
10000.0000	2.655E+06	0.059604		7.848991		8790000	1s2.5p	2P	2.5	1s2.5d	2D	1.5	
50000.0000	7.422E+04	0.055538		18.283910		9576000	1s2.7p	2P	1.5	1s2.7d	2D	0.5	
50000.0000	1.484E+04	0.005554		3.656782		9576000	1s2.7p	2P	1.5	1s2.7d	2D	1.5	
50000.0000	8.906E+04	0.049984		32.911038		9576000	1s2.7p	2P	2.5	1s2.7d	2D	1.5	

CONCLUSION

Li-like isoelectronic ion Sc XIX has been studied for spectral line characteristics: energies, quantum defects, transition probability, oscillator, and line strengths. The following are the main points as concluding remarks.

1. The energies and quantum defects up to $n = 30$ are determined, and the available list of energies and quantum defects (up to $n = 5$) is extended.
2. The energies and quantum defects of five series $1s^2ns$ ($^2S_{1/2}$), $1s^2np$ ($^2P_{1/2}$), $1s^2np$ ($^2P_{3/2}$), $1s^2nd$ ($^2D_{3/2}$), and $1s^2nd$ ($^2D_{5/2}$) have been determined,
3. A comparison of energies with the NIST and Aggarwal et al.'s work shows good agreement results.
4. One thousand eighteen hundred and sixty-two spectral lines are investigated for calculating TP, OS, and LS of Sc XIX ion.
5. Seventy-six spectral lines were found in NIST line data for comparing the results.
6. Only six out of seventy-six lines have a percent error of more than 10%. Most of the results agree with the NIST values.
7. Almost eighteen hundred values of TP, OS, and LS are new.
8. Ninety-six Rydberg's level's lifetime was determined, and compared with the published work, only one value differs significantly.
9. The lifetimes of seventy-five levels are reported for the first time.

ORCID

©Zaheer Uddin, <https://orcid.org/0000-0002-8807-6186>

REFERENCES

- [1] B. Thorsbro, Atomic Data Needs in Astrophysics: The Galactic Center "Scandium Mystery", *Atoms*, **8**(1), 4. (2020). <https://doi.org/10.3390/atoms8010004>
- [2] G. Alecian, F. LeBlanc, and G. Massacrier, "Scandium in AmFm stars in the light of new atomic data," *Astronomy & Astrophysics*, **554**, A89 (2013). <https://doi.org/10.1051/0004-6361/201321156>
- [3] H.W. Zhang, T. Gehren, and G. Zhao, „A non-local thermodynamic equilibrium study of scandium in the Sun," *Astronomy & Astrophysics*, **481**(2), 489-497 (2008). <https://doi.org/10.1051/0004-6361:20078910>
- [4] J.E. Lawler, C. Sneden, G. Nave, M.P. Wood, and J.J. Cowan, "Transition probabilities of Sc I and Sc II and Scandium abundances in the Sun, Arcturus, and HD 84937," *The Astrophysical Journal Supplement Series*, **241**(2), 21 (2019). <https://doi.org/10.3847/1538-4365/ab08ef>
- [5] X. Liu, and J. Zhang, "Quantum defects of $1s^2nh$ configurations in Li-like system from Sc XIX to Zn XXVIII ion," *Journal of the Korean Physical Society*, **80**(12), 1107-1113 (2022). <https://doi.org/10.1007/s40042-022-00465-3>
- [6] V.A. Yerokhin, C.H. Keitel, and Z. Harman, "Two-photon-exchange corrections to the g factor of Li-like ions," *Physical Review A*, **104**(2), 022814 (2021). <https://doi.org/10.1103/PhysRevA.104.022814>
- [7] X. Liu, J.C. Zhang, and Z.W. Wang, "Theoretical calculation of ionization potentials and relativistic energies of high angular momentum $1s2ng$ states of Li-like ions," *Results in Physics*, **12**, 398-402 (2019). <https://doi.org/10.1016/j.rinp.2018.11.087>
- [8] V.A. Yerokhin, and A. Surzhykov, "Energy levels of core-excited $1s2l2l'$ states in lithium-like ions: Argon to uranium," *Journal of Physical and Chemical Reference Data*, **47**(2) (2018). <https://doi.org/10.1063/1.5034574>
- [9] V.M. Shabaev, D.A. Glazov, A.V. Malyshev, and I.I. Tupitsyn, "Recoil effect on the g factor of Li-like ions," *Physical Review Letters*, **119**(26), 263001 (2017). <https://doi.org/10.1103/PhysRevLett.119.263001>
- [10] K.M. Aggarwal, and F.P. Keenan, "Energy levels, radiative rates, and electron impact excitation rates for transitions in Li-like ions with $12 \leq Z \leq 20$," *Atomic Data and Nuclear Data Tables*, **99**(2), 156-248 (2013). <https://doi.org/10.1016/j.adt.2012.03.001>
- [11] J. Sapirstein, and K.T. Cheng, "S-matrix calculations of energy levels of the lithium isoelectronic sequence," *Physical Review A*, **83**(1), 012504 (2011). <https://doi.org/10.1103/PhysRevA.83.012504>
- [12] W. Zhi-Wen, Y. Di, H. Mu-Hong, H. Qiu-Ju, and L. Jin-Ying, "Transition energy and oscillator strength of Sc18+ ion," *Chinese Physics*, **14**(8), 1559 (2005). <https://doi.org/10.1088/1009-1963/14/8/015>
- [13] T. Nishikawa, "Energy level data recommendation by screening constant," *Journal of Quantitative Spectroscopy and Radiative Transfer*, **67**(1), 43-54 (2000). [https://doi.org/10.1016/S0022-4073\(99\)00192-2](https://doi.org/10.1016/S0022-4073(99)00192-2)
- [14] E. BiÉmont, Y. Frémat, and P. Quinet, "Ionization potentials of atoms and ions from lithium to tin ($Z = 50$)," *Atomic Data and Nuclear Data Tables*, **71**(1), 117-146 (1999). <https://doi.org/10.1006/adnd.1998.0803>
- [15] Z.C. Yan, M. Tambasco, and G.W.F. Drake, "Energies and oscillator strengths for lithiumlike ions," *Physical Review A*, **57**(3), 1652 (1998). <https://doi.org/10.1103/PhysRevA.57.1652>
- [16] Q.R. Zhu, S.F. Pan, and T.H. Zeng, "Energy levels, wavelengths, and radiative transition probabilities for the Li-like ions with $20 \leq Z \leq 25$," *Atomic data and nuclear data tables*, **52**(1), 109-141 (1992). [https://doi.org/10.1016/0092-640X\(92\)90010-F](https://doi.org/10.1016/0092-640X(92)90010-F)
- [17] M. Saeed, and Z. Uddin, "Lifetimes of Fine Levels of Li Atom for $20 < n < 31$ by Extended Ritz Formula," *Canadian Journal of Physics*, (January), (2023). <https://doi.org/10.1139/cjp-2023-0220>
- [18] M. Saeed, S.U. Rehman, M.M. Khan, and Z. Uddin, "Computation of Characteristics of C IV Transitions," *East European Journal of Physics*, (2), 165-172 (2023). <https://doi.org/10.26565/2312-4334-2023-2-16>
- [19] R. Siddique, R. Zafar, S. Raza, S.Z. Iqbal, and Z. Uddin, "Mean Lifetimes of ns, np, nd, & nf Levels of NV," *East European Journal of Physics*, (3), 424-429 (2023). <https://doi.org/10.26565/2312-4334-2023-3-46>
- [20] R. Siddiq, M.N. Hameed, M.H. Zaheer, M.B. Khan, and Z. Uddin, "Rydberg energies and transition probabilities of Li I for $np - ms$ ($m \leq 5$) transitions," *Beni-Suef University Journal of Basic and Applied Sciences*, **11**(1), 1-9 (2022). <https://doi.org/10.1186/s43088-022-00224-0>
- [21] National Institute of Standards and Technology, 100 Bureau Drive Gaithersburg, MD 20899, 301-975-2000, USA, https://physics.nist.gov/PhysRefData/ASD/lines_form.html

ІМОВІРНОСТІ ПЕРЕХОДУ, ОСЦИЛЯТОР ТА ІНТЕНСИВНІСТЬ ЛІНІЙ У Sc XIX

Мухаммад Калім^a, Саба Джавайд^b, Рухі Зафар^b, Захір Уддін^a

^aФізичний факультет Університету Карачі, Карачі, Пакистан

^bКафедра фізики, Університет інженерії та технології NED, Карачі, Пакистан

Іон скандію XIX є членом ізоелектронної послідовності Li-подібних іонів. Чисельне кулонівське наближення та квантовий дефект теорія була використана для розрахунку енергій, квантових дефектів і ймовірностей переходу, осцилятора та сили ліній іона Sc XIX для переходів $ns \rightarrow mp$, $np \rightarrow ms$, $pr \rightarrow md$ і $nd \rightarrow mp$ ряд Рідберга. Енергії іонів Sc XIX до $n = 5$ наведено в База даних NIST і література. Ми використали квантову теорію дефектів і визначили енергії та квантові дефекти до $n = 30$. енергії та квантових дефектів 125 рівнів повідомляється вперше. Імовірності переходу іона Sc XIX, осцилятор і лінія сили порівнювали з відповідними значеннями в базі даних спектральних ліній NIST. База даних NIST містить дані про лише сімдесят шість спектральних ліній. Лише шість спектральних ліній мають відсоткову невизначеність понад 10%. Результатів залишилося сімдесят спектральні лінії добре узгоджуються зі значеннями NIST. Майже 1800 ймовірностей переходів, осциляторів і інтенсивності ліній є новими.

Ключові слова: скандій; Li-подібний; рівень Ридберга; квантова теорія дефектів; ймовірність переходу; сила осцилятора; інтенсивність ліній

EVOLUTION OF VECTOR VORTEX BEAMS FORMED BY A TERAHERTZ LASER METAL RESONATOR

✉ **Andrey V. Degtyarev**, ✉ **Mykola M. Dubinin**, ✉ **Vyacheslav A. Maslov***, ✉ **Konstantin I. Muntean**,
✉ **Oleh O. Svystunov**

V.N. Karazin Kharkiv National University, 4 Svoboda Sq., Kharkiv 61022, Ukraine

**Corresponding Author: v.a.maslov@karazin.ua*

Received February 8, 2024; revised March 31, 2024; accepted April 8, 2024

Analytical expressions for the nonparaxial mode diffraction of a terahertz laser metal waveguide resonator are obtained. The study assumes interaction between the modes and a spiral phase plate, considering different topological charges (n). Also, using numerical modeling, the physical features of the emerging vortex beams as they propagate in free space are studied. The Rayleigh-Sommerfeld vector theory is employed to investigate the propagation of vortex laser beams in the Fresnel zone, excited by the modes of a metal waveguide quasi-optical resonator upon incidence on a spiral phase plate. In free space, the spiral phase plate for exciting TE_{11} mode from the profile with the intensity maximum in the center ($n = 0$) forms an asymmetric ring one with two maxima ($n = 1, 2$). For the exciting TE_{01} mode, the initial ring ($n = 0$) structure of the field intensity is transformed into a structure with a maximum radiation intensity in the center ($n = 1$), and later again into a ring ($n = 2$). The phase front of the beam for the E_y component of the linearly polarized along the y axis TE_{11} mode changes from spherical to spiral with one on-axis singularity point. In the phase profile of the transverse components of the azimuthally polarized TE_{01} mode, a region with two and three off-axis phase singularity points appears.

Keywords: *Terahertz laser; Metal waveguide resonator; Spiral phase plate; Vortex beams; Polarization; Radiation propagation*

PACS: 42.55.Lt; 42.60.Da; 42.25.Bs; 47.32.C-

INTRODUCTION

In the past decade, there has been a notable surge in interest regarding the formation of terahertz laser beams [1]. Vortex beams within these wave fields hold a prominent position in research. Their uniqueness stems from the distinct spiral structure of the wavefront, ensuring the presence of an orbital wave momentum with a considerable number of states and, consequently, additional degrees of freedom [2 – 4]. Vortex laser beams demonstrate significant potential for applications in high-speed multiplex terahertz communication systems, tomography, the exploration of linear and nonlinear material responses, the acceleration and manipulation of electron bunches, and the detection of astrophysical sources [5 – 9].

The study of THz vortex beam generation primarily focuses on two principles: wavefront modulation through specialized external devices and direct excitation of vortex beams at the output of the resonator. The extracavity wavefront modulation principle employs various tools such as spiral phase plates, q -plates, achromatic polarization elements, diffractive optical elements, metasurfaces, liquid crystal branched polarization gratings, computer holograms, and spatial modulators [10 – 17]. Techniques like optical rectification, difference-frequency generation, and laser-plasma methods have been proposed for forming vortex beams at the laser resonator output [18 – 20]. However, the majority of these studies utilize broadband radiation from subpicosecond pulse generators based on femtosecond lasers, leading to the complex manufacturing of laser systems and interactions with matter that significantly deviate from continuous radiation.

Optically pumped molecular lasers stand out as the sole compact source of continuous terahertz radiation, offering discrete tunability across the entire terahertz range and boasting a narrow spectral linewidth. The current surge in interest for these generators is attributed to the potential use of continuously tunable mid-IR quantum cascade lasers as pump sources [21]. The utilization of metal waveguide quasi-optical resonators is common in most optically pumped lasers, enabling the achievement of relatively high powers (up to 1 W) in a continuous regime with relatively compact cavity sizes [22]. Among the modes of such resonators, TE_{11} and TE_{01} modes with linear and azimuthal polarization exhibit the lowest losses [23].

One of the most renowned optical elements for generating vortex beams is the spiral phase plate with azimuthally varying thickness [3, 24]. This element enables the direct application of a spiral phase shift to the incident laser beam, converting almost 100 % of the incoming radiation energy into a vortex beam.

This study aims to derive analytical expressions that describe the nonparaxial diffraction of modes a metal waveguide resonator of a terahertz laser when interacting with a spiral phase plate. Additionally, through numerical simulations, the research investigates the physical characteristics of the resulting vortex beams during their propagation in free space.

THEORETICAL RELATIONSHIPS

The well-known vectorial Rayleigh-Sommerfeld integrals in the Cartesian coordinate system will be employed to describe the propagation of laser radiation in free space along the $0z$ axis [25 – 27]:

$$\begin{aligned} E_x(\vec{r}) &= -\frac{1}{2\pi} \int \int_{\Sigma_0} E_x^0(\vec{r}_0) \frac{\partial}{\partial z} \left[\frac{\exp(ikR)}{R} \right] dx_0 dy_0, \\ E_y(\vec{r}) &= -\frac{1}{2\pi} \int \int_{\Sigma_0} E_y^0(\vec{r}_0) \frac{\partial}{\partial z} \left[\frac{\exp(ikR)}{R} \right] dx_0 dy_0, \\ E_z(\vec{r}) &= \frac{1}{2\pi} \int \int_{\Sigma_0} \left\{ E_x^0(\vec{r}_0) \frac{\partial}{\partial x} \left[\frac{\exp(ikR)}{R} \right] + E_y^0(\vec{r}_0) \frac{\partial}{\partial y} \left[\frac{\exp(ikR)}{R} \right] \right\} dx_0 dy_0, \end{aligned} \quad (1)$$

where $E_x^0(\vec{r}_0)$ and $E_y^0(\vec{r}_0)$ are the complex amplitudes of the x and y components of the input electric field, Σ_0 is the area in which the input field is specified, $k = 2\pi/\lambda$ is the wave number, λ is the wavelength, $\vec{r}_0 = x_0 \vec{e}_{x_0} + y_0 \vec{e}_{y_0}$, (x_0, y_0) are the Cartesian coordinates in the source plane, $\vec{r} = x \vec{e}_x + y \vec{e}_y + z \vec{e}_z$, (x, y, z) are the Cartesian coordinates in the observation plane, $R = \sqrt{(x-x_0)^2 + (y-y_0)^2 + z^2}$. Using nonparaxial approximation (1), let us expand R into a series, keeping its first and second terms in the form

$$R \cong r + \frac{x_0^2 + y_0^2 - 2xx_0 - 2yy_0}{2r}, \quad (2)$$

where $r = \sqrt{x^2 + y^2 + z^2}$.

Substituting (2) into the integrand, which includes rapidly oscillating exponents (1), and at other positions $R \cong r$, and then transitioning to cylindrical coordinates, yields expressions for the field components in different diffraction zones:

$$E_x(\rho, \beta, z) = -\frac{iz}{\lambda r^2} \exp(ikr) \int_0^\infty \int_0^{2\pi} E_x^0(\vec{r}_0) \exp\left(ik \frac{\rho_0^2}{2r}\right) \exp\left(-ik \frac{\rho \rho_0 \cos(\varphi - \beta)}{r}\right) \rho_0 d\rho_0 d\varphi, \quad (3.1)$$

$$E_y(\rho, \beta, z) = -\frac{iz}{\lambda r^2} \exp(ikr) \int_0^\infty \int_0^{2\pi} E_y^0(\vec{r}_0) \exp\left(ik \frac{\rho_0^2}{2r}\right) \exp\left(-ik \frac{\rho \rho_0 \cos(\varphi - \beta)}{r}\right) \rho_0 d\rho_0 d\varphi, \quad (3.2)$$

$$\begin{aligned} E_z(\rho, \beta, z) &= \frac{i}{\lambda r^2} \exp(ikr) \int_0^\infty \int_0^{2\pi} \left[E_x^0(\vec{r}_0)(\rho \cos \beta - \rho_0 \cos \varphi) + E_y^0(\rho \sin \beta - \rho_0 \sin \varphi) \right] \\ &\times \exp\left(ik \frac{\rho_0^2}{2r}\right) \exp\left(-ik \frac{\rho \rho_0 \cos(\varphi - \beta)}{r}\right) \rho_0 d\rho_0 d\varphi. \end{aligned} \quad (3.3)$$

Here (ρ, β, z) are cylindrical coordinates in the observation plane and (ρ_0, φ) are the polar coordinates in the area where the input field is specified, $r = \sqrt{\rho^2 + z^2}$.

Investigated metal waveguide resonator modes coincide with the modes of a circular metal waveguide. Hence, in the initial plane, we characterize radiation through linearly and azimuthally polarized waveguide TE_{11} and TE_{01} modes. The normalized Cartesian components of electromagnetic fields for these modes take the following form in the source plane ($z = 0$) [28]:

$$TE_{11} \text{ mode} \begin{cases} E_x^0(\rho_0, \varphi) = A_{11} J_2(\chi_{11} \frac{\rho_0}{a}) \sin(2\varphi), \\ E_y^0(\rho_0, \varphi) = A_{11} [J_0(\chi_{11} \frac{\rho_0}{a}) - J_2(\chi_{11} \frac{\rho_0}{a}) \cos(2\varphi)], \end{cases} \quad (4)$$

$$TE_{01} \text{ mode} \begin{cases} E_x^0(\rho_0, \varphi) = -A_{01} J_1(\chi_{01} \frac{\rho_0}{a}) \sin(\varphi), \\ E_y^0(\rho_0, \varphi) = A_{01} J_1(\chi_{01} \frac{\rho_0}{a}) \cos(\varphi), \end{cases} \quad (5)$$

where a is the waveguide radius, $A_{11} = \frac{\chi_{11}}{a J_1(\chi_{11}) \sqrt{2\pi(\chi_{11}^2 - 1)}}$, $A_{01} = \frac{1}{a \sqrt{\pi} J_0(\chi_{01})}$ are the normalizing factors,

J_j is the Bessel function of the 1st kind of order j ; χ_{mn} is the n -th root of the equation $J_m(\chi) = 0$.

We will explore the interaction between these modes and a spiral phase plate (SPP) with arbitrary topological charge (n) [29]. The SPP is positioned at the output of a waveguide with an aperture of the same diameter, as illustrated in Figure 1. The complex transmission function of an SPP with a radius a is expressed in polar coordinates as follows [3]:

$$T_n(\rho_0, \varphi) = \text{circ}\left(\frac{\rho_0}{a}\right) \exp(in\varphi), \tag{6}$$

where $\text{circ}(\cdot)$ is the circular function.

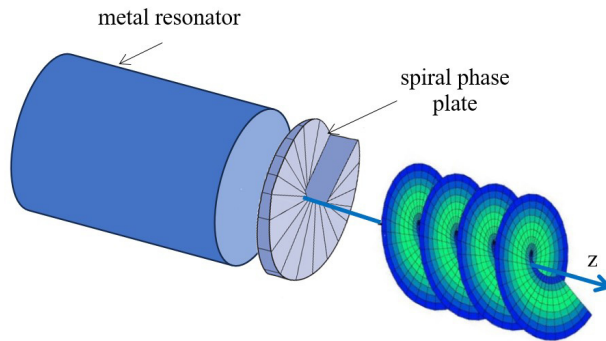


Figure 1. Topology of the model.

For simplifying calculations, integration over the angle φ in equation (3) can be carried out using the established relations for the integer $m \geq 0$, as described in [26]:

$$\int_0^{2\pi} \cos(m\varphi + \varphi_0) \exp[-ix \cos(\varphi - \theta)] d\varphi = 2\pi (-i)^m J_m(x) \cos(m\theta + \varphi_0),$$

$$\int_0^{2\pi} \sin(m\varphi + \varphi_0) \exp[-ix \cos(\varphi - \theta)] d\varphi = 2\pi (-i)^m J_m(x) \sin(m\theta + \varphi_0).$$

Then from here we can obtain the following relation

$$\int_0^{2\pi} e^{-ix \cos(\varphi - \beta)} e^{in\varphi} d\varphi = 2\pi e^{in\beta} (-i)^n J_n(x). \tag{7}$$

Using Euler’s formulas for the trigonometric functions and taking into account Eq. (7), we obtain the expressions for the following integrals:

$$\int_0^{2\pi} e^{-ix \cos(\varphi - \beta)} e^{in\varphi} \sin(m\varphi + \varphi_0) d\varphi = \frac{\pi}{i} \{ e^{i[(n+m)\beta + \varphi_0]} (-i)^{n+m} J_{n+m}(x) - e^{i[(n-m)\beta - \varphi_0]} (-i)^{n-m} J_{n-m}(x) \}, \tag{8.1}$$

$$\int_0^{2\pi} e^{-ix \cos(\varphi - \beta)} e^{in\varphi} \cos(m\varphi + \varphi_0) d\varphi = \pi \{ e^{i[(n+m)\beta + \varphi_0]} (-i)^{n+m} J_{n+m}(x) + e^{i[(n-m)\beta + \varphi_0]} (-i)^{n-m} J_{n-m}(x) \}. \tag{8.2}$$

Then, substituting into (3) the expression for the complex transmission function of the SPP (6) and using formulas (7) and (8.1), we obtain expressions for the field components that describe the nonparaxial diffraction of the TE_{11} mode by the SPP with topological charge n in free space:

$$E_x(\rho, \beta, z) = \frac{(-i)^n kz}{2r^2} \exp[i(n\beta + kr)] A_{11} [\exp(i2\beta) H_{1, n+2}(\rho, z) - \exp(-i2\beta) H_{1, n-2}(\rho, z)], \tag{9.1}$$

$$E_y(\rho, \beta, z) = \frac{(-i)^{n+1} kz}{r^2} \exp[i(n\beta + kr)] A_{11} [H1_{0,n}(\rho, z) + \frac{1}{2} [\exp(i2\beta)H1_{2,n+2}(\rho, z) + \exp(-i2\beta)H1_{2,n-2}(\rho, z)]], \quad (9.2)$$

$$E_z(\rho, \beta, z) = \frac{(-i)^{n+1} k}{2r^2} \exp[i(n\beta + kr)] A_{11} [G1(\rho, \beta, z) + G2(\rho, \beta, z) + 2\rho \sin(\beta)H1_{0,n}(\rho, z)], \quad (9.3)$$

where the following notations are introduced

$$H1_{0,n}(\rho, z) = \int_0^a J_0\left(\chi_{11} \frac{\rho_0}{a}\right) \exp\left(ik \frac{\rho_0^2}{2r}\right) J_n\left(\frac{k\rho\rho_0}{r}\right) \rho_0 d\rho_0, \quad (10.1)$$

$$H1_{2,n}(\rho, z) = \int_0^a J_2\left(\chi_{11} \frac{\rho_0}{a}\right) \exp\left(ik \frac{\rho_0^2}{2r}\right) J_n\left(\frac{k\rho\rho_0}{r}\right) \rho_0 d\rho_0, \quad (10.2)$$

$$G1(\rho, \beta, z) = \int_0^a J_2\left(\chi_{11} \frac{\rho_0}{a}\right) \exp\left(ik \frac{\rho_0^2}{2r}\right) \times \left[\exp(i\beta)J_{n-2}\left(\frac{k\rho\rho_0}{r}\right) - \exp(-i\beta)J_{n+2}\left(\frac{k\rho\rho_0}{r}\right) \right] \rho_0 d\rho_0, \quad (10.3)$$

$$G2(\rho, \beta, z) = \int_0^a \left[J_0\left(\chi_{11} \frac{\rho_0}{a}\right) + J_2\left(\chi_{11} \frac{\rho_0}{a}\right) \right] \exp\left(ik \frac{\rho_0^2}{2r}\right) \times \left[\exp(i\beta)J_{n+1}\left(\frac{k\rho\rho_0}{r}\right) - \exp(-i\beta)J_{n-1}\left(\frac{k\rho\rho_0}{r}\right) \right] \rho_0^2 d\rho_0. \quad (10.4)$$

Also, using formulas (8.1) and (8.2), we obtain expressions for the field components that describe the nonparaxial diffraction of the TE₀₁ mode on the SPP. They look as follows:

$$E_x(\rho, \beta, z) = \frac{(-i)^{n+1} kz}{2r^2} \exp[i(n\beta + kr)] B_{01} [\exp(i\beta)H2_{1,n+1}(\rho, z) + \exp(-i\beta)H2_{1,n-1}(\rho, z)], \quad (11.1)$$

$$E_y(\rho, \beta, z) = \frac{(-i)^{n+2} kz}{2r^2} \exp[i(n\beta + kr)] B_{01} [\exp(i\beta)H2_{1,n+1}(\rho, z) - \exp(-i\beta)H2_{1,n-1}(\rho, z)], \quad (11.2)$$

$$E_z(\rho, \beta, z) = \frac{(-i)^{n+1} k\rho}{2r^2} \exp[i(n\beta + kr)] B_{01} [H2_{1,n+1}(\rho, z) + H2_{1,n-1}(\rho, z)], \quad (11.3)$$

where the following notation is introduced

$$H2_{1,n}(\rho, z) = \int_0^a J_1\left(\chi_{01} \frac{\rho_0}{a}\right) \exp\left(ik \frac{\rho_0^2}{2r}\right) J_n\left(\frac{k\rho\rho_0}{r}\right) \rho_0 d\rho_0.$$

NUMERICAL RESULTS AND DISCUSSIONS

Using the obtained expressions, calculations of the longitudinal and transverse distributions of the total field intensity were carried out. ($I = |E_x|^2 + |E_y|^2 + |E_z|^2$), as well as transverse intensity distributions ($I = |E_i|^2$, $i = x, y$) and phases ($\varphi = \arctg(\text{Im}(E_i) / \text{Re}(E_i))$) fields for individual x, y components of laser radiation beams excited in the Fresnel zone by an asymmetrical linearly polarized along the y axis TE₁₁ mode and a symmetrical azimuthally polarized TE₀₁ mode of a metal waveguide resonator of a terahertz laser during their interaction with the SPP. The transverse distributions of the field intensity and phase for the longitudinal component are not given due to its insignificant influence on the total radiation intensity. The radiation wavelength was chosen in the middle part of the terahertz range $\lambda = 0.4326$ mm (the lasing line of optically excited formic acid molecule HCOOH [30]). The waveguide diameter is chosen to be $2a = 35$ mm. The SPP with an aperture of the same diameter was placed at the output of the waveguide. In this case, the topological charge n changed from zero to two.

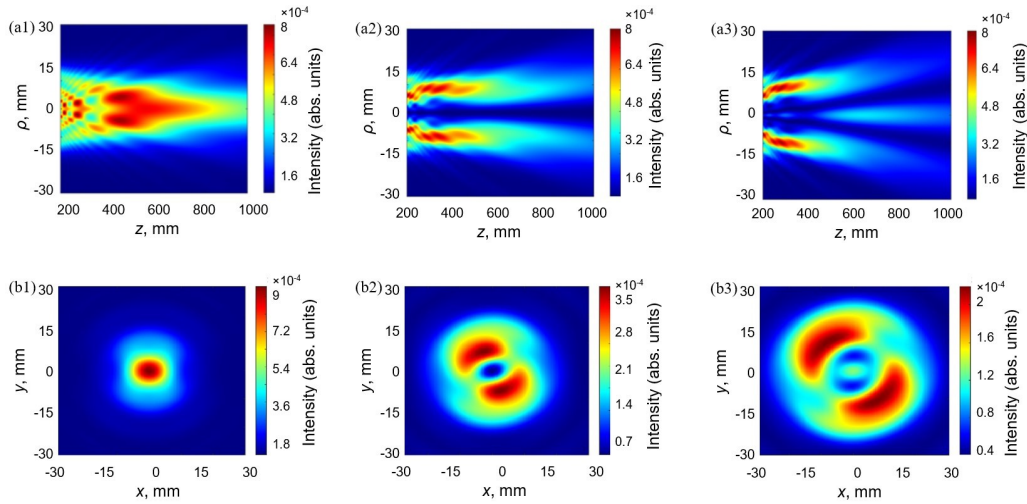


Figure 2. Calculated longitudinal (a1–a3) and transverse (b1–b3) total field intensity distributions of the laser beams excited by the TE_{11} mode in the Fresnel zone for different values of the topological charge. The first, second and third columns correspond to $n = 0$, $n = 1$ and $n = 2$, respectively.

Figure 2 (a1), 2(b1) show the results of numerical simulation for the longitudinal intensity field distribution in the Fresnel zone ($z = 100 - 1000$ mm) and the transverse intensity field distribution excited by the TE_{11} mode for $z = 708$ mm (where the Fresnel number is 1). The results were obtained under the assumption that there is no SPP at the waveguide output. One can observe from the figures that the maximum in the distribution of longitudinal intensity is observed at $z \approx 500$ mm. Notice that the effective beam diameter at a distance of 708 mm for the TE_{11} mode is calculated according to the formula [31]

$$d_{\sigma} = 2 \sqrt{\frac{2 \int_0^{\infty} \int_0^{2\pi} \rho^2 I(\rho, \beta, z) \rho d\rho d\beta}{\int_0^{\infty} \int_0^{2\pi} I(\rho, \beta, z) \rho d\rho d\beta}}$$

and is equal to $d_{\sigma} = 151.3 \lambda$. The transverse field profile has a well-known Gaussian-like shape and a spherical phase front. Installing a SPP at the output of a waveguide with a non-zero topological charge leads in the Fresnel zone to a change in the beam intensity profile to an asymmetric annular one with two maxima (Figure 2 (a2, a3, b2, b3)). The beam diameter increases to $d_{\sigma} = 164.6 \lambda$ at $n = 1$ and $d_{\sigma} = 192.0 \lambda$ at $n = 2$.

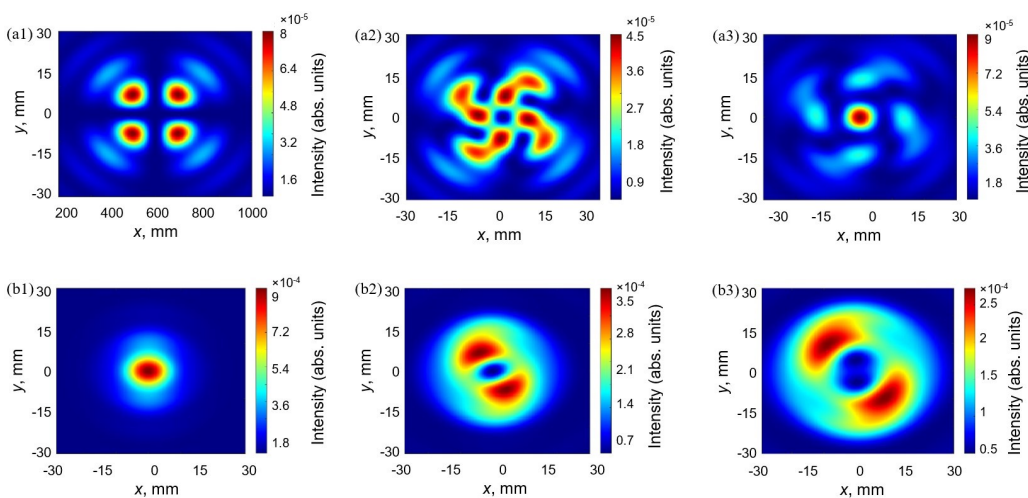


Figure 3. Calculated field intensity distributions for E_x (a1–a3) and E_y (b1–b3) components of the laser beams excited by the TE_{11} mode in the Fresnel zone for different values of the topological charge. The first, second and third columns correspond to $n = 0$, $n = 1$ and $n = 2$, respectively.

Figures 3–4 show the calculated distributions of field intensity and phase for individual transverse components excited in the Fresnel zone by an asymmetric linearly polarized along the y axis TE_{11} mode of a metal waveguide

resonator of a terahertz laser during its interaction with the SPP. These results clearly demonstrate the determining role of the E_y component of the laser beam in the formation of the total transverse intensity profile in Figure 2. Note the observed focusing of the field intensity of the E_x -component of the laser beam in the case of an increase in the value of the topological charge.

As can be seen from Figure 4, the installation of the SPP at the output of the waveguide for the TE_{11} mode leads to the transformation of the beam phase profile from spherical to vortex. In this case, with an increase in the value of the topological charge, the formation of a pronounced helical structure of the wave front and a singularity point for the E_y component of the laser beam is observed.

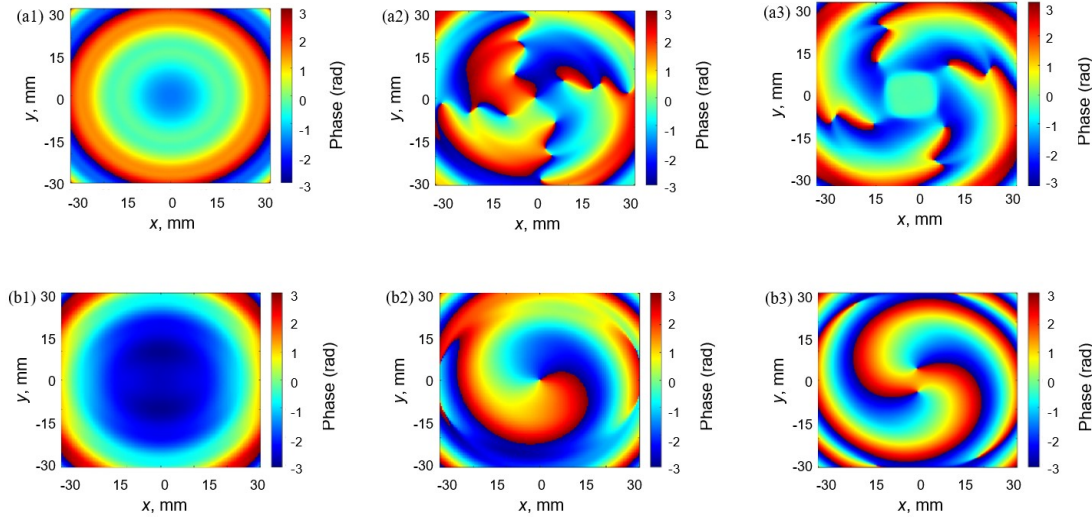


Figure 4. Calculated field phase distributions for E_x (a1–a3) and E_y (b1–b3) components of the laser beams excited by the TE_{11} mode in the Fresnel zone for different values of the topological charge. The first, second and third columns correspond to $n = 0$, $n = 1$ and $n = 2$, respectively.

The installation of the SPP at the output of the waveguide for the TE_{01} mode leads to the transformation of the beam intensity profile from annular to Gaussian-like when the value of the topological charge changes from zero to one (Figure 5). Further increase in the topological charge returns the beam profile to its original annular shape. Mention that the beam diameter at a distance of 708 mm for the TE_{01} mode increases from $d_\sigma = 67.5 \lambda$ at $n = 0$ (in the absence of topological charge) to $d_\sigma = 89.1 \lambda$ at $n = 2$.

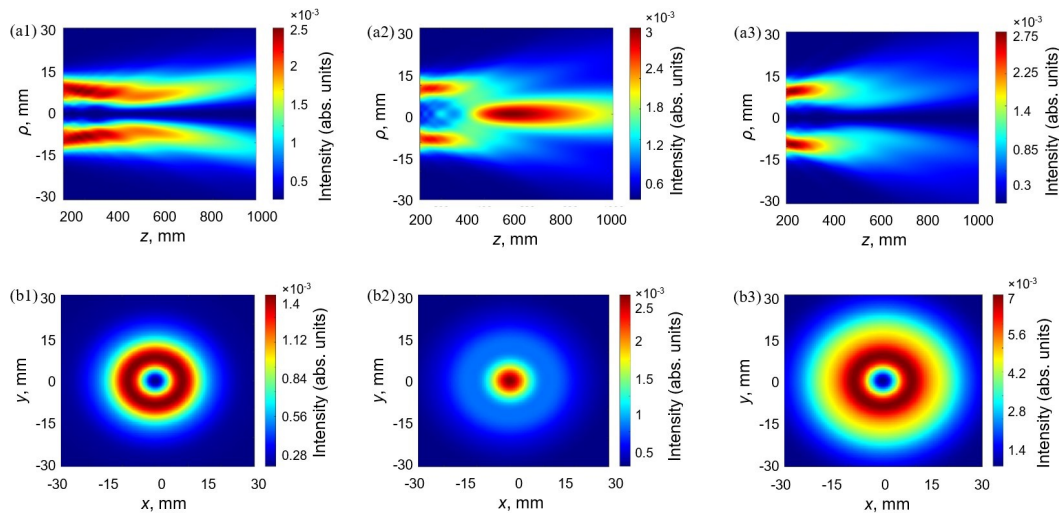


Figure 5. Calculated longitudinal (a1–a3) and transverse (b1–b3) total field intensity distributions excited by the TE_{01} mode in the Fresnel zone for different values of the topological charge. The first, second and third columns correspond to $n = 0$, $n = 1$ and $n = 2$, respectively.

Figure 6 shows the calculated transverse field intensity distributions for individual transverse components of laser radiation beams excited in the Fresnel zone by a symmetrical azimuthally polarized TE_{01} mode of a metal waveguide resonator of a terahertz laser during its interaction with the SPP. These results show the same contribution of the transverse components of the laser beam to the formation of the total intensity profile in Figure 5. Possessing an initially antisymmetrical shape, these components, when added, form a symmetrical beam.

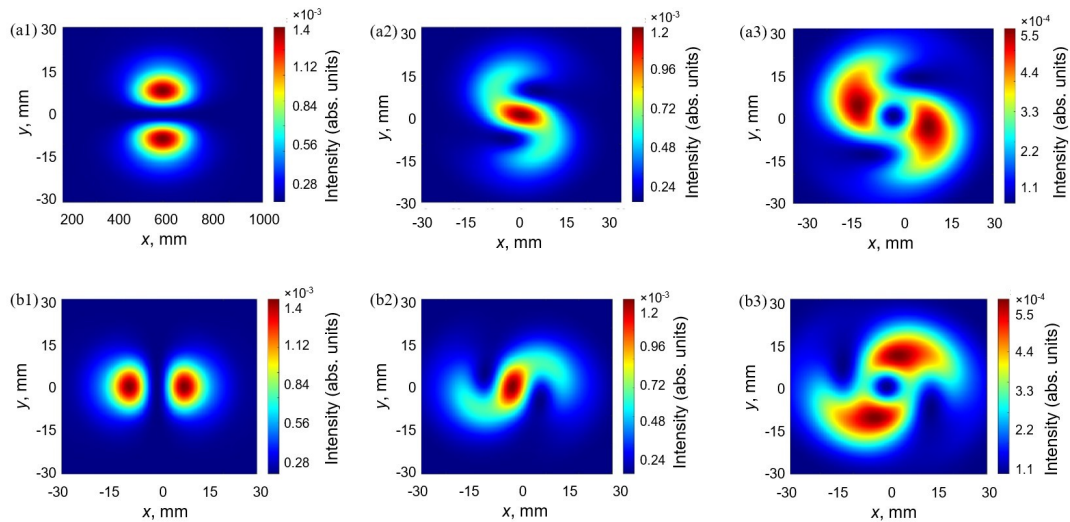


Figure 6. Calculated field intensity distributions for E_x (a1–a3) and E_y (b1–b3) components of the laser beams excited by the TE_{01} mode in the Fresnel zone for different values of the topological charge. The first, second and third columns correspond to $n = 0$, $n = 1$ and $n = 2$, respectively.

Figure 7 shows the phase distributions for the transverse components of the TE_{01} mode in the Fresnel zone when the topological charge changes. Installing the SPP at the output of the waveguide, as for the TE_{11} mode, converts the wavefront of laser beams from spherical to vortex. Note that for $n = 1$ the wavefront has two helical surfaces, and for $n = 2$ it has three.

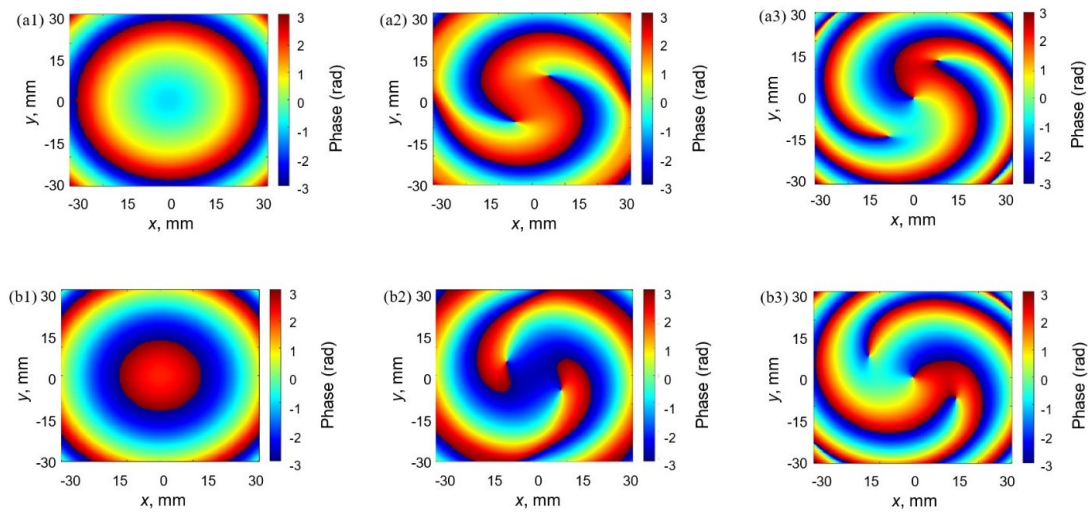


Figure 7. Calculated field phase distributions for E_x (a1–a3) and E_y (b1–b3) components of the laser beams excited by the TE_{01} mode in the Fresnel zone for different values of the topological charge. The first, second and third columns correspond to $n = 0$, $n = 1$ and $n = 2$, respectively.

CONCLUSIONS

Analytical expressions have been obtained to describe the nonparaxial diffraction of modes of a metal waveguide resonator of a terahertz laser during their interaction with a spiral phase plate with different topological charges (n). The determining role of the E_y component of the laser beam for the exciting linearly polarized along the y axis TE_{11} mode and the equal contribution of the transverse components for the exciting azimuthally polarized TE_{01} mode in the formation of the total transverse field are shown.

In free space, the spiral phase plate for TE_{11} mode from the profile with the intensity maximum in the center ($n = 0$) forms an asymmetric ring one with two maxima ($n = 1, 2$). For the TE_{01} mode, the initial ring ($n = 0$) structure of the field intensity is transformed into a structure with a maximum radiation intensity in the center ($n = 1$), and later again into a ring ($n = 2$).

The phase front of the beam for the E_y component of the TE_{11} mode changes from spherical to spiral with one on-axis singularity point. Conversely, in the phase profile of the transverse components of the azimuthally polarized TE_{01} mode, a region with two and three off-axis phase singularity points appears.

ORCID

-  **Andrey V. Degtyarev**, <https://orcid.org/0000-0003-0844-4282>;
  **Mykola M. Dubinin**, <https://orcid.org/0000-0002-7723-9592>
 **Vyacheslav O. Maslov**, <https://orcid.org/0000-0001-7743-7006>;
  **Konstantin I. Muntean**, <https://orcid.org/0000-0001-6479-3511>
 **Oleh O. Svystunov**, <https://orcid.org/0000-0002-4967-5944>

REFERENCES

- [1] D. Headland, Y. Monnai, D. Abbott, C. Fumeaux, and W. Withayachumnankul, "Tutorial: Terahertz beamforming, from concepts to realizations", *Apl. Photonics*, **3**, 051101 (2018). <https://doi.org/10.1063/1.5011063>
- [2] A. Forbes, "Advances in orbital angular momentum lasers", *J. Light. Technol.*, **41**, 2079 (2023). <https://doi.org/10.1109/JLT.2022.3220509>
- [3] H. Wang, Q. Song, Y. Cai, Q. Lin, X. Lu, H. Shangguan, Y. Ai, and S. Xu, "Recent advances in generation of terahertz vortex beams and their applications", *Chin. Phys. B*, **29**, 097404 (2020). <https://doi.org/10.1088/1674-1056/aba2df>
- [4] N.V. Petrov, B. Sokolenko, M.S. Kulya, A. Gorodetsky, and A.V. Chernykh, "Design of broadband terahertz vector and vortex beams: I. Review of materials and components", *Light: Advanced Manufacturing*, **3**, 640 (2022). <https://doi.org/10.37188/lam.2022.043>
- [5] T. Nagatsuma, G. Ducournau, and C. Renaud, "Advances in terahertz communications accelerated by photonics", *Nat. Photonics*, **10**, 371 (2016). <https://doi.org/10.1038/nphoton.2016.65>
- [6] S.C. Chen, Z. Feng, Z. J. Li, W. Tan, L.H. Du, J. Cai, and L.G. Zhu, "Ghost spintronic THz-emitter-array microscope", *Light Sci. Appl.*, **9**, 99 (2020). <https://doi.org/10.1038/s41377-020-0338-4>
- [7] D. Nobahar, S. Khorram, "Terahertz vortex beam propagation through a magnetized plasma-ferrite structure", *Opt. Laser Technol.*, **146**, 107522 (2022). <https://doi.org/10.1016/j.optlastec.2021.107522>
- [8] M.T. Hibberd, A.L. Healy, D.S. Lake, V. Georgiadis, E.J.H. Smith, O.J. Finlay, and S.P. Jamison, "Acceleration of relativistic beams using laser generated terahertz pulses", *Nat. Photonics*, **14**, 755 (2019). <https://doi.org/10.1038/s41566-020-0674-1>
- [9] A. Klug, I. Nape, and A. Forbes, "The orbital angular momentum of a turbulent atmosphere and its impact on propagating structured light fields", *New J. Phys.*, **23**, 093012 (2021). <https://doi.org/10.1088/1367-2630/ac1fca>
- [10] S.W. Pinnock, S. Roh, T. Biesner, A.V. Pronin, and M. Dressel, "Generation of THz vortex beams and interferometric determination of their topological charge", *IEEE Trans. Terahertz Sci. Technol.*, **13**, 44 (2022). <https://doi.org/10.1109/THHZ.2022.3221369>
- [11] A. Rubano, F. Cardano, B. Piccirillo, and L. Marrucci, "Q-plate technology: a progress review [Invited]", *J. Opt. Soc. Am. B*, **36**, D70–D87 (2019). <https://doi.org/10.1364/JOSAB.36.000D70>
- [12] R. Imai, N. Kanda, T. Higuchi, K. Konishi, and M. Kuwata-Gonokami, "Generation of broadband terahertz vortex beams", *Opt. Lett.*, **39**, 3714 (2014). <https://doi.org/10.1364/OL.39.003714>
- [13] Y. Yang, X. Ye, L. Niu, K. Wang, Z. Yang, and J. Liu, "Generating terahertz perfect optical vortex beams by diffractive elements", *Opt. Express*, **28**, 1417 (2020). <https://doi.org/10.1364/OE.380076>
- [14] K. Zhang, Y. Wang, S.N. Burokur, and Q. Wu, "Generating dual-polarized vortex beam by detour phase: from phase gradient metasurfaces to metagratings", *IEEE Trans. Microw. Theory Techn.*, **70**, 200 (2022). <https://doi.org/10.1109/TMTT.2021.3075251>
- [15] X.D. Zhang, Y.H. Su, J.C. Ni, Z.Y. Wang, Y.L. Wang, C.W. Wang, and J.R. Chu, "Optical superimposed vortex beams generated by integrated holographic plates with blazed grating", *Appl. Phys. Lett.*, **111**, 061901 (2017). <https://doi.org/10.1063/1.4997590>
- [16] S.J. Ge, Z.X. Shen, P. Chen, X. Liang, X.K. Wang, W. Hu, Y. Zhang, and Y.Q. Lu, "Generating, separating and polarizing terahertz vortex beams via liquid crystals with gradient-rotation directors", *Crystals*, **7**, 314 (2017). <https://doi.org/10.3390/cryst7100314>
- [17] S. Guan, J. Cheng, and S. Chang, "Recent progress of terahertz spatial light modulators: materials, principles and applications", *Micromachines*, **13**, 1637 (2022). <https://doi.org/10.3390/mi13101637>
- [18] A. Al Dhaybi, J. Degert, E. Brasselet, E. Abraham, and E. Freysz, "Terahertz vortex beam generation by infrared vector beam rectification", *J. Opt. Soc. Am. B*, **36**, 12 (2019). <https://doi.org/10.1364/JOSAB.36.000012>
- [19] K. Miyamoto, K. Sano, T. Miyakawa, H. Niinomi, K. Toyoda, A. Vallés, and T. Omatsu, "Generation of high-quality terahertz OAM mode based on soft-aperture difference frequency generation", *Opt. Express*, **27**, 31840 (2019). <https://doi.org/10.1364/OE.27.031840>
- [20] H. Sobhani, and E. Dadar, "Terahertz vortex generation methods in rippled and vortex plasmas", *J. Opt. Soc. Am. A*, **36**, 1187 (2019). <https://doi.org/10.1364/JOSAA.36.001187>
- [21] P. Chevalier, A. Amirzhan, F. Wang, M. Piccardo, S.G. Johnson, F. Capasso, and H.O. Everitt, "Widely tunable compact terahertz gas lasers", *Science*, **366**, 856 (2019). <https://doi.org/10.1126/science.aay8683>
- [22] J. Farhoomand, and H.M. Pickett, "Stable 1.25 watts CW far infrared laser radiation at the 119 μm methanol line", *Int. J. Infrared Millim. Waves*, **8**, 441 (1987). <https://doi.org/10.1007/BF01013257>
- [23] H.P. Röser, M. Yamanaka, R. Wattenbach, and G.V. Schultz, "Investigations of optically pumped submillimeter wave laser modes", *Int. J. Infrared Millim. Waves*, **3**, 839 (1982). <https://doi.org/10.1007/BF01008649>
- [24] M.W. Beijersbergen, R.P.C. Coerwinkel, M. Kristensen, and J.P. Woerdman, "Helical-wavefront laser beams produced with a spiral phase plate", *Opt. Commun.*, **112**, 321 (1994). [https://doi.org/10.1016/0030-4018\(94\)90638-6](https://doi.org/10.1016/0030-4018(94)90638-6)
- [25] V.V. Kotlyar, and A.A. Kovalev, "Nonparaxial propagation of a Gaussian optical vortex with initial radial polarization", *J. Opt. Soc. Am. A*, **27**, 372 (2010). <https://doi.org/10.1364/JOSAA.27.000372>
- [26] B. Gu, and Y. Cui, "Nonparaxial and paraxial focusing of azimuthal-variant vector beams", *Opt. Express*, **20**, 17684 (2012). <https://doi.org/10.1364/OE.20.017684>
- [27] Y. Zhang, L. Wang, and C. Zheng, "Vector propagation of radially polarized Gaussian beams diffracted by an axicon", *J. Opt. Soc. Am. A*, **22**, 2542 (2005). <https://doi.org/10.1364/JOSAA.22.002542>
- [28] O.V. Gurin, A.V. Degtyarev, V.A. Maslov, V.A. Svich, V.M. Tkachenko, and A.N. Topkov, "Selection of transverse modes in laser cavities containing waveguides and open parts", *Quantum Electron.* **31**, 346 (2001). <https://doi.org/10.1070/QE2001v031n04ABEH001949>

- [29] J.F. Nye, and M.V. Berry, "Dislocations in wave trains", Proceedings of the Royal Society of London. A. Mathematical and Physical Sciences, **336**, 165 (1974). <https://doi.org/10.1098/rspa.1974.0012>
- [30] O.V. Gurin, A.V. Degtyarev, N.N. Dubinin, M.N. Legenkiy, V.A. Maslov, K.I. Muntean, V.N. Ryabykh, and V.S. Senyuta, "Formation of beams with nonuniform polarisation of radiation in a cw waveguide terahertz laser", Quantum Electron., **51**, 338 (2021). <https://doi.org/10.1070/QEL17511>
- [31] A.V. Degtyarev, M.M. Dubinin, O.V. Gurin, V.A. Maslov, K.I. Muntean, V.M. Ryabykh, V.S. Senyuta, and O.O. Svystunov, "Control over higher-order transverse modes in a waveguide-based quasi-optical resonator", Radio Physics and Radio Astronomy, **27**, 129 (2022). <https://doi.org/10.15407/rpra27.02.129>

ЕВОЛЮЦІЯ ВЕКТОРНИХ ВИХРОВИХ ПРОМЕНІВ, СФОРМОВАНИХ ТЕРАГЕРЦОВИМ ЛАЗЕРНИМ МЕТАЛЕВИМ РЕЗОНАТОРОМ





Андрій В. Дегтярьов, Микола М. Дубінін, Вячеслав О. Маслов, Костянтин І. Мунтян, Олег О. Свистунов

Харківський національний університет імені В.Н. Каразіна, майдан Свободи, 4, Харків, Україна, 61022

Отримано аналітичні вирази для непараксильної модової дифракції металевого хвилевідного резонатора терагерцового лазера. Дослідження передбачає взаємодію між модами та спіральною фазовою пластиною з урахуванням різних топологічних зарядів (n). Також за допомогою чисельного моделювання досліджено фізичні особливості вихрових пучків, що виникають, коли вони поширюються у вільному просторі. Векторна теорія Релея-Зоммерфельда використовується для дослідження поширення вихрових лазерних променів у зоні Френеля, збуджених модами металевого хвилевідного квазіоптичного резонатора при падінні на спіральну фазову пластину. У вільному просторі спіральна фазова пластина для збуджуючої моди TE_{11} з профілем з максимумом інтенсивності в центрі ($n = 0$) утворює асиметричне кільце з двома максимумами ($n = 1, 2$). Для збуджуючої TE_{01} моди початкова поперечна кільцева ($n = 0$) структура інтенсивності поля трансформується в структуру з максимальною інтенсивністю випромінювання в центрі ($n = 1$), а потім знову в кільцеву ($n = 2$). Фазовий фронт променя для E_y компоненти лінійно поляризованої вздовж осі y моди TE_{11} змінюється зі сферичного на спіральний з однією осевою точкою сингулярності, тоді як у фазовому профілі поперечних компонентів азимутально поляризованої моди TE_{01} спостерігається область з двома та трьома позаосьовими точками сингулярності фази.

Ключові слова: терагерцовий лазер; металевий хвилевідний резонатор; спіральна фазова пластина; вихрові пучки; поляризація; поширення випромінювання

MATHEMATICAL MODELING OF URANIUM NEUTRON-PRODUCING TARGET OF SUBCRITICAL ASSEMBLY NSC KIPT

 V.V. Gann*,  G.V. Gann,  B.V. Borts, I.M. Karnaukhov,  O.O. Parkhomenko

NSC "Kharkov Institute of Physics and Technology", Kharkov, Ukraine

*Corresponding Author e-mail: gann@kipt.kharkov.ua

Received March 29, 2024; revised May 5, 2024; accepted May 14, 2024

This work is devoted to calculating the rate of radiation damage production in a uranium target irradiated with high-energy electrons with an energy of 100 MeV. The Monte Carlo program MCNPX was used to perform a complete mathematical modeling of a complex of processes occurring in a uranium target when irradiated with high-energy electrons: the development of an electromagnetic shower, the production of photoneutrons, the transport of particles in the target and the creation of radiation damage in it. The analysis showed that fragments of U-238 photo-fission give the main input into the rate of damage production in a uranium target which reaches the value of 100 dpa/year. The expected service life of a uranium target under irradiation is 3 years of operation at full accelerator power.

Keywords: *Uranium; Electron; Subcritical assembly; Radiation damage*

PACS: 621.384.6

INTRODUCTION

The neutron source of the NSC KIPT with a power of 100 kW consists of a linear accelerator of electrons with energy of 100 MeV, which irradiate a thick neutron-producing target; the photoneutrons generated in it enter the subcritical assembly (SCA), where they are multiplied and the neutron flux is increased tens of times. The highest neutron flux can be obtained using a uranium neutron-producing target. The service life of a uranium target under irradiation is largely determined by the dose of radiation damage accumulated in it (in displacements per atom).

Previously, the authors have already estimated the radiation damage production in uranium target irradiated by high-energy electrons with energy of 100 MeV [1]. In this work, a complete mathematical modeling of all nuclear-physical processes in a uranium target was performed using the Monte Carlo program MCNPX. It has been shown that the main contribution to the rate of damage formation in a uranium target when irradiated with electrons with an energy of 100 MeV (1 mA) is made by photofission fragments of U-238, and the expected service life of a uranium target in the subcritical assembly of a neutron source at NSC KIPT has been assessed.

URANIUM TARGET MODEL

The target consists of a set of uranium plates with sizes 66x66 mm and various thicknesses (see Table 1), coated on the both sides with Al layers 0.7 mm thick. The 1.75 mm gap between the plates is filled with water. The target is separated from the vacuum chamber of the electron accelerator by an input window made of aluminum 2 mm thick. Behind the target is a chamber filled with helium (marked in yellow in Fig. 1).

Table 1. Plate thicknesses U (in cm), numbered in Fig. 1 from top to bottom:

No	1	2	3	4	5	6	7	8	9	10	11	12
Thickness	0.3	0.25	0.25	0.25	0.3	0.3	0.4	0.5	0.7	1	1.4	2.25

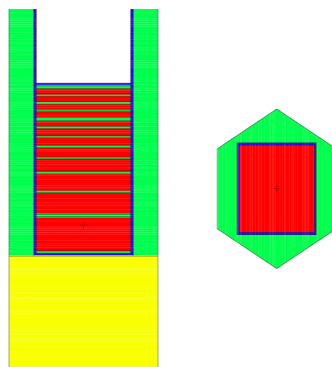


Figure 1. Uranium target of the neutron source NSC KIPT

A plane-parallel beam of electrons with a square cross-section of 64x64 mm with energy of 100 MeV and a power of 100 kW is incident on the target. An electromagnetic shower develops in the target, bremsstrahlung gamma quanta react with atomic nuclei, and as a result of the (γ , n) reaction, neutrons are produced, which enter the subcritical assembly, where they multiply, and radiation damage is created in the target.

RESULTS OF MATHEMATICAL MODELING

The MCNPX program was used [2], which allows to perform the Monte Carlo modeling of all nuclear-physical processes involving electrons, neutrons and gamma quanta, taking into account the specific geometry of the target. Figure 2 shows the profile of the energy release in the target under flow of incident electrons $\Phi = 1.7 \cdot 10^{14}$ el/(cm² s). Energy is mainly released in uranium, with only a small fraction of energy released in aluminum and water.

The distribution of the electron flux along the length of the target is shown in Fig. 3 (per one incident electron). The development of an electromagnetic shower leads to a doubling of the electron flow, and then the electron beam is decelerated due to the processes of ionization and emission of bremsstrahlung gamma quanta.

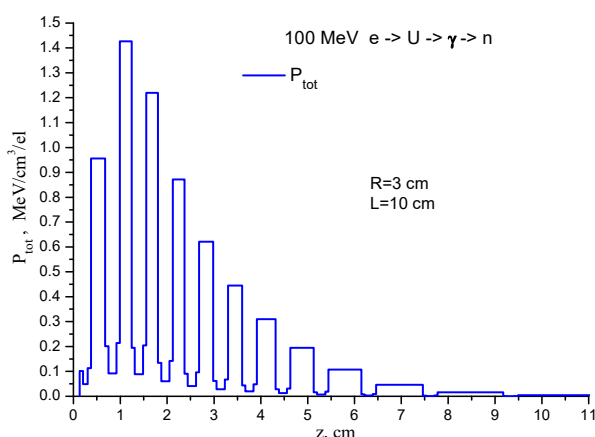


Figure 2. Distribution of energy release in the target

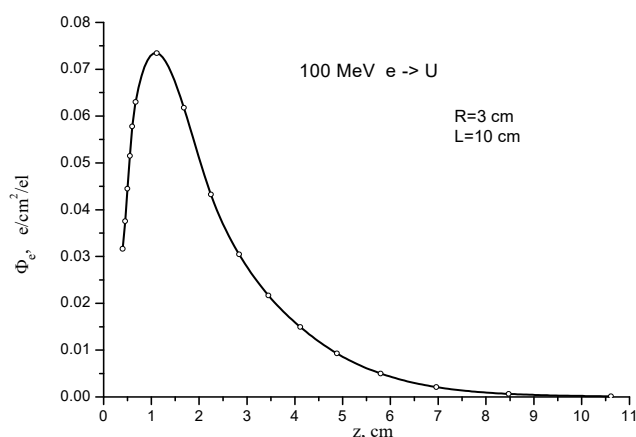


Figure 3. Electron flux distribution along the length of the target

Figure 4 shows the distribution of gamma ray flux density along the length of the target calculated by the MCNPX program (per one incident electron). Such a profile is formed as a result of bremsstrahlung gamma quanta emission, as well as the processes of positron annihilation with the emission of photons. The attenuation of the photon flux occurs due to the creation of electron-positron pairs by photons near the nucleus, as well as the absorption of photons by nuclei and atomic systems. The maximum of photon flux in the target occurs at a depth of 1.6 cm (the depth is measured from the target entrance window).

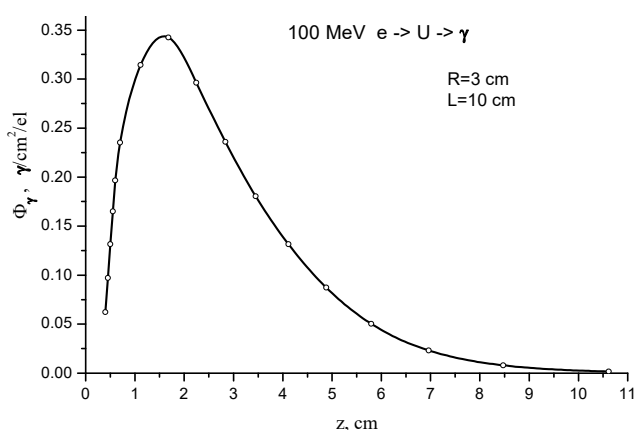


Figure 4. Distribution of the gamma ray flux along the length of the target

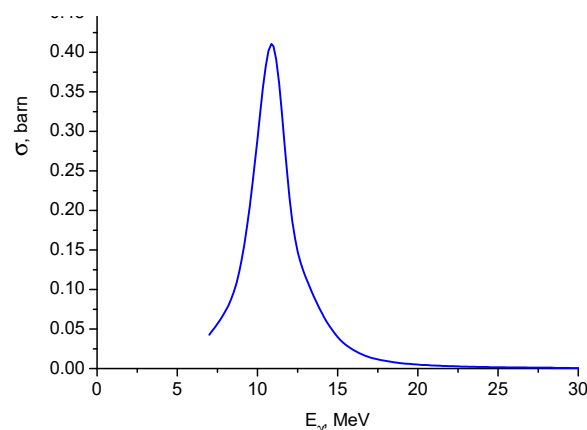


Figure 5. Dependence of the reaction cross section (γ , n) on photon energy for U-238

Photo-neutrons are released from the nuclei under the gamma ray irradiation. The reaction cross section (γ , n) on the U-238 nucleus, taken from the nuclear database [3], is presented in Figure 5. The MCNPX program allows determining the photo-neutron yield at various target depths. The distribution of the resulting photo-neutron flux along the length of the target is shown in Figure 6 (per one incident electron).

The photo-fission reaction of U-238 nuclei can also occur under photon irradiation, the dependence of its cross section on energy [3] is shown in Figure 7.

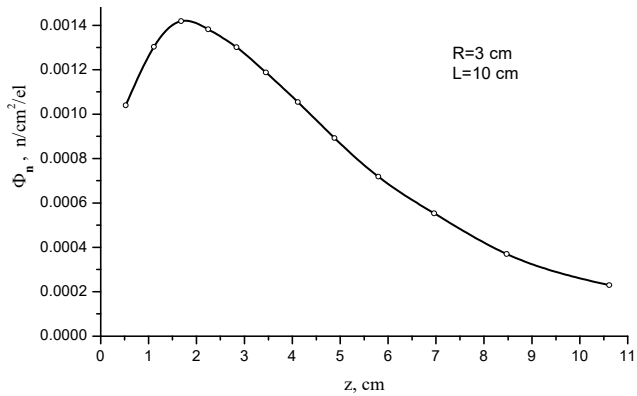


Figure 6. Distribution of neutron flux along the length of the target

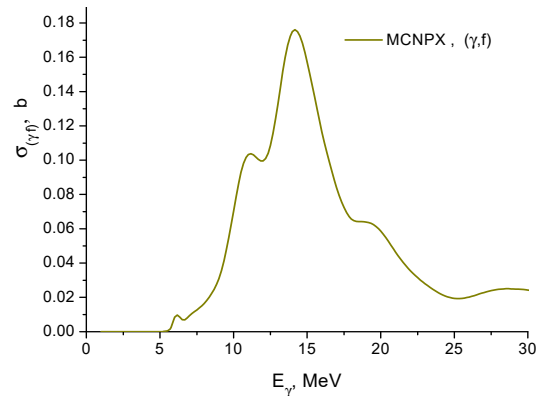


Figure 7. Dependence of the photo-fission cross section for the U-238 nucleus on photon energy

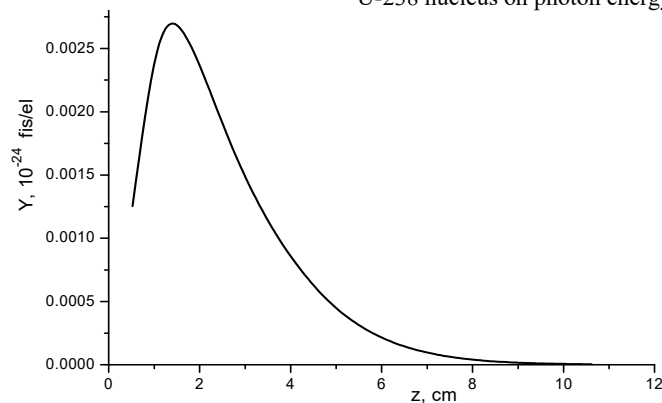


Figure 8. Dependence of the fission probability for the U-238 nucleus on the depth along the length of the target

The MCNPX program allows to calculate the probability distribution of U-238 nuclei fission along the length of the target (see Figure 8).

As one can see in Figure 8, the maximum probability of fission for U-238 is achieved at a depth of ~1.4cm, and the maximum burnup rate of U-238 is 0.055% per year.

CALCULATION OF RADIATION DEFECTS FORMATION RATE IN THE URANIUM TARGET

The rate of radiation damage production in a uranium SCA target was estimated in [1], and it was found that the photo-fission fragments give the main input into the rate of damage formation, and the contribution of all other reactions is only a few percent. In this work, we calculated the damage to a uranium target by photofission fragments using two methods: by calculating cascades of atomic collisions in uranium using the SRIM program [4] and by the NRT standard method [5].

Figure 9 shows the scattering of uranium photo-fission fragments: La-139 with energy of 70 MeV and Mo-96 with energy of 100 MeV, calculated using the SRIM program. Both fragments create cascades of atomic displacements in uranium, in which 190 000 displaced atoms are formed per uranium fission.

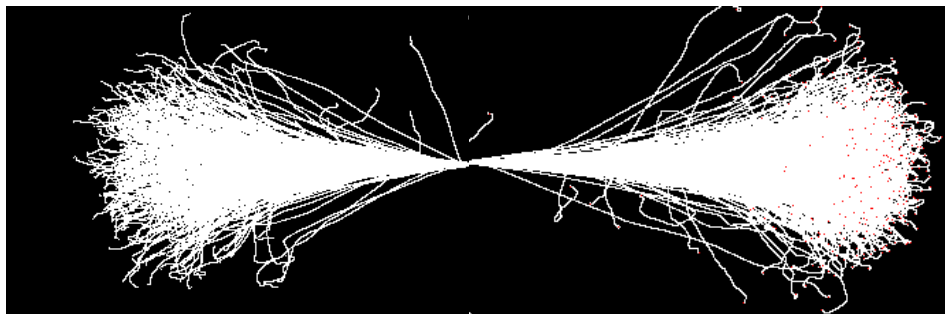


Figure 9. Picture of the scattering of U-238 fission fragments: on the left - the trajectories of La-139, on the right - Mo-96

Figure 10 shows the distribution of radiation defects production rate by fission fragments along the uranium target, calculated using the SRIM program. This rate is 103 dpa per year at the maximum of damage production.

Calculation according to the NRT standard gives 104 000 displaced U atoms per one photo-fission and, accordingly, the value of 50 dpa/year for the maximum rate of damage production.

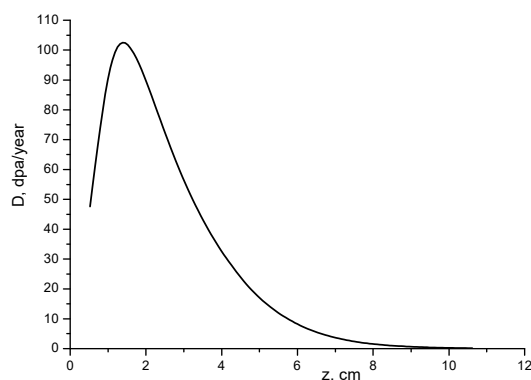


Figure 10. Rate of radiation defects accumulation in U along the length of the target

CONCLUSIONS

The U-238 photo-fission fragments give the main input into the rate of damage formation in the uranium target irradiated by electrons with energy of 100 MeV (1 mA). The contribution of other processes (electrons, photoneutrons, target neutrons, neutrons from the PCS) is only a few percent. The contributions of various defect creation mechanisms to the rate of damage dose accumulation in the uranium target are presented in Table 2.

Table 2. Contributions of radiation damage mechanisms to the rate of NRT dose accumulation

	Electrons 100 MeV	Photoneutrons	Photofission	Target neutrons	Assembly neutrons
Damage rate (dpa/year)	1	0.05	50	2	0.3

The maximum burn-up rate of U-238 is $Y_{max} = 0.055\%$ per year, and the maximum rate of accumulation of the NRT dose of radiation damage in a uranium target is $D_{max} = 50$ dpa/year and is achieved at a depth of ~ 1.4 cm.

An analysis of the dependence of radiation embrittlement on the burn-up of the target material carried out in [6] showed that at burn-up values less than 0.2%, the target material still has a sufficient margin of plasticity. Therefore, the expected service life of the uranium target is 3 years of operation at full accelerator power.

Conflict of Interest

The authors declare that there is no conflict of interest regarding the publication of this paper.

ORCID

© V.V. Gann, <https://orcid.org/0000-0002-3451-1840>; © G.V. Gann, <https://orcid.org/0009-0004-6916-027X>
 © B.W. Borts, <https://orcid.org/0000-0003-0387-3491>; © O.O. Parkhomenko, <https://orcid.org/0000-0001-9671-8874>

REFERENCES.

- [1] V.V. Gann, A.V. Gann, B.V. Borts, I.M. Karnaukhov, and A.A. Parkhomenko, "Radiation damage in uranium target of the accelerator driven system "KIPT Neutron Source". Problems of Atomic Science and Technology, 2021, № 2(132), 24-28. <https://doi.org/10.46813/2021-136-017>
- [2] G.W. McKinney, MCNPX User's Manual, Version 2.6.0. LA-CP-07-1473 (2008). https://www.researchgate.net/publication/263009058_MCNPX_User's_Manual_Version_260
- [3] JANIS Web, <https://www.oecd-nea.org/janisweb/book/>
- [4] J.F. Ziegler, J.P. Biersack, and M.D. Ziegler, *SRIM The Stopping and Ranges of Ions in Matter*, SRIM Co (2008). <http://www.srim.org/>
- [5] M.J. Norgett, M.T. Robinson, and I.M. Torrens, "A proposed method of calculating displacement dose rates," Nucl. Engr. and Design, 33(1), 50 (1975). [https://doi.org/10.1016/0029-5493\(75\)90035-7](https://doi.org/10.1016/0029-5493(75)90035-7)
- [6] B.V. Borts, V.V. Gann, A.Yu. Zelinsky, A.A. Parkhomenko, A.F. Vanzha, Yu.A. Marchenko, and I.V. Patochkin, "Burnup and radiation embrittlement of the U-Mo neutron source target," Problems of Atomic Science and Technology, 2022, № 2(138), 57-61 (2022). <https://doi.org/10.46813/2022-138-057>

МАТЕМАТИЧНЕ МОДЕЛЮВАННЯ УРАНОВОЇ НЕЙТРОНО-УТВОРЮЮЧОЇ МІШЕНІ ПІДКРИТИЧНОЇ ЗБІРКИ ННЦ ХФТІ

В.В. Ганн, Г.В. Ганн, Б.В. Борц, І.М. Карнаухов, О.О. Пархоменко

ННЦ "Харківський фізико-технічний інститут", Харків, Україна

Ця робота присвячена розрахунку швидкості набору дози радіаційних ушкоджень в урановій мішені при опроміненні високоенергетичними електронами з енергією 100 MeV. З використанням програми MCNPX методом Монте-Карло виконано повне математичне моделювання комплексу процесів, що відбуваються в урановій мішені при опроміненні високоенергетичними електронами: розвиток електромагнітної зливи, народження фотонейтронів, транспорт частинок у мішені та створення в ній радіаційних пошкоджень. Аналіз показав, що найбільший внесок у швидкість утворення пошкоджень в мішені вносять уламки фотоподілу U-238, а максимальна швидкість створення дефектів досягає 100 зна/рік. Очікуваний ресурс роботи уранової мішені під опроміненням становить 3 роки на повній потужності прискорювача.

Ключові слова: уран; опромінювання; електрони; підкритична збірка; радіаційні ушкодження

TWO-DIMENSIONAL HYDRODYNAMICS AS A CLASS OF SPECIAL HAMILTONIAN SYSTEMS

 Kostyantyn M. Kulyk^{a,*},  Volodymyr V. Yanovsky^{a,b}

^a*Institute for Single Crystals, Nat. Academy of Science Ukraine, Nauky Ave. 60, Kharkiv 61072, Ukraine*

^b*V.N. Karazin Kharkiv National University, 4, Svoboda Sq., Kharkiv, 61022, Ukraine*

*Corresponding Author e-mail: koskul@isc.kharkov.ua

Received February 13, 2024; revised April 11, 2024; accepted April 27, 2024

The paper defines a class of Hamiltonian systems whose phase flows are exact solutions of the two-dimensional hydrodynamics of an incompressible fluid. The properties of this class are considered. An example of a Lagrangian one-dimensional system is given, which after the transition to the Hamiltonian formalism leads to an unsteady flow, that is, to an exact solution of two-dimensional hydrodynamics. The connection between these formalisms is discussed and the Lagrangians that give rise to Lagrangian hydrodynamics are introduced. The obtained results make it possible to obtain accurate solutions, such as phase flows of special Hamiltonian systems.

Keywords: *Hamiltonian; Lagrangian; Exact solutions; Two-dimensional hydrodynamics; Phase flow*

PACS: 47.10.ab

1. INTRODUCTION

The interest in the formulation of hydrodynamic systems of equations in Hamiltonian form arose quite a long time ago (see, for example, the review [1, 2]). Already G. Lamb has realized in his paper that the Klebsch variables are canonically conjugate variables. This makes it possible to give incompressible fluid equations a Hamiltonian form with a Hamiltonian, the role of which is played by the total kinetic energy of the incompressible fluid. From a general point of view such a problem reduces to generalization of classical mechanics to field systems with an infinite number of freedom degrees. One of the difficulties was the choice of canonically conjugate variables, which did not always take a physically transparent content. Today this problem has been overcome and has lost its relevance. The usefulness of the Hamiltonian approach is especially noticeable when using the Hamiltonian formalism, for example, to develop a general theory of waves in nonlinear media. The foundations of such an approach were laid in [3, 4].

After discovery of a method for nonlinear equations solution using the inverse scattering problem method, it has been found that such equations, in a certain sense, are field analogues of the Hamiltonian equations of classical mechanics [5]. This contributed to using Hamiltonian formalism in the direction of integrating nonlinear equations. Also, the Hamiltonian approach turned out to be useful in searching for invariants of hydrodynamic media [6] (see also [7]).

Infinite-dimensional groups of diffeomorphisms are closely related by hydrodynamic systems [8, 9]. In fact, they are the configuration space for many hydrodynamic equations. Thus, groups of volume-preserving diffeomorphisms are closely related to the Euler equations of incompressible fluid, compressible fluid and ideal magnetohydrodynamics (see, for example, [10]). The approach using Poisson brackets to the description of hydrodynamic systems has also been intensively developed. Mathematical achievements in the Hamiltonian description of hydrodynamic systems can be found in [11, 14]. The development of the formalism of Poisson brackets led to the classification of Poisson brackets of the hydrodynamic type within the framework of the differential geometric approach [11, 12, 13, 14]. Another approach arose earlier from the analogy of barotropic flow of an ideal fluid in a potential force field with Hamiltonian systems [15]. In this paper [15] an attempt was made to extend the analogy between hydrodynamics and Hamiltonian mechanics to the case of arbitrary Hamiltonian systems.

In this paper the interest is rather opposite and is directed to identification of properties of finite-dimensional Hamiltonian systems, which provide a connection with hydrodynamic systems. The reason is that for an arbitrary Hamiltonian system the phase flows do not correspond to hydrodynamic flows. In other words, we are interested in what class of Hamiltonian systems generates hydrodynamic flows. Such Hamiltonian systems are finite-dimensional and in the case of two-dimensional ideal hydrodynamics the dimensionality of the phase space is equal to 2. In this paper we consider two-dimensional hydrodynamics, which has an infinite number of conservation laws [16]. The conditions under which the phase flow of a Hamiltonian system generates the velocity field of two-dimensional hydrodynamics of an incompressible fluid are obtained. An example

of the corresponding flow is given. A special class of one-dimensional Hamiltonian systems associated with hydrodynamic flows is identified.

2. LAGRANGIAN AND HAMILTONIAN FORMALISM

We will discuss the transition from the Lagrangian to the Hamiltonian formalism in two-dimensional hydrodynamics. This transition has unusual features. The equations of motion of Lagrangian particles in Lagrangian variables in two-dimensional hydrodynamics can be easily written as

$$\begin{aligned}\ddot{x} &= -\frac{\partial P(x, y, t)}{\partial x} \\ \ddot{y} &= -\frac{\partial P(x, y, t)}{\partial y}\end{aligned}\quad (1)$$

Here, for simplicity, we have chosen a density $\rho = \text{const}$, which simply renormalizes the pressure $P(x, y, t)$. This system of equations can be obtained from the Lagrange variational principle from the Lagrangian $L = \dot{x}^2/2 + \dot{y}^2/2 - P(x, y, t)$. Pressure plays the role of potential energy. However, this system must be supplemented by the incompressibility condition $\text{div}\vec{V} = 0$. In incompressible hydrodynamics, this condition additionally determines the unknown pressure. The problem is an inadequate type of this condition for the Lagrangian formalism. Availability of a velocity field determining trajectories of Lagrangian particles is an essential property. Enter $\dot{x} = V_1(x, t)$, $\dot{y} = V_2(x, y, t)$, then the incompressibility condition takes the form

$$\frac{\partial \dot{x}}{\partial x} + \frac{\partial \dot{y}}{\partial y} = 0 \quad (2)$$

Entering Lagrangian variables and a velocity field depending only on coordinates assumes consistency with both the incompressibility condition (2) and the equations of motion (1). The incompressibility condition implies the existence of a function such that

$$\begin{aligned}\dot{x} &= \frac{\partial H(x, y, t)}{\partial y} \\ \dot{y} &= -\frac{\partial H(x, y, t)}{\partial x}\end{aligned}\quad (3)$$

In other words, the incompressibility condition means the Hamiltonian description of Lagrangian particles. However, the occurrence of the Hamiltonian description is not connected with the Lejandre Lagrangian transformation of two-dimensional hydrodynamics $L = \dot{x}^2/2 + \dot{y}^2/2 - P(x, y, t)$. This feature of the appearance of the Hamiltonian formalism in hydrodynamic systems has been observed many times. Thus, for example, the Hamiltonian equations of motion of point vortices cannot be formulated in Lagrangian form. The principal difference between the initial Hamiltonian formalism obtained by the Lejandre Lagrangian transformation and the Hamiltonian formalism from the incompressibility condition lies in the difference in the dimensionality of phase spaces. In the first it is 4-dimensional, in the second it is 2-dimensional phase space. It is clear that the transition to lower dimensionality is associated with the conservation of volume $dx dy$. We will discuss this reduction of the initial Hamiltonian formalism a little later. Thus, the main problem is to determine the type of the Hamiltonian and the constraints on it following from the equations of motion (1). Let us proceed to the analysis of these constraints. Differentiating (3) with respect to time, we express \ddot{x}, \ddot{y} through \dot{y}, \dot{x} and H .

$$\begin{aligned}\ddot{x} &= \frac{\partial^2 H}{\partial x \partial y} \dot{x} + \frac{\partial^2 H}{\partial y^2} \dot{y} + \frac{\partial^2 H}{\partial y \partial t} \\ \ddot{y} &= -\frac{\partial^2 H}{\partial x^2} \dot{x} - \frac{\partial^2 H}{\partial x \partial y} \dot{y} - \frac{\partial^2 H}{\partial x \partial t}\end{aligned}\quad (4)$$

Thus, the second derivatives are expressed through the first ones and the coordinates of the Lagrangian particle. Taking into account this relation, let us write the equations of motion (1) in the form solved with respect to \dot{x} and \dot{y} . This is easy to do by considering it as a system of linear algebraic equations relatively to derivatives of coordinates with respect to time.

$$\begin{aligned}\dot{x} \cdot \Delta(x, y, t) &= \frac{\partial^2 H}{\partial y^2} \left(\frac{\partial^2 H}{\partial x \partial t} - \frac{\partial P}{\partial y} \right) - \frac{\partial^2 H}{\partial x \partial y} \left(\frac{\partial^2 H}{\partial y \partial t} + \frac{\partial P}{\partial x} \right) \\ \dot{y} \cdot \Delta(x, y, t) &= -\frac{\partial^2 H}{\partial x^2} \left(\frac{\partial^2 H}{\partial y \partial t} + \frac{\partial P}{\partial x} \right) + \frac{\partial^2 H}{\partial x \partial y} \left(\frac{\partial^2 H}{\partial x \partial t} - \frac{\partial P}{\partial y} \right)\end{aligned}\quad (5)$$

Here the notation is introduced $\Delta(x, y, t) \equiv \frac{\partial^2 H}{\partial x \partial y} \frac{\partial^2 H}{\partial x \partial y} - \frac{\partial^2 H}{\partial x^2} \frac{\partial^2 H}{\partial y^2}$. The condition of matching with (3) restricts the type of functions H and P . Substituting \dot{x} and \dot{y} through the derivatives of the Hamiltonian, we obtain

$$\begin{aligned} \frac{\partial H}{\partial y} \Delta(x, y, t) &= \frac{\partial^2 H}{\partial y^2} \frac{\partial^2 H}{\partial x \partial t} - \frac{\partial^2 H}{\partial x \partial y} \frac{\partial^2 H}{\partial y \partial t} - \frac{\partial P}{\partial y} \frac{\partial^2 H}{\partial y^2} - \frac{\partial P}{\partial x} \frac{\partial^2 H}{\partial x \partial y} \\ \frac{\partial H}{\partial x} \Delta(x, y, t) &= \frac{\partial^2 H}{\partial x \partial y} \frac{\partial^2 H}{\partial x \partial t} - \frac{\partial^2 H}{\partial x^2} \frac{\partial^2 H}{\partial y \partial t} - \frac{\partial P}{\partial x} \frac{\partial^2 H}{\partial x^2} - \frac{\partial P}{\partial y} \frac{\partial^2 H}{\partial x \partial y} \end{aligned} \tag{6}$$

Solving this system of algebraic linear equations with respect to $\frac{\partial^2 H}{\partial x \partial t}$ and $\frac{\partial^2 H}{\partial y \partial t}$ after simple rearrangements, transformations and cancellation $\Delta(x, y, t) \neq 0$, we obtain a system of equations in the form

$$\begin{aligned} \frac{\partial^2 H}{\partial x \partial t} + \frac{\partial^2 H}{\partial x^2} \frac{\partial H}{\partial y} - \frac{\partial^2 H}{\partial x \partial y} \frac{\partial H}{\partial x} &= \frac{\partial P}{\partial y} \\ \frac{\partial^2 H}{\partial y \partial t} + \frac{\partial^2 H}{\partial x \partial y} \frac{\partial H}{\partial y} - \frac{\partial^2 H}{\partial y^2} \frac{\partial H}{\partial x} &= -\frac{\partial P}{\partial x} \end{aligned} \tag{7}$$

In fact, this basic system of equations determines the unknown functions H and P . If these functions are known, then the trajectory of the Lagrangian particle is found by integrating the Hamiltonian system of equations. In other words, it reduces to a problem of classical mechanics. It is convenient to give this system a coordinate-free form using Poisson brackets. Let us introduce the Poisson bracket in the usual way

$$\{A, B\} = \frac{\partial A}{\partial x} \frac{\partial B}{\partial y} - \frac{\partial A}{\partial y} \frac{\partial B}{\partial x}$$

Using this bracket let us write the system of equations (7) in more natural invariant form.

$$\begin{aligned} \frac{\partial}{\partial t} \frac{\partial H}{\partial x} + \left\{ \frac{\partial H}{\partial x}, H \right\} &= \frac{\partial P}{\partial y} \\ \frac{\partial}{\partial t} \frac{\partial H}{\partial y} + \left\{ \frac{\partial H}{\partial y}, H \right\} &= -\frac{\partial P}{\partial x} \end{aligned} \tag{8}$$

or

$$\begin{aligned} \frac{\partial}{\partial t} \frac{\partial H}{\partial x} + \left\{ \frac{\partial H}{\partial x}, H \right\} - \{x, P\} &= 0 \\ \frac{\partial}{\partial t} \frac{\partial H}{\partial y} + \left\{ \frac{\partial H}{\partial y}, H \right\} - \{y, P\} &= 0 \end{aligned} \tag{9}$$

Note, that neither the Hamiltonian nor its first derivatives are conserved with time. However, excluding the pressure from this system it is easy to show that ΔH is conserved. Indeed, the equation for changing the Laplacian H has the form

$$\frac{\partial}{\partial t} \Delta H + \{H, \Delta H\} = 0 \tag{10}$$

In fact, it is the well-known equation for vorticity.

3. THE EXAMPLE OF FLOW OF 2-DIMENSIONAL HYDRODYNAMICS OF INCOMPRESSIBLE FLUID

Let's start with a simple example of a Hamiltonian system with a time-dependent Hamiltonian. This Hamiltonian is a particular solution of equation (10) and has the form

$$H = p^2 \sin^2(\omega t) + x^2 \cos^2(\omega t) \tag{11}$$

It is easy to see that it has special properties. Its main property, which we will discuss below, is the following

$$\Delta H = \text{const} \tag{12}$$

where, $\Delta = \frac{\partial^2}{\partial x^2} + \frac{\partial^2}{\partial p^2}$ is the Laplacian in a phase space. The equations of motion for this system have the form

$$\frac{dx}{dt} = \frac{\partial H}{\partial p} = 2p \sin^2(\omega t)$$

$$\frac{dp}{dt} = -\frac{\partial H}{\partial x} = -2x \cos^2(\omega t) \quad (13)$$

Let us note that equation (10) is satisfied for the Hamiltonian (11) and, therefore, the velocity field (12) satisfies the Euler equations and condition (2) provides an example of a spiral unsteady two-dimensional flow.

By excluding the variable p we obtain the equation for the variable x of the second order

$$\frac{\ddot{x}}{\sin^2(\omega t)} - 2\dot{x} \frac{\omega \cos(\omega t)}{\sin^3(\omega t)} = -4x \cos^2(\omega t) \quad (14)$$

This equation corresponds to Newton's equation and appears as the Lagrangian equation of motion of a one-dimensional physical system. Let us now discuss the Lagrangian system, which is generated by the Hamiltonian system (11). For this purpose we pass by means of the Legendre transformation to the Lagrangian of the initial system.

$$\dot{x} = \frac{\partial H}{\partial p}$$

$$\mathcal{L} = \dot{x}p - H$$

For our particular case

$$\dot{x} = 2p \sin^2(\omega t)$$

and impulse is expressed through velocity according to

$$p = \frac{\dot{x}}{2 \sin^2(\omega t)}$$

Note, that the Legendre transformation coincides with one of the equations of motion. Moreover, this transformation is not well determined everywhere. There are specific peculiarities at $\omega t = \pi k$, where $k = \pm 0, \pm 1, \pm 2, \dots$. We won't pay attention to that for now. Then the Lagrangian type is determined as,

$$\mathcal{L} = \frac{\dot{x}^2}{4 \sin^2(\omega t)} - x^2 \cos^2(\omega t) \equiv \left(\frac{\dot{x}}{2 \sin(\omega t)} + x \cos(\omega t) \right) \left(\frac{\dot{x}}{2 \sin(\omega t)} - x \cos(\omega t) \right) \quad (15)$$

Lagrangian equations of motion have the form

$$\frac{d}{dt} \frac{\partial \mathcal{L}}{\partial \dot{x}} = \frac{\partial \mathcal{L}}{\partial x}$$

and in the case under consideration give the equation (14). Note that this equation describes the behavior of a one-dimensional Lagrangian system of rather exotic physical content. First of all, the particle is in a potential well with oscillating amplitude, which is affected by *friction* changed periodically with time. Note that two-dimensional flow of an incompressible fluid is associated with a special one-dimensional Lagrangian system.

Now let us differentiate the equations (13) with respect to time and proceed to a system of higher order equations in time. After using the equations of motion (13) to eliminate the first derivatives in the right-hand sides of the system, we obtain

$$\frac{d^2 x}{dt^2} = -4x \sin^2(\omega t) \cos^2(\omega t) + 4\omega p \sin(\omega t) \cos(\omega t)$$

$$\frac{d^2 p}{dt^2} = -4p \sin^2(\omega t) \cos^2(\omega t) + 4\omega x \sin(\omega t) \cos(\omega t) \quad (16)$$

It is clear that the solutions of the initial system (13) are also solutions of the obtained system of higher order equations (16). The converse is not true, since new solutions can emerge due to differentiation.

The obtained system of equations (16) has a remarkable special property — it is a natural Lagrangian system, which can be written in the form

$$\frac{d^2 x}{dt^2} = -\frac{\partial U(x, p, t)}{\partial x}$$

$$\frac{d^2 p}{dt^2} = -\frac{\partial U(x, p, t)}{\partial p} \quad (17)$$

where the function $U = U(x, p, t)$ has the meaning of a potential energy in two-dimensional configuration space (x, p) . For the example under consideration

$$U = 2(x^2 + p^2) \sin^2(\omega t) \cos^2(\omega t) - 4\omega p x \sin(\omega t) \cos(\omega t) \tag{18}$$

Thus, differentiation of the Hamiltonian system (13) with respect to time transforms it into a Lagrangian system with Lagrangian

$$L = \frac{\dot{x}^2 + \dot{p}^2}{2} - U(x, p, t) \equiv \frac{\dot{x}^2 + \dot{p}^2}{2} - 2(x^2 + p^2) \sin^2(\omega t) \cos^2(\omega t) + 4\omega p x \sin(\omega t) \cos(\omega t) \tag{19}$$

The Lagrangian dynamics in this special case corresponds not only to the initial Lagrangian $L = \dot{x}^2/2 + \dot{y}^2/2 - P(x, y, t)$, but also to the condition of divergence-free velocity field. Obviously, this is due to specialization of the potential energy. Further we will be interested in the general properties that provide this.

The system of equations (17) can be obtained as,

$$\begin{aligned} \frac{d}{dt} \frac{\partial L}{\partial \dot{x}} &= \frac{\partial L}{\partial x} \\ \frac{d}{dt} \frac{\partial L}{\partial \dot{p}} &= \frac{\partial L}{\partial p} \end{aligned} \tag{20}$$

Just the property (17) distinguishes a special class of Hamiltonian systems. Next, we introduce such a class, determining its characteristic property in the general case. Now it is important that this class of Hamiltonian systems is not trivial, as the example (11) demonstrates.

4. CLASS OF HAMILTONIANS OF HYDRODYNAMIC SOLUTIONS

Let us now distinguish a class of Hamiltonian systems G with special properties.

Determination 1 We will consider the Hamiltonian as belonging to the class G , if the system of equations obtained by time differentiation is a natural Lagrangian system.

It is clear that the class of such systems is not empty. An example of such a system was discussed earlier. Let us consider what conditions the Hamiltonians belonging to the class G satisfy. To do this, consider an arbitrary Hamiltonian system. Its equations of motion have the form

$$\begin{aligned} \frac{dx}{dt} &= \frac{\partial H(x, p, t)}{\partial p} \\ \frac{dp}{dt} &= -\frac{\partial H(x, p, t)}{\partial x} \end{aligned}$$

Let's perform time differentiation

$$\begin{aligned} \frac{d^2x}{dt^2} &= \frac{\partial^2 H(x, p, t)}{\partial p \partial t} + \frac{\partial^2 H(x, p, t)}{\partial p \partial x} \frac{dx}{dt} + \frac{\partial^2 H(x, p, t)}{\partial p^2} \frac{dp}{dt} \\ \frac{d^2p}{dt^2} &= -\frac{\partial^2 H(x, p, t)}{\partial x \partial t} - \frac{\partial^2 H(x, p, t)}{\partial x^2} \frac{dx}{dt} - \frac{\partial^2 H(x, p, t)}{\partial p \partial x} \frac{dp}{dt} \end{aligned}$$

We will use now the initial equations of motion and eliminate $\frac{dp}{dt}$ and $\frac{dx}{dt}$ in this system of equations

$$\begin{aligned} \frac{d^2x}{dt^2} &= \frac{\partial^2 H(x, p, t)}{\partial p \partial t} + \frac{\partial^2 H(x, p, t)}{\partial p \partial x} \frac{\partial H(x, p, t)}{\partial p} - \frac{\partial^2 H(x, p, t)}{\partial p^2} \frac{\partial H(x, p, t)}{\partial x} \\ \frac{d^2p}{dt^2} &= -\frac{\partial^2 H(x, p, t)}{\partial x \partial t} - \frac{\partial^2 H(x, p, t)}{\partial x^2} \frac{\partial H(x, p, t)}{\partial p} + \frac{\partial^2 H(x, p, t)}{\partial p \partial x} \frac{\partial H(x, p, t)}{\partial x} \end{aligned}$$

It is convenient to write these equations using the Poisson bracket

$$\{A, B\} = \frac{\partial A}{\partial x} \frac{\partial B}{\partial p} - \frac{\partial A}{\partial p} \frac{\partial B}{\partial x}$$

Then the system of equations takes the form

$$\frac{d^2x}{dt^2} = \frac{\partial}{\partial t} \frac{\partial H(x, p, t)}{\partial p} + \left\{ \frac{\partial H(x, p, t)}{\partial p}, H(x, p, t) \right\} \tag{21}$$

$$\frac{d^2p}{dt^2} = -\frac{\partial}{\partial t} \frac{\partial H(x, p, t)}{\partial x} - \left\{ \frac{\partial H(x, p, t)}{\partial x}, H(x, p, t) \right\} \quad (22)$$

In order that Hamiltonians to belong to the class G it is necessary and sufficient that the right parts of this system have the form

$$\begin{aligned} \frac{\partial}{\partial t} \frac{\partial H(x, p, t)}{\partial p} + \left\{ \frac{\partial H(x, p, t)}{\partial p}, H(x, p, t) \right\} &= \frac{\partial U(x, p, t)}{\partial x} \\ -\frac{\partial}{\partial t} \frac{\partial H(x, p, t)}{\partial x} - \left\{ \frac{\partial H(x, p, t)}{\partial x}, H(x, p, t) \right\} &= \frac{\partial U(x, p, t)}{\partial p} \end{aligned}$$

The consistency conditions of this system of equations determine the class of Hamiltonians G . Equating the mixed derivatives of the right-hand sides we obtain the consistency condition,

$$\frac{\partial \Delta H(x, p, t)}{\partial t} + \{ \Delta H(x, p, t), H(x, p, t) \} = 0 \quad (23)$$

which determines the type of Hamiltonians belonging to class G . It follows that class G consists only of Hamiltonians that satisfy this equation and are significantly narrower than Hamiltonian systems. At a specified $H(x, p, t)$ the function $U(x, p, t)$ satisfies the equation

$$\Delta U(x, p, t) = 2 \left\{ \frac{\partial H(x, p, t)}{\partial p}, \frac{\partial H(x, p, t)}{\partial x} \right\}$$

Theorem 2 The class of Hamiltonians determines the velocity field of two-dimensional flows of an incompressible ideal fluid.

The proof is trivial, the condition (23) coincides with the equation for the stream function. This theorem leads to justification of singling out this class and the necessity of its study because of its physical importance for hydrodynamic problems.

The possibility of studying hydrodynamic flows exclusively as a special class of mechanical systems is an important ideological change following from the theorem.

5. LAGRANGIAN HYDRODYNAMICS

Let's start with some simple considerations that make sense in purely classical mechanics. Let us find an analogue of differentiation of motion equations in terms of classical mechanics. To do this, consider the classical system with the Lagrangian

$$L = \frac{1}{2} (\dot{x} - A(x, y, t))^2 + \frac{1}{2} (\dot{y} - B(x, y, t))^2 \quad (24)$$

An obvious feature of this Lagrangian is the achievement of a bare minimum of action on the equations of motion

$$\begin{aligned} \dot{x} &= A(x, y, t) \\ \dot{y} &= B(x, y, t) \end{aligned} \quad (25)$$

For now, we will not take into account their Hamiltonian character in order to avoid cumbersome notation. This will simplify writing of subsequent equations. These two functions determine both the potential energy and other contributions linear in velocities. On the other hand, the motion equations for this Lagrangian have the form

$$\begin{aligned} \frac{d}{dt} \frac{\partial L}{\partial \dot{x}} &= \frac{\partial L}{\partial x} \\ \frac{d}{dt} \frac{\partial L}{\partial \dot{y}} &= \frac{\partial L}{\partial y} \end{aligned}$$

For the Lagrangian under consideration

$$\begin{aligned} \ddot{x} &= AA_x + BB_x + \dot{y}(A_y - B_x) + A_t \\ \ddot{y} &= AA_y + BB_y - \dot{x}(A_y - B_x) + B_t \end{aligned} \quad (26)$$

It is easy to see that in solutions (25) the equations coincide with the equations obtained by differentiation of motion equations (25).

Theorem 3 If the Lagrangian of a mechanical system has a bare minimum, then the Lagrangian equations of motion of such a system coincide with the equations obtained by time differentiation of bare minimum coordinates.

Then the condition that this system is a natural mechanical system can be formulated as

$$\begin{aligned} \dot{y}(A_y - B_x) + A_t &= \frac{\partial G}{\partial x} \\ -\dot{x}(A_y - B_x) + B_t &= \frac{\partial G}{\partial y} \end{aligned} \quad (27)$$

when considering the equations (25) they are reduced to a system of equations of the form

$$\begin{aligned} A_t + B(A_y - B_x) &= \frac{\partial G}{\partial x} \\ B_t - A(A_y - B_x) &= \frac{\partial G}{\partial y} \end{aligned} \quad (28)$$

It is easy to check that these equations coincide with the previously obtained (21), (22) constraints to the Hamiltonian type (of course, when specializing to and). In this way we can understand the procedure for raising the order of the motion equations and the resulting constraints to the Lagrangian in terms of classical mechanics only. In fact, we obtain the equivalent equations of two-dimensional hydrodynamics in such a way. From a general point of view, these partial differential equations take place as matching conditions of some ordinary differential equations.

Besides, it is easy to take into account the divergence-free velocity field in this formalism. When specializing to stationary Hamiltonians

$$\begin{aligned} \dot{x} = A &= -\frac{\partial H(x, y)}{\partial y} \\ \dot{y} = B &= \frac{\partial H(x, y)}{\partial x} \end{aligned}$$

motion equations of the Lagrangian system have the form



$$\begin{aligned} \ddot{x} &= \frac{\partial P}{\partial x} - \dot{y}\Delta H \\ \ddot{y} &= \frac{\partial P}{\partial y} + \dot{x}\Delta H \end{aligned} \quad (29)$$

where, $P = \frac{1}{2} \left(\left(\frac{\partial H}{\partial x} \right)^2 + \left(\frac{\partial H}{\partial y} \right)^2 \right)$. It's easy to see that at $\Delta H = const$ the natural Lagrangian system is obtained automatically. This clarifies the original example analyzed in Section 3. Of course, in the more general case, if the condition $\Delta H = f(H)$ is met, these equations also coincide with the natural Lagrangian system.

6. CONCLUSIONS

In this paper a class of Hamiltonian systems G whose phase flows are exact solutions of two-dimensional hydrodynamics of incompressible fluid is identified. An unusual example of a Lagrangian one-dimensional system is given, which, upon transition to the Hamiltonian formalism, generates an unsteady two-dimensional flow. Lagrangian hydrodynamics as a consequence of a special choice of the Lagrangian is introduced. The obtained properties are useful in searching for exact solutions of two-dimensional hydrodynamics.

ORCID

 Kostyantyn M. Kulyk, <https://orcid.org/0000-0001-5552-669X>;  Volodymyr V. Yanovsky, <https://orcid.org/0000-0003-0461-749X>

REFERENCES

- [1] P.J. Morrison, "Hamiltonian description of the ideal fluid," Review of Modern Physics, **70**(2), 467-521 (1998). <https://doi.org/10.1103/RevModPhys.70.467>
- [2] R. Salmon, "Hamiltonian fluid mechanics," Ann. Rev. Fluid Mech, **20**, 225-256 (1988). <http://dx.doi.org/10.1146/annurev.fl.20.010188.001301>
- [3] V.E. Zakharov, "The Hamiltonian Formalism for waves in nonlinear media having dispersion," Radiophys. Quantum Electron. **17**, 326-343 (1974). <https://doi.org/10.1007/BF01036794>
- [4] V.E. Zakharov, and E.A. Kuznetsov, "Hamiltonian formalism for nonlinear waves," Phys. Usp. **40**, 1087 (1997). <https://doi.org/10.1070/PU1997v040n11ABEH000304>

- [5] C.S. Gardner, "The Korteweg-de Vries equation and generalization I. The Korteweg-de Vries equation as a Hamiltonian system," *J. Math. Phys.* **12**(8), 1548-1551 (1971). <https://doi.org/10.1063/1.1665772>
- [6] D. Serre, "Invariants et degenerescence symplectique de l'equation d'Euler des fluids parfaits incompressibles," *C.R. Acad. Sci. Paris. Ser. A*, **298**, 349-352 (1984).
- [7] A.V. Tur, and V.V. Yanovsky, "Invariants in Dissipationless hydrodynamics media", *J. Fluid. Mech.* **248**, 67-106 (1993). <https://doi.org/10.1017/S0022112093000692>
- [8] D.G. Ebin, and J.E. Marsden, "Groups of diffeomorphisms and the solution of the classical Euler equations for a perfect fluid," *Bull. Amer. Math. Soc.* **75**(5), 962-967 (1969). <http://dx.doi.org/10.1090/S0002-9904-1969-12315-3>
- [9] D.G. Ebin, and J.E. Marsden, "Groups of diffeomorphisms and the notion of an incompressible fluid," *Ann. of Math. Second Series*, **92**(1), 102-163 (1970). <https://doi.org/10.2307/1970699>
- [10] B. Khesin, and R. Wendt, *The Geometry of Infinite-Dimensional Groups*, (Springer Berlin, Heidelberg, 2008). <https://doi.org/10.1007/978-3-540-77263-7>
- [11] S.P. Novikov, "The Hamiltonian formalism and a many valued analog of Morse theory," *Russ. Math. Surveys*, **37**(5), 1-56 (1982). <https://doi.org/10.1070/RM1982v037n05ABEH004020>
- [12] A. Maltsev, and S. Novikov, "Poisson Brackets of Hydrodynamic Type and Their Generalizations," *Journal of Experimental and Theoretical Physics*, **132**, 645-657 (2021). <https://doi.org/10.1134/S1063776121040154>
- [13] O.I. Mokhov, "Symplectic and Poisson structures on loop spaces of smooth manifolds, and integrable systems," *Russ. Math. Surv.* **53**, 515-623 (1998). <https://doi.org/10.1070/RM1998v053n03ABEH000019>
- [14] E.V. Ferapontov, "Differential geometry of nonlocal Hamiltonian operators of hydrodynamic type," *Funct. Anal. Its Appl.* **25**, 195-204 (1991). <https://doi.org/10.1007/BF01085489>
- [15] V.V. Kozlov, "Hydrodynamics of Hamiltonian systems," *Vestnik Moskovskogo Universiteta, Serii 1: Matematika, Mekhanika*, Nov.-Dec. 10-22 (1983). (in Russian)
- [16] V.E. Zakharov, "The algebra of integrals of motion of two-dimensional hydrodynamics in clebsch variables," *Funct. Anal. Its Appl.* **23**, 189-196 (1989). <https://doi.org/10.1007/BF01079524>

ДВОВИМІРНА ГІДРОДИНАМІКА ЯК КЛАС СПЕЦІАЛЬНИХ ГАМІЛЬТОНОВИХ СИСТЕМ

Костянтин М. Кулик^a, Володимир В. Яновський^{a,b}

^a Інститут монокристаллов, Національна Академія Наук України, пр. Науки 60, 61072 Харків, Україна

^b Харківський національний університет ім. В.Н. Каразіна, майдан Свободи, 4, 61022, Харків, Україна

У роботі визначено клас гамільтонових систем, фазові потоки яких є точними рішеннями двовимірної гідродинаміки рідини, яка не стискується. Розглянуто властивості цього класу. Наведено приклад лагранжової одновимірної системи, яка після переходу до гамільтонового формалізму приводить до нестационарної течії, тобто до точного рішення двовимірної гідродинаміки. Обговорено зв'язок між цими формалізмами та введено лагранжиани, які породжують лагранжову гідродинаміку. Отримані результати дозволяють отримувати точні рішення, як фазові потоки спеціальних гамільтонових систем.

Ключові слова: гамільтоніан; лагранжиан; точні рішення; двовимірна гідродинаміка; фазовий потік

FREE CONVECTIVE MHD RADIOACTIVE FLOW ACROSS A VERTICAL PLATE ENCLOSED IN A POROUS MEDIUM TAKING INTO ACCOUNT VISCOUS-DISSIPATION, THERMO-DIFFUSION AND CHEMICAL-REACTION

 **Salma Akhtar^a**,  **Keshab Borah^{a*}**,  **Shyamanta Chakraborty^b**

^aDepartment of Mathematics, Gauhati University, Guwahati-781014, Assam, India

^bUGC-HRDC, Gauhati University, Guwahati-781014, Assam, India

*Corresponding Author e-mail: keshabborah388@gmail.com

Received February 23, 2024; revised March 24, 2024; accepted March 30, 2024

The paper examines solution for a two-dimensional steady, viscous, heat dissipation, incompressible hydro-magnetic free convective flow past a uniformly moving vertical porous plate immersed in a porous material in the presence of the Soret effect, Dufour effect and Chemical reaction. A constant magnetic field is directed into the fluid area perpendicular to the plate. The MATLAB built-in `bvp4c` solver approach is used to solve the governing non-dimensional equations. The discussion of the current issue focuses mostly on the impacts of thermal diffusion, magnetic field, thermal radiation, Grashof number, Soret number, Dufour number, and chemical reaction. It is observed that the Soret number improves fluid temperature. In addition, the fluid's temperature, concentration, and velocity all drop as the magnetic field parameter rises. Although the heat dissipation caused by the medium's porosity is usually disregarded in convective MHD flow simulations, it is considered in this work.

Keywords: MHD; Porous medium; Chemical reaction; Radiation; Heat dissipation; Soret effect and Dufour effect

PACS: 44.25+g; 44.05.+e; 44.30.+v; 44.40.+a

INTRODUCTION

The combined effects of magnetic and temperature field on viscous flow are basically studied in a magneto-hydrodynamics (MHD) flow. In addition to many other domains, Magnetohydrodynamic (MHD) flow finds practical applications in diverse fields such as missile technology, plasma physics, geophysics, solar physics, astrophysics etc. Consequently, numerous scientists and engineers are keenly interested in its applications. Khan *et al.* [1] investigated the magnetohydrodynamic free convection flow around an oscillating plate within a porous medium. Fetecau *et al.* [2] explored the unsteady solution of magnetohydrodynamic natural convection flow incorporating radiative effects. Meanwhile, Seth *et al.* [3] delved into the radiative heat transfer in the context of MHD free convection flow past a plate with ramped wall temperature. MHD free convective flow involving chemical reaction over an inclined magnetic field was studied by Sheri *et al.* [4]. In an unstable MHD flow between two porous vertical plates, heat and mass transfer were investigated by Raghunath *et al.* [5]. Zeeshan *et al.* [6] investigated the MHD flow of water/ethylene glycol based nanofluids with natural convection through a porous medium. Their results were substantiated both mathematically and graphically.

Free convection is a method of heat transmission in which buoyancy induced fluid motion is all that occurs. Due to the significance of natural convections in both nature and engineering, several scholars have investigated these issues in depth over the past 20 years. Among them are Ahmed *et al.* [7], Lawal *et al.* [8] and Sedki [9]. Ahmed *et al.* [10] conducted a study on the three-dimensional mixed convective mass transfer flow adjacent to a semi-infinite vertical plate in porous medium. Rajput *et al.* [11] investigated the effects of chemical reactions and radiation on magnetohydrodynamic flow via a vertical plate with changing mass diffusion and temperature. Soret and Dufour effect on MHD micropolar fluid past over a Riga plate was studied by Borah *et al.* [12]. Ahmed [13] examined the impact of Soret and radiation effects on transient magnetohydrodynamic free convection from an impulsively started infinite vertical plate. Patel [14] investigated the thermal radiation effects on magnetohydrodynamic (MHD) flow involving heat and mass transfer of a micropolar fluid between two vertical walls. Reddy *et al.* [15] explored the influence of chemical reactions on magnetohydrodynamic natural flow through a porous medium past an exponentially stretching sheet, considering the presence of heat source/sink and viscous dissipation. Jha *et al.* [16] examined how a heat source or sink affected magnetohydrodynamic free convective flow in a nanofluid-filled channel. The effect of viscous dissipation on magnetohydrodynamic free convection flow around a semi-infinite moving vertical porous plate with chemical reaction and heat sink was investigated by Matta *et al.* [17]. Borah *et al.* [18] investigated the influence of Arrhenius activation energy in magnetohydrodynamic micropolar nanofluid flow along a porous stretching sheet, considering viscous dissipation and heat source. In a recent study, Akhtar *et al.* [19] explored the impacts of radiation and heat dissipation on magnetohydrodynamic convective flow in the presence of a heat sink.

Chemical reactions have a significant impact on studies of thermal and solutal convection in the fields of science and engineering technology. The existence of multi-component species in a system causes the chemical reaction.

Senapati *et al.* [20] conducted a study on the magnetic effects on mass and heat transfer in a hydromagnetic flow past over a vertical oscillating plate in presence of a chemical reaction. Mondal *et al.* [21] examined how radiation and chemical reactions affect the free convection flow of magnetohydrodynamic via a vertical plate in a porous material. Sinha [22] conducted a study on the unsteady MHD free convective flow, considering the effects of a chemical reaction past a permeable plate under sloping temperature conditions. The results showed that the reaction rate increased as the chemical reaction parameter increased. Suresh *et al.* [23] investigated the influence of chemical reaction and radiation on magnetohydrodynamic flow along a moving vertical porous plate with heat source and suction.

Bordoloi *et al.* [24] investigated the analytical solution for a steady, viscous, incompressible hydromagnetic free convective flow in two dimensions that passes in front of a vertical porous plate that is uniformly moving and embedded in a porous material. Their study included the consideration of the Soret effect and chemical reaction. The current research extends this work by incorporating heat dissipation due to the porosity of the medium. Through the use of a vertical plate that is always moving, always experiencing a heat flux, immersed in a porous media, and always under continual suction, the study seeks to understand how chemical reactions and thermal radiation affect natural convective flow. These combined effects, which are not typically examined simultaneously, have wide range of effects on engineering processes such as paper production, plastic sheet extrusion, glass blowing, and more.

BASIC EQUATIONS

The following equations described the continuous convective flow across a porous medium of an electrically conducting, viscous, incompressible fluid while being affected by a magnetic field:

$$\vec{\nabla} \cdot \vec{q} = 0 \quad (1)$$

$$\vec{\nabla} \cdot \vec{B} = 0 \quad (2)$$

$$\vec{J} = \sigma (\vec{E} + \vec{q} \times \vec{B}) \quad (3)$$

$$\rho(\vec{q} \cdot \vec{\nabla})\vec{q} = \rho\vec{g} - \vec{\nabla}p + \vec{J} \times \vec{B} + \mu\nabla^2\vec{q} - \frac{\mu\vec{q}}{K} \quad (4)$$

$$\rho C_p(\vec{q} \cdot \vec{\nabla})T = k\nabla^2T + \phi + \frac{J^2}{\sigma} + Q'(T_\infty - T) - \vec{\nabla} \cdot \vec{q}_r - \frac{\mu}{K}\vec{q}_r^2 \quad (5)$$

$$(\vec{q} \cdot \vec{\nabla})C = D_M\nabla^2C + \frac{D_M K T}{T_m}\nabla^2T + \bar{K}_c(C_\infty - C) \quad (6)$$

$$\rho_\infty = \rho[1 + \beta(T - T_\infty) + \bar{\beta}(C_\infty - C)] \quad (7)$$

Radiation heat flux as per Rosseland approximation,

$$\vec{q}_r = -\frac{4\sigma^*}{3k^*}\vec{\nabla}T^4 \quad (8)$$

MATHEMATICAL FORMULATION

It is considered that a viscous, incompressible, radiating fluid that conducts electricity will pass through a vertical plate embedded in a porous medium with uniform suction when a constant magnetic field is present and directed perpendicularly to the flow. The investigation is guided by the following presumptions:

- I. With the exception of density in the term for the buoyant force, all fluid parameters are constant.
- II. There is very little induced magnetic field.
- III. The plate has no electrical conductivity.
- IV. It receives no external electric field.

Let, \vec{B} and \vec{q} be the applied magnetic field and the flow velocity respectively at the point (x', y', z') .

Since $|T - T_\infty|$ is the very small, T^4 can be expressed as:

$$T^4 = \{T_\infty + (T - T_\infty)\}^4 = 4T_\infty^3 T - 3T_\infty^4. \quad (9)$$

Therefore, equation (8) gives,

$$\vec{q}_r = -\frac{16\sigma^*T_\infty^3}{3k^*}\vec{\nabla}T \quad (10)$$

Equation (10) gives,

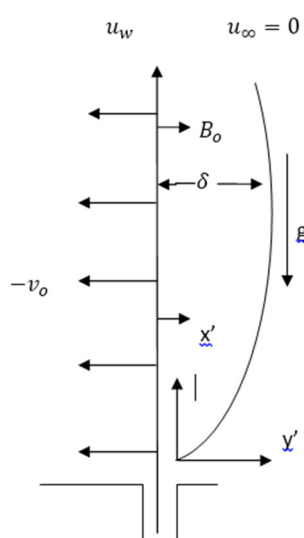


Figure 1. Physical representation of the problem.

$$\vec{\nabla} \cdot \vec{q}_r = - \frac{16\sigma^* T_\infty^3}{3k^*} \nabla^2 T \tag{11}$$

Equation (11) can be used to simplify the energy equation as follows:

$$\rho C_p v' \frac{\partial T}{\partial y'} = k \frac{\partial^2 T}{\partial y'^2} + \mu \left(\frac{\partial u'}{\partial y'} \right) + \sigma B_o^2 u'^2 + \frac{16\sigma^*}{3k^*} T_\infty^3 \frac{\partial^2 T}{\partial y'^2} - \bar{Q}(T_\infty - T) \tag{12}$$

The equation of state (7) yields the following governing equations, which are standard boundary layer approximations.

$$\frac{\partial v'}{\partial y'} = 0, \tag{13}$$

$$v' \frac{\partial u'}{\partial y'} = g\beta(T - T_\infty) + g\bar{\beta}(C - C_\infty) + \vartheta \frac{\partial^2 u'}{\partial y'^2} - \frac{\sigma B_o^2 u'}{\rho} - \frac{\vartheta u'}{K'}, \tag{14}$$

$$\rho C_p v' \frac{\partial T}{\partial y'} = k \frac{\partial^2 T}{\partial y'^2} + \mu \left(\frac{\partial u'}{\partial y'} \right) + \sigma B_o^2 u'^2 + \frac{16\sigma^*}{3k^*} T_\infty^3 \frac{\partial^2 T}{\partial y'^2} - \bar{Q}(T_\infty - T) - \frac{\mu}{k'} u'^2 + \frac{D_M K_T}{C_p C_s}, \tag{15}$$

$$v' \frac{\partial C}{\partial y'} = D_M \frac{\partial^2 C}{\partial y'^2} + \frac{D_M K_T}{T_m} \frac{\partial^2 T}{\partial y'^2} + \bar{K}_c (C_\infty - C), \tag{16}$$

The appropriate boundary conditions for the velocity, temperature and concentration are,

$$\text{At } y' = 0: u' = U, \frac{\partial T}{\partial y'} = -\frac{q^*}{k}, C = C_w \tag{17}$$

$$\text{As } y' \rightarrow \infty: u' \rightarrow 0, T \rightarrow T_\infty, C \rightarrow C_\infty \tag{18}$$

The non-dimensional quantities are introduced as,

$$y = \frac{v_o y'}{v}, \quad u = \frac{u'}{U}, \quad \theta = \frac{T - T_\infty}{\frac{q^* v}{kv_o}}, \quad \varphi = \frac{(C - C_\infty)}{C_w - C_\infty}, \quad G_r = \frac{vg\beta \frac{q^* v}{kv_o}}{U v_o^2}, \quad E = \frac{U^2}{C_p (T_w - T_\infty)},$$

$$P_r = \frac{\mu C_p}{k}, \quad K_c = \frac{\bar{k}_c \vartheta}{v_o^2}, G_m = \frac{g\bar{\beta} \vartheta}{U v_o^2} (C_w - C_\infty), \quad S_c = \frac{\vartheta}{D_M}, \quad M = \frac{\sigma B_o^2 \vartheta}{\rho v_o^2}, R = \frac{4\vartheta I}{\rho C_p v_o^2 q^*}, \quad Q = \frac{\bar{Q} \vartheta}{\rho v_o^2 C_p}, K = \frac{k' v_o^2}{\vartheta^2},$$

$$S_r = \frac{D_M K_T \frac{q^* v}{kv_o}}{\vartheta T_m (C_w - C_\infty)}, D_u = \frac{D_M K_T (C_w - C_\infty)}{C_p C_s (T_w - T_\infty)}, N = \frac{kk^*}{4\sigma^* T_\infty^3}$$

Equation (13) gives,

$$v' = -v_o (v_o > 0) \tag{19}$$

The form of governing equations in dimensionless are as follows:

$$\frac{d^2 u}{dy^2} + \frac{du}{dy} - \left(M + \frac{1}{K} \right) u = -G_r \theta - G_m \varphi \tag{20}$$

$$\frac{d^2 \theta}{dy^2} + \Lambda_1 \frac{d\theta}{dy} - Q_1 \theta = -\Lambda_1 E \left(\frac{du}{dy} \right)^2 - \left(M + \frac{1}{K} \right) \Lambda_1 E u^2 - D_u \Lambda_1 \frac{d^2 \varphi}{dy^2} \tag{21}$$

$$\frac{d^2 \varphi}{dy^2} + S_c \frac{d\varphi}{dy} - K_c \varphi = -S_c S_r \frac{d^2 \theta}{dy^2} \tag{22}$$

Where,

$$\Lambda = 1 + \frac{4}{3N}, \frac{Q}{\Lambda} = Q_1, \text{ and } \Lambda_1 = \frac{Pr}{\Lambda}$$

Corresponding boundary conditions (17)-(18) reduces to

$$\text{At } y = 0: u = 1, \frac{\partial \theta}{\partial y} = -1, \varphi = 1 \tag{23}$$

$$\text{As } y \rightarrow \infty: u \rightarrow 0, \theta \rightarrow 0, \varphi \rightarrow 0 \tag{24}$$

METHOD OF SOLUTION

The ordinary differential equations (20)-(22) with the boundary conditions (23) and (24) are solved by the use of numerical method ‘MATLAB built-in bvp4c solver technique’. The boundary ordinary differential equations are converted into the first order differential equations are as follows:

Let,

$$u = y(1), \quad u' = y(2), \quad \theta = y(3), \quad \theta' = y(4), \quad \varphi = y(5), \quad \varphi' = y(6).$$

Now, we have the following set of first order differential equations:

$$y'(2) = -y(2) - \left(M + \frac{1}{K} \right) y(1) - G_r y(3) - G_m y(5) \tag{25}$$

$$y'(4) = -\frac{Pr}{\left(1 + \frac{4}{3N}\right)} y(4) + \frac{Q}{\left(1 + \frac{4}{3N}\right)} y(3) - \frac{Pr}{\left(1 + \frac{4}{3N}\right)} E y(2) y(2) - \left(M + \frac{1}{K}\right) \frac{Pr}{\left(1 + \frac{4}{3N}\right)} E y(1) y(1) - Du \frac{Pr}{\left(1 + \frac{4}{3N}\right)} y'(6) \tag{26}$$

$$y'(6) = -Sc y(6) + Kc y(5) - Sc Sr y'(4) \tag{27}$$

The boundary conditions of the resulting ordinary differential equations can be expressed as,

$$y0(1) - 1, y0(4) + 1, y0(5) - 1, y1(1) - 0, y1(3) - 0, y1(5) - 0 \tag{28}$$

RESULT AND DISCUSSION

In this study, the effects of various non-dimensional physical parameters such as magnetic parameter (M), radiation parameter (N), thermal diffusion ratio (K_T), heat sink (Q), thermal Grashof number (G_r), solutal Grashof number (G_m), chemical reaction (K_c), Soret number (S_r), Schmidt Number (S_c), Prandlt number (P_r), Dufour number (D_u) and porosity parameter (K) on velocity field (u), temperature field (θ) and concentration field (φ) of the flow system have been studied and their variations with respect to the parameters are shown by graphs. The Variations of fluid velocity, temperature and concentration field are shown in figures 2-20 graphically.

Velocity variation: The velocity profiles are shown in figures 2-9. Figure-2 represents that the fluid velocity u decreases with the increasing values of magnetic parameter (M). This happens as a result of the fluid's velocity decreasing due to the magnetic field's generation of an opposing Lorentz force. Therefore, the increasing value of magnetic field results in the decrease of fluid velocity. Figure-3 shows the effect of the radiation parameter on the velocity profile. It is evident that as the radiation parameter increases, the velocity of fluid particles increases.

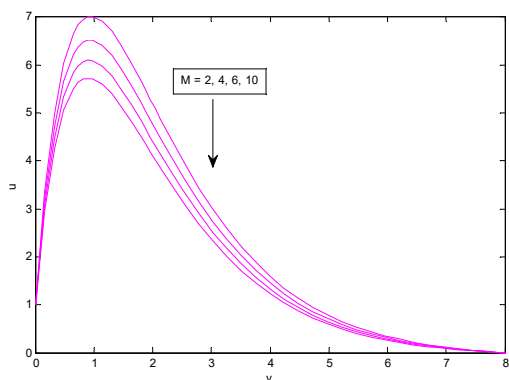


Figure 2. Variation of the velocity with M

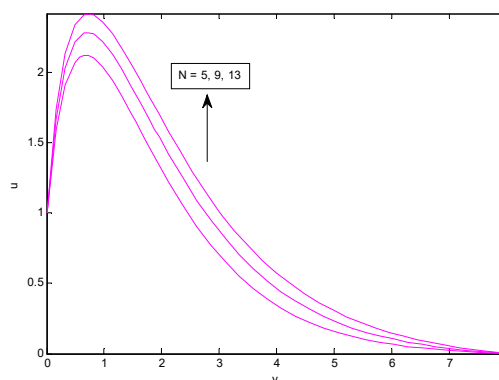


Figure 3. Variation of the velocity with N

Figure-4 shows the impact of chemical reaction parameter K_c on velocity profile. It is observed that fluid velocity (u) decreases with the increase of chemical reaction parameter K_c. Figure-5 shows how fluid velocity changes with thermal Grashof number G_r. It is noted that velocity increases along with the thermal Grashof number.

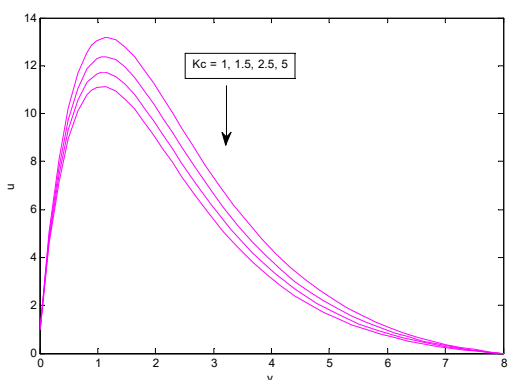


Figure 4. Variation of the velocity with K_c

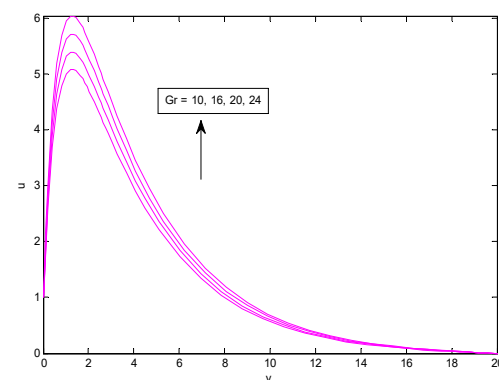


Figure 5. Variation of the velocity with G_r

This can be explained by the observation that temperature gradients rise in proportion to an increase in Grashof number, which ultimately causes the velocity distribution inside the flow to increase. Figure-6 demonstrates how the solutal Grashof number G_m affect the fluid velocity. It is noted that the fluid velocity increases with G_m. The thermal and solutal buoyancy forces cause a considerable rise in the velocity field. This results from the direct relationship between buoyant force and Grashof numbers. Figure-7 depicts the effect of Soret number (S_r) on velocity. It is seen that the fluid

velocity increases due to the increase of Soret number. In figure-8, it has been noted that when the porosity parameter (K) grows, the fluid velocity increases. This happens because a fluid with a higher porosity value has more room to move. Consequently, an increase in the fluid velocity occurs. Figure-9 shows the influence of Dufour number (D_u) on fluid velocity. It is regarded that as Dufour number increases there is monotonic increase in the fluid velocity.

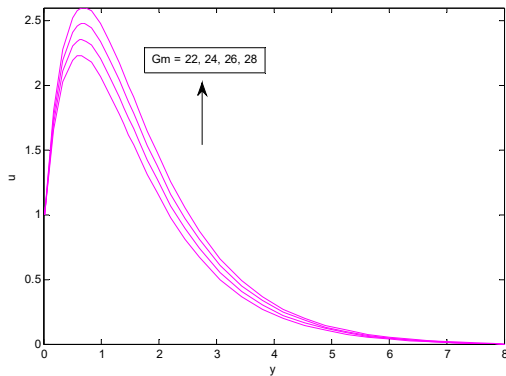


Figure 6. Variation of the velocity with G_m

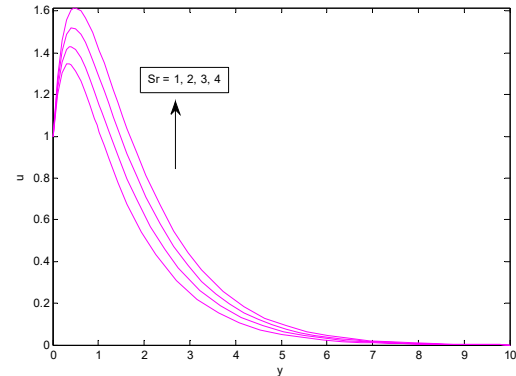


Figure 7. Variation of the velocity with S_r

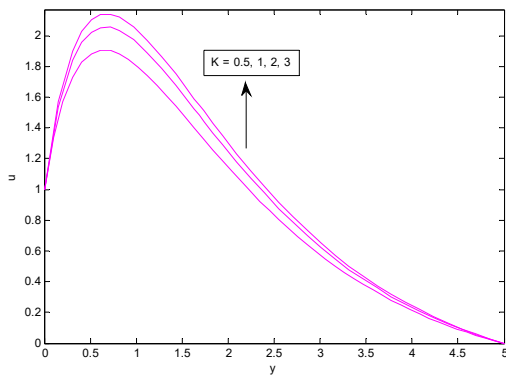


Figure 8. Variation of the velocity with K

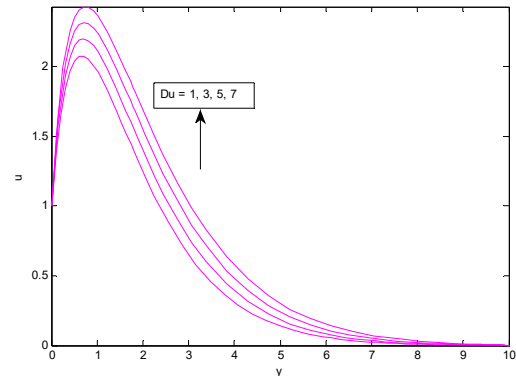


Figure 9. Variation of the velocity with D_u

Temperature Variation: The temperature profiles are shown in figures 10-17. Figure-10 demonstrates how temperature profile changes with heat sink (Q). It is noted that the fluid temperature decreases with the increase of Q . Figure 11 indicates that the fluid temperature decreases as the chemical reaction parameter (K_c) increases. Figure -12 shows how the radiation parameter affects the temperature profile. The observed that the fluid's temperature drops as the radiation parameter increases. Figure-13 illustrates how the fluid temperature drops as the magnetic parameter increases. The increasing values of solutal Grashof number (G_m) and thermal Grashof number (G_r) increases the fluid temperature, as shown in figures 14 and 15. Figure-16 shows a clear rise in the fluid temperature for increasing the Soret number (S_r). Figures-17 describes the effect of Dufour number (D_u) on fluid temperature. The Dufour number signifies the contribution of the concentration gradients to the thermal energy flux in the flow. It is seen that as Dufour number (D_u) increases there is monotonic increase in temperature.

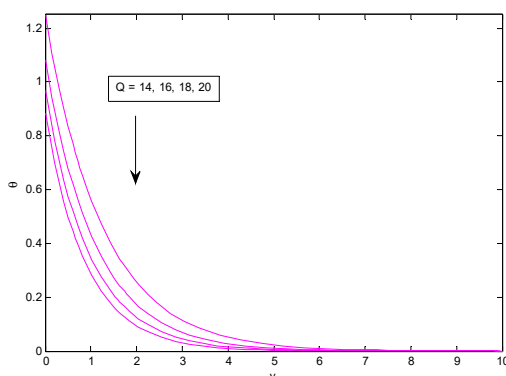


Figure 10. Variation of the temperature with Q

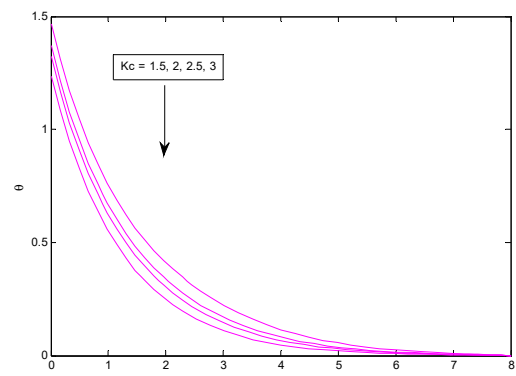


Figure 11. Variation of the temperature with K_c

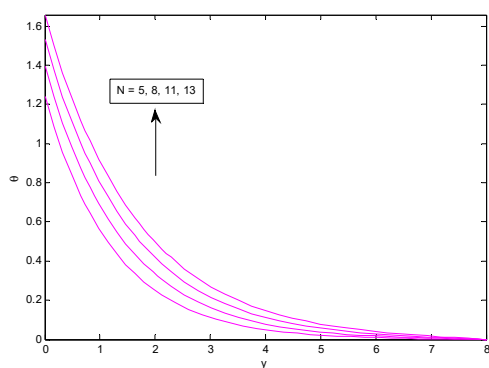


Figure 12. Variation of the temperature with N

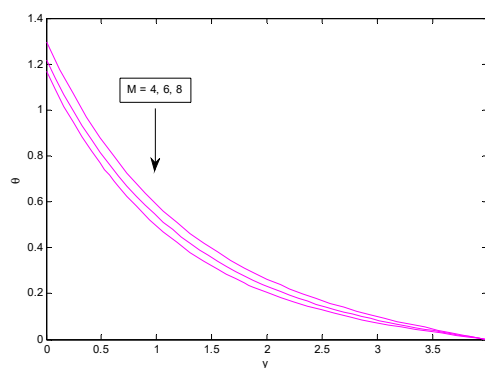


Figure 13. Variation of the temperature with M

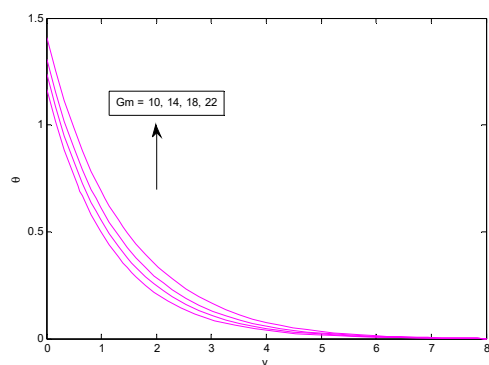


Figure 14. Variation of the temperature with G_m

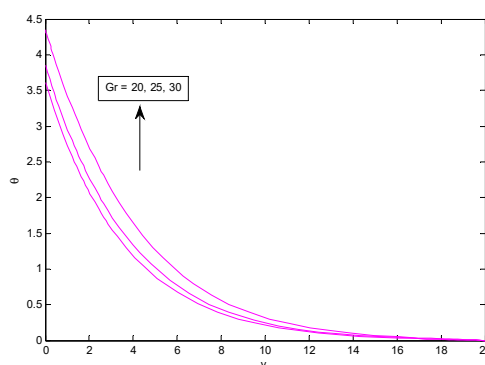


Figure 15. Variation of the temperature with G_r

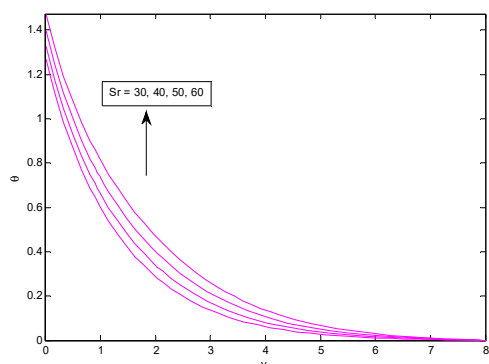


Figure 16. Variation of the temperature with S_r

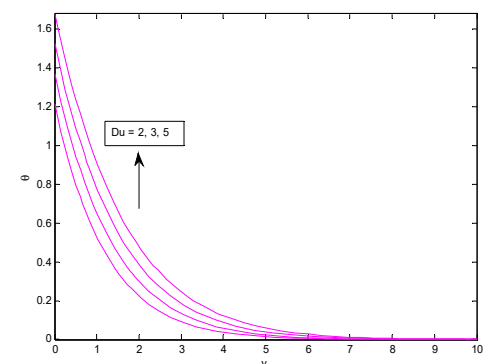


Figure 17. Variation of the temperature with D_u

Concentration Variation: The concentration profiles for the parameters K_c , S_r and D_u are depicted in figures 18-20. Figure-18 illustrates that fluid concentration decreases with increasing chemical reaction parameter(K_c). Figure-19 shows a clear rise in the fluid concentration for increasing the Soret number (S_r). Figure-20 describes the fluid concentration increases due to the increasing value of Dufour number (D_u).

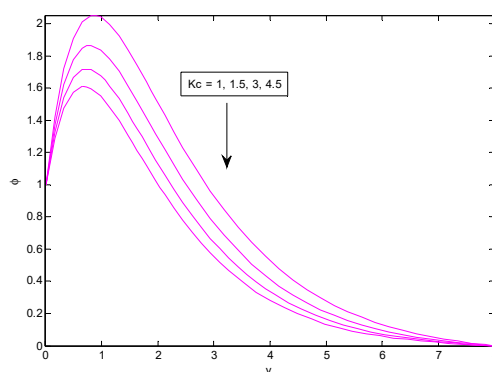


Figure 18. Variation of the concentration with K_c

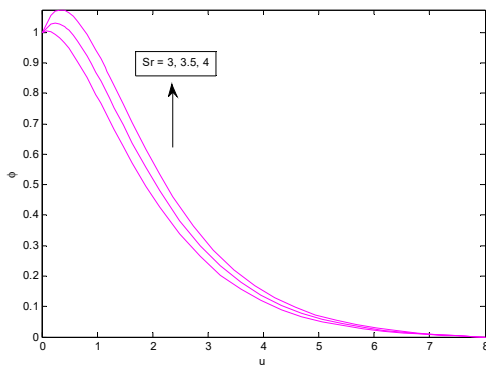


Figure 19. Variation of the concentration with S_r

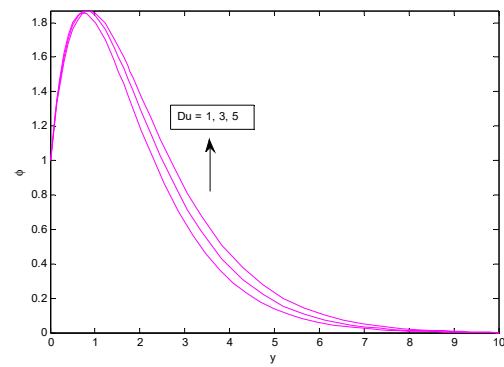


Figure 20. Variation of the concentration with D_u

CONCLUSION

In this inquiry, using the ‘MATLAB built-in bvp4c solver technique’, free convective MHD radioactive flow across a porous vertical plate surrounded by a porous medium has been numerically simulated, accounting for viscous dissipation, thermo-diffusion, and chemical reaction. The investigation's results are noteworthy when fluid temperature rises for high radiation and high thermo-diffusion effects. The consumption of species and magnetic field characteristics is still decreased. As the buoyant force grows, the upsurge concentration rises; nevertheless, as the magnetic parameters grow, it declines. With a rise in magnetic field and intense radiation, the flow slows down. The impact of thermo-diffusion causes the flow to speed up. The application of thermal radiation and magnetic field slows the drag force at the plate. The rate of mass transfer is increased by increasing the thermo-diffusion effect.

NOMENCLATURE

\vec{q}	Fluid velocity vector	U	Free stream velocity
K_T	Thermal diffusion ratio	q^*	Heat flux
ρ	Fluid density	σ^*	Stefan-Boltzmann constant
T	Fluid temperature	q_r	Flux of radiation heat
C_∞	Species concentration in free stream	κ	Thermal conductivity
\vec{B}	Magnetic flux density vector	$\frac{\vec{j}^2}{\sigma}$	Ohmic dissipation of energy per unit volume
ν	Kinematic viscosity	ϕ	Viscous energy dissipation per unit volume
C	Molar species concentration	K_c	Chemical reaction coefficient
\vec{j}	Current density vector	σ	Conductivity of electricity
C_w	Species concentration at the plate	K	Porosity parameter
\vec{j}	Acceleration vector due to gravity	κ^*	Mean absorption coefficient
T_m	Mean fluid temperature	D_M	Mass diffusivity
P	Fluid pressure	β	Coefficient of thermal expansion
\vec{E}	Electrical field	N	Radiation absorption Coefficient
C_p	Specified heat at steady pressure		
μ	Coefficient of viscosity		

ORCID

Salma Akhtar, <https://orcid.org/0009-0003-1793-001X>; Keshab Borah, <https://orcid.org/0009-0005-5486-5784>
Shyamanta Chakraborty, <https://orcid.org/0000-0001-5839-4856>

REFERENCES

- I. Khan, K. Fakhar, and S. Shafie, “Magnetohydrodynamic free convection flow past an oscillating plate embedded in a porous medium,” *Journal of the Physical Society of Japan*, **80**(10), 1–10 (2011). <https://doi.org/10.1143/JPSJ.80.104401>
- C. Fetecau, S. Akhtar, I. Pop, and C. Fetecau, “Unsteady general solution for MHD natural convection flow with radiative effects, heat source and shear stress on the boundary,” *International Journal of Numerical Methods for Heat and Fluid Flow*, **27**(6), 1266-1281 (2017). <https://doi.org/10.1108/HFF-02-2016-0069>
- G.S. Seth, M.S. Ansari, and R. Nandkeolyar, “MHD natural convection flow with radiative heat transfer past an impulsively moving plate with ramped wall temperature,” *Heat and Mass Transfer*, vol. **47**(5) 551–561 (2011). <https://doi.org/10.1007/s00231-010-0740-1>
- S.R. Sheri, S. Jayaprasad, and D. Mahendar, “Soret and Dufour effects on MHD free convection flow past an impulsively moving vertical plate in the presence of inclined magnetic field”, *AIP Conference Proceedings*, **2246**, (2020). <https://doi.org/10.1063/5.0015575>
- K. Raghunath, M. Obulesu, and R. Sivaprasad, “Heat and mass transfer on an unsteady MHD flow through porous medium between two porous vertical plates”, *AIP Conference Proceedings*, **2220**, (2020). <https://doi.org/10.1063/5.0001103>
- A. Zeeshan, R. Ellahi, and M. Hassan, “Magnetohydrodynamic flow of water/ethylene glycol based nanofluids with natural convection through a porous medium,” *The European Physical Journal Plus*, **129**(12), 261 (2014). <https://doi.org/10.1140/epjp/i2014-14261-5>

- [7] N. Ahmed, and D.J. Saikia, "Unsteady MHD free convective flow past a moving vertical plate in a porous medium with radiation and chemical reaction including arbitrary thermal and solutal ramped condition", *Heat Transfer*, **51**(7), 6893-6914 (2022). <https://doi.org/10.1002/htj.22629>
- [8] K.K. Lawal, and H.M. Jibril, "Impact of relative motion of a magnetic field on unsteady magnetohydrodynamic natural convection flow with a constant heat source/sink", *Heat Transfer*, **50**(1), 487-507 (2020). <https://doi.org/10.1002/htj.21888>
- [9] A.M. Sedki, "Effect of thermal radiation and chemical reaction on MHD mixed convective heat and mass transfer in nanofluid flow due to nonlinear stretching surface through porous medium", *Results in Materials*, **16**, 100334 (2022). <https://doi.org/10.1016/j.rinma.2022.100334>
- [10] N. Ahmed, and K. Choudhury, "Heat and mass transfer in three-dimensional flow through a porous medium with periodic permeability", *Heat Transfer-Asian Research*, **48**(2), 644-662 (2019). <https://doi.org/10.1002/htj.21399>
- [11] U.S. Rajput, and G. Kumar, "Effects of radiation and chemical reaction on MHD flow past a vertical plate with variable temperature and mass diffusion", *Journal of Naval Architecture and Marine Engineering*, **16**(2), 99-108 (2019). <https://doi.org/10.3329/jname.v16i2.29526>
- [12] K. Borah, J. Konch, and S. Chakraborty, "Soret and Dufour effects on MHD flow of a micropolar fluid past over a vertical Riga plate," *Journal of Applied Mathematics and Computational Mechanics*, **22**(3), 5-18 (2023). <https://doi.org/10.17512/jamcm.2023.3.01>
- [13] N. Ahmed, "Soret and Radiation Effects on Transient MHD Free Convection From an Impulsively Started Infinite Vertical Plate," *ASME. J. Heat Transfer*, **134**(6), 062701 (2012). <https://doi.org/10.1115/1.4005749>
- [14] H.R. Patel, "Thermal radiation effects on MHD flow with heat and mass transfer of micropolar fluid between two vertical walls," *International Journal of Ambient Energy*, **42**, 1281-1296 (2019). <https://doi.org/10.1080/01430750.2019.1594371>
- [15] N.N. Reddy, V.S. Rao, and B.R. Reddy, "Chemical reaction impact on MHD natural convection flow through porous medium past an exponentially stretching sheet in presence of Heat Source/Sink and viscous dissipation", *Case Studies in Thermal Engineering*, **25**(3), 100879 (2021). <https://doi.org/10.1016/j.csite.2021.100879>
- [16] B.K. Jha, and G. Samaila, "Effect of heat source/sink on MHD free convection flow in a channel filled with nanofluid in the existence of induced magnetic field: an analytic approach," *SN Appl. Sci.* **2**, 1321 (2020). <https://doi.org/10.1007/s42452-020-3139-8>
- [17] S. Matta, B.S. Malga, G.R. Goud, L. Appidi, and P.P. Kumar, "Effects of viscous dissipation on MHD free convection flow past a semi-infinite moving vertical porous plate with heat sink and chemical reaction," *Materials Today: Proceedings*, (2023). <https://doi.org/10.1016/j.matpr.2023.06.108>
- [18] K. Borah, J. Konch, and S. Chakraborty, "Effect of Arrhenius Activation Energy in MHD Micropolar Nanofluid Flow Along a Porous Stretching Sheet with Viscous Dissipation and Heat Source", *East European Journal of Physics*, **4**, 98-108 (2023). <https://doi.org/10.26565/2312-4334-2023-4-10>
- [19] S. Akhtar, K. Borah, and S. Chakraborty, "Effect of radiation and heat dissipation on MHD convective flow in presence of heat sink," *East European Journal of Physics*, **3**, 471-478 (2023). <https://doi.org/10.26565/2312-4334-2023-3-53>
- [20] N. Senapati, and R.K. Dhal, "Magnetic effect on mass and heat transfer of a hydrodynamic flow past a vertical oscillating plate in presence of chemical reaction," *Modelling, Measurement and Control B*, **79**, 60-75 (2010).
- [21] S. Mondal, S. Parvin, and S.F. Ahmmmed, "Effects of radiation and chemical reaction on MHD free convection flow and past a vertical plate in the porous medium", *American Journal of Engineering Research*, **03**(12), 15-22 (2014). [https://www.ajer.org/papers/v3\(12\)/V3\(12\).pdf](https://www.ajer.org/papers/v3(12)/V3(12).pdf)
- [22] S. Sinha, "Effect of chemical reaction on an unsteady MHD free convective flow past a porous plate with ramped temperature," in: *Proc. Int. Conf. Frontiers in Mathematics*, (2015), pp. 204-210.
- [23] P. Suresh, Y.H. Krishna, R.S. Rao, and P.V.J. Reddy, "Effect of Chemical reaction and radiation on MHD flow along a moving vertical porous plate with heat Source and Suction," *International Journal of Applied Engineering Research*, **14**(4), 869-876 (2019). https://www.ripublication.com/ijaer19/ijaerv14n4_04.pdf
- [24] R. Bordoloi, K. Chamuah, and N. Ahmed, "Free convective MHD radiative flow past a porous vertical plate in a porous medium with chemical reaction", *Biointerface Research in Applied Chemistry*, **13**(3), 259 (2023). <https://doi.org/10.33263/BRIAC133.259>

ВІЛЬНИЙ КОНВЕКТИВНИЙ РАДІОАКТИВНИЙ МГД ПОТІК ЧЕРЕЗ ВЕРТИКАЛЬНУ ПЛАСТИНУ В ПОРИСТОМУ СЕРЕДОВИЩІ З УРАХУВАННЯМ В'ЯЗКОВОЇ ДИСИПАЦІЇ, ТЕРМОДИФУЗІЇ ТА ХІМІЧНОЇ РЕАКЦІЇ

Сальма Ахтар^а, Кешаб Борах^а, Шьяманта Чакраборти^б

^аФакультет математики, Університет Гаухаті, Гувахаті-781014, Ассам, Індія

^бUGC-HRDC, Університет Гаухаті, Гувахаті-781014, Ассам, Індія

У статті розглядається рішення для двовимірного постійного, в'язкого, розсіювання тепла, нестисливого гідромагнітного вільного конвективного потоку повз рівномірно рухому вертикальну пористу пластину, занурену в пористий матеріал, за наявності ефекту Сорє, ефекту Дофура та хімічної реакції. Постійне магнітне поле спрямоване в область рідини перпендикулярно до пластини. Вбудований у MATLAB розв'язувач `bvp4c` використовується для розв'язування керівних безвимірних рівнянь. Обговорення поточного питання зосереджено на впливі теплової дифузії, магнітного поля, теплового випромінювання, числа Грасгофа, числа Сорє, числа Дюфура та хімічної реакції. Помічено, що число Сорє покращує температуру рідини. Крім того, температура, концентрація та швидкість рідини падають зі збільшенням параметра магнітного поля. Хоча розсіювання тепла, викликане пористістю середовища, зазвичай не враховується при моделюванні конвективного МГД-потоку, воно розглядається в цій роботі.

Ключові слова: МГД; пористе середовище; хімічна реакція; випромінювання; розсіювання тепла; ефект Сорє і ефект Дюфура

OSCILLATORY MAXWELL-CATTANEO FERROCONVECTION IN A DENSELY PACKED ROTATING POROUS MEDIUM SATURATED WITH A VISCOELASTIC MAGNETIC FLUID

 Naseer Ahmed^{a*},  S. Maruthamanikandan^b

^aDepartment of Mathematics, Presidency College, Kempapura, Hebbal, Bengaluru 560024, India

*Corresponding Author E-mail: naseerahmed.ar2023@gmail.com

^bDepartment of Mathematics, School of Engineering, Presidency University, Bengaluru 560064, India

Email: maruthamanikandan@presidencyuniversity.in

Received September 29, 2023; revised January 13, 2024; accepted January 15, 2024

The combined effect of second sound and the viscoelasticity is examined using the classical stability analysis on the onset of rotating porous medium ferroconvection. Local thermal equilibrium is assumed between the solid matrix and fluid. Present problem is examined by an analytical approach by considering the pertinent boundary conditions. Normal mode analysis technique is utilized for obtaining the critical values for both instabilities namely stationary and oscillatory. We noticed that the oscillatory mode of instability is favored over the stationary mode of instability. We found that magnetic forces, second sound, nonlinearity in magnetization, Vadasz number, stress relaxation due to viscoelasticity and Taylor-Darcy number are in favour of advancing oscillatory porous medium ferroconvection whereas strain retardation postpone the outset of oscillatory porous medium ferroconvection. Convection cell size effects by different parameters and the oscillation's frequency are also noted. This problem shall have significant feasible technological applications wherein viscoelastic magnetic fluids are involved.

Keywords: Convection; Rotation; Viscoelastic fluids; Maxwell equations; Porous media; Navier-Stokes equations for incompressible viscous fluids

AMS Classification: 76E06, 35Q61, 76A10, 76S05, 76D05.

PACS: 47.32.-y, 47.56.+r, 47.65.Cb, 66.20.-d.

1. INTRODUCTION

The dynamics of ferrofluids can be controlled by an externally acting applied magnetic field (Shliomis [1]). Rosensweig [2-4] was the first to synthesize ferrofluids. Considering both magnetic and buoyancy forces, a comprehensive analysis of *RBC* in ferrofluids was reported by Finlayson [5]. The findings of Finlayson [5] were examined both theoretically and experimentally by Schwab *et al.* [6] and Stiles and Kagan [7] respectively. Lalas and Carmi [8] reported the unique results on ferroconvection with energy stability approach. The impact of internal heating on the energy stability of magnetic fluids was documented by Mahajan and Sharma [9]. Nisha Mary and Maruthamanikandan [10] investigated a time-dependent body force effect on magnetic fluid convection. Soya Mathew *et al.* [11] studied porous medium ferroconvection with Maxwell-Cattaneo equation. Laroze and Pleiner [12] examined numerical and theoretical impact on ferroconvection in a viscoelastic carrier liquid. Recently Balaji *et al.* [13] worked on magnetic field modulation affected ferroconvection in a Brinkman porous medium. Vidyashree *et al.* [14] examined the combined effect of variable gravity and MFD viscosity on porous medium ferroconvection. Naseer *et al.* [15] analyzed the dual nature of Prandtl number in the presence and the absence of non-classical conduction.

When it comes to instabilities in viscoelastic fluids, Oldroyd model [16] gives the fundamental rheological equation describing the properties of viscoelastic realistically. In comparison the relaxational time in normal liquids is very short as that of viscoelastic liquids. Green [17] examined that for viscoelastic liquids the principle of exchange of stabilities is invalid when the restoring force is large. Malashetty *et al.* [18] and Jianhong Kang *et al.* [19] studied the rotating *RBC* in viscoelastic fluids by means of both linear and weakly non-linear techniques. Laroze *et al.* [20] presented theoretical and numerical results on ferroconvection in a viscoelastic carrier liquid. Several other researchers contributed to addressing the problem of convective instability of viscoelastic fluids with a variety of constraints techniques (Bhadauria and Kiran [21], Alves *et al.* [22], Sohail Nadeem *et al.* [23], Mahmud *et al.* [24], Sharma and Mondal [25] and Kaiyao *et al.* [26], Dhiman *et al.* [27]).

As for the convection due to porous medium, Saravanan and Sivakumar [28] made an investigation on the impact of vibrations on *RBC* in porous media with arbitrary amplitude and frequency. Very recently, Rudresha *et al.* [29] studied the theoretical influence of time-periodic electric field on electroconvection of Brinkman type. Malashetty and Mahantesh [30] investigated the linear stability of an Oldroyd type viscoelastic liquid filled horizontally asymmetric porous material warmed beneath and chilled from above. More recently, Rudresha *et al.* [31] reported a theoretical investigation of the combine effect of anisotropy and time-periodic electric field on Darcy-electroconvection. Lebon and Cloot [32] studied the effects of Maxwell-Cattaneo model in *RBC* and Marangoni instability. Maruthamanikandan and Smita [33] investigated Rayleigh-Benard instability taking into account second sound in a dielectric fluid. Soya and Maruthamanikandan [34] examined the porous medium ferroconvective instability subjected to the heat flux model.

Recently, Naseer Ahmed and Maruthamanikandan [35] analyzed anisotropic porous medium under Brinkman Model on viscoelastic ferroconvective instability due to Maxwell-Cattaneo.

External rotation in regards with thermal convection has gained a high interest both theoretically and experimentally. Due to its general existence in oceanic flows and geophysical, it is crucial to realize how the Coriolis force ambience the transport properties and structure of thermal convection. The investigation on thermal convection stability in rotating porous media are done by many researchers. Friedrich [36] analyzed the porous layer stability with rotation warmed from underneath considering linear and a nonlinear numerical analysis. This problem with the variable viscosity impact has been addressed by Patil and Vaidyanathan [37]. A fascinating analogy have been well-established by Palm and Tyvand [38] among an anisotropic porous layer and a rotating porous layer. Various researchers have examined the rotation under different constraints as follows Jou and Liaw [39], Qin and Kaloni [40], Vadasz [41], Straughan [42], Govender [43,44], Desai *et al.* [45], Straughan [46], Malashetty and Swamy [47], Dhiman and Sood [48] and Pulkit Kumar Nadian [49].

The present paper concentrates on examining the oscillatory convective instability of viscoelastic ferrofluid saturated in a rotating porous medium using extended Darcy model with second sound as we cannot find any study related to this from the literature review.

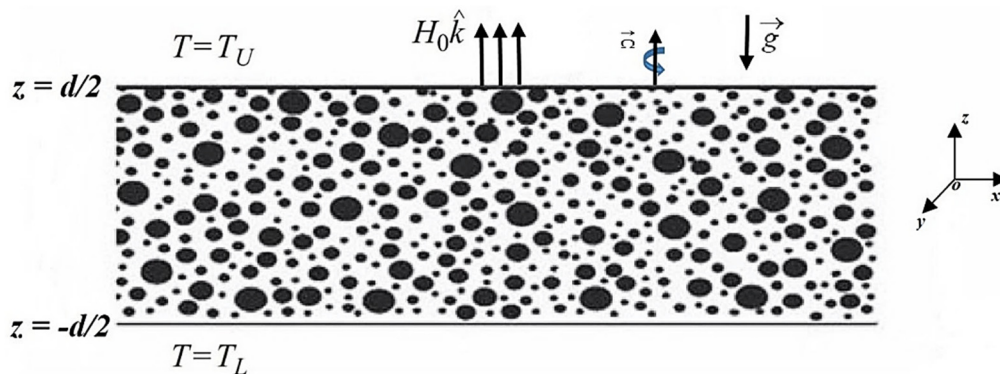


Figure 1. Physical Configuration

2. MATHEMATICAL FORMULATION

Let us consider a Boussinesq viscoelastic ferromagnetic fluid saturated densely distributed porous layer rotating with angular velocity $\vec{\Omega}(0,0,\Omega)$ restricted between two endless horizontal surfaces of height ‘d’. The viscoelastic behaviour is characterized by Oldroyd’s model (non-Newtonian). The above and bottom surface is maintained at T_U and T_L where $T_L > T_U$ (see Fig. 1). Magnetic field \vec{H}_0 acts parallel in the z-axis vertically and the force of gravity assisting vertically descending. The governing equations aiding the Boussinesq approximation are recorded as follows.

$$\nabla \cdot \vec{q} = 0 \tag{2.1}$$

$$\left(1 + \lambda_1 \frac{\partial}{\partial t}\right) \left[\frac{\rho_0}{\varepsilon} \frac{\partial \vec{q}}{\partial t} + \frac{\rho_0}{\varepsilon^2} (\vec{q} \cdot \nabla) \vec{q} + \nabla p - \rho \vec{g} - \nabla \cdot (\vec{H} \vec{B}) + \frac{2}{\varepsilon} (\vec{\Omega} \times \vec{q}) \rho_0 \right] = - \left(1 + \lambda_2 \frac{\partial}{\partial t}\right) \left[\frac{\mu_f}{k} \vec{q} \right] \tag{2.2}$$

$$\varepsilon \left[\rho_0 C_{v,H} - \mu_0 \vec{H} \cdot \left(\frac{\partial \vec{M}}{\partial T} \right)_{v,H} \right] \left[\frac{\partial T}{\partial t} + \vec{q} \cdot \nabla T \right] + (1 - \varepsilon) (\rho_0 C)_s \frac{\partial T}{\partial t} + \mu_0 T \left(\frac{\partial \vec{M}}{\partial T} \right)_{v,H} \cdot \left[\frac{\partial \vec{H}}{\partial t} + (\vec{q} \cdot \nabla) \vec{H} \right] = - \nabla \cdot \vec{Q} \tag{2.3}$$

$$\tau \left[\frac{\partial \vec{Q}}{\partial t} + (\vec{q} \cdot \nabla) \vec{Q} + \vec{\omega} \times \vec{Q} \right] = - \vec{Q} - k_1 \nabla T \tag{2.4}$$

$$\rho = \rho_0 [1 - \alpha (T - T_a)] \tag{2.5}$$

$$M = M_0 + \chi_m (H - H_0) - K_m (T - T_a) \tag{2.6}$$

All the terms above are defined in Naseer *et al.* [15].
Maxwell’s equations (Finlayson [5]).

$$\nabla \cdot \vec{B} = 0, \quad \nabla \times \vec{H} = \vec{0}, \quad \vec{B} = \mu_0 \left(\vec{H} + \vec{M} \right). \tag{2.7}$$

We notice that for $\lambda_2=0$ the fluid scale down to Maxwell’s fluid and also if $\lambda_2=0$ and $\lambda_1=0$ then the fluid scale down to Newtonian fluid.

The basic state equations are as follows

$$\left. \begin{aligned} \frac{\partial}{\partial t} = 0, \quad \vec{q}_b = (0, 0, 0), \quad T = T_b(z), \\ p = p_b(z), \quad \rho = \rho_b(z), \quad \vec{H} = H_b(z), \\ \vec{M} = M_b(z), \quad \vec{B} = B_b(z), \quad \vec{Q} = \vec{Q}_b(0, 0, k_1\beta) \end{aligned} \right\} \tag{2.8}$$

where $\beta = (T_1 - T_0)/2$

The basic state solution reads as follows

$$\rho_b = \rho_0 [1 + \alpha\beta z] \tag{2.9}$$

$$\vec{H}_b = \left[H_0 - \frac{K_m\beta z}{1 + \chi_m} \right] \hat{k} \tag{2.10}$$

$$\vec{M}_b = \left[M_0 + \frac{K_m\beta z}{1 + \chi_m} \right] \hat{k} \tag{2.11}$$

$$\vec{B} = \mu_0 \left[\vec{H} + \vec{M} \right] \hat{k} \tag{2.12}$$

3. STABILITY ANALYSIS

Due to small perturbations, we obtain dimensionless equations for stability analysis embracing normal modes (Finlayson [5]).

After an infinitesimally small perturbations the perturbed state equations are as follows

$$\left. \begin{aligned} \vec{q} = \vec{q}_b + \vec{q}', \quad T = T_b + T', \quad p = p_b + p', \\ \rho = \rho_b + \rho', \quad \vec{H} = \vec{H}_b + \vec{H}', \quad \vec{M} = \vec{M}_b + \vec{M}', \\ \vec{B} = \vec{B}_b + \vec{B}', \quad \vec{Q} = \vec{Q}_b + \vec{Q}', \quad \phi = \phi_b + \phi' \end{aligned} \right\} \tag{3.1}$$

where the perturbed quantities are indicated by primes. Therefore, the linearized equations due to small perturbed governing takes the form.

$$\left(1 + \lambda_1 \frac{\partial}{\partial t} \right) \left[\frac{\rho_0}{\varepsilon} \frac{\partial}{\partial t} (\nabla^2 w') - \alpha g \rho_0 \nabla_1^2 T' + \mu_0 K_m \beta \frac{\partial}{\partial z} (\nabla_1^2 \phi') - \frac{\mu_0 K_m^2 \beta \nabla_1^2 T'}{1 + \chi_m} + \frac{2\rho_0}{\varepsilon} \Omega \frac{\partial \zeta}{\partial z} \right] = \left(1 + \lambda_2 \frac{\partial}{\partial t} \right) \left[-\frac{\mu_t}{k} \nabla^2 w' \right] \tag{3.2}$$

$$\left(1 + \lambda_1 \frac{\partial}{\partial t} \right) \left[\frac{\rho_0}{\varepsilon} \frac{\partial \zeta}{\partial t} - \frac{2\rho_0 \Omega}{\varepsilon} \frac{\partial w'}{\partial z} \right] = - \left(1 + \lambda_2 \frac{\partial}{\partial t} \right) \left[\frac{\mu_t}{k} \zeta \right] \tag{3.2}$$

$$(\rho_0 C)_1 \frac{\partial T'}{\partial t} - \mu_0 T_a K_m \frac{\partial}{\partial t} \left(\frac{\partial \phi'}{\partial z} \right) = -\nabla \cdot \vec{Q}' + \left[(\rho_0 C)_2 - \frac{\mu_0 T_a K_m^2}{1 + \chi_m} \right] \beta w' \tag{3.4}$$

$$\left(1 + \tau \frac{\partial}{\partial t} \right) \vec{Q}' = -\frac{\tau k_1 \beta}{2} \left(\frac{\partial \vec{q}'}{\partial z} - \nabla w' \right) - k_1 \nabla T' \tag{3.5}$$

$$(1 + \chi_m) \frac{\partial^2 \phi'}{\partial z^2} + \left(1 + \frac{M_0}{H_0} \right) \nabla_1^2 \phi' - K_m \frac{\partial T'}{\partial z} = 0 \tag{3.6}$$

Solving equations (3.4) and (3.5) to eliminate \vec{Q}' . The linearized perturbed equations reduce to the following.

$$\left(1 + \lambda_1 \frac{\partial}{\partial t}\right) \left[\frac{\rho_0}{\varepsilon} \frac{\partial}{\partial t} (\nabla^2 w') - \alpha g \rho_0 \nabla_1^2 T' + \mu_0 K_m \beta \frac{\partial}{\partial z} (\nabla_1^2 \phi') - \frac{\mu_0 K_m^2 \beta \nabla_1^2 T'}{1 + \chi_m} + \frac{2 \rho_0}{\varepsilon} \Omega \frac{\partial \zeta}{\partial z} \right] = \left(1 + \lambda_2 \frac{\partial}{\partial t}\right) \left[-\frac{\mu_f}{k} \nabla^2 w' \right] \quad (3.7)$$

$$\left(1 + \lambda_1 \frac{\partial}{\partial t}\right) \left[\frac{\rho_0}{\varepsilon} \frac{\partial \zeta}{\partial t} - \frac{2 \rho_0 \Omega}{\varepsilon} \frac{\partial w'}{\partial z} \right] = \left(1 + \lambda_2 \frac{\partial}{\partial t}\right) \left[-\frac{\mu_f}{k} \zeta \right] \quad (3.8)$$

$$\left(1 + \tau \frac{\partial}{\partial t}\right) \left[(\rho_0 C)_1 \frac{\partial T'}{\partial t} - \mu_0 T_a K_m \frac{\partial}{\partial t} \left(\frac{\partial \phi'}{\partial z} \right) - \left\{ (\rho_0 C)_2 - \frac{\mu_0 T_a K_m^2}{1 + \chi_m} \right\} \beta w' \right] = -k_1 \nabla^2 T' - \frac{\tau k_1 \beta}{2} \nabla^2 w' \quad (3.9)$$

$$(1 + \chi_m) \frac{\partial^2 \phi'}{\partial z^2} + \left(1 + \frac{M_0}{H_0}\right) \nabla_1^2 \phi' - K_m \frac{\partial T'}{\partial z} = 0 \quad (3.10)$$

where

$$(\rho_0 C)_1 = \varepsilon \rho_0 C_{V,H} + \varepsilon \mu_0 H_0 K_m + (1 - \varepsilon) (\rho_0 C)_s, \quad (\rho_0 C)_2 = \varepsilon \rho_0 C_{V,H} + \varepsilon \mu_0 H_0 K_m, \quad \nabla_1^2 = \frac{\partial^2}{\partial x^2} + \frac{\partial^2}{\partial y^2}, \quad \nabla^2 = \nabla_1^2 + \frac{\partial^2}{\partial z^2},$$

$$K_m = -\left(\frac{\partial M}{\partial T}\right)_{H_0, T_a}, \quad \chi_m = \left(\frac{\partial M}{\partial H}\right)_{H_0, T_a} \quad \text{and} \quad \zeta = \frac{\partial v'}{\partial x} - \frac{\partial u'}{\partial y} \quad \text{denotes the z-component of vorticity and } \phi' \text{ being magnetic potential.}$$

Considering the normal mode as follows

$$\begin{bmatrix} w' \\ T' \\ \phi' \\ \zeta' \end{bmatrix} = \begin{bmatrix} W(z) \\ \Theta(z) \\ \Phi(z) \\ \zeta(z) \end{bmatrix} e^{i(lx + my) + \sigma t} \quad (3.11)$$

along x and y directions wave numbers are l and m respectively and σ is the growth rate. Substitution of equation (3.11) into (3.7) to (3.10) leads to

$$\begin{aligned} (1 + \lambda_1 \sigma) \left[\frac{\rho_0}{\varepsilon} \sigma (D^2 - K_h^2) W + \alpha \rho_0 g K_h^2 \Theta - \mu_0 K_m \beta K_h^2 D \Phi + \frac{\mu_0 K_m^2 \beta K_h^2 \Theta}{1 + \chi_m} + \frac{2 \rho_0 \Omega D \zeta}{\varepsilon} \right] \\ = (1 + \lambda_2 \sigma) \left[-\frac{\mu_f}{k} (D^2 - K_h^2) W \right] \end{aligned} \quad (3.12)$$

$$(1 + \lambda_1 \sigma) \left[\frac{\rho_0}{\varepsilon} \sigma \zeta - \frac{2 \rho_0 \Omega}{\varepsilon} D W \right] = (1 + \lambda_2 \sigma) \left[-\frac{\mu_f}{k} \zeta \right] \quad (3.13)$$

$$\begin{aligned} (1 + \tau \sigma) \left[(\rho_0 C)_1 \sigma \Theta - \mu_0 T_a K_m \sigma D \Phi - \left\{ (\rho_0 C)_2 - \frac{\mu_0 T_a K_m^2}{1 + \chi_m} \right\} \beta W \right] \\ = k_1 (D^2 - K_h^2) \Theta - \frac{\tau k_1 \beta}{2} (D^2 - K_h^2) W \end{aligned} \quad (3.14)$$

$$(1 + \chi_m) D^2 \Phi - \left(1 + \frac{M_0}{H_0}\right) K_h^2 \Phi(z) - K_m D \Theta = 0 \quad (3.15)$$

where $D = d/dz$ and $K_h^2 = l^2 + m^2$ is the overall horizontal wave number. Considering the following scaling to non-dimensionalize the equations (3.12) to (3.15)

$$\left. \begin{aligned} W^* &= \frac{Wd}{\kappa}, \quad \Theta^* = \frac{\Theta}{\beta d}, \quad \Phi^* = \frac{\Phi}{\frac{K_m \beta d^2}{1 + \chi_m}}, \\ a &= K_h d, \quad z^* = \frac{z}{d}, \quad \sigma^* = \frac{\sigma}{\frac{\kappa}{d^2}}, \quad \zeta^* = \frac{\zeta}{\frac{\kappa}{d^2}} \end{aligned} \right\} \quad (3.16)$$

we get the following non dimensionless equations (for simplicity asterisks are neglected)

$$(1+F_1\sigma)\left[\frac{\sigma}{Va}(D^2-a^2)W+(1+M_1)Ra^2\Theta-Na^2D\Phi+\sqrt{Ta_D}D\zeta\right]=-(1+F_2\sigma)\left[(D^2-a^2)W\right] \quad (3.17)$$

$$(1+F_1\sigma)\left[\frac{\sigma}{Va}\zeta-\sqrt{Ta_D}DW\right]=-(1+F_2\sigma)\zeta \quad (3.18)$$

$$(1+2G\sigma)\left[\lambda\sigma\Theta-M_2\sigma D\Phi-(1-M_2)W\right]=(D^2-a^2)\Theta-G(D^2-a^2)W \quad (3.19)$$

$$(D^2-M_3a^2)\Phi-D\Theta=0 \quad (3.20)$$

where $\lambda = \frac{(\rho_0 C)_1}{(\rho_0 C)_2}$, $M_2 = \frac{\mu_0 K_m^2 Ta}{(1+\chi_m)(\rho_0 C)_2}$ and $G = \frac{\tau \kappa}{2d^2}$.

Eliminating ζ by substituting ζ from equation (3.18) in (3.17) and then equations (3.17) and (3.18) reduces to one equation as mentioned in equation (3.21), also neglecting M_2 from Finlayson [5] and assuming $\lambda=1$ we have the following

$$\begin{aligned} & \left[(1+F_1\sigma)\frac{\sigma}{Va} + (1+F_2\sigma) \right] (1+F_1\sigma) \left[\frac{\sigma}{Va}(D^2-a^2)W + (1+M_1)Ra^2\Theta - RM_1a^2D\Phi \right] \\ & + (1+F_1\sigma)^2 Ta_D D^2W = - \left[(1+F_1\sigma)\frac{\sigma}{Va} + (1+F_2\sigma) \right] (1+F_2\sigma) \left[(D^2-a^2)W \right] \end{aligned} \quad (3.21)$$

$$(1+2G\sigma)(\sigma\Theta-W) - (D^2-a^2)\Theta + G(D^2-a^2)W = 0 \quad (3.22)$$

$$(D^2-M_3a^2)\Phi - D\Theta = 0 \quad (3.23)$$

where $F_1 = \frac{\lambda_1 \kappa}{d^2}$ is the non-dimensional stress relaxation time, $F_2 = \frac{\lambda_2 \kappa}{d^2}$ is the non-dimensional strain retardation time, $Va = \frac{\varepsilon \mu_f d^2}{\rho_0 \kappa k}$ is the Vadasz number, $R_D = \frac{\alpha g \rho_0 \beta d^2 k}{\mu_f \kappa}$ is the Rayleigh-Darcy number, $M_1 = \frac{\mu_0 K_m^2 \beta}{(1+\chi_m) \alpha g \rho_0}$ is the

Magnetic number, $G = \frac{\tau \kappa}{2d^2}$ is the Cattaneo number, $Ta_D = \left(\frac{2\rho_0 \Omega k}{\mu_f \varepsilon} \right)^2$ is the Taylor-Darcy number and $M_3 = \left(\frac{1 + \frac{M_0}{H_0}}{1 + \chi_m} \right)$

is the non-buoyancy-magnetization parameter. Appropriate boundary conditions are $W = \Theta = D\Phi = 0$ at $z = \pm 1/2$.

3.1. Stationary Instability

For the stationary mode equations from (3.21) - (3.23) turn out to be the following

$$(1+M_1)Ra^2\Theta - RM_1a^2D\Phi + Ta_D D^2W + (D^2-a^2)W = 0 \quad (3.24)$$

$$\left[G(D^2-a^2) - 1 \right] W - (D^2-a^2)\Theta = 0 \quad (3.25)$$

$$(D^2-M_3a^2)\Phi - D\Theta = 0 \quad (3.26)$$

Equations (3.24) – (3.26) embracing an eigenvalue problem along with the boundary conditions with R being eigen value. The forthright solution $W = A_1 \cos(\pi z)$, $\Theta = A_2 \cos(\pi z)$, $\Phi = \frac{A_3}{\pi} \sin(\pi z)$, where A_1 , A_2 and A_3 are constants. On solving we obtain

$$R_D^{st} = \frac{p(a^2 M_3 + \pi^2)(p + \pi^2 Ta_D)}{a^2 (1 + G p) [a^2 (1 + M_1) M_3 + \pi^2]} \quad (3.27)$$

On substitution $G=0$ and $M_3 = 0$ in equation (3.27) exactly coincides with Kang *et al.*, [19] and Vadasz [41] and which is mentioned in equation (3.28). It should be noted that equation (3.27) is stationary Rayleigh-Darcy number is independent of viscoelastic parameters.

$$R_D^{st} = \frac{p^2 + p\pi^2 Ta_D}{a^2} \quad (3.28)$$

where superscript 'st' represents stationary convection.

3.2. Oscillatory Instability

$$\begin{bmatrix} (1+F_1\sigma)^2 \left\{ -\frac{\sigma^2}{Va^2}(\pi^2+a^2) - Ta_D \pi^2 \right\} \\ + (1+F_1\sigma)(1+F_2\sigma) \left(-\frac{2\sigma}{Va} \right) (\pi^2+a^2) \\ - (1+F_2\sigma)^2 (\pi^2+a^2) \end{bmatrix} A_1 + (1+F_1\sigma)(1+M_1) Ra^2 \left[(1+F_1\sigma) \frac{\sigma}{Va} + (1+F_2\sigma) \right] A_2 \quad (3.29)$$

$$\begin{aligned} - (1+F_1\sigma) R M_1 a^2 \left[(1+F_1\sigma) \frac{\sigma}{Va} + (1+F_2\sigma) \right] A_3 &= 0 \\ [1+2G\sigma+G(\pi^2+a^2)] A_1 - [(\pi^2+a^2)+(1+2G\sigma)\sigma] A_2 &= 0 \end{aligned} \quad (3.30)$$

$$\pi^2 A_2 - (\pi^2 + M_3 a^2) A_3 = 0 \quad (3.31)$$

On applying the solvability condition, we obtain

$$R = \frac{(a^2 M_3 + \pi^2)(p + \sigma + 2G\sigma^2) \left[\frac{\pi^2 Ta_D (Va)^2 (1+F_1\sigma)^2}{+ p(Va + \sigma(1+F_2 Va + F_1\sigma))^2} \right]}{a^2 [a^2(1+M_1)M_3 + \pi^2] Va (1+F_1\sigma) \left[\frac{Va(1+F_2\sigma)}{+\sigma(1+F_1\sigma)} \right] [1+G(p+2\sigma)]} \quad (3.32)$$

where $p = \pi^2 + a^2$. Let $\sigma = i\omega$ where ω is frequency of oscillation and we retrieve R in the form $R = R_1 + iR_2$, both R_1 and R_2 are computed by MATHEMATICA SOFTWARE.

4. RESULTS AND DISCUSSION

The aim of the study is to uptight with rotating porous medium ferroconvection in a viscoelastic magnetic fluid with second sound. Conditions for the pair of the stationary as well as oscillatory convection utilizing linear theory, has been established by normal mode technique. Characterization of the system's stability is taken into account by the thermal Rayleigh number R, which is obtained as a function of the various parameters. By utilizing MATHEMATICA software, Eigen value expression and the corresponding critical number are found. Newtonian behavior of viscoelastic fluid in stationary convection can be noticed. In oscillatory mode Rayleigh-Darcy number is derived as a function of Vadasz number, viscoelastic parameters namely strain retardation time and stress relaxation time, non-buoyancy magnetization parameter, Cattaneo number, Taylor-Darcy number and magnetization parameter. The values of the various parameters are fixed as follows $F_1=1.5$, $Va=2$, $F_2=0.3$, $G=0.06$, $M_3=2$ and $Ta_D=0.4$ and from the Figs. (2-8) critical Rayleigh-Darcy number $R_{D_c}^{osc}$ is expressed as a function of magnetic number M_1 .

In Figure 2 as there is an increment in M_1 , R_{D_c} decreases and destabilizes the system. We notice that the exchange principle of instabilities is invalid as stationary convection is not preferred over oscillatory convection as $R_{D_c}^{st}$ is higher than the $R_{D_c}^{osc}$. As the certain ranges of the governing parameters the fluid layer becomes overstable, i.e. the thermal instability gives rise to an oscillatory convective motion. Overstability is possible in the presence of rotation or a magnetic field because they lend an elastic-like behaviour to the fluid thereby enabling it to sustain appropriate modes of wave propagation. It is therefore expected that a layer of viscoelastic fluid can become overstable due solely to heating from below.

In Figure 3 we see that as and how F_1 and M_1 increases there is a decrement in $R_{D_c}^{osc}$ which conveys that the system destabilizes as oscillatory convection is hasten by the stress relaxation parameter F_1 . It is due to the fact that the relaxation time parameter accelerates the convection flow and weakens the viscoelastic fluid elasticity.

In Figure 4 as the the values of F_2 and M_1 increases we note that there is an increment in $R_{D_c}^{osc}$ which reveals that the retardation parameter F_2 halts the onset of oscillatory convection as it enhance the effect of elastic. Hence, the system stabilizes.

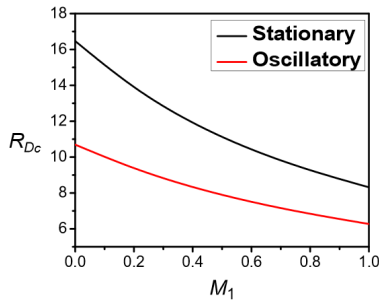


Figure 2. Variation of R with M_1 for $F_1 = 1.5$, $Va = 2$, $F_2 = 0.3$, $G = 0.06$, $M_3 = 2$ and $Ta_D = 0.4$

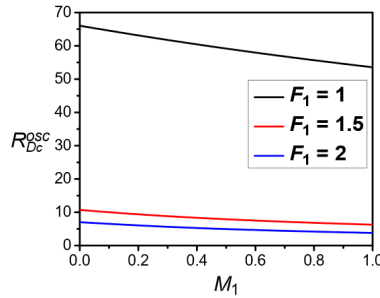


Figure 3. Variation of $R_{D_c}^{osc}$ with M_1 for $F_2 = 0.3$, $Va = 2$, $G = 0.06$, $M_3 = 2$ and $Ta_D = 0.4$

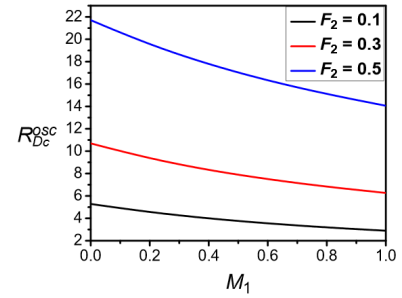


Figure 4. Variation of $R_{D_c}^{osc}$ with M_1 for $F_1 = 1.5$, $Va = 2$, $G = 0.06$, $M_3 = 2$ and $Ta_D = 0.4$

In Figure 5 as Va and M_1 increases there is a decrease in $R_{D_c}^{osc}$ and hence system destabilizes. As Vadasz number is the ratio of porosity, Prandtl number and Darcy number. In Figure 6 as there is an increment in G and M_1 we observe that there is an decrement in $R_{D_c}^{osc}$ due to the presence of dawn value of G and destabilizes the system. As parabolic equation is replaced by the hyperbolic equation in equation of temperature which guarantees the finite transmit of heat signals instead of infinite.

In Figure 7 the magnetic equation linear departure is expressed by the parameter M_3 . We observe from figure 7, as there is an increment in M_1 and M_3 then R_c^{osc} decreases monotonically which conveys that the magnetic equation of state grows larger and larger to nonlinear owed to which ferroconvection is threshold in porous layer with second sound is hastened.

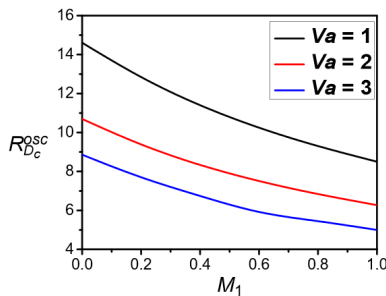


Figure 5. Variation of $R_{D_c}^{osc}$ with M_1 for $F_1 = 1.5$, $G = 0.06$, $F_2 = 0.3$, $M_3 = 2$ and $Ta_D = 0.4$

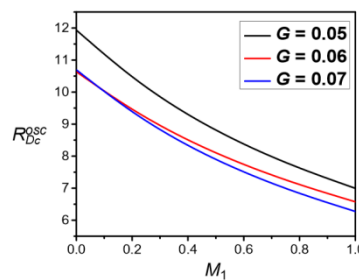


Figure 6. Variation of $R_{D_c}^{osc}$ with M_1 for $F_1 = 1.5$, $Va = 2$, $F_2 = 0.3$, $M_3 = 2$ and $Ta_D = 0.4$

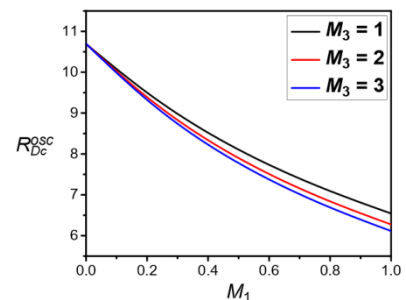


Figure 7. Variation of $R_{D_c}^{osc}$ with M_1 for $F_1 = 1.5$, $Va = 2$, $F_2 = 0.3$, $G = 0.06$ and $Ta_D = 0.4$

We notice from Figure 8, as M_1 and Ta_D increases the $R_{D_c}^{osc}$ monotonically decreases which implies that the system destabilizes as observed in Pérez *et al.* [50]. From Figure 9 through 13 we can observe that all parameters increase ω_c^2 also increases whereas noted from Fig. 14 as parameter increases ω_c^2 decreases. Hence, we can conclude from Figs. (9-14) that for all parameter ω_c is sensitive.

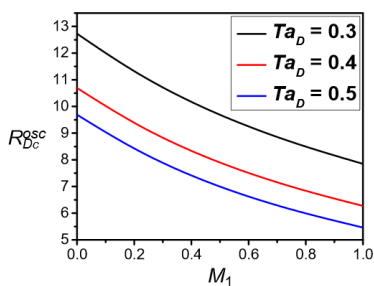


Figure 8. Variation of $R_{D_c}^{osc}$ with M_1 for $F_1 = 1.5$, $Va = 2$, $F_2 = 0.3$, $G = 0.06$ and $M_3 = 2$

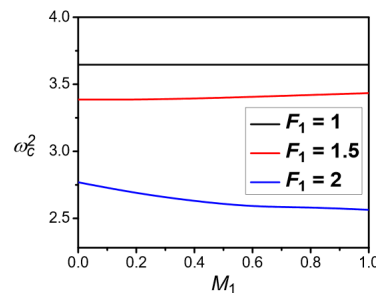


Figure 9. Variation of ω_c^2 with M_1 for $F_2 = 0.3$, $Va = 2$, $G = 0.06$, $M_3 = 2$ and $Ta_D = 0.4$

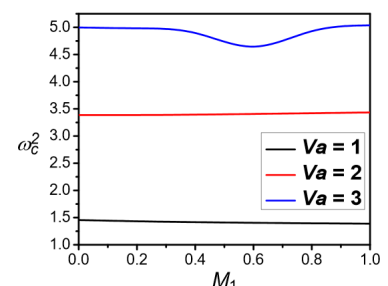


Figure 10. Variation of ω_c^2 with M_1 for $F_1 = 1.5$, $G = 0.06$, $F_2 = 0.3$, $M_3 = 2$ and $Ta_D = 0.4$

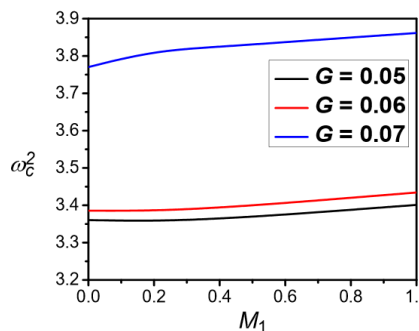


Figure 11. Variation of ω_c^2 with M_1 for $F_1 = 1.5, Va = 2, F_2 = 0.3, M_3 = 2$ and $Ta_D = 0.4$

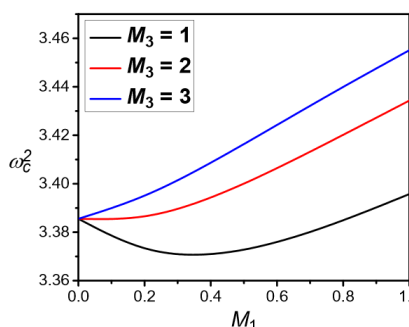


Figure 12. Variation of ω_c^2 with M_1 for $F_1 = 1.5, Va = 2, F_2 = 0.3, G = 0.06$ and $Ta_D = 0.4$

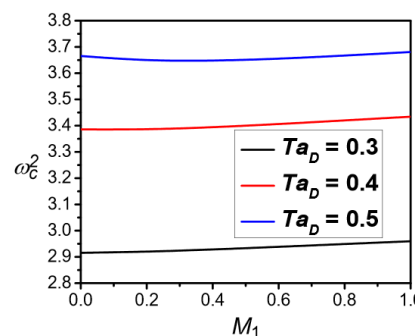


Figure 13. Variation of ω_c^2 with M_1 for $F_1 = 1.5, Va = 2, F_2 = 0.3, G = 0.06$ and $M_3 = 2$

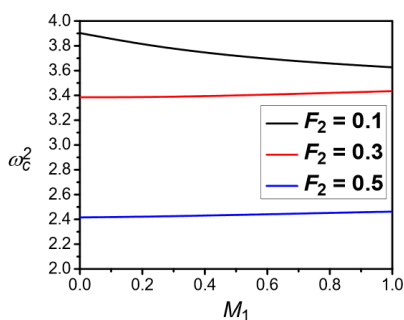


Figure 14. Variation of ω_c^2 with M_1 for $F_1 = 1.5, Va = 2, G = 0.06, M_3 = 2$ and $Ta_D = 0.4$

From Table 1 through 10, we can analyze the effect of $M_1, F_1, F_2, Va, M_3, G$ and Ta_D on wave number which represents the shape and size of the convection cell. If we observe closely α_c increases with an increase in $F_1, Va,$ and Ta_D which implies that the convection cell size is contracted and decrement of α_c with an increment in F_2 and M_3 which implies that the convection cell size is enlarge.

Table 1. Rayleigh-Darcy number and wavenumber critical values for $M_3 = 2, G = 0.06$ and $Ta_D = 0.4$.

M_1	Stationary		Oscillatory ($F_1 = 1.5, F_2 = 0.3$ and $Va = 2$)	
	$R_{D_c}^{st}$	α_c^{st}	$R_{D_c}^{osc}$	α_c^{osc}
0	16.4701	10.37	10.6941	2.95604
0.2	13.7853	11.8764	9.33656	2.95659
0.4	11.8449	13.3015	8.30025	2.9467
0.6	10.3798	14.6747	7.48287	2.93229
0.8	9.23542	16.0167	6.82082	2.91624
1.0	8.31733	17.3428	6.27287	2.89995

Table 2. Rayleigh-Darcy number and wavenumber critical values with variation in F_1 by fixing $F_2 = 0.3, Va = 2, G = 0.06, M_3 = 2$ and $Ta_D = 0.4$

M_1	$F_1 = 1$		$F_1 = 1.5$		$F_1 = 2$	
	$R_{D_c}^{osc}$	α_c	$R_{D_c}^{osc}$	α_c	$R_{D_c}^{osc}$	α_c
0	66.0416	1.0	10.6941	2.95604	7.02019	4.08829
0.2	63.0998	1.0	9.33656	2.95659	6.01014	4.23206
0.4	60.4089	1.0	8.30025	2.9467	5.24903	4.33444
0.6	57.9381	1.0	7.48287	2.93229	4.65661	4.41049
0.8	55.6615	1.0	6.82082	2.91624	4.18356	4.41592
1.0	53.557	1.0	6.27287	2.89995	3.79694	4.44985

Table 3. Rayleigh-Darcy number and wavenumber critical values with variation in F_2 by fixing $F_1=1.5, Va=2, G=0.06, M_3=2$ and $Ta_D=0.4$

M_1	$F_2=0.1$		$F_2=0.3$		$F_2=0.5$	
	$R_{D_c}^{osc}$	α_c	$R_{D_c}^{osc}$	α_c	$R_{D_c}^{osc}$	α_c
0	5.28459	3.73769	10.6941	2.95604	21.7013	2.10033
0.2	4.54376	3.88231	9.33656	2.95659	19.5045	2.09634
0.4	3.98017	3.98809	8.30025	2.9467	17.7445	2.08973
0.6	3.5386	4.06835	7.48287	2.93229	16.2999	2.08205
0.8	3.18399	4.13112	6.82082	2.91624	15.0903	2.07412
1.0	2.89327	4.18153	6.27287	2.89995	14.0605	2.06634

Table 4. Rayleigh-Darcy number and wavenumber critical values with variation in Va by fixing $F_1=1.5, F_2=0.3, G=0.06, M_3=2$ and $Ta_D=0.4$

M_1	$Va=1$		$Va=2$		$Va=3$	
	$R_{D_c}^{osc}$	α_c	$R_{D_c}^{osc}$	α_c	$R_{D_c}^{osc}$	α_c
0	14.6089	2.86345	10.6941	2.95604	8.85992	3.42225
0.2	12.7803	2.88742	9.33656	2.95659	7.6532	3.43747
0.4	11.3542	2.90293	8.30025	2.9467	6.74327	3.43444
0.6	10.2125	2.91381	7.48287	2.93229	5.83093	3.86296
0.8	9.27831	2.92172	6.82082	2.91624	5.4638	3.40712
1.0	8.50012	2.92776	6.27287	2.89995	4.99651	3.38998

Table 5. Rayleigh-Darcy number and wavenumber critical values with variation in G by fixing $F_1=1.5, F_2=0.3, Va=2, M_3=2$ and $Ta_D=0.4$

M_1	$G=0.05$		$G=0.06$		$G=0.07$	
	$R_{D_c}^{osc}$	α_c	$R_{D_c}^{osc}$	α_c	$R_{D_c}^{osc}$	α_c
0	11.9367	2.93641	10.6352	2.51388	10.6941	2.95604
0.2	10.4218	2.93976	9.42077	2.5064	9.33656	2.95659
0.4	9.26372	2.93204	8.47648	2.49413	8.30025	2.9467
0.6	8.3496	2.91933	7.71939	2.48015	7.48287	2.93229
0.8	7.60895	2.90462	7.09719	2.46593	6.82082	2.91624
1.0	6.99591	2.8894	6.57551	2.45216	6.27287	2.89995

Table 6. Rayleigh-Darcy number and wavenumber critical values with variation in M_3 by fixing $F_1=1.5, F_2=0.3, Va=2, G=0.06$ and $Ta_D=0.4$

M_1	$M_3=1$		$M_3=2$		$M_3=3$	
	$R_{D_c}^{osc}$	α_c	$R_{D_c}^{osc}$	α_c	$R_{D_c}^{osc}$	α_c
0	10.6941	2.95604	10.6941	2.95604	10.6941	2.95604
0.2	9.45654	2.97246	9.33656	2.95659	9.26594	2.94614
0.4	8.48826	2.97412	8.30025	2.9467	8.18962	2.92977
0.6	7.71149	2.96775	7.48287	2.93229	7.34809	2.91153
0.8	7.07459	2.95709	6.82082	2.91624	6.6709	2.89336
1.0	6.54253	2.94429	6.27287	2.89995	6.11327	2.87608

Table 7. Rayleigh-Darcy number and wavenumber critical values with variation in Ta_D by fixing $F_1=1.5, F_2=0.3, Va=2, G=0.06$ and $M_3=2$

M_1	$Ta_D=0.3$		$Ta_D=0.4$		$Ta_D=0.5$	
	$R_{D_c}^{osc}$	α_c	$R_{D_c}^{osc}$	α_c	$R_{D_c}^{osc}$	α_c
0	12.7272	2.4949	10.6941	2.95604	9.69108	3.39212
0.2	11.2701	2.49011	9.33656	2.95659	8.37313	3.41198
0.4	10.1351	2.47993	8.30025	2.9467	7.37744	3.4126
0.6	9.22452	2.46759	7.48287	2.93229	6.59972	3.40376
0.8	8.47612	2.45467	6.82082	2.91624	5.9755	3.3904
1.0	7.84879	2.44195	6.27287	2.89995	5.46319	3.37507

CONCLUSIONS

The onset of thermal ferro-convection in a viscoelastic fluid saturated rotating porous layer with second sound is examined analytically using linear stability analysis. The linear theory provides the onset criteria for both stationary and oscillatory convection. The following conclusions are drawn:

- The most favorable mode of thermal instability is the oscillatory mode.
- Ferro-convective viscoelastic fluid coincides with the ferro-convective Newtonian fluid saturated rotating porous layer with second sound in stationary case. It is due to the fact that the base state has no flow and any viscoelastic fluid of simple fluid type becomes Newtonian when the flow is steady and weak.
- Magnetic parameters M_1 and M_3 , viscoelastic stress relaxation parameter F_1 , Vadasz number Va and Cattaneo number G strengthens the destabilizing effect of Taylor-Darcy number Ta_D in the oscillatory mode.
- Viscoelastic strain retardation parameter F_2 , advances the oscillatory mode.
- Critical frequency and wavenumber of oscillatory motions are determined as functions of all the parameters of the problem. For all the parameters they are sensitive.

ORCID

✉Naseer Ahmed, <https://orcid.org/0000-0002-5327-9362>; ✉S. Maruthamanikandan, <https://orcid.org/0000-0001-9811-0117>

REFERENCES

- [1] M.T. Shliomis, "Magnetic fluid," *Sov. Phys. Usp.* **17**, 53–169 (1974). <https://doi.org/10.1070/PU1974v017n02ABEH004332>
- [2] R.E. Rosensweig, *Ferrohydrodynamics*, (Cambridge University Press, Cambridge, 1985).
- [3] R.E. Rosensweig, J.W. Nestor, and R.S. Timmins, *Ferrohydrodynamic Fluids for Direct Conversion of Heat Energy. Materials Associated with Direct Energy Conversion*, (Avco Corporation, Wilmington, 1965).
- [4] R.E. Rosensweig, *Ferrohydrodynamics*, (Dover Publications, Courier Corporation, Mineola, New York, 1997).
- [5] B.A. Finlayson, "Convective instability of ferromagnetic fluids," *Journal of Fluid Mechanics*, **40**(4), 753–767 (1970). <https://doi.org/10.1017/S0022112070000423>
- [6] L. Schwab, U. Hildebrandt, and K. Stierstadt, "Magnetic Bénard convection," *Journal of Magnetism and Magnetic Materials*, **39**(2), 113–124 (1983). [https://doi.org/10.1016/0304-8853\(83\)90412-2](https://doi.org/10.1016/0304-8853(83)90412-2)
- [7] P.J. Stiles, and M. Kagan, "Thermoconvective instability of a horizontal layer of ferrofluid in a strong vertical magnetic field," *Journal of magnetism and magnetic materials*, **85**(1), 196–198 (1990). [https://doi.org/10.1016/0304-8853\(90\)90050-Z](https://doi.org/10.1016/0304-8853(90)90050-Z)
- [8] D.P. Lalas, and S. Carmi, "Thermoconvective stability of ferrofluids," *Phys. Fluids*, **14**(2), 436–437 (1971). <https://doi.org/10.1063/1.1693446>
- [9] A. Mahajan, and M.K. Sharma, "Penetrative convection in magnetic nanofluids via internal heating," *Phys. Fluids*, **29**, 034101 (2017). <https://doi.org/10.1063/1.4977091>
- [10] N.M. Thomas, and S. Maruthamanikandan, "Gravity modulation effect on ferromagnetic convection in a Darcy-Brinkman layer of porous medium," *J. Phys. Conf. Ser.* **1139**(1), 1–10 (2018). <https://doi.org/10.1088/1742-6596/1139/1/012022>
- [11] S. Mathew, S. Maruthamanikandan, and S.N. Smita, "Gravitational instability in a ferromagnetic fluid saturated porous medium with non-classical heat conduction," *IOSR Journal of Mathematics*, **6**, 7–18 (2013). <https://doi.org/10.9790/5728-0610718>
- [12] D. Laroze, and H. Pleiner, "Thermal convection in a nonlinear non-Newtonian magnetic fluid," *Communications in Nonlinear Science and Numerical Simulation*, **26**(3), 167–183 (2015). <https://doi.org/10.1016/j.cnsns.2015.01.002>
- [13] C. Balaji, C. Rudresha, V.V. Shree, and S. Maruthamanikandan, "Ferroconvection in a sparsely distributed porous medium with time-dependent sinusoidal magnetic field," *Journal of Mines, Metals and Fuels*, **70**(3A), 28–34 (2022). <https://doi.org/10.18311/jmmf/2022/30664>
- [14] V.V. Shree, C. Rudresha, C. Balaji, and S. Maruthamanikandan, "Effect of MFD viscosity on ferroconvection in a fluid saturated porous medium with variable gravity," *Journal of Mines, Metals and Fuels*, **70**(3A), 98–103 (2022). <https://doi.org/10.18311/jmmf/2022/30675>
- [15] N. Ahmed, S. Maruthamanikandan, and B.R. Nagasmita, "Oscillatory porous medium ferroconvection in a viscoelastic magnetic fluid with non-classical heat conduction," *East Eur. J. Phys.* **2**, 296–309 (2023). <https://doi.org/10.26565/2312-4334-2023-2-34>
- [16] J.G. Oldroyd, "On the formulation of rheological equations of state," *Proc. R. Soc. Lond. A*, **200**, 523–541 (1950). <https://doi.org/10.1098/rspa.1950.0035>
- [17] T. Green, "Oscillating convection in an elasticoviscous liquid," *Phys. Fluids*, **11**, 1410–1414 (1968). <https://doi.org/10.1063/1.1692123>
- [18] M.S. Malashetty, M.S. Swamy, and W. Sidram, "Thermal convection in a rotating viscoelastic fluid saturated porous layer," *International Journal of Heat and Mass Transfer*, **53**(25), 5747–5756 (2010). <https://doi.org/10.1016/j.ijheatmasstransfer.2010.08.008>
- [19] J. Kang, C. Fu, and W. Tan, "Thermal convective instability of viscoelastic fluids in a rotating porous layer heated from below," *Journal of Non-Newtonian Fluid Mechanics*, **166**(1), 93–101 (2011). <https://doi.org/10.1016/j.jnnfm.2010.10.008>
- [20] D. Laroze, J. Martinez-Mardones, and H. Pleiner, "Bénard-Marangoni instability in a viscoelastic ferrofluid," *The European Physical Journal Special Topics*, **219**, 71–80 (2013). <https://doi.org/10.1140/epjst/e2013-01782-6>
- [21] B.S. Bhadauria, and P. Kiran, "Heat and mass transfer for oscillatory convection in a binary viscoelastic fluid layer subjected to temperature modulation at the boundaries," *International Communications in Heat and Mass Transfer*, **58**, 166–175 (2014). <https://doi.org/10.1016/j.icheatmasstransfer.2014.08.031>
- [22] L.S. de B. Alves, S.C. Hirata, and M.N. Ouarzazi, "Linear onset of convective instability for Rayleigh-Bénard-Couette flows of viscoelastic fluids," *Journal of Non-Newtonian Fluid Mechanics*, **231**, 79–90 (2016). <https://doi.org/10.1016/j.jnnfm.2016.03.007>
- [23] S. Nadeem, S. Ahmad, and N. Muhammad, "Cattaneo-Christov flux in the flow of a viscoelastic fluid in the presence of Newtonian heating," *Journal of Molecular liquids*, **237**, 180–184 (2017). <https://doi.org/10.1016/j.molliq.2017.04.080>
- [24] M.N. Mahmud, Z. Siri, J.A. Vélez, L.M. Pérez, and D. Laroze, "Chaotic convection in an Oldroyd viscoelastic fluid in saturated porous medium with feedback control," *Chaos: An Interdisciplinary Journal of Nonlinear Science*, **30**(7), 73109–73121 (2020). <https://doi.org/10.1063/5.0002846>
- [25] R. Sharma, and P.K. Mondal, "Thermosolutal Marangoni instability in a viscoelastic liquid film: Effect of heating from the free surface," *Journal of Fluid Mechanics*, **909**, 1–24 (2021). <https://doi.org/10.1017/jfm.2020.880>

- [26] K. Song, G. Jin, D. Jia, R. Hua, T. Ye, Z. Sun, and Z. Liu, "Effects of viscoelastic fluid on noise reduction of the flow over a circular cylinder," *Journal of Fluids and Structures*, **122**, 103976 (2023).
- [27] J.S. Dhiman, P.M. Patil, and S. Sood, "Modified stability analysis of double-diffusive convection in viscoelastic fluid layer saturating porous media," *Heat Transfer*, **52**, 1497-1528 (2023). <https://doi.org/10.1002/htj.22752>
- [28] S. Saravanan, and T. Sivakumar, "Onset of filtration convection in a vibrating medium: The Brinkman model," *Physics of Fluids*, **22**(3), 34104–34120 (2010). <https://doi.org/10.1063/1.3358461>
- [29] C. Rudresha, C. Balaji, V. Vidya Shree, and S. Maruthamanikandan, "Effect of electric field modulation on electroconvection in a dielectric fluid-saturated porous medium," *Journal of Mines, Metals and Fuels*, **70**(3A), 35–41 (2022). <https://doi.org/10.18311/jmmf/2022/30665>
- [30] M.S. Malashetty, and M. Swamy, "The onset of convection in a viscoelastic liquid saturated anisotropic porous layer," *Transport in Porous Media*, **67**(2), 203–218 (2007). <https://doi.org/10.1007/s11242-006-9001-7>
- [31] C. Rudresha, C. Balaji, V.V. Shree, and S. Maruthamanikandan, "Effect of electric field modulation on the onset of electroconvection in a dielectric fluid in an anisotropic porous layer," *Journal of Computational Applied Mechanics*, **53**(4), 510-523 (2022). <https://doi.org/10.22059/jcamesh.2022.348183.753>
- [32] G. Lebon, and A. Clout, "Benard-Marangoni instability in a Maxwell-Cattaneo fluid," *Physica A*, **105**, 361–364 (1984). [https://doi.org/10.1016/0375-9601\(84\)90281-0](https://doi.org/10.1016/0375-9601(84)90281-0)
- [33] S. Maruthamanikandan, and S.S. Nagouda, "Convective heat transfer in Maxwell-Cattaneo dielectric fluids," *International Journal of Computational Engineering Research*, **3**(3), 347–355 (2013).
- [34] S. Mathew, and S. Maruthamanikandan, "Oscillatory porous medium ferroconvection with Maxwell-Cattaneo law of heat conduction," *J. Phys. Conf. Ser.*, **1850**(1), 012024 (2021). <https://doi.org/10.1088/1742-6596/1850/1/012024>
- [35] N. Ahmed, and S. Maruthamanikandan, "Oscillatory Thermoconvective Instability in a Viscoelastic Magnetic Fluid Saturated Anisotropic Porous Medium with Second Sound," *Eur. Chem. Bull.* **12**(6), 899–928 (2023).
- [36] R. Friedrich, "Einflug der Prandtl-Zahl auf die Zellularkonvektion in einem rotierenden mit Fluid gesättigten porösen medium," *Z. Angew. Math. Mech.* **63**, 246–249 (1983).
- [37] P.R. Patil, and G. Vaidyanathan, "On setting up of convective currents in a rotating porous medium under the influence of variable viscosity," *Int. J. Eng. Sci.* **21**, 123–130 (1983). [https://doi.org/10.1016/0020-7225\(83\)90004-6](https://doi.org/10.1016/0020-7225(83)90004-6)
- [38] E. Palm, and A. Tyvand, "Thermal convection in a rotating porous layer," *Z. Angew. Math. Phys.* **35**, 122–123 (1984). <https://doi.org/10.1007/BF00945182>
- [39] J.J. Jou, and J.S. Liaw, "Thermal convection in a porous medium subject to transient heating and rotating," *Int. J. Heat Mass Transfer*, **30**, 208–211 (1987).
- [40] Y. Qin, and P.N. Kaloni, "Nonlinear stability problem of a rotating porous layer," *Quart. Appl. Math.* **53**(1), 129–142 (1995). <https://www.ams.org/journals/qam/1995-53-01/S0033-569X-1995-1315452-3/S0033-569X-1995-1315452-3.pdf>
- [41] P. Vadasz, "Coriolis effect on gravity-driven convection in a rotating porous layer heated from below," *J. Fluid Mech.* **376**, 351-375 (1998). <https://doi.org/10.1017/S0022112098002961>
- [42] B. Straughan, "A sharp nonlinear stability threshold in rotating porous convection," *Proc. Roy. Soc. Lond. A*, **457**, 87–93 (2001). <https://doi.org/10.1098/rspa.2000.0657>
- [43] S. Govender, "Oscillating convection induced by gravity and centrifugal forces in a rotating porous layer distant from the axis of rotation," *Int. J. Eng. Sci.* **41**, 539-545 (2003). [https://doi.org/10.1016/S0020-7225\(02\)00182-9](https://doi.org/10.1016/S0020-7225(02)00182-9)
- [44] S. Govender, "Coriolis effect on the linear stability of convection in a porous layer placed far away from the axis of rotation," *Transport Porous Media*, Vol. 51, pp. 315–326, 2003.
- [45] Th. Desaive, M. Hennenberg, and G. Lebon, "Thermal instability of a rotating saturated porous medium heated from below and submitted to rotation," *Eur. Phys. J. B*, **29**, 641–647 (2002). <https://doi.org/10.1140/epjb/e2002-00348-9>
- [46] B. Straughan, "Global non-linear stability in porous convection with a thermal non-equilibrium model," *Proc. Roy. Soc. Lond. A*, **462**, 409-418 (2006). <https://doi.org/10.1098/rspa.2005.1555>
- [47] M.S. Malashetty, and M. Swamy, "The effect of rotation on the onset of convection in a horizontal anisotropic porous layer," *Int. J. Therm. Sci.* **46**, 1023–1032 (2007). <https://doi.org/10.1016/j.ijthermalsci.2006.12.007>
- [48] J.S. Dhiman, and S. Sood, "Linear and weakly non-linear stability analysis of oscillatory convection in rotating ferrofluid layer," *Applied Mathematics and Computation*, **430**, 127239 (2022). <https://doi.org/10.1016/j.amc.2022.127239>
- [49] P.K. Nadian, "Thermoconvection in a kuvshiniski ferrofluid in presence of rotation and varying gravitational field through a porous medium," *South East Asian Journal of Mathematics & Mathematical Sciences*, **19**(1), 433-446 (2023). <https://doi.org/10.56827/SEAJMMS.2023.1901.33>
- [50] L.M. Pérez, D. Laroze, P. Díaz, J. Martinez-Mardones, and H.L. Mancini, "Rotating convection in a viscoelastic magnetic fluid," *Journal of Magnetism and Magnetic Materials*, **364**, 98–105 (2014). <https://doi.org/10.1016/j.jmmm.2014.04.027>

ОСЦИЛЯЦІЙНА ФЕРОКОНВЕКЦІЯ МАКСВЕЛЛА-КАТТАНЕО В ЩІЛЬНОУПАКОВАНОМУ ОБЕРТОВОМУ ПОРИСТОМУ СЕРЕДОВИЩІ, НАСИЧЕНОМУ В'ЯЗКОПРУЖНОЮ МАГНІТНОЮ РІДИНОЮ

Насір Ахмед^а, С. Марутаманікандан^б

^аDepartment of Mathematics, Presidency College, Kempapura, Hebbal, Bangalore 560024, India

^бДепартамент математики, Інженерна школа, Президентський університет, Бенгалур, 560064, Індія

За допомогою класичного аналізу стабільності на початку фeroконвекції обертового пористого середовища досліджено комбінований ефект другого звуку та в'язкопружності. Передбачається локальна теплова рівновага між твердою матрицею та рідиною. Поточна проблема розглядається за допомогою аналітичного підходу з урахуванням відповідних граничних умов. Техніка аналізу нормального режиму використовується для отримання критичних значень для обох видів нестабільностей, а саме стаціонарної та коливальної. Ми помітили, що коливальний режим нестабільності має перевагу над стаціонарним режимом нестабільності. Ми виявили, що магнітні сили, другий звук, нелінійність намагніченості, число Вадаша, релаксація напруги через в'язкопружність і число Тейлора-Дарсі сприяють розвитку осцилюючої пористої фeroконвекції середовища, тоді як затримка деформації відкладає початок коливальної пористої фeroконвекції середовища. Також відзначено вплив розміру конвекційної комірки за різними параметрами та частотою коливань. Ця проблема матиме значні можливі технологічні застосування, у яких задіяні в'язкопружні магнітні рідини.

Ключові слова: конвекція; обертання; в'язкопружні рідини; рівняння Максвелла; пористі середовища; рівняння Нав'є-Стокса для нестисливих в'язких рідин